

NUMERICAL METHODS FOR SHAPE OPTIMIZATION OF PHOTONIC NANOSTRUCTURES

Zur Erlangung des akademischen Grades eines
DOKTORS DER NATURWISSENSCHAFTEN (Dr. rer. nat.)

von der KIT-Fakultät für Physik
des Karlsruher Instituts für Technologie (KIT)
angenommene
DISSERTATION

von

M. Sc. Xavier García Santiago

am Institut für Theoretische Festkörperphysik

Tag der mündlichen Prüfung: 27. November 2020
Referent: Prof. Dr. Carsten Rockstuhl
Korreferent: Prof. Dr. Thomas Pertsch



This document (with the exception of reprinted figures for which the copyright is held by the respective journal) is licensed under the Creative Commons AttributionShareAlike 4.0 International License. To view a copy of this license, visit <https://creativecommons.org/licenses/by-sa/4.0/>.

Abstract

Inverse design is an important discipline in any field of engineering and science. Optics and photonics is not an exception. Together with improved fabrication technologies, design optimization is one of the main drivers of the tremendous advances in photonic technologies. The appearance of modern computers and software, able to solve electromagnetic field propagation problems, semi-automatized the tasks of design optimization. The final goal of this field would be to achieve full automation. That means, a design process completely computer-driven, able to find optimal designs, compatible with available fabrication processes, and without involving in the process the intuition and knowledge of the researcher or designer.

The optimization methods that get close to this idea are freeform shape optimization and topology optimization. The efficiency of both methods strongly relies on another computational ability related to solving electromagnetic field propagation: the computation of shape and material derivatives. Developments to achieve this ability are a fundamental building block of this thesis and they appear, in one way or another, throughout all chapters.

In this thesis, we study different numerical tools for computational inverse design of photonic structures. We focus on global optimization, as opposed to local optimization methods, and we investigate the use of a technique borrowed from the field of machine learning, Gaussian processes, to do global optimization using, at the same time, shape and material derivatives. We contribute to this field proposing two numerical techniques to improve the performance of Gaussian processes in the optimization of photonic structures.

Furthermore, we design and study the performance of two photonic structures that are interesting from theoretical and technological aspects: maximally electromagnetic chiral scatterers and waveguide edge couplers. Maximally electromagnetic chiral scatterers are objects that show an extraordinary difference in their interaction with fields of different helicity. Finding objects with such characteristics at optical and near infrared frequencies would enable a series of interesting applications. We obtain optimal designs of chiral scatterers at a wide range of illumination frequencies and highlight their extreme properties when they interact with light. The other structure studied, waveguide edge couplers, is a fundamental component to improve the power efficiency of integrated photonic circuits, therefore, a key component for the further development of the global optical communication network. We optimized and studied two types of edge couplers, including freeform shape designs, whose optimization lead to compact and energy efficient structures. For the optimization of both photonic structures, we combined the use of Bayesian optimization with Gaussian processes and the calculation of shape derivatives. Furthermore, the design of these structures required the development of additional numerical tools, e.g., methods for the analyses of isolated scatterers, that became an important part of this thesis by themselves.

Contents

List of publications	1
1 Introduction	5
2 Theoretical background	11
2.1 Introduction	11
2.2 Electromagnetic field theory	11
Maxwell's equations	11
The wave equation	14
Scattering by isolated objects	18
The helicity operator	19
Waveguide theory	20
2.3 The finite element method	23
Description of the method	24
Shape and material derivatives	29
The direct and the adjoint methods	32
3 Bayesian optimization	35
3.1 Introduction	35
3.2 Gaussian Processes	38
Definition	38
Gaussian process regression	40
Gaussian process regression with derivative information	42
Model selection	43
3.3 Bayesian Optimization Using Gaussian Processes	45
General description	45
Bayesian Optimization using derivative information	47
3.4 Scalable Bayesian Optimization	49
The scalability problem	49
Matrix update of the Cholesky decomposition	51
Bayesian optimization with a local Gaussian process model	54
3.5 Conclusions	57
4 Design of isolated scatterers	59
4.1 Introduction	59
4.2 Decomposition of scattered fields into VSWFs using surfaces with general shapes	61
Mathematical derivation	61
FEM implementation of the decomposition	66
Decomposition of fields scattered from cylindrically symmetric objects	71
4.3 Calculation of the T-matrix	73

Description	73
Example: Design of dual cylinders	75
4.4 Calculation of shape and material derivatives for T-matrices	77
4.5 The adjoint method for multi-scattering problems	78
Description	78
Example: metasurface hologram	81
4.6 Conclusions	83
5 Application examples	85
5.1 Maximal electromagnetic chiral helices	85
Introduction	85
Electromagnetic chirality	87
Simulation setup	88
Results of the optimization	91
Conclusions	97
5.2 Waveguide coupler for photonic inter-chip communication	99
Introduction	99
Parametric waveguide coupler	102
Freeform waveguide coupler	106
Conclusions	111
6 Conclusions	113
Bibliography	117
Appendices	139
A Definition of the vector spherical wave functions	141
B Multipole decomposition of a plane wave	143
Acknowledgements	145
Selbstständigkeitserklärung	147

List of publications

Published peer-review scientific publications

1. X. Garcia-Santiago, S. Burger, C. Rockstuhl, and P.-I. Schneider, "Bayesian optimization with improved scalability and derivative information for efficient design of nanophotonic structures", Accepted for publication in *Journal of Lightwave Technology* (2020)
2. D. Werdehausen, X. Garcia-Santiago, S. Burger, I. Staude, T. Pertsch, C. Rockstuhl, M. Decker, "Modelling Optical Materials at the Single Scatterer Level - The Transition from Homogeneous to Heterogeneous Materials", Accepted for publication in *Advance Theory and Simulations* (2020)
3. J. Feis, D. Beutel, J. Köpfler, X. Garcia-Santiago, C. Rockstuhl, M. Wegener, and I. Fernandez-Corbaton, "Helicity-preserving optical cavity modes for enhanced sensing of chiral molecules", *Physical Review Letters*, **124** (3), 033201 (2020)
4. P. Gutsche, X. Garcia-Santiago, P.-I. Schneider, K. M. McPeak, M. Nieto-Vesperinas, and S. Burger, "Role of Geometric Shape in Chiral Optics", *Symmetry*, **12** (1), 158 (2020)
5. A. Rahimzadegan, D. Arslan, D. Dams, A. Groner, X. Garcia-Santiago, R. Alaei, I. Fernandez-Corbaton, T. Pertsch, I. Staude, and C. Rockstuhl, "Beyond dipolar Huygens' metasurfaces for full-phase coverage and unity transmittance", *Nanophotonics*, **9** (1), 75-82 (2020)
6. P.-I. Schneider, X. Garcia-Santiago, V. Soltwisch, M. Hammerschmidt, S. Burger, C. Rockstuhl, "Benchmarking five global optimization approaches for nano-optical shape optimization and parameter reconstruction", *ACS Photonics*, **6** (11), 2726-2733 (2019)
7. F. Graf, J. Feis, X. Garcia-Santiago, M. Wegener, C. Rockstuhl, and I. Fernandez-Corbaton, "Achiral, helicity preserving, and resonant structures for enhanced sensing of chiral molecules", *ACS Photonics*, **6** (2), 482-491 (2019)
8. X. Garcia-Santiago, M. Hammerschmidt, S. Burger, C. Rockstuhl, I. Fernandez-Corbaton, and L. Zschiedrich, "Decomposition of scattered electromagnetic fields into vector spherical wave functions on surfaces with general shapes", *Physical Review B*, **99** (4), 045406 (2019)
9. X. Garcia-Santiago, S. Burger, C. Rockstuhl, and I. Fernandez-Corbaton, "Measuring the electromagnetic chirality of 2D arrays under normal illumination", *Optics Letters*, **45** (20), 4075-4078 (2017)

Submitted peer-review scientific publications

1. P. Scott, X. Garcia-Santiago, D. Beutel, C. Rockstuhl, M. Wegener, and I. Fernandez-Corbaton, "On enhanced sensing of chiral molecules in optical cavities", *Submitted to Applied Physics Reviews*

Scientific publications in preparation

1. X. Garcia-Santiago, M. Hammerschmidt, S. Burger, J. Sachs, P. Fisher, M. Knöller, T. Arens, F. Hettlich, R. Griesmaier, I. Fernandez-Corbaton, and C. Rockstuhl, "Towards maximal electromagnetically chiral scatterers at optical frequencies"

Conference contributions

1. X. Garcia-Santiago, P.-I. Schneider, S. Burger, and C. Rockstuhl, "Global optimization of a free-form waveguide coupler", *Workshop on Theoretical and Numerical Tools for Nanophotonics (TNTN2020)*, (Berlin, 02-2020)

2. X. Garcia-Santiago, P.-I. Schneider, S. Burger, and C. Rockstuhl, "Towards Scalable Bayesian Optimization", *12th Annual Meeting Photonic Devices*, (Berlin, 02-2019)

3. P.-I. Schneider, X. Garcia-Santiago, L. Zschiedrich, C. Rockstuhl, and S. Burger, "Optimization of quantum optical devices with machine learning approaches", *Workshop Quantum Optics and Secure Optical Transmission*, (Berlin, 18-10-2018)

4. X. Garcia-Santiago, P.-I. Schneider, S. Burger, and C. Rockstuhl, "Shape optimization of nanostructures with Bayesian optimization and derivative information", *European Optical Society Biennial Meeting*, (Delft 8-10-2018)

5. P.-I. Schneider, X. Garcia-Santiago, F. Binkowski, P. Gutsche, T. Hoehne, M. Hammerschmidt, L. Zschiedrich, and S. Burger, "Engineering electromagnetic fields in nanoscale environments by numerical optimization", *Workshop: Modeling, analysis, and approximation theory toward applications in tomography and inverse problems*, (Berlin, 08-2018)

6. P.-I. Schneider, X. Garcia-Santiago, F. Binkowski, P. Gutsche, T. Hoehne, M. Hammerschmidt, L. Zschiedrich, and S. Burger, "Light Management for Engineering Luminescence in Nanoscale Environments by Numerical Optimization", *233rd ECS Meeting*, (Seattle, 16-05-2018)

7. P.-I. Schneider, L. Zschiedrich, X. Garcia-Santiago, and S. Burger, "Optimization of quantum optical devices with machine learning", *OWTNM 2018* (Bad Sassendorf, 13-04-2018)

8. M. Hammerschmidt, P.-I. Schneider, X. Garcia-Santiago, L. Zschiedrich, and S. Burger, "Quantifying uncertainties of reconstructed parameters in optical scatterometry of nanostructured surfaces", *10th Workshop Ellipsometry (WSE 10)*, (Chemnitz, 19-03-2018)

9. P.-I. Schneider, X. Garcia-Santiago, and S. Burger, "Comparison of different optimization algorithms for improving a single-photon source", *11th Annual Meeting Photonic Devices*, (Berlin, 10-02-2018)

10. X. Garcia-Santiago, P.-I. Schneider, C. Rockstuhl, and S. Burger, "Optimization of diffractive optical elements using machine-learning approaches", *SPIE PW 18*, (San Francisco, 30-01-2018)

11. X. Garcia-Santiago, P.-I. Schneider, C. Rockstuhl, and S. Burger, "Shape design of a reflecting surface using Bayesian Optimization", *Journal of Physics: Conference Series*, **963**, 012003 (2018)

12. X. Garcia-Santiago "Global optimization of complex optical structures using Bayesian optimization based on Gaussian processes", *Karlsruhe Days of Optics and Photonics*, (Karlsruhe, 11-2017)

13. M. Hammerschmidt, M. Weiser, X. Garcia-Santiago, L. Zschiedrich, B. Bodermann,

and S. Burger, "Quantifying parameter uncertainties in optical scatterometry using Bayesian inversion", *Proceedings of SPIE*, **10330**, 1033004 (06-2017)

14. P.-I. Schneider, X. Garcia Santiago, C. Rockstuhl, and S. Burger, "Global optimization of complex optical structures using Bayesian optimization based on Gaussian processes", *Proceedings of SPIE*, **10335**, 141-149 (06-2017)

15. X. Garcia-Santiago, S. Burger, C. Rockstuhl, and I. Fernandez-Corbaton, " Electromagnetic chirality of 2D arrays under normal illumination", *10th Annual Meeting Photonic Devices*, (Berlin, 10-02-2017)

1 | Introduction

Optics and nanophotonics technologies provide crucial technological components to our society. The chips that build our computers, mobile phones, data centers and supercomputers are made thanks to lithographic processes [1–4]. The large internet global network is implemented on optical fibers [5, 6], complex multi-lens systems allow the implementation of compact high resolution cellphone cameras, and solar energy is a strategical technology for the decarbonization of energy production [7, 8], just to name a few.

Despite the incredible advances we have witnessed in the last decades, there is a continuous need of improving optical technologies. The increasing demand of data rates, mainly driven by the appearance of data centers, requires faster and more energy efficient optical networks [9, 10]. Improvements in the efficiency and costs of solar cells [11–15] are also of huge importance for the health of the planet and the possibility to fabricate smaller electrical transistors enables more powerful and energy efficient computer chips. Furthermore, new technologies yet to reach a mature status, e.g., quantum computers [16–20], promises another revolution that could drastically shape our society as we understand it nowadays.

The main aspects behind the improvements in photonic technologies are better fabrication techniques, but also the incorporation of new physical concepts and the improvement in the designs. Decades ago, the design of the different components of a photonic device was based on the knowledge and intuition of the researchers and developers. Nowadays, this knowledge continues to play an important role. However, with the emergence of modern computers and computer programs able to solve electromagnetic field propagation problems in an affordable amount of time, the process of designing the components of a photonic device has become more and more computer-driven.

Computational inverse design for photonic devices has evolved considerably along the last three decades. The holy grail of this task is to obtain designs for photonic devices that show extremely good performances, that are as simple to fabricate as possible, and that are obtained without the intervention of any person during the design process. However, quite frequently the main characteristics of the final designs obtained for the photonic structures are fixed by the designer at the early stages of the design process. In these instances, the designer proposes a geometrical model in which some of their characteristics are described by a few non-fixed parameters. Then, a computer program tries to find the optimal values for these parameters based on a function that measures the performance of the structure, called the objective function, obtained from electromagnetic simulations of the structure.

The two principle techniques that try to reduce the influence of human intervention in the design process are freeform shape optimization [21, 22] and topology optimization [23–26]. In freeform shape optimization, the shape of the structure is very often described using a series of b-spline curves or surfaces. The shape of the photonic structure

is then controlled by the weights and control points of the b-splines. In topology optimization, the photonic structure is discretized in, usually, thousands of different small pixels whose material properties are to be set during the optimization process. The main idea behind both approaches is to restrict as less as possible the geometry of the photonic component aimed to be designed, and to let the optimization algorithm to identify the most optimal design in this non-restricted design space. In this sense, topology optimization is an even more flexible method than freeform shape optimization.

The performance of both optimization techniques is closely linked to the development of numerical methods that solve Maxwell's equations and that also return the derivatives of the solution with respect to the design variables. The techniques used to compute the derivatives, the forward and the adjoint method, provide this extra derivative information adding a small computational overhead to the calculation of Maxwell's equations. Even though both the forward and the adjoint method have been used for more than fifteen years, a few issues remain yet to be solved, especially in the case of calculating shape derivatives. The main issue is that shape derivatives are not easy to implement for complicated structures, which are the result of applying multiple geometrical operations in a computer aided design software. The integration of shape derivatives within CAD software in a fully automated manner is a rather complicated task. Another issue is that most of the commercial software packages available for solving Maxwell's equations do not integrate the feature of providing the shape or material derivatives for all the offered post-processing quantities derived from the solution of Maxwell's equations. This aspect also limits the applicability of the methods.

However, the main problem that limits the applicability of both the freeform shape optimization and topology optimization methods is the difficulty to incorporate fabrication constraints within the optimization process. Although these methods can lead to designs with remarkable performances, in most of the cases these designs are also extremely difficult to implement with the available fabrication techniques. Effort is being put into this problem and some methods to obtain more robust designs have been proposed [27–31]. However, it is still not possible, in general, to efficiently integrate into the optimization process all the constraints emerging from the technological limits of the fabrication techniques. This is one of the reasons why even if nowadays both freeform optimization and topology optimization can be considered standard methods within the field of photonic design, many photonic structures are still designed using other approaches, such as the use of conventional parametric models.

A second limitation of any inverse design process, no matter which parametrization is used, has to do with the capacity of a computer to find the most optimal design within a given design space. In multimodal optimization problems, where the objective function has multiple local minima, the time needed to explore the entire design space grows exponentially with respect to the number of dimensions of the design space. Once assumed that this exploration is not possible to be done, the use of optimization algorithms aims to find a design as good as possible constrained to the amount of time available for this required task. The optimization algorithm is an important aspect of the design process. There is a wide range of optimization algorithms available and one needs to choose among them depending on the characteristics of the problem to optimize. Driven by the advances and the research effort that has been put in the field of machine learning, different machine learning techniques have been borrowed to solve photonic inverse design problems [32]. The goal of both fields is similar, machine learning aims to learn the response of a system of many input variables using the least number of observation data points. Inverse design aims to obtain the input point with the highest value of the objective function using the least number of observation data points. Among the differ-

ent techniques borrowed from the field of machine learning, different works propose the use of convolutional neural networks [33–38] to perform inverse design of photonic structures. However, as this technique usually requires large amounts of data, it is limited to problems where one can generate large sets of observation data points. Therefore, the technique is limited to problems where it is possible to obtain fast solutions of the electromagnetic field. Another optimization method that uses techniques of machine learning, and that we investigate in this work, is Bayesian optimization with Gaussian processes. Bayesian optimization does a fully statistical treatment of the objective function to obtain optimal values with the least number of observations. Moreover, Gaussian processes can incorporate derivative information fully analytically, allowing to exploit the use of shape derivatives. The main drawback that limits the applicability of Gaussian processes is their bad scaling with respect to the number of observation data points, which makes the optimization to become slower and slower with each observation added. Therefore, its use is usually suggested only for the optimization of computationally expensive problems. In this thesis we discuss this topic of the scaling and propose different methods to reduce the scalability issues of Gaussian processes in Bayesian optimization.

Regarding this thesis, the initial goal of this PhD project was to design different optical nanostructures in which we were interested from both theoretical and practical perspectives. The project started with a few clear ideas, we had available a tool to simulate electromagnetic field propagation in nanostructures that also provides shape derivatives and we wanted to see how we could use it to design the different photonic structures we were interested in. As inevitably in any research project, along this process different problems and questions with regards to the optimization process started to appear, e.g., the calculation of shape derivatives in complicated geometries, the lack of some tools that we needed for the design of isolated scatterers, questions about how to take the most out of the information provided by the shape derivatives, the scalability problem of Gaussian processes, etc. This thesis became a result of this process to solve the problems and to answer the questions that arose during the process of optimization of the different photonic structures. It tries to make a modest contribution to the enormous field of research of photonic inverse design. Along the thesis, we contribute to different topics of relevance for the design of photonic structures: optimization algorithms, numerical methods to solve or to measure relevant quantities of electromagnetic fields, or the calculation of shape derivatives for complicated geometries.

Still, even if the development of all these tools became an important part of the work, the initial goal of the project was not forgotten during this process. We have applied all these methods to design different photonic structures. Emphasis was put into the design of optimal electromagnetic chiral scatterers and the design of compact and energy efficient freeform waveguide edge couplers. Both of them are discussed in this document.

The optimization of chiral helices is a relevant topic from a theoretical point of view. It is interesting to know how feasible it is to obtain, at optical and mid-infrared frequencies, scatterers with the extraordinary properties that maximal electromagnetically chiral objects present. Once available, of course, they would also unlock interesting applications. On the other side, edge couplers are components of crucial importance for the development of photonic integrated circuits as they can connect different components of photonic chips. Photonic integrated circuits have numerous applications, but one of special relevance for our near future is their use in communication optical networks. There, photonic integrated circuits are a key element for achieving reductions in energy consumption and increments in data rates. In this context, the design of more efficient and more compact edge couplers is a task of great interest from a general perspective.

Structure of the thesis

The thesis is structured into six chapters. After this introductory chapter, a theoretical background chapter is presented. This second chapter is divided into two main parts. The first part introduces the basic electromagnetic theory that is needed along the thesis. It starts from Maxwell's equations and describes some of its most fundamental solutions: the plane waves and the vector spherical wave functions. After that, it continues with the introduction of the scattering problem, the helicity operator and its link to circularly polarized waves, and the basics of waveguide theory. The second part of the second chapter is devoted to the introduction of the finite element method. It will be the main technique to solve Maxwell's equations in this thesis. This part starts with the description of the main properties of the finite element method. After the working principles of the finite element method are presented, the chapter continues with the description of the calculation of the shape and material derivatives. Finally, the chapter ends with the description of the two main different techniques used to calculate the shape derivatives for a number of different design variables: the forward and the adjoint method. As we will see, the calculation of the shape derivatives is a tool of special relevance in this thesis, and all the other chapters to come are linked, in one way or another, to this important tool for the field of inverse photonic design.

The third chapter is about the use of Bayesian optimization with Gaussian processes to design photonic structures. It starts with a description of Gaussian processes and Gaussian process regression. One section of the chapter is devoted to the description of the incorporation of derivative information into the Gaussian process model. After that, the chapter continues with the description of Bayesian optimization, particularly, it describes how Gaussian processes can be used to perform global optimization. Once the details about how to implement Bayesian optimization are introduced, the chapter discusses the scalability problems of Gaussian processes at the end and it proposes two different techniques to mitigate the impact of the scalability issues in the design of photonic structures.

The fourth chapter presents a numerical method to calculate the decomposition of scattered fields into vector spherical wave functions. The chapter starts by introducing the mathematical description of the method to then show results of its numerical implementation into a finite element solver. The decomposition allows for an easy procedure to implement the calculation of the T-matrix for scatterers with generally complicated shapes and also to implement the calculation of shape and material derivatives of the T-matrix. The description of these two procedures constitutes the next part of the chapter. Finally, the chapter proposes the use of the mentioned techniques for not just optimizing isolated scatterers, but also for optimizing photonic structures that are composed of a series of isolated scatterers, such as, e.g., metasurfaces. The results of this chapter came from our need for tools that facilitate the design of isolated scatterers, such as, e.g., the optimal chiral helices presented in chapter five.

The fifth chapter presents the design and analysis of two photonic structures: optimal electromagnetically chiral helices and edge couplers for the interconnection of different photonic integrated circuits. The chapter is divided into two main sections, each of them corresponds to one of the applications presented. Each of these main sections starts with a description of the problem and why it is of interest to find optimal designs. They continue with a description of the optimization method used to design the structures. Finally, the results of the optimization are presented and the optimal designs are analyzed. The chapter, besides showing the design of two interesting photonic structures, can be seen as the part of the thesis where the different numerical techniques proposed

and developed in the previous chapters are merged and applied to the final objective for which they have been developed: the efficient optimization of photonic structures with complicated geometries.

The thesis finalizes with the chapter dedicated to the conclusions and outlook, where we take a general look at the results obtained and we give a series of proposals on how the work could be extended based on what has been done.

2 | Theoretical background

2.1 Introduction

This thesis deals with the design of photonic structures and their optimization. That is, this is a work about the design of structures devised to manipulate the propagation of light and so, accomplish a certain desired functionality. It is then logical to start the document introducing the equations that govern light propagation at the relevant spatial and temporal scales for such photonic structures and describing the methods that we will use to solve these equations. This is the purpose of this chapter. It presents the fundamentals of light propagation that will be required in the discussions of the following chapters of the thesis and the main method that we use to solve light propagation.

This chapter is divided into two main sections. The first part of the chapter introduces the basics of propagation field theory in the different situations that we will encounter along the document. The second part is devoted to the description of the finite element method and the calculation of shape and material derivatives within the finite element method. The finite element method is a numerical method used to solve systems of differential equations, usually in situations where these equations are defined over complicated geometrical models. It is the method on which we will mainly rely to solve Maxwell's equations over the photonic structures. Given the importance of the method in this work, the description that we give in the chapter of some of its implementation details comes with a certain amount of detail. However, we consider this detailed explanation necessary to fully understand the procedure for the calculation of shape derivatives, quantities that play a fundamental role in the development of the thesis.

2.2 Electromagnetic field theory

This section introduces the main equations describing the propagation of electromagnetic fields and some fundamental solutions of these equations that are extensively used throughout the thesis. This section starts by stating Maxwell's equations in both time and frequency domain. It then continues describing the wave equation and some of its most fundamental solutions: the plane waves and the vector spherical wave functions. After that, two different particularizations of Maxwell's equations to two specific scenarios, light scattering and light propagation through waveguides, are discussed. Additionally, the section discusses the concept of helicity and its link to circularly polarized plane waves. These concepts will be often encountered along the thesis.

Maxwell's equations

Maxwell's equations [39] are a set of four coupled equations that describe the propagation of electromagnetic fields through structured materials. In their partial differential form they can be written as (see, e.g., [40] chapter 1 or [41] chapter 6)

$$\nabla \times \mathbf{E}(\mathbf{r}, t) = -\frac{\partial \mathbf{B}(\mathbf{r}, t)}{\partial t}, \quad (2.1)$$

$$\nabla \times \mathbf{H}(\mathbf{r}, t) = \frac{\partial \mathbf{D}(\mathbf{r}, t)}{\partial t} + \mathbf{J}(\mathbf{r}, t), \quad (2.2)$$

$$\nabla \cdot \mathbf{D}(\mathbf{r}, t) = \rho(\mathbf{r}, t), \quad (2.3)$$

$$\nabla \cdot \mathbf{B}(\mathbf{r}, t) = 0, \quad (2.4)$$

where $\mathbf{E}(\mathbf{r}, t)$ (V/m) and $\mathbf{H}(\mathbf{r}, t)$ (A/m) are the electric and magnetic fields, $\mathbf{D}(\mathbf{r}, t)$ (As/m²) is the electric displacement, $\mathbf{B}(\mathbf{r}, t)$ (Vs/m²) is the magnetic flux density, $\rho(\mathbf{r}, t)$ the charge density (As/m³), and $\mathbf{J}(\mathbf{r}, t)$ the current density (A/m²), respectively.

Given the spatial and temporal dynamics of the charge and current distributions that act as sources, Maxwell's equations describe the values of the electromagnetic fields at every point of space \mathbf{r} and at each moment of time t .

As an equivalent representation to the fields in time, one can describe within the context of linear electrodynamics the fields in frequency domain by applying the Fourier transform to their representation in time domain. The Fourier transformed fields read as

$$\tilde{\mathbf{E}}(\mathbf{r}, \omega) = \int \mathbf{E}(\mathbf{r}, t) e^{i\omega t} dt. \quad (2.5)$$

If one applies the Fourier transform to Maxwell's equations one gets

$$\nabla \times \tilde{\mathbf{E}}(\mathbf{r}, \omega) = i\omega \tilde{\mathbf{B}}(\mathbf{r}, \omega), \quad (2.6)$$

$$\nabla \times \tilde{\mathbf{H}}(\mathbf{r}, \omega) = -i\omega \tilde{\mathbf{D}}(\mathbf{r}, \omega) + \mathbf{J}(\mathbf{r}, \omega) \quad (2.7)$$

$$\nabla \cdot \tilde{\mathbf{D}}(\mathbf{r}, \omega) = \tilde{\rho}(\mathbf{r}, \omega), \quad (2.8)$$

$$\nabla \cdot \tilde{\mathbf{B}}(\mathbf{r}, \omega) = 0. \quad (2.9)$$

Taking a look into Eqns. (2.1)-(2.4) or equivalently to Eqns. (2.6)-(2.9), one can see that there are more unknowns than equations. To make them complete, it is necessary to add the constitutive relations that link the electric displacement and magnetic flux density to the electric and magnetic fields. In time domain they can be written as

$$\mathbf{D}(\mathbf{r}, t) = \mathbf{D}(\mathbf{r}, t, \mathbf{E}, \mathbf{H}), \quad (2.10)$$

$$\mathbf{B}(\mathbf{r}, t) = \mathbf{B}(\mathbf{r}, t, \mathbf{E}, \mathbf{H}). \quad (2.11)$$

The specific form of the above equations is given by the electromagnetic properties of the materials. In vacuum, these relations are simply $\mathbf{D}(\mathbf{r}, t) = \epsilon_0 \mathbf{E}(\mathbf{r}, t)$ and $\mathbf{B}(\mathbf{r}, t) = \mu_0 \mathbf{H}(\mathbf{r}, t)$. Here, ϵ_0 is the electric permittivity and μ_0 the magnetic permeability of free space.

In most situations where matter is present, the fields \mathbf{D} and \mathbf{B} can be accurately described in terms of the electric polarization \mathbf{P} and the magnetization \mathbf{M} ,

$$\mathbf{D}(\mathbf{r}, t) = \epsilon_0 \mathbf{E}(\mathbf{r}, t) + \mathbf{P}(\mathbf{r}, t), \quad (2.12)$$

$$\mathbf{B}(\mathbf{r}, t) = \mu_0 (\mathbf{H}(\mathbf{r}, t) + \mathbf{M}(\mathbf{r}, t)). \quad (2.13)$$

Both quantities $\mathbf{P}(\mathbf{r}, t)$ and $\mathbf{M}(\mathbf{r}, t)$ can be seen, in a classical interpretation, as macroscopic space averages over the microscopic molecular dipole moments and molecular magnetic moments in the materials that compose the medium ([41] section 6.6). The polarization and magnetization, in general, depend on both electric and magnetic fields for a general bi-anisotropic material. The dependency can be expressed using a convolution with some material specific response function. The response function here expresses the induced polarization for a delta-type excitation in time domain. That convolution in time domain is somehow cumbersome to evaluate. Therefore, constitutive relations are usually evaluated in frequency domain where the convolution from the time domain simply gets a product. This renders the constitutive relations to be rather simple algebraic expression. For most of the materials that one encounters in optical applications and provided that the intensity of the involved fields is sufficiently small, the electric polarization $\mathbf{P}(\mathbf{r}, \omega)$ and the magnetization $\mathbf{M}(\mathbf{r}, \omega)$ in frequency domain relate linearly with the electric and magnetic fields, respectively, given as a result the following constitutive relations for linear media,

$$\tilde{\mathbf{D}}(\mathbf{r}, \omega) = \underline{\epsilon}'(\mathbf{r}, \omega) \tilde{\mathbf{E}}(\mathbf{r}, \omega), \quad (2.14)$$

$$\tilde{\mathbf{B}}(\mathbf{r}, \omega) = \underline{\mu}(\mathbf{r}, \omega) \tilde{\mathbf{H}}(\mathbf{r}, \omega), \quad (2.15)$$

where $\underline{\epsilon}'(\mathbf{r}, \omega)$ and $\underline{\mu}(\mathbf{r}, \omega)$ are the electric permittivity tensor and magnetic permeability tensor, respectively.

Similarly, also the currents induced by the electric fields can, as an approximation, be linearly related to the electric field,

$$\tilde{\mathbf{J}}(\mathbf{r}, \omega) = \underline{\sigma}_c(\mathbf{r}, \omega) \tilde{\mathbf{E}}(\mathbf{r}, \omega) + \tilde{\mathbf{J}}_{\text{ext}}(\mathbf{r}, \omega), \quad (2.16)$$

where $\tilde{\mathbf{J}}(\mathbf{r}, \omega)$ is the total current, $\tilde{\mathbf{J}}_{\text{ext}}(\mathbf{r}, \omega)$ the non-induced externally applied current, and $\underline{\sigma}_c(\mathbf{r}, \omega)$ the conductivity tensor. The above equations implicitly ignore nonlocality in space, which is a good approximation for most of the natural materials at optical frequencies.

Additionally to the constitutive relations, some boundary conditions need to be imposed when solving the system of differential Maxwell's equations. In section 2.2, we will introduce the radiation boundary condition, used to solve electromagnetic fields produced by localized sources.

From this point, we will always assume fields with a time harmonic dependency, unless otherwise stated,

$$\mathbf{E}(\mathbf{r}, t) = \bar{\mathbf{E}}(\mathbf{r}) e^{-i\omega_0 t}, \quad (2.17)$$

$$\tilde{\mathbf{E}}(\omega, t) = \bar{\mathbf{E}}(\mathbf{r}) \delta(\omega - \omega_0). \quad (2.18)$$

$$(2.19)$$

Therefore, we will skip their explicit time or frequency dependency and discuss eventually only the spatial dependent part. Also, from this point we will omit the bar in the time independent field $\bar{\mathbf{E}}(\mathbf{r})$ and we will simply denote it by $\mathbf{E}(\mathbf{r})$.

Regarding the energy carried by electromagnetic fields, the energy conservation law for time averaged harmonic fields is given by the below equation (see, e.g., [41] Eqn. 6.134),

$$-\frac{1}{2} \int_V \operatorname{Re} \{ \mathbf{J}^*(\mathbf{r}) \cdot \mathbf{E}(\mathbf{r}) \} dV = \quad (2.20)$$

$$-\omega_0 \int_V \frac{1}{2} \operatorname{Im} \{ (\mathbf{E}(\mathbf{r}) \cdot \mathbf{D}^*(\mathbf{r}) - \mathbf{B}(\mathbf{r}) \cdot \mathbf{H}^*(\mathbf{r})) \} dV + \int_S \frac{1}{2} \operatorname{Re} \{ \mathbf{E}(\mathbf{r}) \times \mathbf{H}^*(\mathbf{r}) \} \cdot d\mathbf{S}. \quad (2.21)$$

This equation states that the time averaged rate of work done by the field on the sources contained within a volume V equals the volume integral of the time averaged rate of the fields energy density plus the time averaged power flux through the boundary S of the volume. The term within the last integral of the expression is the time averaged Poynting vector $\langle \mathbf{S} \rangle$,

$$\langle \mathbf{S} \rangle = \frac{1}{2} \operatorname{Re} \{ (\mathbf{E}(\mathbf{r}) \times \mathbf{H}^*(\mathbf{r})) \}. \quad (2.22)$$

It gives the power flux carried by an electromagnetic field.

The wave equation

One particularly interesting situation to solve the time harmonic Maxwell equations is a homogeneous, isotropic, and linear media. In this case, the spatial dependent electric permittivity tensor $\underline{\epsilon}'(\mathbf{r})$ and the permeability tensor $\underline{\mu}(\mathbf{r})$ become two scalars, ϵ' and μ , that do not depend on space anymore. Under this conditions, Maxwell's equations can translate into a system of decoupled equations for the electric and magnetic fields (see, e.g., [40] section 1.3) called the wave equations,

$$\nabla \times \nabla \times \mathbf{E}(\mathbf{r}) - k^2 \mathbf{E}(\mathbf{r}) = i\omega\mu \mathbf{J}_{\text{ext}}(\mathbf{r}), \quad (2.23)$$

$$\nabla \times \nabla \times \mathbf{H}(\mathbf{r}) - k^2 \mathbf{H}(\mathbf{r}) = \nabla \times \mathbf{J}_{\text{ext}}(\mathbf{r}). \quad (2.24)$$

The quantity k is the wave number. It is defined as $k^2 = \omega_0^2 \mu \epsilon$ where $\epsilon = \epsilon' + i \frac{\sigma_c}{\omega_0}$ is the generalized complex dielectric function. In the case of no external sources, the above equations translate into two identical equations for the electric and magnetic fields, the homogeneous wave equations,

$$\nabla^2 \mathbf{E}(\mathbf{r}) + k^2 \mathbf{E}(\mathbf{r}) = 0, \quad (2.25)$$

$$\nabla^2 \mathbf{H}(\mathbf{r}) + k^2 \mathbf{H}(\mathbf{r}) = 0. \quad (2.26)$$

The above equations have an enormous importance in optics, as due to the linearity of Maxwell's equations, the general solution produced by any current distribution can be obtained as the linear combination of a particular solution plus the solution of the homogeneous equations.

We will revise now two fundamental solutions of the homogeneous wave equations that we will use extensively throughout the thesis.

Plane waves

First, we introduce the plane wave. The electric field of a plane wave reads as

$$\mathbf{E}(\mathbf{r}) = \mathbf{A}e^{i\mathbf{k}\cdot\mathbf{r}}. \quad (2.27)$$

The vector \mathbf{A} is in general a complex vector. It gives the amplitude and the direction of oscillation of the electric field. The vector \mathbf{k} is the wave vector. It can also be complex valued in the general case,

$$\mathbf{k} = k\hat{\mathbf{k}} = k(\hat{\mathbf{k}}_r + i\hat{\mathbf{k}}_i), \quad (2.28)$$

with k being the wave number and $\hat{\mathbf{k}}_r$ and $\hat{\mathbf{k}}_i$ being vectors defined in \mathbb{R}^3 . The real and imaginary parts of $\hat{\mathbf{k}}$ fulfill the below properties,

$$|\hat{\mathbf{k}}_r|^2 - |\hat{\mathbf{k}}_i|^2 = 1, \quad (2.29)$$

$$\hat{\mathbf{k}}_r \cdot \hat{\mathbf{k}}_i = 0. \quad (2.30)$$

If the wave vector of a plane wave has only a real part, the plane wave is called a homogeneous plane wave. Otherwise it is called an inhomogeneous plane wave. Even in a lossless medium, with a real valued wave number k , the wave vector of a plane wave can be complex valued. In this case, the plane wave is called an evanescent wave.

The vectors \mathbf{A} and \mathbf{k} are also orthogonal to each other,

$$\mathbf{k} \cdot \mathbf{A} = 0. \quad (2.31)$$

Here, the dot product used is the one defined for real valued vectors, even if they are in general complex valued. That is the result of the requirement that the field needs to be free of divergence.

As \mathbf{A} must be contained in a plane perpendicular to \mathbf{k} , it can be decomposed using a base of two orthonormal vectors whose directions are also contained in that plane. Let us name these vectors by $\hat{\mathbf{v}}_1$ and $\hat{\mathbf{v}}_2$. Then,

$$\mathbf{A} = A_1\hat{\mathbf{v}}_1 + A_2\hat{\mathbf{v}}_2. \quad (2.32)$$

If one now looks at the temporal evolution of the real part of the electric field at a fixed position \mathbf{r}_0 one obtains,

$$\text{Re}\{\mathbf{A}\}(\mathbf{r}_0, t) = \hat{\mathbf{v}}_1|A_1|\cos(\phi(A_1) + \mathbf{k} \cdot \mathbf{r}_0 - \omega_0 t) + \hat{\mathbf{v}}_2|A_2|\cos(\phi(A_2) + \mathbf{k} \cdot \mathbf{r}_0 - \omega_0 t), \quad (2.33)$$

with the function $\phi(\alpha)$ denoting the phase of the complex number α .

From Eqn. (2.33) one can see that when both coefficients A_1 and A_2 have the same phase or a phase difference of 180 degrees, the electric field oscillates along a fixed direction. In this case the plane wave is linearly polarized. If the two coefficients A_1 and A_2 have the same absolute value and the relative phase between them equals ± 90 degrees, the plane wave is circularly polarized. That means that the direction of the electric field at each point rotates over time. In any other case, the plane wave is elliptically polarized.

In the case of a circularly polarized plane wave, the electric field can rotate into two different directions. It means that it can be a right handed or a left handed circularly polarized

plane wave. Two conventions exist to define the sense of rotation. In this work we say that the wave is right circularly polarized when,

$$\mathbf{v}_i \times \mathbf{v}_j = \frac{\mathbf{k}}{k}, \{i, j\} \in \{1, 2\}, i \neq j, \quad (2.34)$$

$$\phi(A_i) - \phi(A_j) = \pi/2. \quad (2.35)$$

Figure 2.1 shows the convention used in the thesis at the example of a right circularly polarized plane wave.

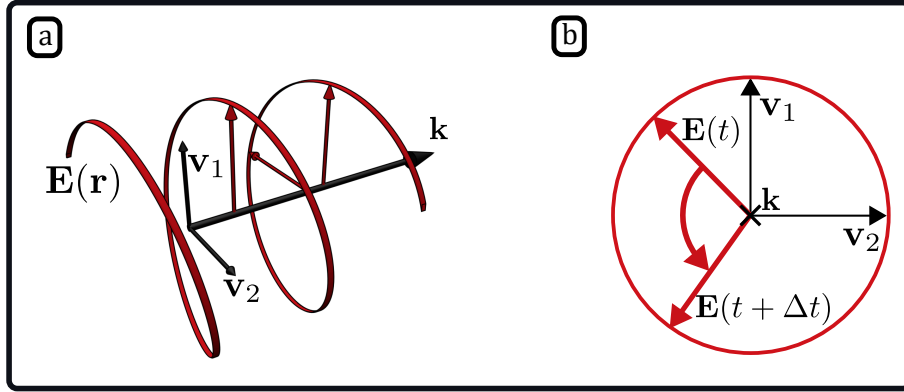


Figure 2.1: Spatial and temporal representation of the direction of the electric field for a right circularly polarized plane wave. The definition of a circularly polarized plane wave to be right or left circularly polarized depends on the convention used. This sketch shows the convention used in this thesis and described by Eqns. (2.34) and (2.35). **a.** Direction of the electric field strength of a right circularly polarized plane wave along space. **b.** Evolution of the direction of the electric field strength of a right circularly polarized plane wave in time for a fixed position in space.

Plane waves are used to expand the solution of the electromagnetic field in many different types of problems. Examples are the scattering of isolated objects, in diffraction by periodic gratings, or for layered media.

One method for expanding the field in a homogeneous region into plane waves is the use of the angular spectrum representation. The angular spectrum representation is obtained by applying a Fourier transform to the electric field $\mathbf{E}(\mathbf{r})$ over an infinitely extended plane in space. The plane chosen to perform the Fourier transform is normally a characteristic plane of the problem, e.g., in layered media structures it is chosen to be a plane parallel to the material interfaces. The angular spectrum representation $\hat{\mathbf{E}}(k_x, k_y)$ of an electric field calculated in the plane $z = z_0$ reads as

$$\hat{\mathbf{E}}(k_x, k_y) = \frac{1}{2\pi} \int_{-\infty}^{+\infty} \int_{-\infty}^{+\infty} \mathbf{E}(\mathbf{r}) e^{-i(k_x x + k_y y + k_z(z-z_0))} dy dx, \quad (2.36)$$

$$\mathbf{E}(x, y, z) = \frac{1}{2\pi} \int_{-\infty}^{+\infty} \int_{-\infty}^{+\infty} \hat{\mathbf{E}}(k_x, k_y) e^{i(k_x x + k_y y + k_z(z-z_0))} dk_y dk_x. \quad (2.37)$$

As one can see from the above equations, the angular spectrum representation is a function of only two of the components of the wave vector. The third component is automatically determined by the wave number,

$$k_x^2 + k_y^2 + k_z^2 = k_\rho^2 + k_z^2 = k^2 = \omega_0^2 \mu \epsilon. \quad (2.38)$$

The angular spectrum representation is composed of both plane waves, $k_\rho^2 \leq k^2$, and evanescent waves, $k_\rho^2 > k^2$.

For a plane wave, the time average Poynting vector, Eqn. (2.22), reads as,

$$\langle \mathbf{S} \rangle = \frac{1}{\omega_0 \mu} |\mathbf{A}|^2 \text{Re} \{ \mathbf{k} \}. \quad (2.39)$$

One can see from Eqn. (2.39) that an evanescent plane wave does not carry power along the direction in which its amplitude exponentially decays.

Vector spherical wave functions

Another important set of solutions to the homogeneous wave equation are the vector spherical wave functions (VSWFs) $\mathbf{N}_{m,n}^{(J)}(\mathbf{r})$ and $\mathbf{M}_{m,n}^{(J)}(\mathbf{r})$. These functions are obtained when solving the wave equation in spherical coordinates. Different definitions can be found in literature for the VSWFs [41–44]. In this work, we will use the VSWFs as defined in [42], which are summarized in appendix A of the thesis.

The VSWFs form a complete set of solutions to the wave equation. The field produced by a set of localized charges, for example, can be described by

$$\mathbf{E}(\mathbf{r}) = \sum_{n=1}^{\infty} \sum_{m=-n}^n a_{m,n} \mathbf{N}_{m,n}^{(3)}(\mathbf{r}) + b_{m,n} \mathbf{M}_{m,n}^{(3)}(\mathbf{r}), \quad (2.40)$$

with $a_{m,n}$ and $b_{m,n}$ being complex valued scalars.

The fields $\mathbf{N}_{m,n}^{(J)}(\mathbf{r})$ and $\mathbf{M}_{m,n}^{(J)}(\mathbf{r})$ are often called electric and magnetic multipole fields, respectively. This nomenclature comes from the fact that ideal infinitesimal electric and magnetic multipole moments of degree n oscillating in time with frequency $e^{-i\omega_0 t}$ would radiate electromagnetic fields whose field components would be given by the electric fields $\mathbf{E}(\mathbf{r}) = \mathbf{N}_{m,n}^{(3)}(\mathbf{r})$ and the magnetic fields $\mathbf{H}(\mathbf{r}) = \mathbf{M}_{m,n}^{(3)}(\mathbf{r})$, respectively ([41] section 9.10). The VSWFs with different multipole orders m and same multipole degree n would just be generated by multipole moments with different spatial orientation.

The electric and magnetic multipoles are transverse to each other,

$$\nabla \times \mathbf{N}_{m,n}^{(J)}(\mathbf{r}) = k \mathbf{M}_{m,n}^{(J)}(\mathbf{r}), \quad (2.41)$$

$$\nabla \times \mathbf{M}_{m,n}^{(J)}(\mathbf{r}) = k \mathbf{N}_{m,n}^{(J)}(\mathbf{r}), \quad (2.42)$$

with k being the wave number.

The superscript J of the VSWFs denotes their radial dependency. The multipoles with J equal to 3 represent fields that fulfill the outwards radiation condition. This condition is presented in the next section when discussing the scattering problem. These multipoles diverge in the limit for $|\mathbf{r}|$ going to 0 and they decay with $|\mathbf{r}|$ for large values of $|\mathbf{r}|$. The superscript $J = 1$ represents regular fields, with a well defined behavior at the origin. These regular VSWFs can be used, e.g., to expand the field of a plane wave $\mathbf{E}(\mathbf{r}) = \mathbf{A} e^{i\mathbf{k} \cdot \mathbf{r}}$,

$$\mathbf{E}(\mathbf{r}) = \sum_{n=1}^{\infty} \sum_{m=-n}^n c_{\text{pw},m,n} \mathbf{N}_{m,n}^{(1)}(\mathbf{r}) + d_{\text{pw},m,n} \mathbf{M}_{m,n}^{(1)}(\mathbf{r}), \quad (2.43)$$

with the coefficients $c_{pw,m,n}$ and $d_{pw,m,n}$ given by the Eqns. (B.2)-(B.3) in the appendix B.

The VSWFs fulfill the orthogonality relations

$$\int_{S_R^2} \mathbf{N}_{m,n}^{(J)*}(\mathbf{r}) \cdot \mathbf{M}_{m,n}^{(J)}(\mathbf{r}) \, dS = 0, \quad (2.44)$$

$$\int_{S_R^2} \mathbf{N}_{m,n}^{(J)*}(\mathbf{r}) \cdot \mathbf{N}_{m',n'}^{(J)}(\mathbf{r}) \, dS = \int_{S_R^2} |\mathbf{N}_{m,n}^{(J)}|^2(\mathbf{r}) \, dS \delta_{m,m'} \delta_{n,n'}, \quad (2.45)$$

$$\int_{S_R^2} \mathbf{M}_{m,n}^{(J)*}(\mathbf{r}) \cdot \mathbf{M}_{m',n'}^{(J)}(\mathbf{r}) \, dS = \int_{S_R^2} |\mathbf{M}_{m,n}^{(J)}|^2(\mathbf{r}) \, dS \delta_{m,m'} \delta_{n,n'}, \quad (2.46)$$

which can be used to obtain the coefficients $a_{m,n}$ and $b_{m,n}$ that expand a given electric field into the set of VSWFs.

With the definition of the VSWFs used in this thesis, the total time averaged power radiated by a field can be expressed using the coefficients of its multipole expansion, Eqn. (2.40), as

$$P = \frac{1}{2Zk^2} \sum_{n=1}^{\infty} \sum_{m=-n}^n (|a_{m,n}|^2 + |b_{m,n}|^2). \quad (2.47)$$

Scattering by isolated objects

In scattering theory, one is interested in the solution of electromagnetic fields that propagate in an unbounded exterior domain that are produced by objects upon a given illumination. The situation can be described as follows: a certain object with permittivity and permeability distributions $\epsilon_2(\mathbf{r})$ and $\mu_2(\mathbf{r})$, respectively, is embedded into a homogeneous medium with permittivity ϵ_1 and permeability μ_1 . The object is illuminated with a field $\mathbf{E}_{\text{inc}}(\mathbf{r})$ and we are interested in obtaining the total field as a result of the interaction of $\mathbf{E}_{\text{inc}}(\mathbf{r})$ with the object.

The total field $\mathbf{E}(\mathbf{r})$ can be decomposed into the contribution of the illumination and the scattered field,

$$\mathbf{E}(\mathbf{r}) = \mathbf{E}_{\text{inc}}(\mathbf{r}) + \mathbf{E}_{\text{scat}}(\mathbf{r}), \quad (2.48)$$

where the illumination $\mathbf{E}_{\text{inc}}(\mathbf{r})$ is a solution to Maxwell's equations for a homogeneous medium with permittivity ϵ_1 and permeability μ_1 .

The field $\mathbf{E}(\mathbf{r})$ must be also a solution of the Maxwell equations without sources. Therefore, we can write

$$\begin{aligned} \nabla \times \left(\frac{1}{\mu(\mathbf{r})} \nabla \times \mathbf{E}(\mathbf{r}) \right) - \omega^2 \epsilon(\mathbf{r}) \mathbf{E}(\mathbf{r}) &= 0 \rightarrow \\ \nabla \times \left(\frac{1}{\mu(\mathbf{r})} \nabla \times (\mathbf{E}_{\text{scat}}(\mathbf{r}) + \mathbf{E}_{\text{inc}}(\mathbf{r})) \right) - \omega^2 \epsilon(\mathbf{r}) (\mathbf{E}_{\text{scat}}(\mathbf{r}) + \mathbf{E}_{\text{inc}}(\mathbf{r})) &= 0 \rightarrow \\ \nabla \times \left(\frac{1}{\mu(\mathbf{r})} \nabla \times \mathbf{E}_{\text{scat}}(\mathbf{r}) \right) - \omega^2 \epsilon(\mathbf{r}) \mathbf{E}_{\text{scat}}(\mathbf{r}) &= \nabla \times \left(\frac{1}{\mu(\mathbf{r})} \nabla \times \mathbf{E}_{\text{inc}}(\mathbf{r}) \right) - \omega^2 \epsilon(\mathbf{r}) \mathbf{E}_{\text{inc}}(\mathbf{r}). \end{aligned} \quad (2.49)$$

Because the field $\mathbf{E}_{\text{inc}}(\mathbf{r})$ fulfills Maxwell's equations in the embedding medium, the term on the right hand side of the above equation is different from zero only within the object,

where $\epsilon(\mathbf{r}) \neq \epsilon_1$ and $\mu(\mathbf{r}) \neq \mu_1$. This term effectively act as a source and the problem can be stated as a radiative problem of localized sources for the scattered field $\mathbf{E}_{\text{scat}}(\mathbf{r})$.

Additionally, the scattered field $\mathbf{E}_{\text{scat}}(\mathbf{r})$ must satisfy the Silver-Müller outwards radiation condition. In a linear, homogeneous, and isotropic medium, the Silver-Müller radiation condition for time harmonic fields reads as ([40] Eqn. 1.20)

$$\lim_{r \rightarrow \infty} \left[\left(\frac{1}{\sqrt{\mu_1}} \nabla \times \mathbf{E}_{\text{scat}}(\mathbf{r}) \right) \times \mathbf{r} - |\mathbf{r}| i \omega \sqrt{\epsilon_1} \mathbf{E}_{\text{scat}}(\mathbf{r}) \right] = 0. \quad (2.50)$$

Solving Eqn. (2.49) together with Eqn. (2.50) ensures the existence of a unique solution for scattering problems ([40] section 3.2.3).

Once the scattered field is known, many interesting quantities of practical relevance can be obtained, e.g., the time averaged power absorbed, P_{abs} , or scattered, P_{scat} , by the object. The sum of both quantities, i.e., the total power taken from the illumination field by the object, is called the extinction power, P_{ext} . These quantities are normally given as cross sections, i.e., as powers normalized by the time averaged power flux of the given illumination, $|\langle \mathbf{S}_{\text{inc}} \rangle|$,

$$\sigma_{\text{abs}} = \frac{P_{\text{abs}}}{|\langle \mathbf{S}_{\text{inc}} \rangle|}, \quad \sigma_{\text{scat}} = \frac{P_{\text{scat}}}{|\langle \mathbf{S}_{\text{inc}} \rangle|}, \quad \sigma_{\text{ext}} = \frac{P_{\text{ext}}}{|\langle \mathbf{S}_{\text{inc}} \rangle|}. \quad (2.51)$$

If $|\langle \mathbf{S}_{\text{inc}} \rangle|$ can not be assumed to be homogeneous over the volume of the scatterer, the average of $|\langle \mathbf{S}_{\text{inc}} \rangle|(\mathbf{r})$ over its volume must then be considered in the above expressions.

Considering the expansions of the illumination and scattered fields into regular and radiative vector spherical wave functions, respectively, the absorption and extinction cross sections for plane wave illumination can be expressed as (see, e.g., [42] Eqns. 5.18a-5.18b)

$$\sigma_{\text{scat}} = \frac{1}{k^2 |\mathbf{A}|^2} \sum_{n=1}^{\infty} \sum_{m=-n}^n (|a_{m,n}|^2 + |b_{m,n}|^2), \quad (2.52)$$

$$\sigma_{\text{ext}} = \frac{1}{k^2 |\mathbf{A}|^2} \sum_{n=1}^{\infty} \sum_{m=-n}^n \text{Re} (c_{\text{pw},m,n} a_{m,n}^* + d_{\text{pw},m,n} b_{m,n}^*), \quad (2.53)$$

where $c_{\text{pw},m,n}$ and $d_{\text{pw},m,n}$ are the coefficients of the multipole expansion for a plane wave, Eqns. (B.2)-(B.3).

The helicity operator

This section introduces the helicity operator and its link to the polarization state of plane waves and vector spherical wave functions. These concepts play an important role in the study of chiral light matter interactions and they will be used along chapters 4 and 5. All the information presented in this section was obtained from [45].

The helicity operator Λ is defined as the projection of the total angular momentum operator, \mathbf{J} , onto the direction of the linear momentum operator, \mathbf{P} ,

$$\Lambda = \frac{\mathbf{J} \cdot \mathbf{P}}{|\mathbf{P}|}. \quad (2.54)$$

For monochromatic fields, Λ can be represented as

$$\Lambda = \frac{\nabla \times}{k}. \quad (2.55)$$

The helicity operator has two different eigenvalues, $\lambda = \pm 1$. The associated eigenvectors, $\mathbf{G}_{\pm}(\mathbf{r})$, are the Riemann–Silberstein linear combinations [46]

$$\mathbf{G}_{\pm}(\mathbf{r}) = \frac{1}{\sqrt{2}} (\mathbf{E}(\mathbf{r}) \pm iZ\mathbf{H}(\mathbf{r})), \quad (2.56)$$

where $Z = \sqrt{\mu/\epsilon}$ is the impedance of the medium.

The eigenvalues of the helicity operator can be used as an index that defines the polarization state of a given field. For plane waves, the fields of pure helicity correspond to circularly polarized plane waves. Right handed circularly polarized plane waves are eigenstates of the helicity operator with eigenvalue +1 and left handed circularly polarized plane waves are eigenvectors with eigenvalue equal to -1. That is, for a right circularly polarized plane wave, the combination $\mathbf{G}_{-}(\mathbf{r})$ is always zero. Actually, the link between eigenvectors of the helicity operator and circularly polarized plane waves is broader. The plane wave decomposition of any field that is an eigenvector of the helicity operator with eigenvalue +1(-1) contains only right(left) circularly polarized plane waves. This relation goes also in the other direction. If a field is composed of only right handed or left handed circularly polarized plane waves, then this field is an eigenvector of the helicity operator with eigenvalue +1 or -1, respectively.

Similarly, one finds a relation between the VSWFs, presented in section 2.2, and the eigenvectors $\mathbf{G}_{\pm}(\mathbf{r})$. Using the representation of Λ given by Eqn. (2.55) and Eqns. (2.41)-(2.42), it can be seen that the linear combination of the electric and magnetic vector spherical waves of the same multipolar order m , multipolar degree n , and radial dependence J

$$\mathbf{G}_{m,n}^{(J),+}(\mathbf{r}) = \frac{\mathbf{N}_{m,n}^{(J),+}(\mathbf{r}) + \mathbf{M}_{m,n}^{(J),+}(\mathbf{r})}{\sqrt{2}}, \quad (2.57)$$

$$\mathbf{G}_{m,n}^{(J),-}(\mathbf{r}) = \frac{\mathbf{N}_{m,n}^{(J),+}(\mathbf{r}) - \mathbf{M}_{m,n}^{(J),+}(\mathbf{r})}{\sqrt{2}}, \quad (2.58)$$

are eigenvectors of Λ ,

$$\Lambda \mathbf{G}_{m,n}^{(J),\pm}(\mathbf{r}) = \pm \mathbf{G}_{m,n}^{(J),\pm}(\mathbf{r}). \quad (2.59)$$

Therefore, it is possible to expand a field, solution to the wave equation, into a basis of vector spherical waves of well defined helicity. Based on the things said above, it follows that a circularly polarized plane wave can be expanded only by the fields $\mathbf{G}_{m,n}^{(J),+}(\mathbf{r})$ or $\mathbf{G}_{m,n}^{(J),-}(\mathbf{r})$ depending on its handedness. The coefficients of this decomposition can be derived from Eqn. (B.2)-(B.3). This link between circularly polarized plane waves and the fields $\mathbf{G}_{m,n}^{(J),+}(\mathbf{r})$ and $\mathbf{G}_{m,n}^{(J),-}(\mathbf{r})$ will be used in sections 4.3 and 5.1.

Waveguide theory

This sections presents the basics of waveguide theory. The concepts presented here will later become useful, when we present the optimization of a waveguide coupler in section 5.2.

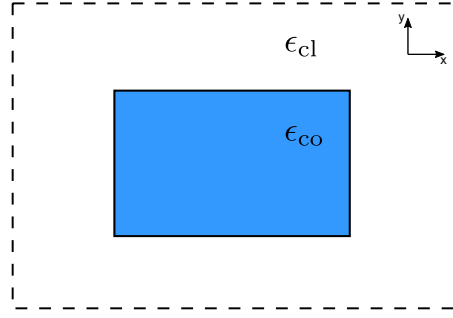


Figure 2.2: Sketch of a dielectric rectangular waveguide. The waveguide has a rectangular core with permittivity ϵ_{CO} . The core is surrounded by the cladding, which extends till infinity and has a permittivity ϵ_{CL} . The geometry of the waveguide is invariant along z -direction.

An optical waveguide is a photonic structure used to propagate light in a confined manner. In its basic architecture, the waveguide consists of two regions with two different material properties: the waveguide core and the cladding. In all-dielectric waveguides, the permittivity of the core, ϵ_{CO} , is higher than that of the cladding, ϵ_{CL} . This keeps light beams confined within the core due to total internal reflection [47]. Figure 2.2 shows a sketch of the cross section of a basic all-dielectric waveguide. The waveguide has a core with a rectangular cross section and it is invariant along a third direction, in this case we will use the z -axis as the invariant direction. The cladding, with permittivity equal to ϵ_{CL} , extends to infinity.

If the material properties of a waveguide are invariant along the z -direction, one can express the solution of Maxwell's equations as a superposition of fields with the form ([48] section 30-1)

$$\mathbf{E}(\mathbf{r}) = \mathbf{E}(x, y)e^{ik_z z}, \quad (2.60)$$

$$\mathbf{H}(\mathbf{r}) = \mathbf{H}(x, y)e^{ik_z z}. \quad (2.61)$$

Such an Ansatz basically respects the invariance of the geometry in the z -direction by using a plane wave Ansatz for the dependency along z . It is furthermore useful, for translational invariant waveguides, to decompose the fields into transverse and z -components,

$$\mathbf{E}(\mathbf{r}) = (\mathbf{E}_t(x, y) + E_z(x, y)\hat{\mathbf{z}})e^{ik_z z}, \quad (2.62)$$

$$\mathbf{H}(\mathbf{r}) = (\mathbf{H}_t(x, y) + H_z(x, y)\hat{\mathbf{z}})e^{ik_z z}. \quad (2.63)$$

Such decomposition allows for waveguides invariant in z -direction to write solutions to Maxwell's equations as a pair of coupled equations between only the z -components of the fields ([48] section 30-8),

$$\begin{aligned}
 & (\nabla_t^2 + k_t^2) E_z(x, y) - \frac{k_z^2}{k_t^2(x, y)} \nabla_t E_z(x, y) \cdot \nabla_t \ln(\epsilon(x, y)) = \\
 & - Z_0 \frac{k_0 k_z}{k_t(x, y)} \hat{\mathbf{z}} \cdot (\nabla_t H_z(x, y) \times \nabla_t \ln(\epsilon(x, y))), \tag{2.64}
 \end{aligned}$$

$$\begin{aligned}
 & (\nabla_t^2 + k_t^2(x, y)) H_z(x, y) - \frac{\epsilon(x, y) k_0^2}{k_t^2} \nabla_t H_z(x, y) \cdot \nabla_t \ln(\epsilon(x, y)) = \\
 & \frac{1}{Z_0} \frac{\epsilon(x, y) k_0 k_z}{k_t(x, y)} \hat{\mathbf{z}} \cdot (\nabla_t E_z(x, y) \times \nabla_t \ln(\epsilon(x, y))), \tag{2.65}
 \end{aligned}$$

where Z_0 is the impedance of free space and $k_t^2 = k_0^2 \epsilon(x, y) - k_z^2$.

The transverse components can be obtained from the solutions of the z -components ([48] Eqn. 11-43).

The above equations describe an eigenvalue problem. One needs to determine the values of the fields and the propagation constant k_z that together solve Eqns. (2.64)-(2.65). The solutions can be separated into a finite set of guided modes, $\mathbf{E}_m(\mathbf{r})$, and a radiative field $\mathbf{E}_{\text{rad}}(\mathbf{r})$ as

$$\mathbf{E}(\mathbf{r}) = \sum_m \left(a_m \mathbf{E}_m(x, y) e^{ik_{z,m}z} + a_{-m} \mathbf{E}_{-m}(x, y) e^{-ik_{z,m}z} \right) + \mathbf{E}_{\text{rad}}(\mathbf{r}) \tag{2.66}$$

The guided modes are solutions for which the field is mainly guided within the core region and whose power does not decay along the propagation direction z . That is, the imaginary part of the propagation constant $k_{z,m}$ of a guided mode equals to zero. However, the existence of guided modes is not assured in any waveguide and for any frequency. Their existence strongly depends on the dimensions of the waveguide core and on the material properties. The larger the waveguide core, the more likely that more guided modes are sustained. The propagation constant of the guided modes is bounded by the relation $k_0^2 \epsilon_{\text{cl}} \leq k_{z,m} \leq k_0^2 \epsilon_{\text{co}}$. The mode with the largest real part of the propagation constant k_z is called the fundamental mode. The associated mode subscript given to this mode is usually the zero, $\mathbf{E}_0(\mathbf{r})$.

Looking at Eqn. (2.64), one can see that the z -components of the electric and magnetic fields are coupled by the term $\ln(\epsilon(x, y))$. In some situations, the modes are decoupled and one can obtain solutions with $E_z(x, y) = 0$, called transverse electric (TE) modes, and solutions with $H_z(x, y) = 0$, called transverse magnetic (TM) modes. However, except in a few very specific cases, e.g., waveguides with a perfect electric conductor cladding or planar waveguides, both TE and TM fields are present in the same mode. These last modes are called hybrid modes. Still, in all-dielectric waveguides with homogeneous permittivities in the core and the cladding it is often the case that the magnitude of one of the TE or TM components of a hybrid mode is much stronger than the other.

The guided modes of a waveguide fulfill orthogonality relations between them ([48] Eqn. 11-14),

$$\int_{S_\infty} (\mathbf{E}_m(\mathbf{r}) \times \mathbf{H}_n(\mathbf{r})) \cdot \hat{\mathbf{z}} dS = 2\delta_{m,n}; \quad m \neq n. \tag{2.67}$$

and also with the radiative field ([48] Eqn. 11-11),

$$\int_{S_\infty} (\mathbf{E}_m(\mathbf{r}) \times \mathbf{H}_{\text{rad}}(\mathbf{r})) \cdot \hat{\mathbf{z}} dS = 0. \tag{2.68}$$

These orthogonal relations are important, e.g., to compute the coupling strength of a given field $\mathbf{E}_{\text{scat}}(\mathbf{r})$ at the end facet of the waveguide into the different guided modes of the waveguide ([48] Eqn. 20-2),

$$a_i = \frac{1}{2} \int_{S_\infty} (\mathbf{E}_{\text{scat}}(\mathbf{r}) \times \mathbf{H}_m(\mathbf{r})) \cdot \hat{\mathbf{z}} dS. \quad (2.69)$$

Equation (2.67) assumes that the guided modes used to expand the field in Eqn. (2.66) are set to have unit norm. In this case, the power carried along the waveguide by each normalized guided mode is given by

$$P_{m,i} = |a_{m,i}|^2. \quad (2.70)$$

Equations (2.69) and (2.70) will be used to measure the performance of waveguide couplers in section 5.2.

2.3 The finite element method

As we have seen in section 2.2, the values of the electromagnetic field produced by oscillating charges are given by Maxwell's equations. By solving this set of equations, one gets access to the values of the fields and to other derived quantities, e.g., power losses, power radiated, etc.

When focusing on the design of a photonic structure, it is fundamental to know the value of the electromagnetic field when one aims to optimize the structure, as any value that measures the performance of the design will depend on the values of the electromagnetic field at or within certain spatial regions. However, except in some selected simple cases, as for example for an infinitely extended homogeneous medium, the solution to Maxwell's equations can not be obtained by analytical means anymore. Instead, one then needs to solve them numerically.

There exist a wide range of numerical methods used to solve Maxwell's equations. The choice between them depends on different characteristics of the problem, such as the geometry and materials of the structures, if one is interested in obtaining the time evolution of the fields or only in solving it for a specific time harmonic excitation, etc. Some methods, such as the finite-difference time-domain (see, e.g., [49, 50] and [51] chapter 3), the finite-difference frequency-domain [52–54], the finite element method [55–59], or the boundary integral method, are very versatile in terms of the types of geometries that they can solve. Other methods are meant to solve Maxwell's equations in more specific situations, such as plane wave propagation in stratified media [60, 61] or light scattering by spheres [42, 62, 63]. For these specific cases, using the specialized methods generally leads to shorter calculation times.

This thesis will develop around the use of the finite element method. We aim to develop an optimization strategy to find optimal shapes for generally complex photonic structures. In this context, a versatile numerically method is needed. The choice of the finite element method is based on its ability to accurately model complicated geometries. Furthermore, the finite element method allows to calculate the derivatives of the electromagnetic field with respect to parameters used to parametrize the shape of a structure. Having access to the shape derivatives of the electromagnetic field can speed up considerably the optimization process, as we will discuss in the next chapter.

In the following sections, we present the basics of the finite element method and of the calculation of the field derivatives with respect to the design parameters of the geometry

of the model. Although in the thesis we rely on the commercial finite element package for solving Maxwell's equations JCMSuite [57, 58], the description of the finite element method is given with a significant level of detail regarding some of its working principles. The reason behind this detailed description is that it is necessary to understand sufficiently well how the process of computing the derivatives of the electromagnetic field works. This applies particularly to the case of shape derivatives. Given the importance that the calculation and use of the shape derivatives have in this thesis, we consider it appropriate.

Description of the method

If one wants to describe what the finite element method is in a few words, one could probably list the main characteristics of the method: the discretization of the geometry into small patches, the use of polynomial vector basis functions to expand the electromagnetic field onto these patches, and the use of the weak formulation of Maxwell's equations to build a linear system of equations that solves for the amplitudes of each of these basis functions on each individual patch.

We proceed now to describe these main steps that compose the method. To make the process simpler to understand, we use a simple two-dimensional toy example to which we will apply some of the steps. The toy example, whose schematic is shown in Fig. 2.3, consists of a two dimensional model of an infinitely extended cylinder with a circular cross section made from a dielectric material embedded into a free space squared cavity. The cavity is bound by perfect electric conductor walls and the system is excited with a line source placed above the cylinder. The geometry of this model is infinitely extended in the $\pm z$ -directions.

The first step in the process of solving Maxwell's equations with the finite element method is the creation of a computer geometrical model of the problem. When defining the problem to solve, one needs to describe the geometries and materials that composes it. To do that, a CAD software is generally used [64–68]. Figure 2.3a shows a visual representation of the example model. After the geometry of the problem is defined, a mesh generator [69] discretizes the geometry into connected simpler geometrical shapes. Triangles and rectangles in two dimensional models and tetrahedrals or hexahedrals in three dimensional models are the main geometrical basis elements employed in the FEM method. Figure 2.3b, shows the discretization \mathcal{T} of the example geometry. In the example, the discretization \mathcal{T} is composed of a number of triangles \mathcal{T}_i , $\mathcal{T} = \cup \mathcal{T}_i$.

A good quality mesh is important to obtain accurate solutions. The quality of the mesh can be established by a series of different properties of the mesh elements (see, e.g., [70] chapter 15). Among them, the discretization of the geometry should have mesh elements with a low aspect ratio, i.e., with a small difference between the length of its edges. The faces of the mesh elements should be as close to ideal as possible, and the transition in the size of the mesh elements should be smooth. After producing a discretization, the mesh generators performs a series of quality measures to identify mesh elements with poor quality [71, 72] and to replace them with elements of higher quality.

To solve the electromagnetic field, the finite element method uses the weak formulation of Maxwell's equations (see, e.g., [56] chapter 4). For time harmonic fields, this can be obtained by multiplying the wave equation, Eqn. (2.23), with a test function $\mathbf{U}(\mathbf{r}) \in S = H(\text{curl}, \Omega)$ and then integrating the expression across the computational domain Ω ,

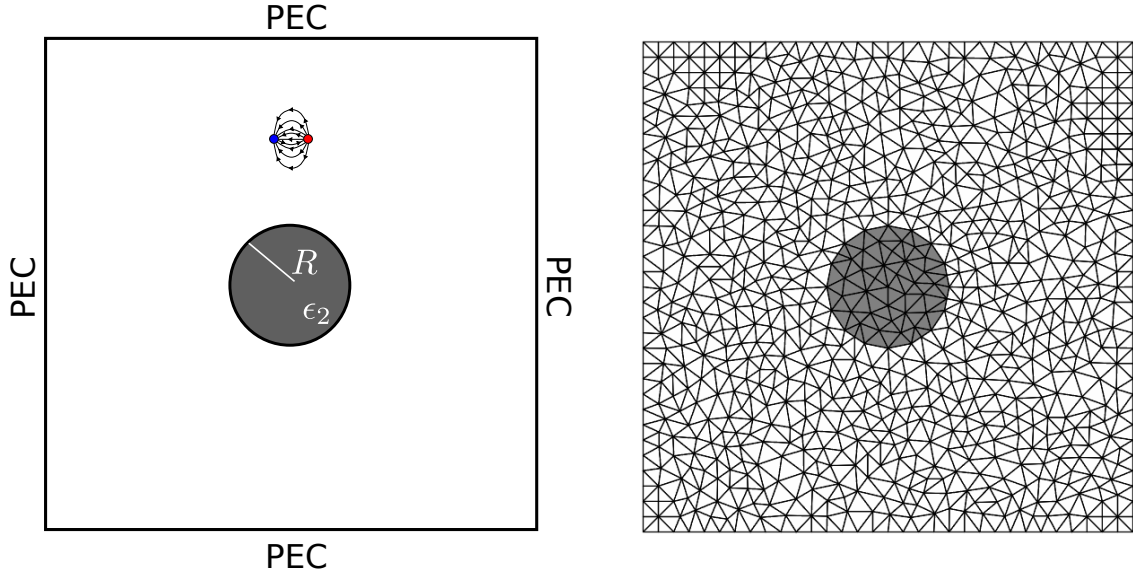


Figure 2.3: a. Two dimensional model used to describe how to solve the electromagnetic field in a geometry using the finite element method. The model consist of a square, free space, cavity bounded by perfect electric conductor walls. Centered inside the cavity, there is a cylinder of radius $R = 200$ nm made from a material with permittivity $\epsilon_2 = 2.5$. The cavity is excited by a line source with an excitation wavelength of $\lambda_0 = 450$ nm. **b.** Finite element discretization of the computational domain Ω shown in figure a. The domain Ω is discretized into a series of connected triangles \mathcal{T}_i that compose the discretization \mathcal{T} .

$$\int_{\Omega} \left\{ \mathbf{U}^*(\mathbf{r}) \cdot \left(\frac{1}{\underline{\mu}(\mathbf{r})} (\nabla \times \mathbf{E}(\mathbf{r})) - \omega^2 \underline{\epsilon}(\mathbf{r}) \mathbf{E}(\mathbf{r}) \right) \right\} dV = \int_{\Omega} i\omega \mathbf{U}^*(\mathbf{r}) \cdot \mathbf{J}(\mathbf{r}) dS. \quad (2.71)$$

The Sobolev space $S = H(\text{curl}, \Omega)$ is the vector space composed by the functions that have a finite L2 norm and whose curl has also a finite L2 norm.

Applying a partial integration to the left hand side of Eqn. 2.71, the solution to Maxwell's equations can be stated as [58]: Find the field $\mathbf{E}(\mathbf{r}) \in S$ such that,

$$\begin{aligned} \int_{\Omega} \frac{1}{\underline{\mu}(\mathbf{r})} (\nabla \times \mathbf{E}(\mathbf{r})) \cdot (\nabla \times \mathbf{U}^*(\mathbf{r})) - \omega^2 \underline{\epsilon}(\mathbf{r}) \mathbf{E}(\mathbf{r}) \cdot \mathbf{U}^*(\mathbf{r}) dV &= \int_{\Omega} i\omega \mathbf{J}(\mathbf{r}) \cdot \mathbf{U}^*(\mathbf{r}) dV \\ - \int_{\partial\Omega} \mathbf{U}^*(\mathbf{r}) \cdot \mathbf{F}(\mathbf{r}) dS \quad \forall \mathbf{U} \in S, & \end{aligned} \quad (2.72)$$

where $\mathbf{F}(\mathbf{r})$ expresses a given Neuman boundary condition,

$$\mathbf{F}(\mathbf{r}) = \mathbf{n}(\mathbf{r}) \times \left(\frac{1}{\underline{\mu}(\mathbf{r})} \nabla \times \mathbf{E}(\mathbf{r}) \right), \quad (2.73)$$

with $\mathbf{n}(\mathbf{r})$ being the unitary vector normal to the boundary $\partial\Omega$ of the computational domain Ω .

Depending on the type of problem that one wants to solve, different boundary conditions must be applied. Examples are the perfect electric conductor boundary condition, $\mathbf{n}(\mathbf{r}) \times$

$\left(\frac{1}{\underline{\mu}(\mathbf{r})}\nabla \times \mathbf{E}(\mathbf{r})\right) = 0$, periodic boundary conditions for gratings or photonic crystals ([73] chapter 5), or implementations of the radiation condition using perfectly matched layers [74–76] used to solve scattering problems.

The definition of $\mathbf{E}(\mathbf{r})$ and $\mathbf{U}(\mathbf{r})$ as elements of the Sobolev space $S = H(\text{curl}, \Omega)$ of complex valued vectors allows for solutions that present discontinuities at some points of space. Note that such discontinuities in the electric and magnetic fields are often encountered on the boundaries between domains with different material properties.

Defining the bilinear and linear functionals $a(\mathbf{u}, \mathbf{v})$ and $f(\mathbf{u})$,

$$a(\mathbf{u}, \mathbf{v}) = \int_{\Omega} (\nabla \times \mathbf{u}^*(\mathbf{r})) \cdot \frac{1}{\underline{\mu}(\mathbf{r})} (\nabla \times \mathbf{v}(\mathbf{r})) - \omega^2 \underline{\epsilon}(\mathbf{r}) \mathbf{u}^*(\mathbf{r}) \cdot \mathbf{v}(\mathbf{r}) dV, \quad (2.74)$$

$$f(\mathbf{u}, \mathbf{j}) = \int_{\Omega} i\omega \mathbf{u}^*(\mathbf{r}) \cdot \mathbf{j}(\mathbf{r}) dV - \int_{\partial\Omega} \mathbf{u}^*(\mathbf{r}) \cdot \mathbf{F}(\mathbf{r}) dS, \quad (2.75)$$

the solution of Maxwell's equations requires to find the field $\mathbf{E}(\mathbf{r}) \in S$ such that,

$$a(\mathbf{U}, \mathbf{E}) = f(\mathbf{U}), \forall \mathbf{U} \in S. \quad (2.76)$$

To numerically solve Eqn. (2.72), a finite set of basis functions $e_i(\mathbf{r}) \in S$ are used to construct an approximate solution, $\mathbf{E}_h(\mathbf{r})$, of $\mathbf{E}(\mathbf{r})$,

$$\mathbf{E}_h(\mathbf{r}) = \sum_{i=1}^{N_h} e_{h,i} \mathbf{b}_i(\mathbf{r}). \quad (2.77)$$

The basis functions $\mathbf{b}_i(\mathbf{r})$ generate a subspace $S_h \subset S$. The discretized system that approximates Maxwell's equations can be solved by finding a solution $\mathbf{E}_h(\mathbf{r}) \in S_h$ such that

$$a(\mathbf{U}_h, \mathbf{E}_h) = f(\mathbf{U}_h), \forall \mathbf{U}_h \in S_h. \quad (2.78)$$

The basis functions $\mathbf{b}_i(\mathbf{r})$ are generally polynomials of a certain degree n whose support is contained in just one or a few patches of the discretization. Generally, the basis elements used to solve Maxwell's equations are combinations of the so called Nédelec or edge basis elements [77]. These elements ensure the continuity of the tangential components of the fields $\mathbf{E}(\mathbf{r})$ and $\mathbf{H}(\mathbf{r})$ across the boundaries between neighboring patches.

One example of two dimensional vector elements are the Nédelec elements of order 1. They are shown in Fig. 2.4 for the case of a isosceles right triangle with shorter sides of length 1, \mathcal{T}_0 . Their values are given by the below equations [58]

$$\bar{\mathbf{n}}_1(\bar{x}, \bar{y}) = (1 - \bar{y}) \hat{\mathbf{x}} + \bar{x} \hat{\mathbf{y}}, \quad (2.79)$$

$$\bar{\mathbf{n}}_2(\bar{x}, \bar{y}) = -\bar{y} \hat{\mathbf{x}} + \bar{x} \hat{\mathbf{y}}, \quad (2.80)$$

$$\bar{\mathbf{n}}_3(\bar{x}, \bar{y}) = -\bar{y} \hat{\mathbf{x}} + (\bar{x} - 1) \hat{\mathbf{y}}. \quad (2.81)$$

$$(2.82)$$

The support of these basis elements lays on the reference triangle \mathcal{T}_0 . This triangle is just a reference triangle, not part of the triangularization of the geometry, \mathcal{T} . The expression of the Nédelec functions on each triangle \mathcal{T}_i , $\mathbf{n}_{i,m}(\mathbf{r})$ with $m \in \{1, 2, 3\}$, depends on the

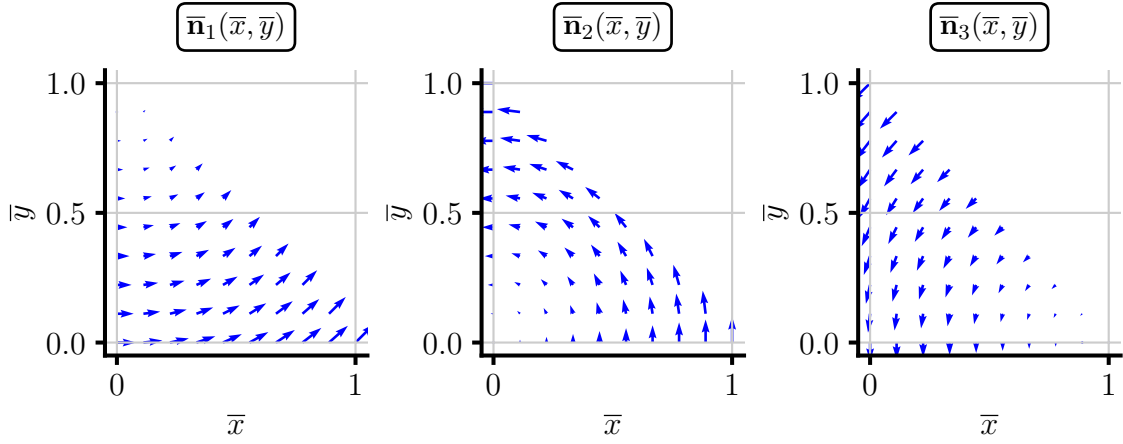


Figure 2.4: Vector basis functions $\bar{\mathbf{n}}_1(\bar{x}, \bar{y})$, $\bar{\mathbf{n}}_2(\bar{x}, \bar{y})$, and $\bar{\mathbf{n}}_3(\bar{x}, \bar{y})$ of degree $n = 1$ used to expand the solution of the electric field in a reference isosceles right triangle \mathcal{T}_0 . The vector functions are defined by Eqns. (2.79)-(2.81).

values of the vertices of \mathcal{T}_i , $(x_{v,i1}, y_{v,i1})$, $(x_{v,i2}, y_{v,i2})$, and $(x_{v,i3}, y_{v,i3})$. Instead of calculating the values of these functions explicitly, one could use the fact that every triangle can be mapped into the reference isosceles right triangle \mathcal{T}_0 shown in Fig. 2.4 using the transformation

$$\begin{bmatrix} x \\ y \end{bmatrix} = \begin{bmatrix} x_{v,i1} \\ y_{v,i1} \end{bmatrix} + \underline{T}_i \begin{bmatrix} \bar{x} \\ \bar{y} \end{bmatrix} = \begin{bmatrix} x_{v,i1} \\ y_{v,i1} \end{bmatrix} + \begin{bmatrix} x_{v,i2} - x_{v,i1} & x_{v,i3} - x_{v,i1} \\ y_{v,i2} - y_{v,i1} & y_{v,i3} - y_{v,i1} \end{bmatrix} \begin{bmatrix} \bar{x} \\ \bar{y} \end{bmatrix}. \quad (2.83)$$

When using the Nédelec elements of order 1, each one of the global basis functions $\mathbf{b}_i(\mathbf{r})$ of Eqn. (2.77) is defined over two triangles that share one edge. In each one of the triangles, the values of $\mathbf{b}_i(\mathbf{r})$ are given by one of the three Nédelec functions defined on it. For first order elements, there is only one global basis function $\mathbf{b}_i(\mathbf{r})$ associated to each edge of the discretization.

Once a discretization of the geometry and a set of basis functions over it is established, the problem given by Eqn. (2.78) can be solved. To fulfill Eqn. (2.78) for every \mathbf{U}_h in S_h is equivalent to fulfill it for each element $\mathbf{b}_i(\mathbf{r})$ of the basis. Applying Eqn. (2.78) to each vector function of the basis that expands S_h leads to a system of linear equations described by a matrix \underline{A} and a right hand side vector \mathbf{f} ,

$$\underline{A}\mathbf{e}_h = \mathbf{f}, \quad (2.84)$$

where \mathbf{e}_h is the vector composed by the amplitudes $e_{h,i}$ of the expansion given by Eqn. (2.77). The elements $\underline{A}_{[i,j]}$ of the system matrix \underline{A} are given by

$$\underline{A}_{[i,j]} = a(\mathbf{b}_i, \mathbf{b}_j). \quad (2.85)$$

The entries of the vector \mathbf{f} can be similarly obtained from the evaluation of the linear functional

$$\mathbf{f}_{[i]} = f(\mathbf{b}_i). \quad (2.86)$$

Let us use the toy example described in Fig. 2.3 to show parts of the steps used to calculate matrix \underline{A} . As the geometry and the source of the example are z invariant, two independent

solutions, both depending only on the x and y coordinates can be obtained. The electric field of one of the solutions has only x and y -components, the other solution has only a z -component [78]. Here we will describe the process for the vectorial solution, with x and y -components, using the two-dimensional Nédelec elements of degree one. Let us note that these first order elements are rarely used, as the trade-off between the accuracy of the result and the computational costs is generally not favourable to the use of these basis elements. We use them here because of their simplicity with respect to other basis elements of a higher polynomial degree. The idea here is to present the main techniques used in the implementation of the finite element method for a rather simple example. However, the main concepts can be easily extrapolated to problems that use higher order polynomial basis functions and that are defined in three dimensional geometries.

As said before, for the case of the Nédelec elements of degree one, the basis elements $\mathbf{b}_i(\mathbf{r})$ have support on only two neighbored triangles. That means that only a few entries $\underline{A}_{[i,j]}$ for each fixed row i are non-zero. Those correspond to the basis elements $\mathbf{b}_j(\mathbf{r})$ whose support overlaps with the support of $\mathbf{b}_i(\mathbf{r})$. For all the other basis functions, the bilinear functional $a(\mathbf{b}_i(\mathbf{r}), \mathbf{b}_j(\mathbf{r}))$ of Eqn. (2.85) will be zero. The overlap region between two different overlapping basis elements $\mathbf{b}_i(\mathbf{r})$ and $\mathbf{b}_j(\mathbf{r})$ is only one of the triangles of the discretization \mathcal{T} . Let us denote this triangle by \mathcal{T}_t . That is, \mathcal{T}_t is the triangle contained in the support of the two global basis functions $\mathbf{b}_i(\mathbf{r})$ and $\mathbf{b}_j(\mathbf{r})$. The values of $\mathbf{b}_i(\mathbf{r})$ and $\mathbf{b}_j(\mathbf{r})$ on \mathcal{T}_t are given by two of the three Nédelec elements defined on this triangle. We can denote them, e.g., by $\mathbf{n}_{t,l(i)}(\mathbf{r})$ and $\mathbf{n}_{t,l(j)}(\mathbf{r})$ respectively. That is, the function $l(i)$ gives the index in the set of local Nédelec vector functions on the triangle \mathcal{T}_t corresponding to the global basis function $\mathbf{b}_i(\mathbf{r})$.

Let us compute the entry $\underline{A}_{[i,j]}$. As in this example the permittivity and the permeability are scalar homogeneous values within each triangle \mathcal{T}_i , they can be taken out of the integrals and one obtains,

$$\underline{A}_{[i,j]} = \frac{1}{\mu} \int_{\mathcal{T}_t} (\nabla \times \mathbf{b}_i^*(\mathbf{r})) \cdot (\nabla \times \mathbf{b}_j(\mathbf{r})) \, dx dy - \omega^2 \epsilon_{\mathcal{T}_t} \int_{\mathcal{T}_t} \mathbf{b}_i^*(\mathbf{r}) \cdot \mathbf{b}_j(\mathbf{r}) \, dx dy, \quad (2.87)$$

$$\begin{aligned} \underline{A}_{[i,j]} &= \frac{1}{\mu} \int_{\mathcal{T}_t} \left(\nabla \times \mathbf{n}_{t,l(i)}^*(\mathbf{r}) \right) \cdot \left(\nabla \times \mathbf{n}_{t,l(j)}(\mathbf{r}) \right) \, dx dy \\ &\quad - \omega^2 \epsilon_{\mathcal{T}_t} \int_{\mathcal{T}_t} \mathbf{n}_{t,l(i)}^*(\mathbf{r}) \cdot \mathbf{n}_{t,l(j)}(\mathbf{r}) \, dx dy. \end{aligned} \quad (2.88)$$

Using the the mapping given by Eqn. (2.83), Eqn. (2.87) can be described as a function of the Nédelec basis functions defined in the reference triangle \mathcal{T}_0 given by Eqns. (2.79)-(2.81) ([79] section 1.7.4),

$$\begin{aligned} \underline{A}_{[i,j]} &= + \frac{1}{\mu \det(\underline{T}_t)} \int_{\mathcal{T}_0} \left(\nabla \times \bar{\mathbf{n}}_{l(i)}^*(\bar{x}, \bar{y}) \right) \cdot \left(\underline{G}^t (\nabla \times \bar{\mathbf{n}}_{l(j)}(\bar{x}, \bar{y})) \right) \, d\bar{x} d\bar{y} \\ &\quad - \omega^2 \epsilon_{\mathcal{T}_t} \det(\underline{T}_t) \int_{\mathcal{T}_0} \bar{\mathbf{n}}_{l(i)}^*(\bar{x}, \bar{y}) \cdot \left(\underline{N}^t \bar{\mathbf{n}}_{l(j)}(\bar{x}, \bar{y}) \right) \, d\bar{x} d\bar{y}, \end{aligned} \quad (2.89)$$

with \underline{G}^i and \underline{N}^i being the covariant and contravariant metric tensors, result of the change of vector fields under the linear mapping for the triangle \mathcal{T}_i . Their expressions are given by

$$\underline{G}_{[l,m]}^i = \sum_{\nu=1}^{n_{\text{dim}}} \underline{T}_{i,[\nu,l]} \underline{T}_{i,[\nu,m]}, \quad (2.90)$$

$$\underline{N}_{[l,m]}^i = \sum_{\nu=1}^{n_{\text{dim}}} \left(\underline{T}_i^{-T} \right)_{[\nu,l]} \left(\underline{T}_i^{-T} \right)_{[\nu,m]}. \quad (2.91)$$

Using some linear algebra, one can obtain an equivalent expression to Eqn. (2.89) which involves integrals whose values are not dependent on the specific triangle. In this way, it is possible to obtain the complete matrix \underline{A} without having to calculate the integrals for each entry of the matrix. As example, the second integral term of Eqn. (2.89) can be expressed as

$$\omega^2 \epsilon_{\mathcal{T}_i} \det(\underline{T}_t) \sum_{\nu=1}^2 \sum_{\eta=1}^2 N_{[\nu,\eta]}^t \int_{\mathcal{T}_0} \bar{\mathbf{n}}_{l(i)}^* (\bar{x}, \bar{y}) \cdot \hat{\mathbf{e}}_{\nu} (\hat{\mathbf{e}}_{\eta} \cdot \bar{\mathbf{n}}_{l(j)} (\bar{x}, \bar{y})) \, d\bar{x}d\bar{y} = \quad (2.92)$$

$$\omega^2 \epsilon_{\mathcal{T}_i} \det(\underline{T}_t) \sum_{\nu=1}^2 \sum_{\eta=1}^2 N_{[\nu,\eta]}^t I_{\nu,\eta}^{l(i),l(j),2}. \quad (2.93)$$

Similar integrals can be obtained for the first integral of the right hand side of Eqn. (2.89), $I_{\nu,\eta}^{l(i),l(j),1}$. One obtains

$$\underline{A}_{[i,j]} = + \frac{1}{\mu} \frac{1}{\det(\underline{T}_t)} \sum_{\nu=1}^{n_{\text{dim}}} \sum_{\eta=1}^{n_{\text{dim}}} G_{[\nu,\eta]}^t I_{\nu,\eta}^{l(i),l(j),1} - \omega^2 \epsilon_{\mathcal{T}_i} \det(\underline{T}_t) \sum_{\nu=1}^{n_{\text{dim}}} \sum_{\eta=1}^{n_{\text{dim}}} N_{[\nu,\eta]}^t I_{\nu,\eta}^{l(i),l(j),2}. \quad (2.94)$$

As one can see, once the integral values $I_{\nu,\eta}^{l(i),l(j),2}$ are obtained, the entry of each matrix is just given by the values of the material properties and the linear mapping between the triangles \mathcal{T}_i and the reference triangle \mathcal{T}_0 .

Once computed the system matrix, one needs to obtain the right hand side of Eqn. (2.84) and solve the linear system. In the example of the circle, as the walls are assumed to be perfect electric conductor, the only entries in \mathbf{f} would come from the integral evaluation of the line source over the triangle where the source is placed.

Shape and material derivatives

In many cases along this thesis we are optimizing different nanostructures for which we will exploit the use of derivative information. What this means is that, during the optimization process, we will compute how a merit function $f_{\text{ob}}(\mathbf{x})$, that measures the performance of the nanostructure, changes with respect to an infinitesimal change of the design variables x_i that parametrize the shape of the structure or its material properties. To obtain those quantities, a required intermediate step is the calculation of the derivatives of the solution of the electromagnetic field with respect to those design variables x_i . That holds because $f_{\text{ob}}(\mathbf{x})$ will be in all the considered cases a function dependent on the solution of the field $\mathbf{E}(\mathbf{r})$. This section describes how to calculate the shape and material derivatives of the field $\mathbf{E}(\mathbf{r})$ obtained with the finite element method. As we did for describing the finite element method itself, we will use the example of Fig. 2.3 to show the process.

A field $\mathbf{E}_h(\mathbf{r})$ obtained with the finite element method is the solution of the linear system of equations given by Eqn. (2.84). If one differentiates Eqn. (2.84) with respect to a design parameter x_i one obtains

$$\begin{aligned} \frac{d\underline{A}}{dx_i} \mathbf{e}_h + \underline{A} \frac{d\mathbf{e}_h}{dx_i} &= \frac{d\mathbf{f}}{dx_i} \rightarrow \\ \frac{d\mathbf{e}_h}{dx_i} &= \underline{A}^{-1} \left(-\frac{d\underline{A}}{dx_i} \mathbf{e}_h + \frac{d\mathbf{f}}{dx_i} \right). \end{aligned} \quad (2.95)$$

Therefore, to obtain the desired quantity $\frac{d\mathbf{E}_h}{dx_i}$, one needs to calculate the derivatives of the system matrix \underline{A} and the right hand side term \mathbf{f} . Let us note that the inverse of the matrix \underline{A} has previously already been calculated while solving Eqn. (2.84). A further computation is not necessary, which clearly highlight the use of the finite element method for our problems at this level already.

Let us now use the toy example of the perfect electric conductor cavity to describe the details of this calculation. We aim to compute the derivatives of \mathbf{E}_h with respect to the permittivity ϵ_2 and the radius R of the cylinder. Let us first describe how to compute the derivatives with respect to ϵ_2 .

Equation 2.89 shows how to obtain the entries of the system matrix \underline{A} linked to the triangle \mathcal{T}_t of the discretization when the solution of Maxwell's equations are approximated by the edge basis elements $\mathbf{b}_i(\mathbf{r})$. For the triangles that discretize the cylinder, the permittivity entries $\epsilon_{\mathcal{T}_t}$ are equal to ϵ_2 . Therefore, the derivatives of the entries of the matrix with respect to ϵ_2 will equal

$$\frac{dA_{[i,j]}}{d\epsilon_2} = -\omega^2 \det(\underline{T}_t) \sum_{\nu=1}^2 \sum_{\eta=1}^2 \underline{G}_{[\nu,\eta]}^t T_{\nu,\eta}^{l(i),l(j)}, \quad (2.96)$$

This calculation needs to be done for all the pairs of basis functions with support on the the circle and it will be equal to 0 for the rest of the entries of \underline{A} .

As one can see, once the matrix \underline{A} has been computed and if the values of the second integral terms given by Eqn. (2.92) were stored, obtaining the derivatives of \underline{A} with respect to the permittivities does not involve any extra computational effort.

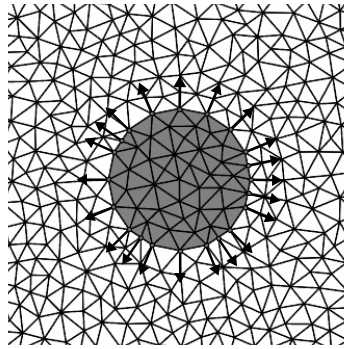


Figure 2.5: Calculation of the shape derivative of the finite element discretization with respect to the radius of the circle, R . The change in the radius imply a change of the position of the vertices that compose the boundary of the circle. The calculation of the shape derivatives of the mesh discretization is one of the main steps necessary to compute the shape derivatives of the electromagnetic field with the finite element method.

Computing the shape derivatives, i.e., the derivatives of the solution \mathbf{E}_h with respect to some parameter that describes some feature of the structure, is a similar process. However, it is a slightly more complicated task. The first step is to determine how the discretization of the structure changes with an infinitesimal change of the design parameter x_i . In the example of the cylinder, we chose the radius R . If one changes the radius, the vertices of the triangles that compose the boundary of the circle will move in radial direction with respect to the center of the cylinder, as shown in Fig. 2.5. Depending of the complexity of the geometry, obtaining the derivatives of the vertices can be a non-trivial task.

Once the derivatives of the mesh vertices, $d(x_{vt}, y_{vt})/dR$, are obtained, one can obtain the derivatives of the matrices \underline{T}_t by applying the chain rule. These matrices describe the mapping between the triangles \mathcal{T}_t and the reference triangle \mathcal{T}_0 . From there, one can obtain the derivative of the determinant of \underline{T}_t , applying Jacobi's formula ([80] chapter 8), and of the matrices \underline{N}^t and \underline{G}^t .

Once all these derivatives are obtained, the shape derivative of the entries of the matrix linked to the triangle \mathcal{T}_t can be calculated,

$$\begin{aligned} \frac{dA_{[i,j]}}{dR} = & + \frac{1}{\mu} \frac{1}{\det(\underline{T}_t)^2} \sum_{\nu=1}^2 \sum_{\eta=1}^2 \left(\frac{dG_{[\nu,\eta]}^t}{dR} \det(\underline{T}_t) - \frac{d \det(\underline{T}_t)}{dR} G_{[\nu,\eta]}^t \right) I_{\nu,\eta}^{l(i),l(j),1} \\ & - \omega^2 \epsilon_{\mathcal{T}_t} \det(\underline{T}_t) \sum_{\nu=1}^2 \sum_{\eta=1}^2 \left(\frac{dN_{[\nu,\eta]}^t}{dR} \det(\underline{T}_t) + \frac{d \det(\underline{T}_t)}{dR} N_{[\nu,\eta]}^t \right) I_{\nu,\eta}^{l(i),l(j),2}. \end{aligned} \quad (2.97)$$

With this last step, the process of computing $\frac{dA}{dR}$ is concluded.

As already commented at the beginning of section 2.3, we use the software JCMSuite [57, 58] for the finite element calculations done in this thesis. The same also applies for the calculation of the shape and material derivatives. Once described all the processes required to obtain the solution of the electromagnetic field for the toy example of the cavity, one can get an idea of how the complexity of the problem scales when one considers problems in three dimensions, with more complicated structures, different types of boundary conditions and using basis elements of a higher polynomial degree.

Although JCMSuite already integrates most of the features to compute the shape and material derivatives, the task of calculating the shape derivatives of the mesh elements must be done by the user. This task is different depending on the type of structure. For two dimensional structures or three dimensional structures that can be defined as extrusions of two dimensional models along a third dimension, we can directly provide the derivatives of the geometry during the step of defining the computational model. This type of geometries are frequently encountered in structures fabricated by photolithographic processes. This method is used, e.g., in section 5.2 to optimize a freeform waveguide coupler.

For more complex three dimensional models, the procedure is a little bit more elaborated. First, the computational domain needs to be discretized. Once the mesh is created, JCMSuite will return the vertices of the boundary of the structure aimed to differentiate. Then, in a Python script, we need to retrieve the values of the design parameters x_i corresponding to each vertex and compute the corresponding shape derivatives of the vertices. The derivatives of the vertices are then returned to JCMSuite. The rest of the process described in this section is then automatically performed by JCMSuite. We use this second methodology to compute the shape derivatives of helices in, e.g., section 5.1.

Regarding the reuse of the discretization mesh between different simulations in an optimization process, we choose to recalculate it for each new simulation. The other option would be to simply change the vertices of the mesh when one needs to simulate geometries which are very similar to each other. First, as we will mainly perform global optimization, it is usually not the case that the geometries of consecutive iterations are similar. Secondly, even in case of doing some local optimization, the step size can be large enough such that remeshing is needed to avoid bad quality mesh elements. In any case, the time needed to perform the meshing is a small fraction with respect to the

time needed to solve the linear system. Therefore, the benefit gained with this process does not generally compensate the increase in complexity required for its implementation.

The direct and the adjoint methods

The previous section explained how to obtain the shape and material derivatives of the finite element method solution for the electric field. In the process of designing a photonic structure, these derivatives are an intermediate step necessary to obtain the aimed shape and material derivatives of a given merit function $f_{\text{ob}}(\mathbf{x})$. To obtain these last quantities, there are two main methods that one can use: the direct method and the adjoint method. We proceed now to describe both methods and their main differences. Based on their characteristics, we finally discuss why we choose the direct method as the method used in this thesis.

Let us first shortly review the main results of the finite element method that we described above. The solution of the electromagnetic field in a problem solved with the finite element method is given by a vector \mathbf{e}_h that contains the coefficients of the expansion of the field into a set of vector basis functions. This vector \mathbf{e}_h is the solution of a linear system of equations given by Eqn. (2.84). Once the solution of the field is obtained, one can use it, together with the decomposition of the system matrix \underline{A} , to compute shape and material derivatives of \mathbf{e}_h with respect to different design variables. The procedure is given by Eqn. (2.95).

Now we want to go one step further and calculate the derivatives of the merit function, $f_{\text{ob}}(\mathbf{x})$, that measures the performance of the structure aimed to design. The merit function is a function of n different design parameters $\mathbf{x} = [x_1, \dots, x_n]^T$ that parametrize the structure. However, this is usually an indirect dependence. Because of the merit function measures the performance of a photonic structure, its values will directly depend on the values of the electric field $\mathbf{E}_h(\mathbf{r})$ at certain regions of space. Equivalently, they will depend on the values of the vector \mathbf{e}_h given by Eqn. (2.84). The dependence of the merit function with the design variables $[x_1, \dots, x_n]$ comes from the fact that the variables parametrize the structure, therefore the solution of \mathbf{e}_h is a function of these variables,

$$f_{\text{ob}}(x_1, \dots, x_n) = f_{\text{ob}}(\mathbf{E}_h(x_1, \dots, x_n)). \quad (2.98)$$

If one wants to obtain the derivatives of the objective function with respect to the design variables, one simply needs to propagate the derivatives using the chain rule,

$$\frac{df_{\text{ob}}(\mathbf{x})}{dx_i} = \frac{df_{\text{ob}}(\mathbf{x})}{d\mathbf{e}_h^T} \frac{d\mathbf{e}_h}{dx_i}. \quad (2.99)$$

Using Eqn. (2.95) one gets

$$\frac{df_{\text{ob}}(\mathbf{x})}{dx_i} = -\frac{df_{\text{ob}}(\mathbf{x})}{d\mathbf{e}_h^T} \underline{A}^{-1} \frac{d\underline{A}}{dx_i} \mathbf{e}_h, \quad (2.100)$$

where we have assumed that the term accounting for the illumination does not depend on the design variables.

The above equation describes the procedure that one would follow to compute the derivatives using the direct method [81–83] within the finite element method. It is important to note that the actual inverse of the system matrix \underline{A} is not computed when using the finite element method. The use of the actual inverse of a matrix is rarely used in computational methods, as it is an unstable technique. Instead, one usually calculates the LU

factorization (see, e.g., [84] lecture 20) of matrix \underline{A} and uses this factorization to solve a linear system through forward and back substitutions. The reason why this is important has to do with the use of the adjoint method.

To not have to solve a linear system for every design parameter x_i , one can exploit the below property of the adjoint of an operator,

$$\frac{df_{\text{ob}}(\mathbf{x})}{d\mathbf{e}_h^T} \underline{A}^{-1} \frac{d\underline{A}}{dx_i} \mathbf{e}_h = \left(\left(\underline{A}^\dagger \right)^{-1} \frac{df_{\text{ob}}(\mathbf{x})}{d\mathbf{e}_h} \right)^T \frac{d\underline{A}}{dx_i} \mathbf{e}_h, \quad (2.101)$$

with the superscript \dagger denoting the transpose complex conjugated of a matrix.

Solving the below system

$$\underline{A}^\dagger \lambda = \frac{df_{\text{ob}}(\mathbf{x})}{d\mathbf{e}_h}, \quad (2.102)$$

one can obtain the derivatives of the merit function with respect to the design parameters as

$$\frac{df_{\text{ob}}(\mathbf{x})}{dx_i} = -\lambda^T \frac{d\underline{A}}{dx_i} \mathbf{e}_h. \quad (2.103)$$

This procedure is called the adjoint method [82, 85, 86]. As one can see, the adjoint method requires to solve another system of equations, Eqn. (2.102). However, once this is done, obtaining the design derivatives with respect to each parameter does not require any extra Gaussian elimination.

Regarding the computational overhead, computing the design derivatives with the direct method requires a matrix-vector multiplication, then a posterior Gaussian elimination, and a final vector-vector multiplication. All this operations need to be repeated for each design parameter. The adjoint method requires to initially calculate a LU factorization for the adjoint system, Eqn. (2.102), and then it requires to perform a matrix-vector multiplication and a vector-vector multiplication per design parameter. If the system matrix \underline{A} of the finite element method were dense and one would need to solve the adjoint system, then the advantages of using the adjoint method would be negligible in almost any situation due to the computational overhead of computing the LU factorization for the adjoint system. However, because the matrix \underline{A} is a sparse matrix, there are some problems in which using the adjoint method results to be more efficient than the direct method. These problems are the problems where the number of design parameters x_i are in the order of the number of unknowns of the finite element system.

Topology optimization of photonic devices [25, 26, 87, 88] is one of the cases where the use of the adjoint method results usually more efficient than the use of the direct method. In these problems, one aims to obtain the derivatives with respect to the permittivity values of a big number of discretization elements $\epsilon_{\mathcal{T}_i}$. We saw in the previous section that computing the derivative of \underline{A} with respect to the permittivity value $\epsilon_{\mathcal{T}_i}$ requires a negligible computational overhead. Furthermore, $d\underline{A}/dx_i$ will have only a very small number of entries different than zero, and the time required by the matrix-vector multiplication could be also neglected. Therefore, the computational overhead per design parameter would be mainly given by the vector-vector multiplication. Moreover, if the simulated structure does not present absorption, the physical problem is hermitian and the LU factorization of the adjoint system is not required to solve it.

Because in this thesis we focus in problems of shape optimization, with structures parametrized with a maximum number of a few tens of parameters, the direct method results more efficient to compute the shape and material derivatives. This is, therefore, the method that we use in this thesis.

3 | Bayesian optimization

3.1 Introduction

The process of designing an optimal nanophotonic device consists in finding the combination of materials and geometry that results in a device with the best performance. The materials and geometries available for the design are often constrained by limitations of fabrication technology, costs, and time requirements. To find the optimal design, one needs to describe the set of feasible geometries and materials with a parametrization that uses a vector of d design variables $\mathbf{x} = [x_1, x_2, \dots, x_d]^T$. The set of all possible points \mathbf{x} composes the design space \mathcal{D} of the device. Then, a numerical method is needed to measure the performance of each possible device characterized by \mathbf{x} with the use of an objective function, $f_{\text{ob}}(\mathbf{x})$. The aim of the game is to find the point \mathbf{x}_{opt} in the design space that fulfills

$$f_{\text{ob}}(\mathbf{x}_{\text{opt}}) \leq f_{\text{ob}}(\mathbf{x}) \forall \mathbf{x} \in \mathcal{D}. \quad (3.1)$$

That corresponds to finding the global optimum. The maximum theoretically performance achievable by the optimization is directly limited by the chosen parametrization, i.e., by the range of possible devices considered. Generally, the higher the number of parameters used in the design space, the larger the range of devices that one can address. However, due to the curse of dimensionality [89], also known as the Hughes effect [90, 91], the computational demand of finding a global optimum increases exponentially with the number d of parameters, unless $f_{\text{ob}}(\mathbf{x})$ is a convex function. In nanophotonic devices, the objective function depends on the values of the electromagnetic field in a given structure and one generally needs to solve Maxwell's equations to evaluate $f_{\text{ob}}(\mathbf{x})$. The evaluation of Maxwell's equations for a given structure is in general resource demanding and, strongly depending on the complexity, the geometrical dimensionality, and the presence or absence of possible geometrical symmetries, this is a task that requires computational times between a few minutes and several hours.

The combination of computationally highly demanding objective functions and exponentially scaling design spaces makes the problem of finding the optimal nanophotonic device an intractable problem even for medium size dimensional problems, where d ranges in the order of 10 till 20. Only for highly symmetric devices, where one can exploit the symmetries to drastically reduce the computation times of the evaluation of $f_{\text{ob}}(\mathbf{x})$ or in problems where a high parallelization of the evaluation of $f_{\text{ob}}(\mathbf{x})$ is possible, finding a global optimum can still be a feasible task in a reasonable amount of time.

However, even if *a priori* finding a global optimum must be assumed as unlikely, it is still important to find a device that performs as good as possible within the available time for the given task. This is the purpose of optimization algorithms. To do that, the optimization algorithms choose the next evaluation points for the objective function based on a

certain optimization strategy and on information obtained from the previously evaluated points of $f_{\text{ob}}(\mathbf{x})$ to possibly identify x_{opt} .

The optimization strategy can consist of a few simple steps based on some heuristic criteria or it can rely on more complex surrogate models. Generally, heuristic algorithms are simpler to implement and they require relatively low computational time overheads. When the time required to evaluate the objective function is short, on time scales shorter than a second, it is normally preferable to use simple but fast optimization algorithms. Examples are particle swarm optimization [92–96], evolutionary algorithms [97–102] or simulated annealing [103–106]. Many different open source implementations of these methods can be found [107–110].

On the contrary, model-based [111–117] algorithms usually require longer computational times than heuristic global optimization algorithms. The underlying models of these algorithms are permanently updated based on the information obtained from the evaluated points thus far to better describe the most likely behavior of $f_{\text{ob}}(\mathbf{x})$. To decide where to perform the next evaluation of the objective function, the surrogate model is used to either infer the values of $f_{\text{ob}}(\mathbf{x})$ in points where its behavior is unknown or to compute other different expectation quantities [118]. Because all previous evaluations are taken into account for determining the next sampling point, these algorithms can show a better iteration convergence, i.e., they often require a smaller number of evaluations of the objective function to reach a similar performance [119, 120, A1]. Therefore, they are usually beneficial when optimizing objective functions with long evaluation times [121]. This is frequently the case when optimizing optical nano-structures. In these problems, the extra computational overhead required by the use of a more complex surrogate model can compensate the smaller number of required evaluations.

Among the different surrogate models, one can find models based on polynomial response surfaces [118, 122], radial basis functions [123, 124] or Gaussian processes [125–129]. Neural networks have also been used, for example for the design of photonic structures [36–38].

A well known surrogate based optimization algorithm is Bayesian optimization [130–133]. Bayesian optimization obtains a probabilistic distribution for $f_{\text{ob}}(\mathbf{x})$ conditioning a prior stochastic model over the set of observation points using Bayes' theorem [134]. Although different surrogate models have been proposed for the algorithm [133, 135–137], most implementations use Gaussian processes as the surrogate stochastic model [138–144].

The Gaussian process (GP) model is a nonparametric stochastic model [145–147] of an objective function $f_{\text{ob}}(\mathbf{x})$. That means that the model does not have a fixed number of degrees of freedom, such as, e.g., a polynomial fit. Instead, the model complexity is automatically adapting to the amount of available data. The GP assigns prior distributions directly over the values of $f_{\text{ob}}(\mathbf{x})$ (see, e.g., [126] section 3.1). They can be actually seen as stochastic parametric models with an infinite number of parameters. In fact, a GP can be interpreted as a neural network with a single hidden layer and an infinite amount of nodes, in which the weight nodes are treated as probabilistic variables following Gaussian distributions (see, e.g., [126] section 3.4.2 or [148]).

One of the key advantages of GPs is the fully probabilistic treatment of available data. In other words, it returns the most probable function value given the data. This posterior distribution over functions, conditioned on the evaluations of $f_{\text{ob}}(\mathbf{x})$, can be described by a simple analytical expression. Furthermore, a GP can incorporate derivative information of the objective function in a simple and natural way. These properties make GPs

a powerful tool to obtain relatively accurate posterior distributions of the modelled function with respect to the number of evaluations used. This is a very desired characteristic when performing global optimization.

For the above reasons, this work proposes the use of Bayesian optimization with Gaussian processes for the optimization of photonic devices. Its good iteration convergence makes it one of the best options to optimize photonic devices for low and medium dimensional design spaces [A1]. Furthermore, having access to the shape derivatives of the solutions of Maxwell's equations is a powerful tool in the optimization of photonic devices, and Bayesian optimization is one of the few global optimization algorithms that can efficiently exploit this information.

However, Gaussian processes also possess some problems. Mainly its scalability with respect to the number of observation points N_{obs} used to obtain the posterior distribution. Its time requirements scale as $\mathcal{O}(N_{\text{obs}}^3)$ and the memory usage as $\mathcal{O}(N_{\text{obs}}^2)$. This translates in that a GP starts to perform badly when one has access to a large number of evaluations of the objective function [149]. For many optimization problems this can severely limit the applicability of Bayesian optimization. There are multiple situations where the evaluation of the objective function does not require long computational times and many evaluation values are available, therefore. Examples are highly symmetric devices, where one can exploit the symmetries to reduce the dimensionality of the computational model, or any case in which one has access to a high parallelization. In these cases, the scalability problems of Bayesian optimization play an important role in the final efficiency of the method, as we will show in this chapter.

Different methods have been recently proposed to solve or mitigate the scalability problems of Bayesian optimization. One of the approaches consists in the use of a surrogate model with a fixed number of parameters instead of a Gaussian process. To be precise, two different works [135, 150] propose the use of a deep neural network formed by several layers and a Bayesian linear regressor as output layer of the network. To obtain a Bayesian optimization algorithm with a better scalability but without sacrificing the qualities of Gaussian processes, other methods propose the use of a set of different local Gaussian processes that model the objective function based on different subsets of the observations [151, 152].

In this work, we propose two additional techniques to mitigate the scalability problems of Bayesian optimization. Both of them are based on the use of Gaussian processes. One of the two methods reduces the scalability of Bayesian optimization without requiring any sort of approximation with respect to the standard Bayesian optimization algorithm. The other method shares some of the fundamental working principles with [151, 152]. This method does not scale with the number of observations. However, it only uses a fraction of all the available information to decide on the next evaluation point. It is, therefore, an approximation to the standard algorithm.

The chapter first describes the Gaussian process model and Bayesian optimization using Gaussian processes. Emphasis is put on the methodology to incorporate shape and material derivatives, as presented in section 2.3, into the optimization algorithm. After that, the chapter focuses on the scalability problems of Bayesian optimization. After the scalability problem is first described, the two methods to improve the scalability of Bayesian optimization are presented. Except the work presented in section 3.4, the contents in this chapter have been published in [A1–A4].

3.2 Gaussian Processes

Definition

A Gaussian process $\mathcal{GP}(m, k)$ is a stochastic model that offers a probability distribution over the values of a function $f(\mathbf{x})$. It belongs to the class of nonparametric distributions [145, 147]. It is formally defined as a collection of random variables, any finite number of which follow a joint multivariate Gaussian distribution ([125], Def. 2.1). The properties of the distribution are controlled by the mean $m(\mathbf{x})$ and covariance function $k(\mathbf{x}, \mathbf{x})$. Those functions fully characterize a GP. Given any set of points in \mathbb{R}^n , $\underline{X}_{\text{set}} = [\mathbf{x}_1, \mathbf{x}_2, \dots, \mathbf{x}_N]$, the probability distribution of the function $f(\mathbf{x})$ over these points $\mathbf{f}_{\text{set}} = [f(\mathbf{x}_1), f(\mathbf{x}_2), \dots, f(\mathbf{x}_N)]^T$ is given by a multivariate Gaussian distribution,

$$\mathbf{f}_{\text{set}} \sim \mathcal{N}(\mathbf{m}_{\text{set}}, \underline{K}_{\text{set}}), \quad (3.2)$$

where \mathbf{m}_{set} is the vector of mean values $[m(\mathbf{x}_1), m(\mathbf{x}_2), \dots, m(\mathbf{x}_N)]^T$ and $\underline{K}_{\text{set}}$ is the covariance matrix for the set of points. The i - j element of the covariance matrix is obtained by evaluating the covariance function for the pair of points $k(\mathbf{x}_i, \mathbf{x}_j)$. For the mean function, it is common to use a constant value $m(\mathbf{x}) = \mu$.

From Eqn. (3.2), one gets that the probability density function for a set of points $\underline{X}_{\text{set}}$ of a function $f(\mathbf{x})$ modeled by a Gaussian process is given by,

$$\mathcal{P}(\mathbf{f}_{\text{set}}) = \frac{1}{\sqrt{(2\pi)^N \det(\underline{K}_{\text{set}})}} \frac{1}{\det(\underline{K}_{\text{set}})} e^{-\frac{1}{2}(\mathbf{f}_{\text{set}} - \mathbf{m}_{\text{set}})\underline{K}_{\text{set}}^{-1}(\mathbf{f}_{\text{set}} - \mathbf{m}_{\text{set}})^T}. \quad (3.3)$$

The covariance function has to be positive definite and it is frequently a stationary function. The covariance matrix obtained from a positive definite covariance function is always positive semi-definite. For any point $\mathbf{z} \in \mathbb{R}^N$

$$\mathbf{z}^T \underline{K} \mathbf{z} \geq 0. \quad (3.4)$$

A covariance function is stationary if

$$k(\mathbf{x}, \mathbf{x}') = k(\mathbf{x} + \mathbf{t}, \mathbf{x}' + \mathbf{t}) \forall \mathbf{x}, \mathbf{x}', \mathbf{t} \in \mathbb{R}^n. \quad (3.5)$$

The covariance function establishes a relation of similarity between function values at different points depending of the values of the points. Many different types of covariance functions can be used (see, e.g., [125] section 4.2 or [153] section 4). Two of the most used covariance functions in the field of machine learning are the squared exponential covariance function and the family of Matérn functions. Both of them are stationary functions. The exponential covariance function reads as

$$k_{\text{exp}}(\mathbf{x}_i, \mathbf{x}_j) = \sigma^2 e^{-d(\mathbf{x}_i, \mathbf{x}_j)}, \quad (3.6)$$

with the parameter σ being the standard deviation and the function $d(\mathbf{x}_i, \mathbf{x}_j)$ a scaled distance, i.e.,

$$d(\mathbf{x}_i, \mathbf{x}_j) = \sqrt{\sum_{k=1}^d \frac{(x_{i,[k]} - x_{j,[k]})^2}{l_k^2}}. \quad (3.7)$$

The parameters l_i are called length scales. The parameters μ , σ , and l_i are together called the hyper-parameters of the model.

The family of Matérn covariance functions can be written as,

$$k_{\text{Matérn},\nu}(\mathbf{x}_i, \mathbf{x}_j) = \frac{\sigma^2}{\Gamma(\nu) 2^{\nu-1}} \left(\sqrt{2\nu}d(\mathbf{x}_i, \mathbf{x}_j) \right)^\nu K_\nu \left(\sqrt{2\nu}d(\mathbf{x}_i, \mathbf{x}_j) \right), \quad (3.8)$$

where $K_\nu(x)$ is the modified Bessel function of the second kind. Within the family of Matérn covariance functions, the most frequently used are the $k_{\text{Matérn},3/2}$ and $k_{\text{Matérn},5/2}$,

$$k_{\text{Matérn},3/2} = \sigma^2 \left(1 + \sqrt{3}d \right) e^{-\sqrt{3}d}, \quad (3.9)$$

$$k_{\text{Matérn},5/2} = \sigma^2 \left(1 + \sqrt{5}d + \frac{5}{3}d^2 \right) e^{-\sqrt{5}d}. \quad (3.10)$$

Some authors [154] recommends to use the Matérn covariance functions rather than the exponential covariance function for modeling physical processes, due to the smoothness properties of k_{exp} . In this thesis we use the Matérn $k_{\text{Matérn},5/2}$, based on the results of the analysis done in [A4].

The covariance function describes a correlation between the values of the function at different input points. The *a priori* behavior of a function $f(\mathbf{x})$ is not only controlled by the chosen covariance function, it is also strongly influenced by the values of the hyper-parameters. Figure 3.1 shows function samples generated using a Matérn covariance function $k_{\text{Matérn},5/2}$ with two different sets of hyper-parameters. As seen in the figure, longer length scales establish a stronger relation between the function values of close points, generating smoother samples.

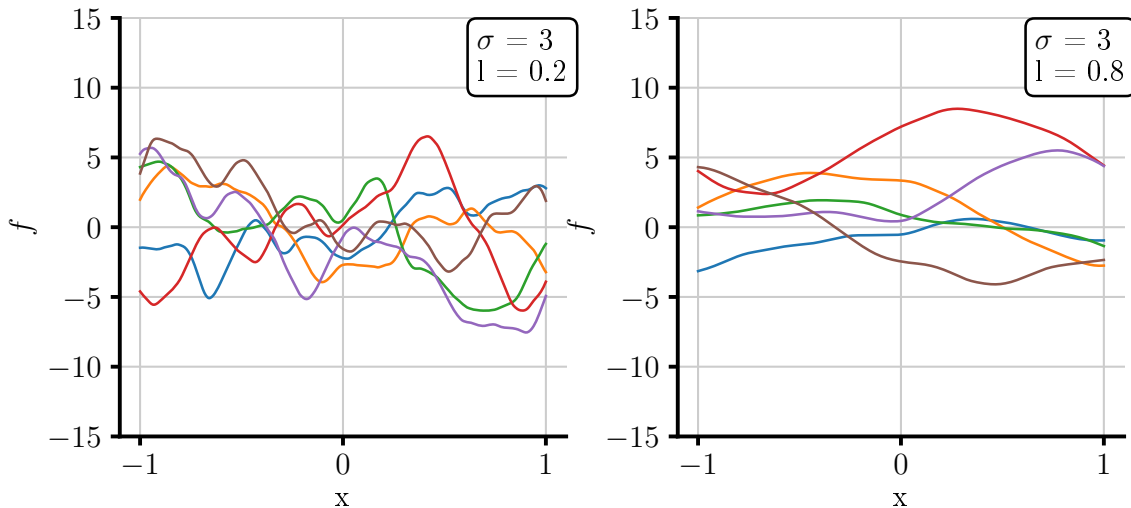


Figure 3.1: Random function samples generated from a GP modelled with a Matérn $k_{\text{Matérn},5/2}$ covariance function. The two plots correspond to samples generated using covariance functions with different hyperparameters. The corresponding hyperparameters are indicated in the plots.

Gaussian process regression

The goal of using a stochastic model for the optimization is to be able to obtain a probabilistic distribution for the values of $f(\mathbf{x})$ at points where those values are unknown. If one can calculate the true values of the modelled function $f(\mathbf{x})$ at some set of points $\underline{X}_{\text{obs}} = [\mathbf{x}_{\text{obs},1}, \mathbf{x}_{\text{obs},2}, \dots, \mathbf{x}_{\text{obs},N_{\text{obs}}}]$, one can then obtain a posterior distribution over $f(\mathbf{x})$. Given another set of points $\underline{X}_* = [\mathbf{x}_{*,1}, \mathbf{x}_{*,2}, \dots, \mathbf{x}_{*,N_*}]$ one can calculate the joint Gaussian multivariate prior distribution of the two sets $\underline{X}_{\text{obs}}$ and \underline{X}_* ,

$$\begin{bmatrix} \mathbf{f}_{\text{obs}} \\ \mathbf{f}_* \end{bmatrix} \sim \mathcal{N} \left(\begin{bmatrix} \mathbf{m}_{\text{obs}} \\ \mathbf{m}_* \end{bmatrix}, \begin{bmatrix} \underline{K}_{\text{obs},*}^T & \underline{K}_{\text{obs},*} \\ \underline{K}_{\text{obs},*}^T & \underline{K}_{*,*} \end{bmatrix} \right), \quad (3.11)$$

where $\underline{K}_{\text{obs}}$ and \underline{K}_* are the $N_{\text{obs}} \times N_{\text{obs}}$ and $N_* \times N_*$ covariance matrices for the sets $\underline{X}_{\text{obs}}$ and \underline{X}_* respectively, and $\underline{K}_{\text{obs},*}$ is the $N_{\text{obs}} \times N_*$ cross-covariance matrix between the two sets.

Conditioning the distribution of the set of points \underline{X}_* on the values of $(\underline{X}_{\text{obs}}, \mathbf{f}_{\text{obs}})$ using Bayes' theorem [134] one gets

$$\mathbf{f}_* | \underline{X}_*, \underline{X}_{\text{obs}}, \mathbf{f}_{\text{obs}} \sim \mathcal{N}(\mathbf{m}_p, \underline{K}_p), \quad (3.12)$$

where \mathbf{m}_p and \underline{K}_p are the posterior mean vector and posterior covariance matrix respectively ([125] Eqn. 2.19),

$$\mathbf{m}_p = \mathbf{m}_* + \underline{K}_{\text{obs},*}^T \underline{K}_{\text{obs}}^{-1} (\mathbf{f}_{\text{obs}} - \mathbf{m}_{\text{obs}}), \quad (3.13)$$

$$\underline{K}_p = \underline{K}_* + \underline{K}_{\text{obs},*}^T \underline{K}_{\text{obs}}^{-1} \underline{K}_{\text{obs},*}. \quad (3.14)$$

The standard deviation at a point $\mathbf{x}_{*,i}$, $\sigma_p(\mathbf{x}_{*,i})$, is given by the square root of the i -th diagonal element of \underline{K}_p .

Taking a look to Eqns. (3.13) and (3.14), one can see that the main operations required to calculate the mean value and the standard deviation are the inversion of the covariance matrix $\underline{K}_{\text{obs}}$ and its posterior multiplication by a column vector. For the mean value, the vector is independent of the point \mathbf{x}_* where one wants to evaluate it. In practice, the inverse of $\underline{K}_{\text{obs}}$ is never computed because $\underline{K}_{\text{obs}}$ is generally ill-conditioned [155, 156]. Different numerical techniques are used instead, where the Cholesky decomposition is one of the most used. An analyses of different regularization techniques frequently used is presented in section 3.4.

Using the Cholesky decomposition of $\underline{K}_{\text{obs}}$ one obtains a matrix $\underline{L}_{K_{\text{obs}}}$ such that,

$$\underline{K}_{\text{obs}} = \underline{L}_{K_{\text{obs}}} \underline{L}_{K_{\text{obs}}}^T, \quad (3.15)$$

with $\underline{L}_{K_{\text{obs}}}$ being a lower triangular matrix. Using the decomposition one gets that the last term of the right hand side of Eqn. (3.14) can be written as,

$$\underline{K}_{*,\text{obs}} \underline{K}_{\text{obs}}^{-1} \underline{K}_{*,\text{obs}}^T = \underline{K}_{*,\text{obs}} \underline{L}_{K_{\text{obs}}}^{-T} \underline{L}_{K_{\text{obs}}}^{-1} \underline{K}_{*,\text{obs}}^T = \mathbf{b}^T \cdot \mathbf{b}. \quad (3.16)$$

with \mathbf{b} being,

$$\mathbf{b} = \underline{L}_{K_{\text{obs}}}^{-1} \cdot \underline{K}_{*,\text{obs}}^T. \quad (3.17)$$

The vector \mathbf{b} is normally calculated solving the triangular system $\underline{L}_{K_{\text{obs}}} \cdot \mathbf{b} = \underline{K}_{*,\text{obs}}^T$ using forward and backward substitution.

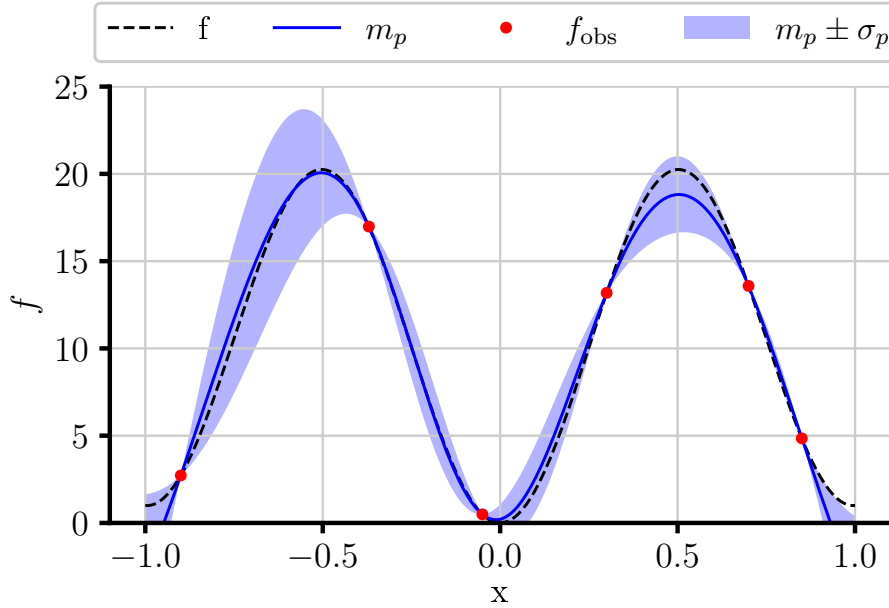


Figure 3.2: Posterior mean, m_p , and standard deviation, σ_p , for a function $f(x)$ obtained from a prior GP and a set of six observations of $f(x)$. The dash line shows the real values of $f(x)$. The prior Gaussian process is governed by the $k_{\text{Matérn},5/2}$ kernel function. The plot shows the probability distribution of a function from which only six points are known. This distribution is represented by its mean and standard deviation values, which are obtained using Eqns. (3.13) and (3.14). As one can see, the Gaussian process generates a probability distribution that perfectly matches the behavior of the real function $f(x)$ at the six observation points and that predicts with a good accuracy the behavior of $f(x)$ in the regions between the observations.

Figure 3.2 shows the posterior mean and standard deviation calculated for a function $f(x)$ conditioned on a set of six observations. The figure shows the values of the function $f(x)$ and the values of the statistical function distribution obtained using Gaussian process regression. Given a set of points $\underline{X}_{\text{obs}}$ where the values of the function are known, to obtain the statistical model of the function $f(x)$ one first computes the covariance matrix for this set of points. The mean values of the statistical function distribution are then given by Eqn. (3.13), and the standard deviation by Eqn. (3.14). In those two equations, the set of points \underline{X}^* represents the points where one wants to obtain the values of the mean and the standard deviation. The known values of the function are represented by red dots in Fig. 3.2. The mean function corresponds to the blue line and the shadowed area represents the region within the $\pm\sigma$ interval. As it can be seen in the figure, the standard deviation at the observation points $\mathbf{x}_{\text{obs},i}$ is zero. What that means is that the posterior Gaussian process generates a function probability distribution that only takes into account functions that perfectly agree with the given observation values. This can be seen also in Fig. 3.3. This figure shows some function samples obtained from the posterior distribution. As one can see, all the possible realizations of $f(x)$ go through the exact values of the observation points. To generate the plots of these function realizations, one uses a multivariate normal random generator providing the posterior covariance function

$\underline{K}_{\text{obs}}$ given by Eqn.(3.14) for the set of points aimed to represent.

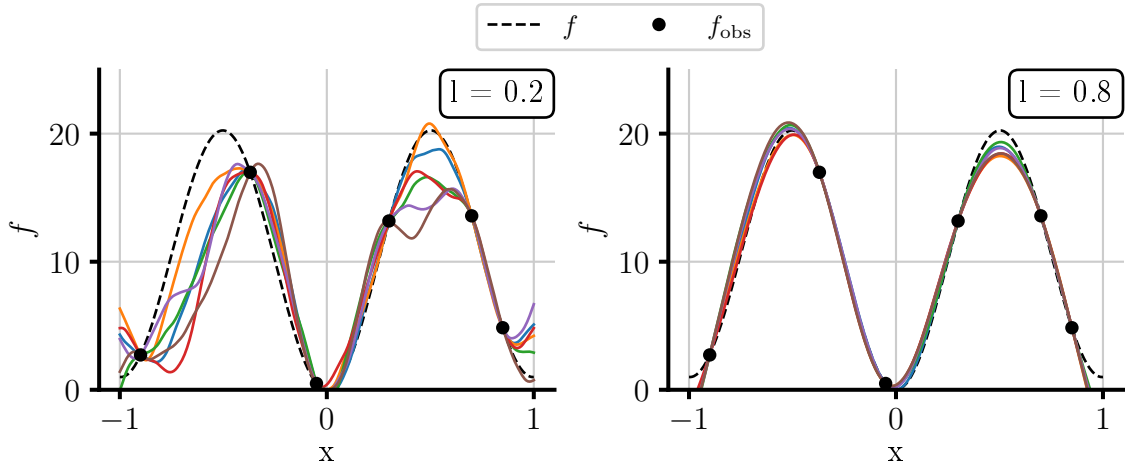


Figure 3.3: Random function samples generated from the posterior Gaussian process distribution conditioned on a series of evaluations of $f(\mathbf{x})$. The two plots show samples obtained from two different posterior Gaussian process distributions. Their difference rely on the value of the length scale l .

Gaussian process regression with derivative information

Derivative information can be included into the Gaussian process model in a simple and natural form [157–159]. If a function $f(\mathbf{x})$ is modeled as a Gaussian process $\mathcal{GP}(m, k)$, then the joint process of the function $f(\mathbf{x})$ and its derivatives $\nabla f(\mathbf{x})$ also follows a Gaussian process. Given a set of observations of $f(\mathbf{x})$ and of its derivatives $df(\mathbf{x})/dx_i$, the covariance matrix of the joint process

$$\begin{bmatrix} \mathbf{f}_{\text{set}}(\mathbf{x}) \\ \nabla \mathbf{f}_{\text{set}}(\mathbf{x}) \end{bmatrix} \sim \mathcal{N}(\mathbf{m}_{\text{set}}, \underline{K}_{\text{set}}^{\nabla}), \quad (3.18)$$

can be obtained as ([125] section 9.4 or [160] chapter 10)

$$\underline{K}_{\text{set}}^{\nabla} = \begin{bmatrix} \underline{K}_{\text{set},f,f} & \underline{K}_{\text{set},f,\nabla f} \\ \underline{K}_{\text{set},\nabla f,f} & \underline{K}_{\text{set},\nabla f,\nabla f} \end{bmatrix}, \quad (3.19)$$

where the submatrices are obtained using the respective subcovariance functions [161],

$$k_{f,f}(\mathbf{x}, \mathbf{x}') = \text{cov}(f(\mathbf{x}), f(\mathbf{x}')) = k(\mathbf{x}, \mathbf{x}'), \quad (3.20)$$

$$k_{f,\nabla f}(\mathbf{x}, \mathbf{x}') = \text{cov}(f(\mathbf{x}), \nabla f(\mathbf{x}')) = \nabla_{\mathbf{x}'} k(\mathbf{x}, \mathbf{x}'), \quad (3.21)$$

$$k_{\nabla f,f}(\mathbf{x}, \mathbf{x}') = \text{cov}(\nabla f(\mathbf{x}), f(\mathbf{x}')) = \nabla_{\mathbf{x}} k(\mathbf{x}, \mathbf{x}'), \quad (3.22)$$

$$k_{\nabla f,\nabla f}(\mathbf{x}, \mathbf{x}') = \text{cov}(\nabla f(\mathbf{x}), \nabla f(\mathbf{x}')) = \nabla_{\mathbf{x}} \nabla_{\mathbf{x}'} k(\mathbf{x}, \mathbf{x}'). \quad (3.23)$$

Similarly as discussed earlier, one can obtain the joint process between two sets $\underline{X}_{\text{obs}}$ and \underline{X}_{*} , where $\underline{X}_{\text{obs}}$ includes observations of the first derivative of $f(\mathbf{x})$. Then, it is possible to obtain the posterior distribution for the set of points \underline{X}_{*} applying Bayes' theorem,

$$\mathbf{m}_p = \underline{K}_{*,\text{obs}}^\nabla \underline{K}_{\text{obs}}^\nabla^{-1} [\mathbf{f}_{\text{obs}}^T, \nabla \mathbf{f}_{\text{obs}}^T]^T, \quad (3.24)$$

$$\underline{K}_p = \underline{K}_* - \underline{K}_{*,\text{obs}}^\nabla \underline{K}_{\text{obs}}^\nabla^{-1} \underline{K}_{*,\text{obs}}^{\nabla T}. \quad (3.25)$$

Note that Eqns. (3.24) and (3.25) are equivalent to Eqns. (3.13)-(3.14) but applied to a set of observations that contains derivative information.

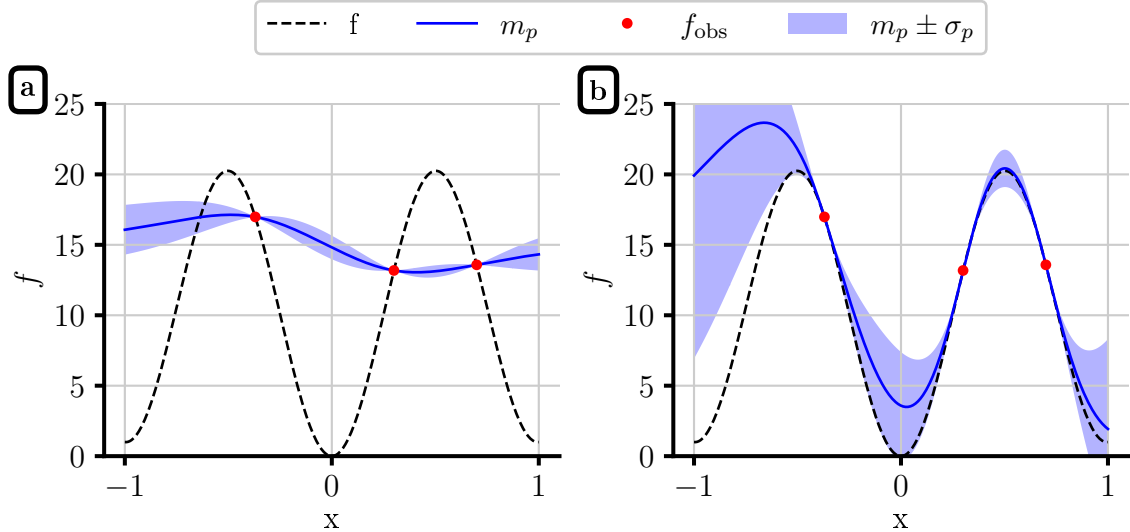


Figure 3.4: **a.** Posterior distribution for a function $f(\mathbf{x})$ obtained with a Gaussian process and generated using observations of $f(\mathbf{x})$ but without derivative information. **b.** Posterior distribution for a function $f(\mathbf{x})$ obtained with a Gaussian process and generated using observations of $f(\mathbf{x})$ and of its derivative. The use of derivative information produces a more accurate estimation of the real function.

Figure 3.4b shows the posterior mean and standard deviation for a function $f(x)$ conditioned on both observations of $f(x)$ and of its first derivative. The function $f(x)$ used for the example is the same as the used for Fig. 3.2 and Fig. 3.3. As it can be seen, comparing it with Fig. 3.4a, the accuracy of the prediction for $f(x)$ increases considerably with the use of the derivative information.

Model selection

As mentioned earlier and shown in Fig. 3.1, the hyper-parameters of a GP strongly influence the distribution over functions. Their effect is also important in the posterior distribution, as shown in Fig. 3.3. The two posterior distributions shown there are conditioned on the same set of evaluations and their difference only comes from the different values of the hyper-parameters used for the prior GP.

In general, one can not know *a priori* the values of the hyper-parameters that allow the GP to predict better the behavior of $f(\mathbf{x})$. One way to overcome this difficulty is to also set prior probability distributions over the values of the hyper-parameters and to obtain the posterior distribution also for the hyper-parameters. Then, the predictions over points \mathbf{x}_* would be obtained by integrating the posterior distribution over all the values of the hyper-parameters ([126] section 3.2.1). However, as explained in [126], this problem is

intractable by analytical means. There, the author proposes the use of some approximation techniques to compute the posterior using, e.g., the Markov-Chain-Monte-Carlo method. However, the solution most frequently used, and the one followed in this work, is to not consider the posterior distribution conditioned also in the hyper-parameters but to rather set them to certain fixed values that were chosen using some point estimate. The estimate most frequently used is the marginal likelihood ([125] section 5.8 or [126] section 3.2.1),

$$(\mu_{\text{opt}}, \sigma_{\text{opt}}, l_{1,\text{opt}}, \dots, l_{d,\text{opt}})^* = \arg \max_{\mu, \sigma, l_1, \dots, l_d} \log p(\mathbf{f}_{\text{obs}} | \underline{X}_{\text{obs}}, \mu, \sigma, l_1, \dots, l_d). \quad (3.26)$$

For the Gaussian process model, the logarithm of the marginal likelihood takes the form of the expression ([125] Eqn. 5.8)

$$\log p(\mathbf{f}_{\text{obs}} | \underline{X}_{\text{obs}}, \sigma, l_1, \dots, l_d) = -\frac{1}{2} (\mathbf{f}_{\text{obs}} - \mu)^T \underline{K}_{\text{obs}}^{-1} (\mathbf{f}_{\text{obs}} - \mu) - \frac{1}{2} \log |\underline{K}_{\text{obs}}| - \frac{N_{\text{obs}}}{2} \log 2\pi. \quad (3.27)$$

Taken a look at Eqn. (3.27), it can be seen that the first term of the right hand side depends on the values of the observations, the second term only depends on the values of the covariance function, and the third term is a normalization constant. The first term is related with the data fit of the model and the second term is a complexity penalty depending on the covariance function used. Smaller length scale values will make the likelihood to be smaller. Therefore, the marginal likelihood automatically penalizes complex models when compared to simpler ones.

The values of μ and σ that maximize the likelihood can be obtained analytically, as shown in [A3],

$$\mu_{\text{opt}} = \sum_{i,j} \frac{(\underline{K}_{\text{obs}}^{-1})_{[i,j]} \mathbf{f}_{\text{obs}[j]}}{(\underline{K}_{\text{obs}}^{-1})_{[i,j]}}, \quad (3.28)$$

$$\sigma_{\text{opt}}^2 = \frac{1}{N_{\text{obs}}} (\mathbf{f}_{\text{obs}} - \mu)^T \underline{K}_{\text{obs}}^{-1} (\mathbf{f}_{\text{obs}} - \mu). \quad (3.29)$$

For obtaining the optimal length scales, one needs to use some optimization algorithm. As one can see in Eqn. (3.27), the calculation of the likelihood requires the inversion of the covariance matrix $\underline{K}_{\text{obs}}$. This makes the optimization a computationally expensive task that is prohibitive to run every time a new observation is added to the Gaussian process model. Instead, we proposed to use an estimator of the possible improvement of the likelihood [A3],

$$I = \max \left(l_i \frac{\partial \log p(\mathbf{f}_{\text{obs}} | \underline{X}_{\text{obs}}, \mu, \sigma, l_1, \dots, l_d)}{\partial l_i} \right). \quad (3.30)$$

The length scales are only optimized when

$$I > 0.1 \log p(\mathbf{f}_{\text{obs}} | \underline{X}_{\text{obs}}, \mu, \sigma, l_1, \dots, l_d). \quad (3.31)$$

Once the data set contains more than 300 observations, the length scales are no longer optimized, independently of the value of the estimator I .

3.3 Bayesian Optimization Using Gaussian Processes

In the previous sections, the basics of the GP model were presented, but how to use it for an actual optimization has not yet been described. The basic strategy of Bayesian optimization consists in combining the data obtained from the evaluations of the objective function $f_{\text{ob}}(\mathbf{x})$ and the GP model to obtain a posterior probabilistic distribution of the objective function with respect to the design parameters. The probability distribution is then used to determine the points in the design space, which are the best candidates for being a global optimum. As next, the objective function is evaluated at these data points and added to data set underlying the GP that in turn refines the probabilistic distribution of the objective function. Advancing with this scheme promises to identify the global optimum in an ongoing process of the objective function.

Although Bayesian optimization is frequently applied using a Gaussian process as a stochastic model, it is not limited to it. It could be implemented with any stochastic model, which gives a probabilistic distribution over functions. One of the first proposals for Bayesian optimization [133] was indeed described in terms of general Bayesian networks [162] and even implementations with neural networks have been recently proposed [135, 150]. However, this thesis will focus on Bayesian optimization using Gaussian processes [163]. As we have seen in the previous sections, Gaussian processes are very powerful models in order to learn arbitrarily complex objective functions and their main drawback, their poor scalability, is not generally a problem for most of the applications in photonic design. However, the topic will be discussed again in section 3.4, where some proposals to improve the scalability will be presented. With these improvements, one can extend the efficient applicability of Bayesian optimization to cover most of the applications in photonic design.

General description

This section describes the general steps of the Bayesian optimization algorithm using Gaussian processes.

The Bayesian optimization algorithm starts with the initialization of the posterior Gaussian process model for the objective function $f_{\text{ob}}(\mathbf{x})$. To create the Gaussian process model, a set of evaluations of $f_{\text{ob}}(\mathbf{x})$ is calculated. The number of initial evaluations is generally rather small and the evaluation points are normally picked using some random distribution over the design space.

Once obtained, the statistical surrogate model for $f_{\text{ob}}(\mathbf{x})$ is used to calculate some statistical quantity $\alpha(\mathbf{x})$ used to predict the best possible candidates in the design space for being the optimum. This statistical quantity $\alpha(\mathbf{x})$ is called the acquisition function. The candidate point \mathbf{x}_α where to evaluate the objective function next, is given by the global optimum of the acquisition function,

$$\mathbf{x}_\alpha = \arg \max_{\mathbf{x} \in \mathcal{D}} \alpha(\mathbf{x}). \quad (3.32)$$

There are different expressions used as acquisition functions [118, A4, 164]. Among the most frequently used ones, one finds the probability of improvement, $\alpha_{\text{PI}}(\mathbf{x})$ and the expected improvement $\alpha_{\text{EI}}(\mathbf{x})$. The probability of improvement is defined as,

$$\alpha_{\text{PI}}(\mathbf{x}) = p(f_{\text{ob}}(\mathbf{x}) < T) = \Phi\left(\frac{T - m_p(\mathbf{x})}{\sigma_p(\mathbf{x})}\right), \quad (3.33)$$

where T is a number smaller than the current minimum in the data set of observations, $f_{\text{obs,min}}$, and Φ is the cumulative density function of the standard normal distribution. The functions $m_p(\mathbf{x})$ and $\sigma_p(\mathbf{x})$ are the posterior mean and standard deviation of the GP modeling $f_{\text{ob}}(\mathbf{x})$, obtained from Eqns. (3.13) and (3.14), respectively. The expected improvement, $\alpha_{\text{EI}}(\mathbf{x})$ reads as

$$\begin{aligned} \alpha_{\text{EI}}(\mathbf{x}) &= \mathbb{E} [\min(0, f_{\text{obs,min}} - f_{\text{ob}}(\mathbf{x}))] \\ &= (f_{\text{obs,min}} - m_p(\mathbf{x})) \Phi \left(\frac{f_{\text{obs,min}} - m_p(\mathbf{x})}{\sigma_p(\mathbf{x})} \right) + \sigma_p(\mathbf{x}) \phi \left(\frac{f_{\text{obs,min}} - m_p(\mathbf{x})}{\sigma_p(\mathbf{x})} \right), \end{aligned} \quad (3.34)$$

being $\phi(x)$ the probability density function of the standard normal distribution.

It has been proven that, under certain conditions, both the probability of improvement and the expected improvement find the global minimum of the objective function [165, 166].

Another acquisition function that combines both exploitation and exploration strategies is the lower confidence bound [144, 167, 168] $\alpha_{\text{LCB}}(\mathbf{x})$,

$$\alpha_{\text{LCB}}(\mathbf{x}) = -m_p(\mathbf{x}) - \beta_{\text{LCB}}\sigma_p, \quad (3.35)$$

where β_{LCB} is a hyper-parameter of the model [144].

Figure 3.5 illustrates the optimization process using GP and $\alpha_{\text{EI}}(\mathbf{x})$ for a simple one dimensional test function. The different subplots correspond to different iterations. After every iteration, the posterior distribution is updated and the optimal point of the acquisition function is then computed.

The performance and behavior of Bayesian optimization depending on the considered acquisition function have been analyzed in [118]. Also, [A4] analyzes the performance of Bayesian optimization for the case of optimizing different photonic devices depending on the acquisition function used. In [118], despite showing a remarkable iteration convergence of Bayesian optimization using any of the mentioned acquisition functions, it is also shown that $\alpha_{\text{LCB}}(\mathbf{x})$ can lead to the omission of regions of the search space and that $\alpha_{\text{PI}}(\mathbf{x})$ and $\alpha_{\text{EI}}(\mathbf{x})$ can be deceptive. In other words, they are prone to get stuck into a local minimum for a considerably large number of iterations and to not explore other regions of the design space. In the case of $\alpha_{\text{PI}}(\mathbf{x})$, this behavior happens for values of the parameter T close to the current minimum in the data set. In general, the convergence rate of $\alpha_{\text{PI}}(\mathbf{x})$ depends considerably on the value of T chosen. To mitigate this sensitivity with respect to the optimal value of T , the author proposes different solutions, e.g., to evaluate different candidate points \mathbf{x}_α obtained using $\alpha_{\text{PI}}(\mathbf{x})$ with a range of different values of T . As [118] shows, this strategy would be completely equivalent to use instead $\alpha_{\text{LCB}}(\mathbf{x})$ with a range of different β_{LCB} .

Here in this work, we mainly use the expected improvement as acquisition function for the optimization tasks. To mitigate the problems with deceptive points, we simply added a condition statement to not search around the current optimum after a few iterations if the new observations around this point do not improve the current optimum in more than a one percent. In order to reduce the stability problems, the algorithm implemented in this work also avoids evaluation points which are closer than one hundred of the length scale to any evaluation point in the data set. If one is interested in a fine tuning of the

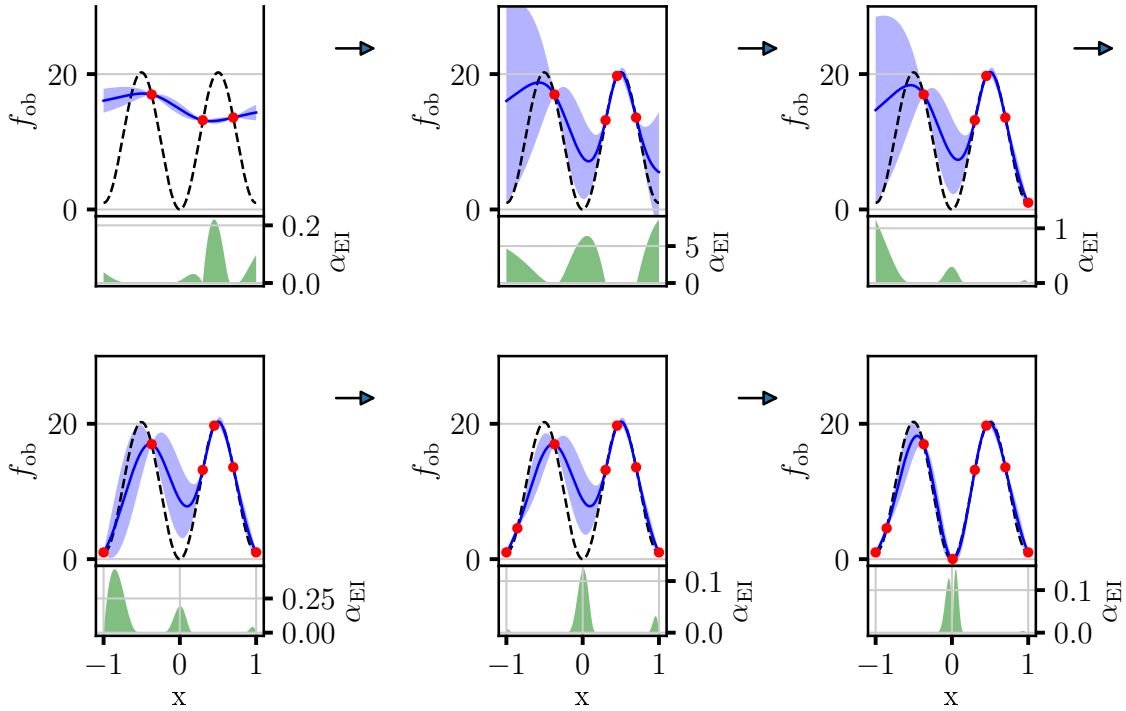


Figure 3.5: Optimization process using a GP and the expected improvement. After every evaluation of $f_{\text{ob}}(\mathbf{x})$, the GP model is updated. The expected improvement is computed using the updated GP posterior distribution and a new evaluation is calculated in the point with the highest expected improvement. The dashed line shows the function $f_{\text{ob}}(\mathbf{x})$ aimed to optimize.

global optimum, one can always run a gradient descent search using the global minimum found by Bayesian optimization as starting point.

As described, the Bayesian optimization algorithm implies to solve another global optimization problem within each iteration, Eqn. (3.32). In principle, this methodology might seem to produce a large penalty in the efficiency of the algorithm with respect to many other global optimization algorithms where the computation overhead can be negligible. Indeed, this is correct for a wide range of objective functions for which evaluations times are shorter than a second. However, let us note that this work focuses on the optimization of expensive objective functions that depend on the solution of Maxwell's equations. In these problems, where one can not run the optimization for more than a few thousands of iterations at maximum, the prediction power of Gaussian processes compensates the computation time overhead required in each iteration. This behavior has been analyzed in [A1], where Bayesian optimization was benchmarked with respect to a series of different global and local optimization algorithms in the optimization of a variety of different photonic devices. The results shown there confirm Bayesian optimization with Gaussian processes to be an efficient tool for design of photonic devices.

Bayesian Optimization using derivative information

Section 2.3 presented the calculation of shape and material derivatives of photonic structures using the finite element method. Having access to the gradient of the objective function with respect to the design parameters offers a better knowledge of $f_{\text{ob}}(\mathbf{x})$ which, if used efficiently, should lead to a better convergence rate in its optimization.

The most used methods to exploit the gradients of $f_{\text{ob}}(\mathbf{x})$ for its optimization are the gradient descent methods or quasi-Newton methods such as L-BFGS-B [169–171]. Those methods are used to find a local optimum of $f_{\text{ob}}(\mathbf{x})$. The direction given by the gradient or the gradient and Hessian, in the case of quasi-Newton methods, ensures that the local optimum can be found. The mentioned methods are commonly used for the design of multiple types of photonic devices, especially in the field of topology optimization, where locally optimized devices show good performances [25, 27, 87, 88, 172–174].

In the context of global optimization, the use of derivative information is not as common as for local optimization. There are not many algorithms that can exploit the derivatives efficiently. The most frequently used strategy consists in applying a gradient descent method at different initial points within the design space to find multiple local minima [175].

Because Gaussian processes can easily incorporate derivative information, Bayesian optimization provides an alternative to multi-start gradient descent. Once the posterior distribution conditioned on values of $f_{\text{ob}}(\mathbf{x})$ and its derivatives is obtained, see section 3.2, the same procedure as for the case without derivative observations applies to perform Bayesian optimization. Figure 3.6 shows the optimization process of the same one dimensional test function as already presented in Fig. 3.5 when the Gaussian process includes also derivative information. As it can be seen, the optimization finds the global minimum faster than for the case without derivative observations.

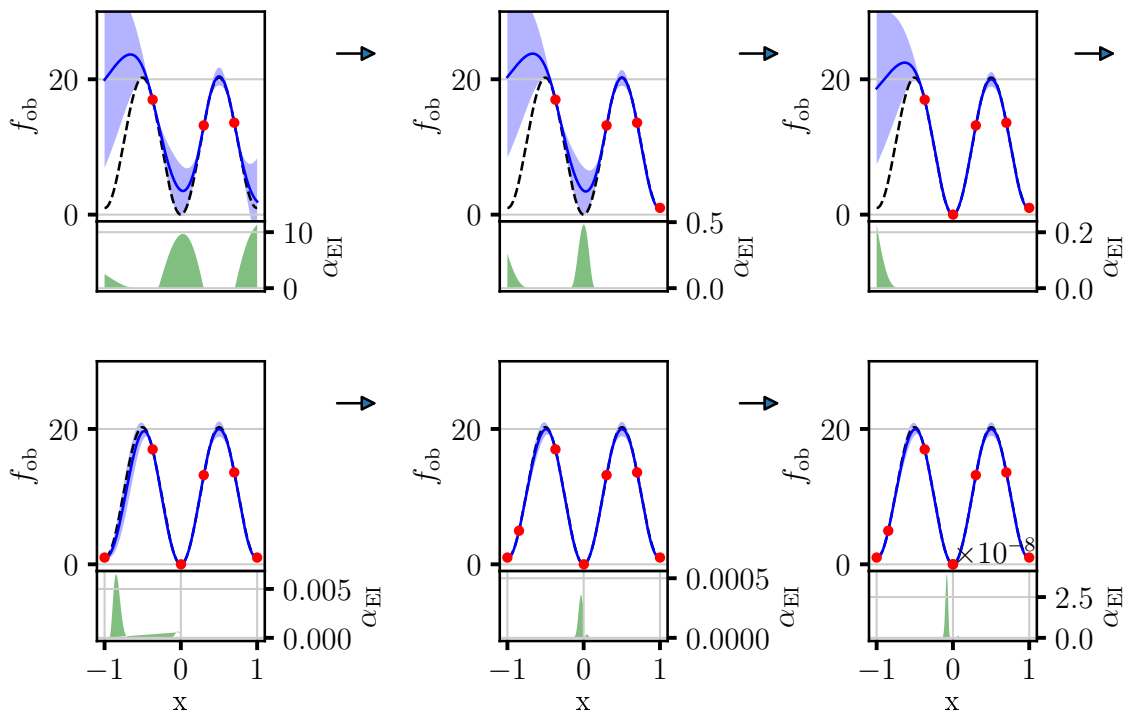


Figure 3.6: Example of Bayesian optimization using Gaussian processes with observations of the derivative and the use of the expected improvement as acquisition function. The objective function used as example is the same as used in Fig. 3.5. Note how the algorithm converges faster to the global minimum at $x = 0$ when compared to the case where derivative observations were not included, i.e. Fig. 3.5.

Gaussian processes with derivative information have been used in the context of Bayesian

optimization in [A1, A2, 161, 176]. The improvement in the convergence rate of the optimization with respect to the algorithm without derivative observations depends on the behavior of the objective function, as it can be seen in [A1]. There, Bayesian optimization with derivative information has been used to optimize different photonic devices and its performance was compared against Bayesian optimization without derivative information. The algorithm using derivative information shows a better performance for all the test cases, although it can be seen how the difference in the convergence rate between both algorithms is strongly influenced by the specific test case.

3.4 Scalable Bayesian Optimization

The scalability problem

Bayesian optimization shows excellent performance in terms of convergence. However, its use is generally limited to the optimization of problems with objective functions that are expensive to evaluate. The reason for that is the poor scalability of Gaussian processes with the number of observations. Every time a new observation is added to the model, the size of the covariance matrix $\underline{K}_{\text{obs}}$ increases with an extra row and column. To infer the behavior of $f_{\text{ob}}(\mathbf{x})$, one needs to calculate the Cholesky decomposition of $\underline{K}_{\text{obs}}$, Eqn. (3.16), and then one needs to perform a forwards and a backward substitution for the different points \mathbf{x} . The number of operations to calculate the Cholesky decomposition requires $\mathcal{O}(N_{\text{obs}}^3)$ operations and every forward and backward substitution requires $\mathcal{O}(N_{\text{obs}}^2)$ operations. The scaling in time is directly proportional to the scaling in the number of operations.

The poor scaling of Bayesian optimization is not a major problem for the optimization of many photonic devices, as the computational costs of computing the objective function are generally high, already limiting the number of evaluations that one can perform. However, there are other applications of interest where one can solve the objective function in a few seconds. This is the case, for example, for highly symmetric photonic devices, where one can use the symmetries to reduce the computational costs, or in situations where one can perform many evaluations of the objective function in parallel. Therefore, reducing the effective time per simulation. In these cases, it is possible to perform thousands of simulations within a few days and there, the scalability of Gaussian processes become a major limiting factor of the optimization process.

Figure 3.7 shows the time needed to perform the Cholesky decomposition and the singular value decomposition of $\underline{K}_{\text{obs}}$ as a function of the number of evaluations N_{ev} of the objective function, i.e., the number of times that one calculates the objective function at different points of the design space. As one can see, the time follows a third-order power law with respect to the number of evaluations for both methods. The poor scaling becomes a major limiting factor especially when one can obtain derivative information via the direct or the adjoint method. In this case, one gets $1+d$ observations with each evaluation. That is to say, with the addition of d derivative observations per simulation, the number of observations, which lead to new extra rows and columns in the covariance matrix, equals $(1+d)N_{\text{ev}}$. This is visible in Fig. 3.7, which also shows the time required to perform the Cholesky decomposition after every evaluation of the objective function when the derivative observations of 10 parameters are included. As one can see, after three thousand simulations, decomposing $\underline{K}_{\text{obs}}$ already takes a few tens of seconds. To give an idea, computing ten thousand simulations of many two dimensional models with the finite element method is a task that can be done in a few hours exploiting parallelization. We have already discussed how the use of derivative information in Bayesian opti-

mization is, in principle, beneficial, as it allows to obtain even better convergence rates. However, because of the scalability problems, the use of derivative information may not be beneficial in some of the cases when one has access to tens of thousands of evaluations and the derivatives do not improve the convergence rate significantly. Knowing in advance to which of the problems this applies is a non-trivial task.

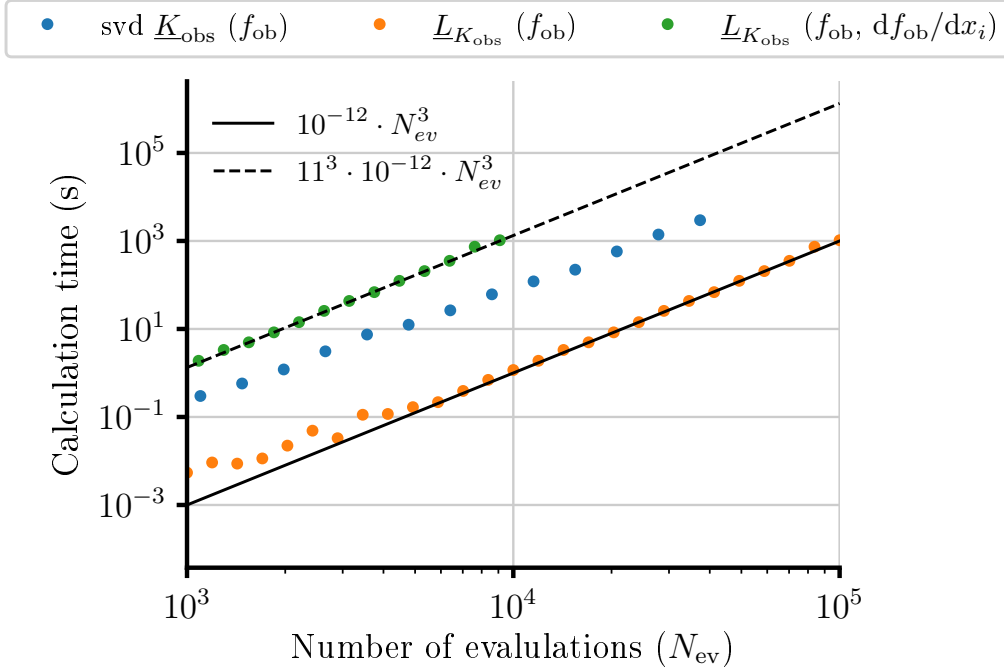


Figure 3.7: Time needed to perform the Cholesky decomposition of the covariance matrix $\underline{K}_{\text{obs}}$ for a problem with $d = 10$ parameters. The results are shown for the case where only observations of $f_{\text{ob}}(\mathbf{x})$ are included (orange dots) and for the case when one gets observations of the derivatives of $f_{\text{ob}}(\mathbf{x})$ respect to 10 parameters with each evaluation (green dots). The plot shows also the time needed for computing the singular value decomposition (SVD) of $\underline{K}_{\text{obs}}$ (blue dots).

In addition to the decomposition of $\underline{K}_{\text{obs}}$, it is also necessary to perform a forward and a backward substitution to infer the standard deviation at a point in the design space, Eqn. (3.16). Although the time required to perform this operation is much shorter than the time required to compute $\underline{L}_{K_{\text{obs}}}$, this operation is required multiple times during the optimization of the acquisition function, Eqn. (3.32). One technique that we use to mitigate this issue is to use optimization methods for the acquisition that evaluate the acquisition function at many points in parallel. With this approach, one can reduce the times for accessing the memory to read the entries of $\underline{L}_{K_{\text{obs}}}$. Another method proposed, and that it is also used in this work, consists in obtaining the next evaluation point at the same time the objective function is solved [A1, 135, 177].

Below we present two different methods to mitigate the scalability problems of Bayesian optimization and we discuss about their performance. Both methods are still based on Gaussian processes as the surrogate model. The first method exploits a specific numerical scheme on the matrix update of the Cholesky decomposition of $\underline{K}_{\text{obs}}$. This method reduces the scalability problem from $\mathcal{O}(N_{\text{obs}}^3)$ to $\mathcal{O}(N_{\text{obs}}^2)$ without the need to use any approximation with respect to the standard Bayesian optimization method. The second method is similar to the method proposed in [152]. It is based on the use of a lo-

cal Bayesian optimization model and a data structure to efficiently generate the local model. However, unlike [152], in the method proposed here the local model is not fixed and it evolves with the candidate point \mathbf{x}_* . In the following subsections each of these approaches are described.

Matrix update of the Cholesky decomposition

Let us start describing the first proposed method. It is based on the work that we presented in [A2]. In the suggested approach with use of derivative information, we update the Gaussian process model with a new set of $d + 1$ observations. These observations lead to $d + 1$ extra rows and columns that are added to the covariance matrix. Then, the Cholesky decomposition of the covariance matrix needs to be re-calculated. However, the Cholesky decomposition of a major block of the covariance matrix was already computed in the previous iteration of the Bayesian optimization algorithm. If we split the covariance matrix into four blocks,

$$\underline{K}_{\text{obs}} = \begin{bmatrix} \underline{A} & \underline{B}^T \\ \underline{B} & \underline{C} \end{bmatrix}, \quad (3.36)$$

the Cholesky decomposition of $\underline{K}_{\text{obs}}$ can be described in terms of the four blocks. Here, \underline{A} represents the covariance matrix computed in the previous iteration of the Bayesian optimization algorithm.

The covariance matrix of $\underline{K}_{\text{obs}}$, $\underline{L}_{K_{\text{obs}}}$, can be obtained in terms of the blocks \underline{A} , \underline{B} and \underline{C} as ([178] section 6.5.4)

$$\underline{L}_{K_{\text{obs}}} = \begin{bmatrix} \underline{L}_A & \underline{0} \\ \underline{B} \cdot \underline{L}_A^{-T} & \underline{L}_S \end{bmatrix}, \quad (3.37)$$

with \underline{S} being the Schur complement of $\underline{K}_{\text{obs}}$,

$$\underline{S} = \underline{C} - \underline{B} \cdot \underline{A}^{-1} \cdot \underline{B}^T. \quad (3.38)$$

The second term of the above expression can be written as a vector-vector multiplication,

$$\underline{S} = \underline{C} - \underline{X} \cdot \underline{X}^T. \quad (3.39)$$

For that, we used the equality between the Cholesky decomposition of the inverse of a matrix and the inverse transpose of the Cholesky decomposition of the matrix,

$$\underline{M} = \underline{L}_M \cdot \underline{L}_M^T, \quad (3.40)$$

$$\underline{M}^{-1} = \underline{L}_M^{-T} \cdot \underline{L}_M^{-1}, \quad (3.41)$$

$$\underline{M}^{-1} = \underline{L}_{M^{-1}} \cdot \underline{L}_{M^{-1}}^T, \quad (3.42)$$

$$\underline{L}_{M^{-1}} \cdot \underline{L}_{M^{-1}}^T = \underline{L}_M^{-T} \cdot \underline{L}_M^{-1}. \quad (3.43)$$

\underline{X}^T can be obtained solving the triangular system $\underline{L}_A \cdot \underline{X}^T = \underline{B}^T$.

Finally, one gets the aimed expression,

$$\underline{L}_{K_{\text{obs}}} = \begin{bmatrix} \underline{L}_A & 0 \\ \underline{X} & \underline{L}_S \end{bmatrix}. \quad (3.44)$$

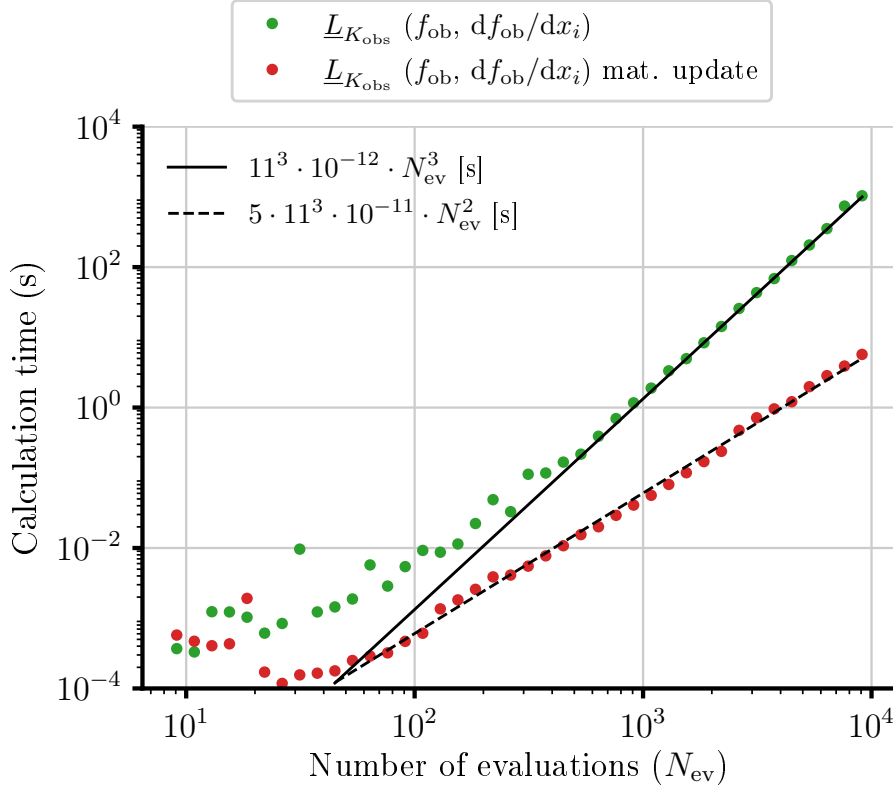


Figure 3.8: Time needed to perform the Cholesky decomposition of the covariance matrix $\underline{K}_{\text{obs}}$ for a problem with $d = 10$ parameters computing the full Cholesky decomposition (green dots) and using the matrix update scheme (red dots). The results are shown for the case where observations of the derivatives of f_{ob} respect to the 10 parameters are included into the GP model.

The numerical implementation of the matrix update scheme that we made is based on a C implementation of the BLAS [179] and LAPACK [180] libraries. Figure 3.8 shows the calculation times required to compute the Cholesky decomposition of $\underline{K}_{\text{obs}}$ as a function of the number of evaluations, using the matrix update scheme. As in Fig. 3.7, the results are shown for the case of adding the observation of $f_{\text{ob}}(\mathbf{x})$ and for the case of adding also the derivatives $df_{\text{ob}}(\mathbf{x})/dx_i$ for 10 different parameters. As it can be seen, the new scheme scales with $\mathcal{O}(N_{\text{obs}}^2)$ instead of with $\mathcal{O}(N_{\text{obs}}^3)$. For example, calculating the Cholesky decomposition after 10 thousand evaluations with derivative observations of 10 parameters requires 5 seconds using the matrix update scheme. The standard scheme requires one and a half minutes, as shown in Fig. 3.7. Note that the use of the matrix update scheme does not imply any approximation of the standard Bayesian optimization technique. Therefore, it keeps the same convergence properties as the standard algorithm, provided that the matrix update does not introduce numerical errors. The stability of the method will be discussed below.

Stability of Gaussian processes

We have just described a technique to reduce the scaling of Bayesian optimization from $\mathcal{O}(N_{\text{obs}}^3)$ to $\mathcal{O}(N_{\text{obs}}^2)$. The method does not rely on any approximation but on the exploitation of the information that one already has about the Cholesky decomposition of the covariance matrix from previous iterations. This fact implies that the convergence optimization rate of the method is the same as of the standard Bayesian optimization, if one can show that the numerical procedure does not add extra numerical errors when performing the inference. This is a fair question especially in Bayesian optimization, as it is known that the covariance matrix becomes increasingly ill-conditioned with the number of iterations, especially upon incorporation derivative observations [176].

To mitigate the numerical errors produced by the ill-conditioned covariance matrix, different regularization techniques have been proposed [155]. The most frequently used methods are the use of the Cholesky decomposition ([125] section 2.2), the truncated singular value decomposition [181] (TSVD) or the use of the LU decomposition ([182] section 3.1.1). The TSVD is the most flexible method, in the sense that one has more control over the error that the algorithm introduces. However, the Cholesky decomposition is usually preferred in many implementations, as it is the fastest method among the three mentioned above and shows simultaneously a good stability. The Cholesky decomposition and the LU decomposition require in the order of $1/3 N_{\text{obs}}^3$ and $2/3 N_{\text{obs}}^3$ floating point operations respectively ([84] section 23) and the first phase of the SVD, generally the most expensive part of the algorithm, requires $8/3 N_{\text{obs}}^3$ floating point operations if one uses the Golub-Kahan bidiagonalization ([84] section 31).

To see if the matrix update scheme introduces significant errors in the posterior Gaussian process model, the method is compared with other different methods used to perform the inference of the Gaussian process model: the Cholesky decomposition of the covariance matrix, the truncated singular value decomposition, and the direct inversion of the covariance matrix. The comparison measures the error produced by the different methods in the value of σ_p at all the observation points of a data set obtained during the Bayesian optimization of an objective function. The error assigned to each method is the maximum error in σ_p obtained from all the observation points. Note that in an error free method, σ_p should be zero at all the observation points. The results are shown in Fig. 3.9.

The results for the direct inversion show how the error of the model explodes when no regularization method is used. This clearly indicates that the use of some regularization technique is in fact needed. The error of the truncated singular value decomposition follows the same behavior of the direct inversion until it reaches an error of around 10^{-9} . The reason for that is the cutoff limit imposed for the singular values. The inverse of the singular values was set to zero to all singular values obtained lower than 10^{-9} . However, the most important result of the comparison is the confirmation that the matrix update scheme remains stable and that the error produced by it is as low as the error produced by the full Cholesky decomposition. The reason behind this result could be explained by the fact that the algorithm for the Cholesky decomposition also builds the matrix row-by-row or column-by-column without pivoting [178].

In addition to the matrix update of the Cholesky decomposition, in [A2] we also proposed and analyze the use of a matrix update scheme for the inverse of the Cholesky decomposition. This scheme would allow to make the inference twice faster than with the use of the Cholesky decomposition. However, the results that we present there show that, in contrast to the Cholesky decomposition, the method is unstable.

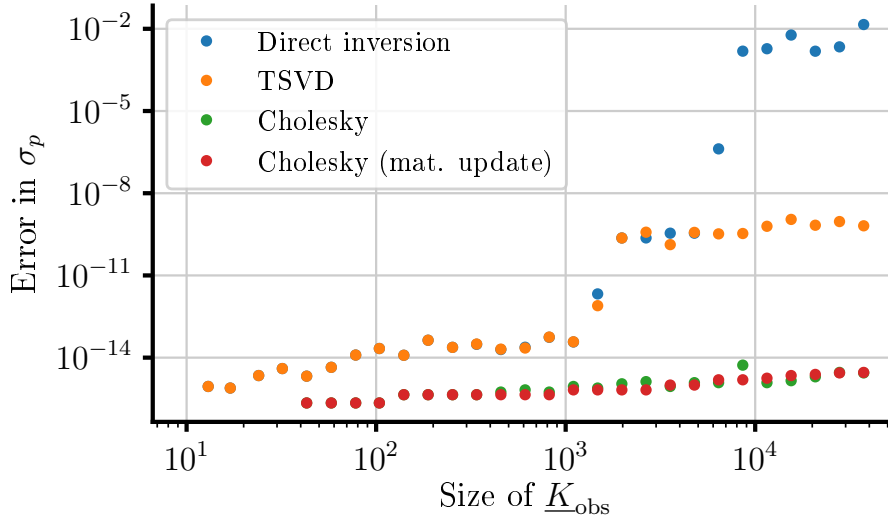


Figure 3.9: Error produced for the inference of K_{obs} using different techniques to solve the linear system of Eqn. (3.14): the Cholesky decomposition, the matrix update of the Cholesky decomposition, and the singular value decomposition.

Bayesian optimization with a local Gaussian process model

The second proposed method to improve the scalability of the Bayesian optimization consists in the use of an updated local Gaussian process model that contains a maximum fixed number of observations. For a given point \mathbf{x}_* where the value of the acquisition function is needed, the algorithm generates a posterior distribution based on a Gaussian process model that uses only a subset with the nearest N_{nearest} observations of the data set. The reason to explain why a local GP model can work is related to the exponential behavior of the covariance functions generally used, see Eqns. (3.6)-(3.10). The further away a point of the data set is from the point \mathbf{x}_* , the less correlated are their values, and the correlation factor contains an exponential decaying factor with the distance between the two points. Therefore, the estimation values for \mathbf{x}_* will not be strongly influenced by the points further away in the data set. A different strategy to the use of a fixed number N_{nearest} can be to use only the points for which the correlation value with \mathbf{x}_* is lower than $1/(100\Delta f_{\text{ob}})$, being Δf_{ob} the maximum difference between the different values of the objective value in the data set of observations.

Given the point \mathbf{x}_* , the first step of the algorithm consists in determining which of the N_{obs} observations are the nearest neighbours to this point \mathbf{x}_* . There are many algorithms to efficiently determine the nearest neighbors, as the k-d tree algorithm [183–185], the cover tree algorithm [186, 187], the R-tree [188–190] or uniform grid cell structures [191, 192]. Here, we use a grid-R-tree [193] algorithm. The design space is divided into hypercubes whose side lengths equal to half the length scales of the hyper-parameters, l_i . A list stores the indices of the cells that are populated with at least one observation point. The list also contains their population number and it is updated with each new observation obtained. With this structure, the search for the nearest neighbours can be done in a sub-linear time with respect to N_{obs} .

Once the subset of observations is chosen, the posterior Gaussian process is calculated. Note that this requires the calculation of the covariance matrix and its Cholesky decomposition to perform the inference, needed for the calculation of the acquisition function.

To not recompute the covariance function and the Cholesky decomposition too often, as the optimization for the acquisition function continues sampling at different points \mathbf{x}_* , the subset for the local Gaussian process is not continuously updated. It only updates when more than a γ_{update} percentage of the closest neighbours for the current \mathbf{x}_* is not contained in the subset used the last time that the covariance matrix was computed. In practice, if one uses a gradient descent algorithm to optimize the acquisition function, the update is required a few times at maximum for each starting point of the gradient descent. The tests of the implementation show that the posterior Gaussian process, when used in combination with a gradient descent strategy for the optimization of the acquisition function, needs to be updated in average once every 10 evaluations of the acquisition function. This number has been obtained for a N_{nearest} value of 300 and a γ_{update} of 15%.

With this implementation, the scaling of the method is sublinear once the number of total observations N_{obs} exceeds N_{nearest} and if the algorithm does not increase the number of starting points for the optimization of the acquisition function with the number of total observations N_{obs} . However, there are two main fundamental questions that need to be answered. The first one is how much time the algorithm requires per observation, and if this time is actually lower than the average time required by the standard implementation of Bayesian optimization in practical applications. Although the algorithm does not scale with the number of observations, at least in a certain range after N_{obs} exceeds N_{nearest} , the proposed method must be slower than the standard implementation of Bayesian optimization, as different covariance matrices and their respective Cholesky decompositions must be computed. The second important aspect that needs to be answered is how the convergence rate of the algorithm performs with respect to the standard approach. The use of a local surrogate model implies that not all the available information is accessible for each candidate \mathbf{x}_* and how this affects the convergence of the method must be measured.

To obtain an approximate idea for these two aspects, the performance of the method is compared with respect to the standard implementation of Bayesian optimization for a series of optimization runs of a test function. The comparison consists in the optimization of the Rastrigin function [194, 195] in a parameter space of five dimensions,

$$f_{\text{Rastrigin}} = 50 + \sum_{i=1}^5 x_i^2 - 10 \cos(2\pi x_i), \quad (3.45)$$

and for a design space bounded by $|x_i| \leq 10$. The Rastrigin function has a global optimum of $f_{\text{Rastrigin}}(\mathbf{x}_{\text{opt}}) = 0$ at the point $\mathbf{x}_{\text{opt}} = [0,0,0,0,0]$. Within the design space considered, the function contains around 4 million local minima.

The optimization is performed four different times for both algorithms. The optimizations run until they reach three thousand iterations. All the different aspects of the optimization algorithm, as the number of starting points used for the acquisition function, the criteria for choosing the starting points for the local optimizations, etc. are identical for the two algorithms. Also the length scales are kept fixed in both methods, with a value of $l_i = 0.7$ for all the dimensions. To optimize the acquisition function both algorithms run twenty local optimizations using the L-BFGS-B algorithm [169, 171]. For this test, the local optimizations are run sequentially. Both algorithms include also the observations of the derivatives of the test function.

The results for the optimization convergence with respect to the number of evaluations of $f_{\text{Rastrigin}}(\mathbf{x})$ are shown in Fig. 3.10 for both methods, the standard Bayesian optimization

and the local approximation proposed here. The results shown correspond to the average results of the four different runs for each of the two methods. As one can see, for this particular test and implementation of both algorithms, the standard algorithm shows a slightly better convergence, although the differences are within the σ bands of both algorithms.

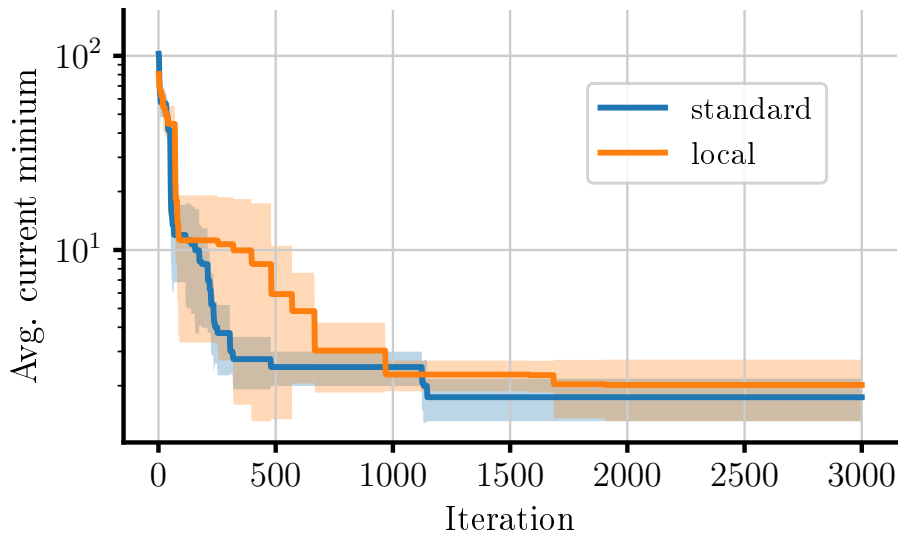


Figure 3.10: Comparison of the convergence of the two different Bayesian optimization algorithms with respect to the number of evaluations of the objective function. The results are shown for a standard Bayesian optimization algorithm and for the local approximation proposed in this work. The objective function to be optimized is the Rastrigin function in five dimensions, shown in Eqn. (3.45). Every iteration corresponds to the addition of one observation of the objective function and of its derivatives with respect to each input parameter. The results shown for each of the algorithms are the average of four different optimization runs. The shadowed area indicates the region within one standard deviation of the multiple runs performed.

Figure 3.11 shows the averaged computation time required by the last 50 iterations as a function of the iteration number. There, one can see how the time required by the local approach does not scale. Note that the times required by the standard Bayesian optimization algorithm are generally smaller than the ones shown in Fig. 3.11, as one would normally run the optimizations for the expected improvement in parallel and not sequentially. However, the scaling would still be similar and the difference with respect to the results of Fig. 3.11 would be a constant scaling factor.

Although with the method proposed in the previous section one can already efficiently cover most of the applications of interest in the design of photonic nanostructures without the need to use any approximation, altogether, the results obtained seem to point that the proposed use of local Gaussian processes can be a promising substitute of the standard Bayesian optimization for problems with moderately fast objective functions. Also, the use of local Gaussian processes results in a highly parallelizable method, since the memory usage per local Gaussian process is low. Further research on this method could also analyze the impact of optimizing the hyperparameters for each of the local Gaussian process in the optimization convergence and in the computational overhead.

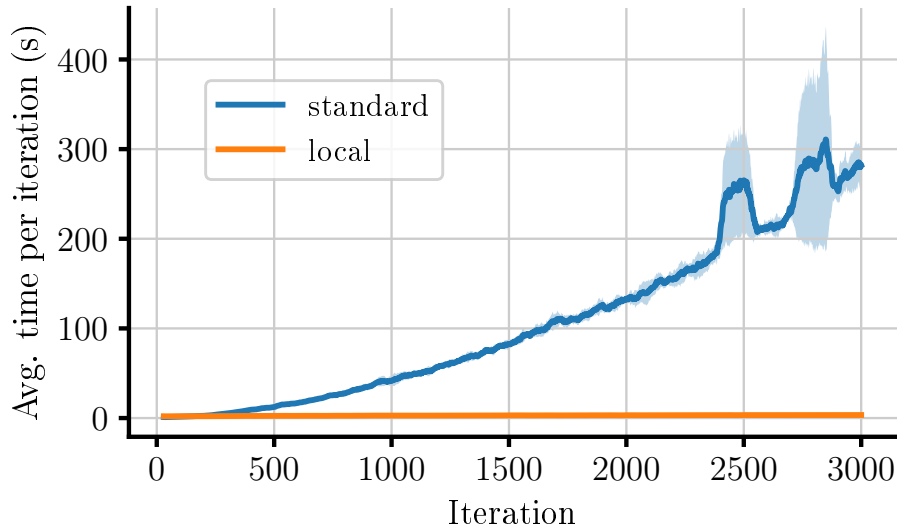


Figure 3.11: Time per evaluation required by a standard Bayesian optimization algorithm and the scalable proposed algorithm to obtain the next point where to evaluate the objective function. The objective function to be optimized is the Rastrigin function in five dimensions, shown in Eqn. (3.45). Both algorithms include derivative observations with respect to the five input parameters.

3.5 Conclusions

This chapter proposes and describes an implementation of Bayesian optimization for the global optimization of nanophotonic devices. The use of Gaussian processes as stochastic model provides a method able to incorporate both the objective value and its derivatives obtained from the finite element solver, which offers high predictive capabilities. These factors translate in an optimization method with a good iteration convergence, as it has been shown in several benchmarks. Furthermore, the chapter proposes two different techniques to improve the scalability issues of Bayesian optimization. These methods extend the efficient usage of Gaussian processes into a wider range of optimization problems for photonic applications.

The optimization methods presented here are the fundamental tool used in the next chapters of the thesis for the design of photonic structures. Specially in chapter 5, where we present the design of photonic structures used for different applications.

Once explained the optimization method developed for the optimization of photonic structures, in the next chapter we present some numerical tools to analyze and optimize isolated scatterers and the structures obtained from these elements, e.g., metasurfaces. Finally, chapter 5 combines the use of Bayesian optimization and the tools presented in chapter 4 to show, with some examples of design of photonic structures, the relevance of the developed tools.

4 | Design of isolated scatterers

4.1 Introduction

Among the multiple types of photonic devices used to manipulate and control light, there is a wide range of them that are either entirely or in part composed of isolated scatterers embedded in a homogeneous medium. Examples of these kind of devices are nano-antennas [196–200], devices used to promote the interaction of light [201–203], and metamaterials in general [204–207]. Here, arrangements made from a larger number of small scatterers are used to create artificial photonic materials capable of controlling light propagation in manners inaccessible with homogeneous natural materials. Further devices that are made from ensembles of scatterers are metalenses that can be used for different applications [208–210] or photonic crystals with spatially dependent properties [211]. Ensembles of many scattering particles also find use in layers that offer longer effective photon path lengths to improve absorption in thin-film solar cells [212] or as chiral metamaterials that can act as a direction independent circular polarization filters [213]. In all these examples for possible devices, the position, shape, and materials of the scatterers are design parameters, which one can optimize for the desired application. The purpose of this chapter is to describe a strategy to design isolated scatterers according to a predefined purpose. That requires to describe the interaction of light with such a scatterer at first.

One very well established tool to study the interaction of a given scatterer with a given illumination bases on the multipole expansion. There, the scattered field from the object is expanded in frequency domain into a basis of radiative vector spherical wave functions, VSWFs,

$$\mathbf{E}_{\text{scat}}(\mathbf{r}) = \sum_{n=1}^{\infty} \sum_{m=-n}^n \left[a_{m,n} \mathbf{N}_{m,n}^{(3)}(\mathbf{r}) + b_{m,n} \mathbf{M}_{m,n}^{(3)}(\mathbf{r}) \right]. \quad (4.1)$$

The fields $N_{m,n}^{(3)}(\mathbf{r})$ and $M_{m,n}^{(3)}(\mathbf{r})$ are the electric and magnetic VSWFs, respectively. Their definition and properties are presented in section 2.2. The complex coefficients $a_{m,n}$ and $b_{m,n}$ capture the contribution of the respective multipoles to the scattered field. The decomposition shown in Eqn. (4.1) is valid everywhere outside the smallest sphere circumscribing the scatterer. There is not yet a proof about the validity of the decomposition in the region inside the sphere. The assumption that the expression is valid inside the sphere is known as the Rayleigh hypothesis [214–216].

In addition to the valuable information that the multipole expansion directly provides for studying and designing scatterers, the multipole expansion is also an important ingredient to construct the T-matrix of a given object [42, 217, 218]. The T-matrix of an object provides the field scattered by any field illuminating the object. The T-matrix expresses how an incident field, expanded into a series of incident VSWFs, is scattered into a set of

outgoing VSWFs. With that it contains all the information about how an object interact with light; it is the most comprehensive representation of the object concerning its optical properties. The T-matrix can be used to obtain different quantities, such as the total interaction cross section of a scatterer with light, the absorption of the object under a certain illumination ([42] section 5.1) or the duality of the object or its electromagnetic chirality [213]. However, the T-matrix is also important to calculate the optical response from clusters that consist of a large numbers of scatterers [219, 220]. When solving this multiple scattering problem, the scatterers themselves are represented only on the base of their T-matrix. Current computational resources allow for clusters with half a million scatterers to be solved numerically [A5].

There are different numerical methods for calculating the T-matrix of an object. The validity and efficiency of each method depends on the symmetries of the object and its material and geometrical complexity. For example, the T-matrix of a sphere can be obtained analytically using Mie theory [62, 63]. For homogeneous scatterers, composed of only one material, but with geometries different than a sphere, the extended boundary condition method (see, e.g., [217, 221] or [42] section 5.8) is an efficient method for calculating the T-matrix. However, this method is only valid for objects homotopic to a sphere. To compute the T-matrix of objects composed of multiple materials and with more complex geometries, a more general method for solving Maxwell's equations is needed. The finite element method is especially suitable for dealing with complex geometries. Here, the procedure to compute the T-matrix of an object consists of two main steps. In a first step, the finite element method is used to solve the scattered fields, \mathbf{E}_{scat} , for a set of different illuminations. In a second step, the scattered fields are expanded into the basis of VSWF. For that, one uses the orthogonal properties of the VSWF, Eqns. (2.44)-(2.44), and the complex expansion coefficients of the scattered field are calculated as

$$a_{m,n} = \frac{\int_{S_R^2} \mathbf{N}_{m,n}^{(3)*}(\mathbf{r}) \cdot \mathbf{E}_{\text{scat}}(\mathbf{r}) \, dS}{\int_{S_R^2} |\mathbf{N}_{m,n}^{(3)}(\mathbf{r})|^2 \, dS}, \quad (4.2)$$

$$b_{m,n} = \frac{\int_{S_R^2} \mathbf{M}_{m,n}^{(3)*}(\mathbf{r}) \cdot \mathbf{E}_{\text{scat}}(\mathbf{r}) \, dS}{\int_{S_R^2} |\mathbf{M}_{m,n}^{(3)}(\mathbf{r})|^2 \, dS}. \quad (4.3)$$

The elements $a_{m,n}$ and $b_{m,n}$ of the multipole decomposition either directly correspond to entries of the T-matrix, if one uses regular VSWFs as illuminations, or an intermediate linear system has to be solved to link the values $a_{m,n}$ and $b_{m,n}$ with the entries of the T-matrix. This last procedure is needed in the case that another type of illuminations is used, as for example plane waves [222].

In Eqns. (4.2) and (4.3), the decomposition is obtained as a series of surface integrals across the boundary of a sphere circumscribing the scatterer, S_R . The fact that this surface has to be a sphere presents some drawbacks. To perform the integral, the scattered field has to be interpolated across the surface of the sphere. The interpolation suffers from accuracy losses and it also makes the calculation computationally more expensive and, therefore, slower. One possible solution to this drawback consists of performing the decomposition based on volume integrals of the induced currents in the object [205, 223, 224]. In this chapter, another method is presented, extending the orthogonality property of the VSWFs to surfaces with general shapes. This contribution has been discussed in [A6]. With such a generalization, one can use the boundaries of the computational domain or the boundary of the scatterer to perform the decomposition. Computing surface integrals over these natural surfaces is not only easier, but also frequently more efficient.

Most numerical solvers for Maxwell's equations already provide efficient methods to accurately compute surface integrals over these boundaries for quantities dependent on the scattered field. For similar reasons, if the numerical solver provides shape and material derivatives for similar surface integrals, such as the integral of the Poynting vector, they can be easily modified to obtain the shape and material derivatives of the multipole decomposition. This allows for the computation of the derivatives of T-matrices of general complex scatterers, enabling the efficient optimization of such scatterers. The shape derivatives can be used for the optimization of a single scatterer or for the optimization of multiple scatterers in a more complex system, combining the multi-scattering method with the adjoint method [225]. The next chapter presents one relevant example of design of an isolated chiral scatterer where one can benefit from these developments.

This chapter is devoted to the description of different methods related to the multipole decomposition, used to analyze and design single scatterers or clusters of them. The first section presents the derivation of the multipole decomposition using surfaces of general shapes. After that, its numerical implementation is outlined using the finite element method. An extra section is used to present the implementation for the specific case of cylindrically symmetric objects. Cylindrically symmetric scatterers are widely used in many different applications and this implementation drastically reduces the computational time and resources with respect to the more general implementation. A fourth section describes a proposed method to compute the T-matrix of complex objects. After that, the implementation of the calculation for shape and material derivatives of the T-matrix is presented. Finally, the last section describes an implementation of the adjoint method for multi-scattering problems based on the T-matrix method and the shape derivatives of the T-matrix.

Most of the numerical tools presented in this chapter will be used in the following chapter for designing maximal em-chiral scatterers. These scatterers show considerable differences in their interaction strength with plane waves of different circular polarization handedness and for multiple illumination angles, which makes them interesting for different applications.

4.2 Decomposition of scattered fields into VSWFs using surfaces with general shapes

Mathematical derivation

This section derives the general orthogonality relation for VSWFs. This expression consists of an integral evaluation over a general closed surface that encloses the scattering object.

The derivation assumes that the scattering object is surrounded by a homogeneous, isotropic, and lossless medium. To obtain the expression, we start by taking two vector fields that are solutions of the same wave equation, Eqn. (2.23), $\mathbf{E}_{\text{scat}}(\mathbf{r})$ and $\mathbf{F}(\mathbf{r})$. $\mathbf{E}_{\text{scat}}(\mathbf{r})$ is the scattered field produced by the object under a certain illumination and $\mathbf{F}(\mathbf{r})$ is another field that equally fulfills the Silver-Mueller radiation condition, Eqn. (2.50). The generic field $\mathbf{F}(\mathbf{r})$ is used for simplicity, and only in the last step of the derivation it will be replaced by the radiative VSWFs to obtain the final desired expression.

To obtain a scalar product between the two fields $\mathbf{E}_{\text{scat}}(\mathbf{r})$ and $\mathbf{F}_{\text{scat}}(\mathbf{r})$, we start by multiplying the wave equation for the field $\mathbf{E}_{\text{scat}}(\mathbf{r})$ by the complex conjugate of $\mathbf{F}(\mathbf{r})$,

$$\mathbf{F}^*(\mathbf{r}) \cdot \{\nabla \times (\nabla \times \mathbf{E}_{\text{scat}}(\mathbf{r}))\} - k^2 \mathbf{F}^*(\mathbf{r}) \cdot \mathbf{E}_{\text{scat}}(\mathbf{r}) = 0. \quad (4.4)$$

The above expression is then integrated over a volume V that surrounds the object but it shall not contain any source of the scattered field. To be specific, V denotes a closed region that surrounds the object, but which does not contain it, as illustrated in Fig. 4.1,

$$\int_V (\mathbf{F}^*(\mathbf{r}) \cdot \{\nabla \times (\nabla \times \mathbf{E}_{\text{scat}}(\mathbf{r}))\} - k^2 \mathbf{F}^*(\mathbf{r}) \cdot \mathbf{E}_{\text{scat}}(\mathbf{r})) dV = 0. \quad (4.5)$$

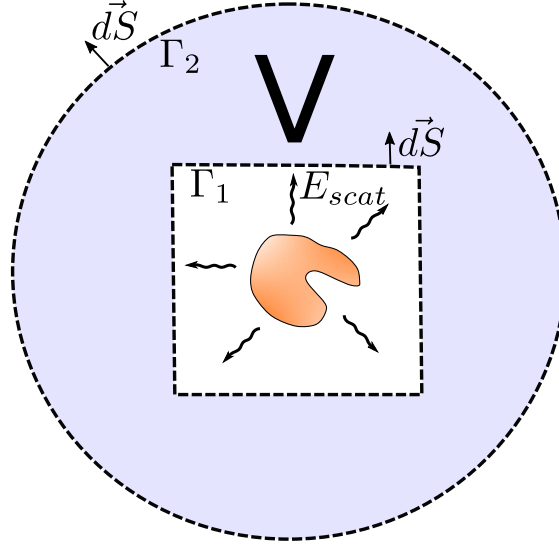


Figure 4.1: Sketch of geometry considered in the derivation of the multipole expansion of scattered fields using surfaces with general shapes. An object within a homogeneous background medium produces a scattered field. Equation (4.5), which involves the radiated field, is integrated across a volume V that surrounds the object without containing it. The volume is delimited by an inner boundary Γ_1 and an outer boundary Γ_2 . At the end of the derivation, only the field across the boundary Γ_1 is necessary to obtain the expansion.

We apply the generalized Stokes' theorem [226] to Eqn. (4.5) twice to convert part of the volume integral into a surface integral across the boundaries of V ,

$$\begin{aligned} 0 &= \int_{\Gamma} \{(\nabla \times \mathbf{E}_{\text{scat}}(\mathbf{r})) \times \mathbf{F}^*(\mathbf{r})\} \cdot d\mathbf{S} \\ &+ \int_V \{(\nabla \times \mathbf{E}_{\text{scat}}(\mathbf{r})) \cdot (\nabla \times \mathbf{F}^*(\mathbf{r})) - k^2 \mathbf{F}^*(\mathbf{r}) \cdot \mathbf{E}_{\text{scat}}(\mathbf{r})\} dV \\ &= \int_{\Gamma} \{(\nabla \times \mathbf{E}_{\text{scat}}(\mathbf{r})) \times \mathbf{F}^*(\mathbf{r}) + \mathbf{E}_{\text{scat}}(\mathbf{r}) \times (\nabla \times \mathbf{F}^*(\mathbf{r}))\} \cdot d\mathbf{S} \\ &+ \int_V (\mathbf{E}_{\text{scat}}(\mathbf{r}) \cdot \{\nabla \times (\nabla \times \mathbf{F}^*(\mathbf{r}))\} - k^2 \mathbf{F}^*(\mathbf{r}) \cdot \mathbf{E}_{\text{scat}}(\mathbf{r})) dV \end{aligned} \quad (4.6)$$

Using now the assumption that $\mathbf{F}(\mathbf{r})$ also fulfills the homogeneous wave equation, and therefore also $\mathbf{F}^*(\mathbf{r})$, the volume integral in Eqn. (4.6) vanishes and we obtain an expression involving only a surface integral,

4.2. Decomposition of scattered fields into VSWFs using surfaces with general shapes

$$\int_{\Gamma} \{(\nabla \times \mathbf{E}_{\text{scat}}(\mathbf{r})) \times \mathbf{F}^*(\mathbf{r}) - (\nabla \times \mathbf{F}^*(\mathbf{r})) \times \mathbf{E}_{\text{scat}}(\mathbf{r})\} \cdot d\mathbf{S} = 0. \quad (4.7)$$

In the next step, we split the surface integral into the contributions of the inner surface Γ_1 and the outer surface Γ_2 , see Fig. 4.1,

$$\begin{aligned} & - \int_{\Gamma_1} \{(\nabla \times \mathbf{E}_{\text{scat}}(\mathbf{r})) \times \mathbf{F}^*(\mathbf{r}) - (\nabla \times \mathbf{F}^*(\mathbf{r})) \times \mathbf{E}_{\text{scat}}(\mathbf{r})\} \cdot d\mathbf{S} \\ & + \int_{\Gamma_2} \{(\nabla \times \mathbf{E}_{\text{scat}}(\mathbf{r})) \times \mathbf{F}^*(\mathbf{r}) - (\nabla \times \mathbf{F}^*(\mathbf{r})) \times \mathbf{E}_{\text{scat}}(\mathbf{r})\} \cdot d\mathbf{S} \\ & = I_1 + I_2 = 0. \end{aligned} \quad (4.8)$$

The minus sign in the above expression comes from the definition used for the differential surface elements, with $d\mathbf{S}$ pointing inwards the volume V on Γ_1 and outwards on Γ_2 .

Up to this point, no restriction was imposed on the shape of the boundaries Γ_1 or Γ_2 . For the remainder of this derivation, the outer surface Γ_2 is assumed to be a sphere of radius R , S_R . Applying the circular shift theorem over I_2 one gets,

$$\begin{aligned} I_2 &= \int_{S_R^2} \{(\nabla \times \mathbf{E}_{\text{scat}}(\mathbf{r})) \times \mathbf{F}^*(\mathbf{r})\} \cdot d\mathbf{S} - \{(\nabla \times \mathbf{F}^*(\mathbf{r})) \times \mathbf{E}_{\text{scat}}(\mathbf{r})\} \cdot d\mathbf{S} \\ &= \int_{S_R^2} \{d\mathbf{S} \times (\nabla \times \mathbf{E}_{\text{scat}}(\mathbf{r}))\} \cdot \mathbf{F}^*(\mathbf{r}) - \{d\mathbf{S} \times (\nabla \times \mathbf{F}^*(\mathbf{r}))\} \cdot \mathbf{E}_{\text{scat}}(\mathbf{r}). \end{aligned} \quad (4.9)$$

We now assume that the radius R is large enough such that the far-field radiation condition (2.50) is fulfilled,

$$\lim_{R \rightarrow \infty} (\nabla \times \{\mathbf{E}_{\text{scat}}(\mathbf{r}), \mathbf{F}(\mathbf{r})\}) \times R\hat{\mathbf{r}} = + \lim_{R \rightarrow \infty} ikR \{\mathbf{E}_{\text{scat}}(\mathbf{r}), \mathbf{F}(\mathbf{r})\}. \quad (4.10)$$

Expressing the differential surface element of the sphere in spherical coordinates,

$$d\mathbf{S} = R^2 \sin \theta d\theta d\phi \hat{\mathbf{r}}, \quad (4.11)$$

we can integrate it into the far-field condition,

$$\lim_{R \rightarrow \infty} (\nabla \times \{\mathbf{E}_{\text{scat}}(\mathbf{r}), \mathbf{F}(\mathbf{r})\}) \times d\mathbf{S} = + \lim_{R \rightarrow \infty} ikdS \{\mathbf{E}_{\text{scat}}(\mathbf{r}), \mathbf{F}(\mathbf{r})\}. \quad (4.12)$$

Substituting this last expression into Eqn. (4.9) we obtain,

$$\lim_{R \rightarrow \infty} I_2 = - \lim_{R \rightarrow \infty} ik \int_{S_R^2} (\mathbf{E}_{\text{scat}}(\mathbf{r}) \cdot \mathbf{F}^*(\mathbf{r}) + \mathbf{F}^*(\mathbf{r}) \cdot \mathbf{E}_{\text{scat}}(\mathbf{r})) dS. \quad (4.13)$$

Finally, the generic field \mathbf{F} is replaced by the radiative VSWF $\mathbf{N}_{m,n}^{(3)}(\mathbf{r})$ or $\mathbf{M}_{m,n}^{(3)}(\mathbf{r})$,

$$\begin{aligned}
 & \int_{\Gamma_1} \left\{ (\nabla \times \mathbf{E}_{\text{scat}}(\mathbf{r})) \times \{\mathbf{M}, \mathbf{N}\}_{m,n}^{(3)*}(\mathbf{r}) \right. \\
 & \left. - (\nabla \times \{\mathbf{M}, \mathbf{N}\}_{m,n}^{(3)*}(\mathbf{r})) \times \mathbf{E}_{\text{scat}}(\mathbf{r}) \right\} \cdot d\mathbf{S} \\
 & = \lim_{R \rightarrow \infty} 2ik \int_{S_R^2} \mathbf{E}_{\text{scat}}(\mathbf{r}) \cdot \{\mathbf{M}, \mathbf{N}\}_{m,n}^{(3)*}(\mathbf{r}) d\mathbf{S}.
 \end{aligned} \tag{4.14}$$

If we compare the term on the right hand side of the above expression with Eqns. (4.2)-(4.3), we see that it equals the complex coefficients of the multipole expansion times the norm of the VSWF at infinity, which is equal to $\frac{1}{k}$ ([42] Eqn. (C.152)),

$$\begin{aligned}
 & \int_{\Gamma_1} \left\{ (\nabla \times \mathbf{E}_{\text{scat}}(\mathbf{r})) \times \{\mathbf{M}, \mathbf{N}\}_{m,n}^{(3)*}(\mathbf{r}) \right. \\
 & \left. - (\nabla \times \{\mathbf{M}, \mathbf{N}\}_{m,n}^{(3)*}(\mathbf{r})) \times \mathbf{E}_{\text{scat}}(\mathbf{r}) \right\} \cdot d\mathbf{S} \\
 & = \{a, b\}_{m,n} 2ik \lim_{R \rightarrow \infty} \int_{S_R^2} |\{\mathbf{M}, \mathbf{N}\}_{m,n}^{(3)}(\mathbf{r})|^2 d\mathbf{S} \\
 & = \{a, b\}_{m,n} \frac{2i}{k}.
 \end{aligned} \tag{4.15}$$

Therefore, we obtained an expression to calculate the expansion of the scattered fields into VSWFs using integrals across a surface with a general shape,

$$a_{m,n} = \frac{k}{2i} \int_{\Gamma_1} \left\{ (\nabla \times \mathbf{E}_{\text{scat}}(\mathbf{r})) \times \mathbf{M}_{m,n}^{(3)*}(\mathbf{r}) - k\mathbf{N}_{m,n}^{(3)*}(\mathbf{r}) \times \mathbf{E}_{\text{scat}}(\mathbf{r}) \right\} \cdot d\mathbf{S}. \tag{4.16}$$

$$b_{m,n} = \frac{k}{2i} \int_{\Gamma_1} \left\{ (\nabla \times \mathbf{E}_{\text{scat}}(\mathbf{r})) \times \mathbf{N}_{m,n}^{(3)*}(\mathbf{r}) - k\mathbf{M}_{m,n}^{(3)*}(\mathbf{r}) \times \mathbf{E}_{\text{scat}}(\mathbf{r}) \right\} \cdot d\mathbf{S}. \tag{4.17}$$

Equations (4.16)-(4.17) can be also obtained using Lemma 6.38 of [227], applying it to $\mathbf{E}_{\text{scat}}(\mathbf{r})$ and the VSWF. They are the central result of this section.

Once the scattered field is known, these two equations allow us to calculate the coefficients of its multipole decomposition over any surface enclosing the scatterer. This result is particularly interesting for practical reasons, as one can directly apply the equations on the boundaries of the computational domain used to solve the scattered field.

Note that the surface Γ_1 can contain points or can be completely embedded into the region where the Rayleigh hypothesis may not hold true and still the expressions would be valid. This can be seen in Eqn. (4.14), where Eqns. (4.16) and (4.17) are linked to the values of the decomposition of the scattered field in the far-field region.

To test the above expressions, we considered a test field, $\mathbf{E}_{\text{test}}(\mathbf{r})$, composed of different VSWF terms with well defined amplitudes,

$$\mathbf{E}_{\text{test}}(\mathbf{r}) = (0.5 + 0.5i) \mathbf{M}_{0,1}^{(3)}(\mathbf{r}) + 0.03 \mathbf{N}_{3,3}^{(3)}(\mathbf{r}), \tag{4.18}$$

and calculate the decomposition of $\mathbf{E}_{\text{test}}(\mathbf{r})$ into a set of different VSWF. The decomposition is done using a cube of side length l_{cube} centered at the origin as the surface of

4.2. Decomposition of scattered fields into VSWFs using surfaces with general shapes

integration. For the test, a non-adaptive trapezoidal integration method was used. The number of grid points used for the numerical integration was 40,000 for each face of the cube. The results obtained for the expansion are shown in Fig. 4.2a as a function of the cube side length.

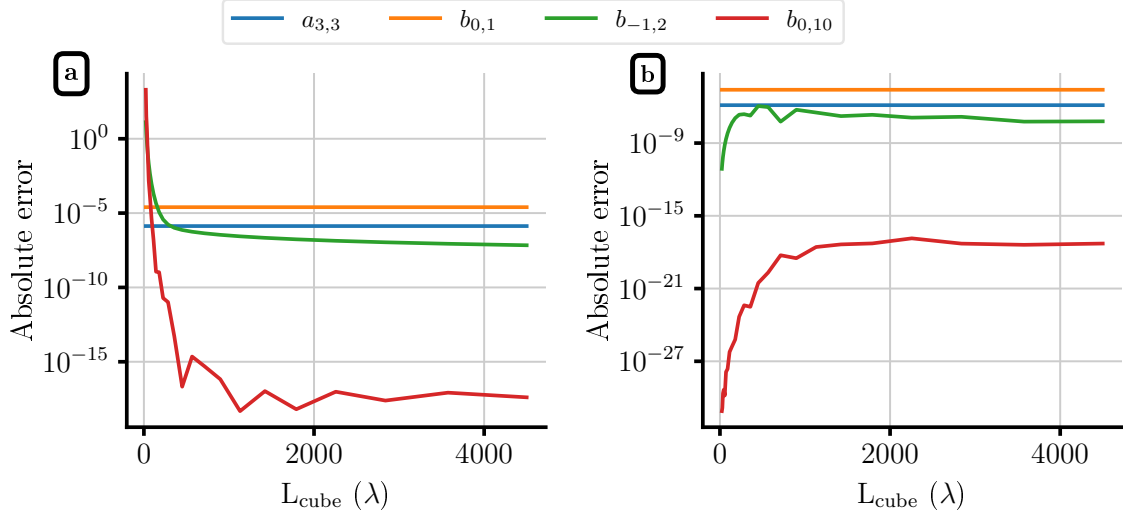


Figure 4.2: Error in different terms of the multipole expansion of a scattered field. The scattered field is given by Eqn. (4.18). **a.** Decomposition using the radiative VSWF, Eqn. (4.16). **b.** Decomposition using the regular VSWF, Eqns. (4.21)-(4.22).

As we can see, for a fixed number of integration grid points, the error of the expansion worsens the closer the boundaries of the integration surface are to the origin of the coordinates. The reason for that comes from the singular behavior of the radiative VSWFs at the origin. It causes numerical instabilities due to the finite precision of the digital representation of the numbers and due to the finite discretization used for the surface integral.

One possible solution to reduce this problem and improve the stability of the method could be to check if the radiative VSWF can be replaced by the regular VSWF in Eqn (4.16). The regular VSWFs differ from the radiative ones only in their radial dependence and they do not suffer from the singular behavior, so it is in principle reasonable to think that they might fulfill a similar orthogonality expression.

To check this, we substitute $\mathbf{F}(\mathbf{r})$ with $\mathbf{N}_{m,n}^{(1)}(\mathbf{r})$ into Eqn. (4.8). An equivalent procedure to the one done here for the fields $\mathbf{N}_{m,n}^{(1)}(\mathbf{r})$ can be done for the fields $\mathbf{M}_{m,n}^{(1)}(\mathbf{r})$.

Using the fact that the regular VSWFs can be expressed as a combination of the radiative VSWFs and the VSWFs of type 4,

$$\mathbf{N}_{m,n}^{(1)}(\mathbf{r}) = \frac{\mathbf{N}_{m,n}^{(3)}(\mathbf{r}) + \mathbf{N}_{m,n}^{(4)}(\mathbf{r})}{2}, \quad (4.19)$$

and that the fields $\mathbf{N}_{m,n}^{(4)}(\mathbf{r})$ fulfill an inwards Silver–Müller radiation condition, Eqn. (4.13) now reads as,

$$\begin{aligned}
 \lim_{R \rightarrow \infty} I_2 &= \lim_{R \rightarrow \infty} -ik \int_{S_R^2} \left(\mathbf{E}_{\text{scat}}(\mathbf{r}) \cdot \frac{\mathbf{N}_{m,n}^{(3)*}(\mathbf{r}) + \mathbf{N}_{m,n}^{(4)*}(\mathbf{r})}{2} \right. \\
 &\quad \left. + \frac{\mathbf{N}_{m,n}^{(3)*}(\mathbf{r}) - \mathbf{N}_{m,n}^{(4)*}(\mathbf{r})}{2} \cdot \mathbf{E}_{\text{scat}}(\mathbf{r}) \right) dS \\
 &= \lim_{R \rightarrow \infty} -ik \int_{S_R^2} \mathbf{E}_{\text{scat}}(\mathbf{r}) \cdot \mathbf{N}_{m,n}^{(3)*}(\mathbf{r}) dS.
 \end{aligned} \tag{4.20}$$

Therefore, we obtain an expansion for the scattered field into the radiative VSWFs using an expression that only involves the regular VSWFs,

$$\begin{aligned}
 a_{m,n} &= -ik \int_{\Gamma_1} \left\{ (\nabla \times \mathbf{E}_{\text{scat}}(\mathbf{r})) \times \mathbf{N}_{m,n}^{(1)*}(\mathbf{r}) \right. \\
 &\quad \left. - k \mathbf{M}_{m,n}^{(1)*}(\mathbf{r}) \times \mathbf{E}_{\text{scat}}(\mathbf{r}) \right\} \cdot d\mathbf{S},
 \end{aligned} \tag{4.21}$$

$$\begin{aligned}
 b_{m,n} &= -ik \int_{\Gamma_1} \left\{ (\nabla \times \mathbf{E}_{\text{scat}}(\mathbf{r})) \times \mathbf{M}_{m,n}^{(1)*}(\mathbf{r}) \right. \\
 &\quad \left. - k \mathbf{N}_{m,n}^{(1)*}(\mathbf{r}) \times \mathbf{E}_{\text{scat}}(\mathbf{r}) \right\} \cdot d\mathbf{S}.
 \end{aligned} \tag{4.22}$$

Equations (4.21) and (4.22) are equivalent to Eqn. 5.175 of [42], derived there on the boundary of the scatterer, and used in the context of the extended boundary condition method.

To see if the change improves the numerical stability of the expansion, the same test as shown in Fig. 4.2a is now repeated using Eqns. (4.21)-(4.22). The results are shown in Fig. 4.2b. As we can see, the error in the expansion using the regular VSWFs does not exponentially increase with the reduction of the cube length and it remains stable. Therefore, Eqns. (4.21) and (4.22) are more suitable for a numerical implementation of the multipole decomposition. These are the expressions we will finally use in our FEM implementation of the multipole decomposition, which we proceed to describe below.

FEM implementation of the decomposition

Having now checked the numerical suitability of the expressions, the next step is to implement them into the finite element solver.

Equations (4.21)-(4.22) have two terms, one that depends on the electric field and another that depends on its curl. As the electric field is expanded into a basis of polynomial functions of a certain degree, its curl will be given by an expansion of a lower polynomial degree. That implies that the numerical accuracy of the term depending on the curl is worse than the one of the directly computed field.

To improve the accuracy of the solution, one technique frequently used is to convert the part of the surface integral that contains the curl of the field into a volume integral,

$$\int_{\Gamma_1} \{\mathbf{F}^*(\mathbf{r}) \times (\nabla \times \mathbf{E}_{\text{scat}}(\mathbf{r}))\} \cdot d\mathbf{S} = \int_{V_1} \left((\nabla \times \mathbf{E}_{\text{scat}}(\mathbf{r})) \cdot (\nabla \times \mathbf{F}^*(\mathbf{r})) - k^2 \mathbf{F}^*(\mathbf{r}) \cdot \mathbf{E}_{\text{scat}}(\mathbf{r}) \right) dV, \quad (4.23)$$

where V_1 is the volume contained by the surface Γ_1 . Note that this is not the same volume as the volume V used in the derivation of Eqns. (4.2)-(4.3).

Actually, the numerical technique does not evaluate the volume integral over the entire volume V_1 . It uses only the field of the FEM mesh elements that are part of the surface Γ_1 . This is done to not increase the computational cost of having to solve an integral over the whole volume V_1 . In order to do that, a zero extension operator [228] is applied, to create a decaying continuation of the scattered field over Γ_1 towards the interior of the volume. This technique is not specifically used for the decomposition given by Eqns. (4.21) and (4.22). It is a common technique used in the FEM for computing different surface integrals, as for example the surface integral of the Poynting vector. The numerical trick is automatically applied by the solver JCMSuite [229].

To test the FEM implementation¹, first we compute the expansion of the field scattered by a sphere when it is illuminated by a linearly polarized plane wave. The VSWF expansion of the scattered fields produced by a sphere is a well known solution [62, 63], which has an analytical expression. Figure 4.3 shows the scattering cross section split into the contributions of the different multipoles for different frequencies of the illumination, obtained using both the FEM implementation and Mie theory. The link between the coefficients of the multipole decomposition and the scattering cross section has been described in section 2.2. The details of the simulation are described in the caption of the figure. As it can be seen, the results of the FEM solution match the analytical solution up to a certain numerical precision.

To further ascertain the accuracy of the method, we perform a convergence test of the error of the decomposition with respect to the side length of the mesh elements used in the FEM discretization, h_{FEM} . The results are shown in Fig. 4.4. As it can be seen, the errors in the decomposition decrease with the decrease of the mesh side length. An additional line was included showing the values of $0.8 \cdot 10^{-4} \cdot h_{\text{FEM}}^2$. This behavior coincides with the behavior of the relative error of the decomposition for the magnetic hexapole. The relative errors of the different multipoles show similar power law behaviors. These results are in agreement with the theoretical asymptotic FEM convergence behavior of h^p for the electromagnetic fields ([231] section 5.7).

As a second test, the total scattering cross section of a silver nanorod is computed for a wavelength range between 250 nm and 2 μm . The nanorod is modeled as an ellipsoid with a semi-major axis of 225 nm and a semi-minor axis of 37.5 nm. The major axis is parallel to the x -axis. The nanorod is illuminated with a linearly polarized plane wave with wave vector pointing in the $-z$ -direction. The electric field is parallel to the x -axis.

To check the validity of the decomposition, the total scattering cross section as computed from the multipole coefficients, Eqn. (2.52), is compared with the value obtained from the calculation of the total scattered power using the time averaged Poynting vector, $\langle \mathbf{S} \rangle(\mathbf{r})$,

¹After implementing and testing the decomposition with JCMSuite using an external Python module, the decomposition was then fully integrated into JCMSuite as an extra feature of the software package. This final integration was mainly done by Martin Hammerschmidt. My work in this integration process was to test it and to help in the identification of the sources of errors.

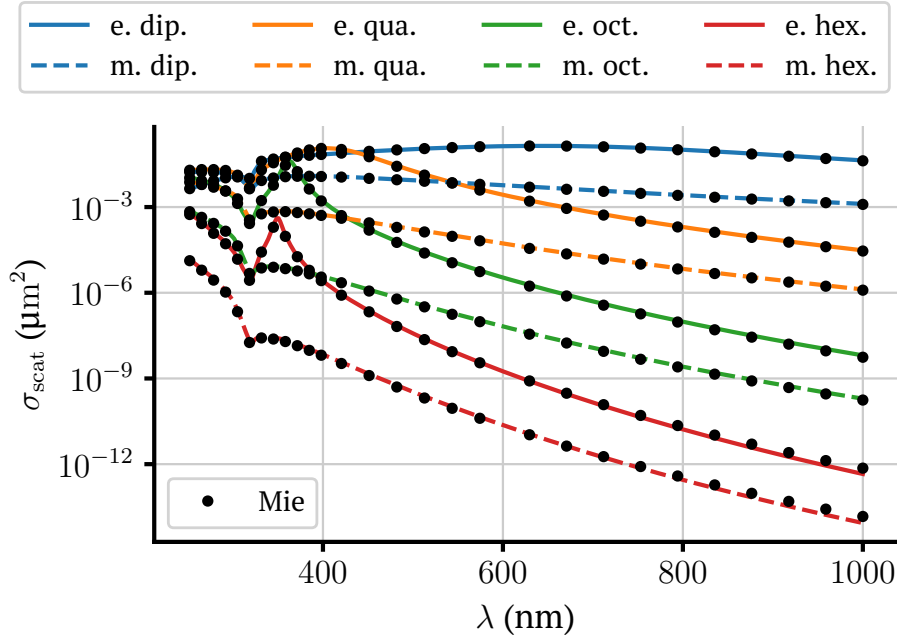


Figure 4.3: Multipole decomposition of the field scattered by a silver sphere illuminated by a plane wave. The wave vector of the plane wave is oriented in the $-z$ -direction. Its electric field is linearly polarized in the x -direction with an amplitude of 1 V/m. The sphere has a radius of 112.5 nm and its permittivity at each wavelength is interpolated from a database [230].

$$\sigma_{\text{scat}} = \frac{\int_S \langle \mathbf{S} \rangle(\mathbf{r}) \cdot d\mathbf{S}}{2Z_0^2 |\mathbf{E}_i|^2}, \quad (4.24)$$

with S being a surface surrounding a volume that contains the nanorod, Z_0 the characteristic impedance of free space, and \mathbf{E}_i the amplitude of the plane wave.

For this example, the expressions (4.21) and (4.22) for the multipole expansion were evaluated directly on the boundary of the nanorod. The decomposition is shown in Fig. 4.5. The results obtained from both methods are in good agreement with each other.

As it can be seen in the decomposition, the nanorod sustains a principle resonance at a wavelength of 1225 nm. At this wavelength, most notably the electric dipole moment is resonantly excited. To be precise, the dipole moment oriented along the major axis of the nanorod is resonantly excited, corresponding to the vectorial orientation of the electric field used to illuminate the nanorod. Symmetry reasons prevent any electrical dipole moment oriented in a direction other than the x -axis from being excited. This can be seen in Fig. 4.6, which shows the contribution of the different components of the electric dipole moments in the Cartesian basis to the scattering cross section. The electric dipole moments oriented along the Cartesian axis and the electric dipole moments that produce the VSWF fields $\mathbf{N}_{m,1}^3(\mathbf{r})$ are related as

$$\begin{bmatrix} p_x \\ p_y \\ p_z \end{bmatrix} = \frac{1}{\sqrt{2}} \begin{bmatrix} 1 & 0 & -1 \\ -i & 0 & -i \\ 0 & \sqrt{2} & 0 \end{bmatrix} \begin{bmatrix} p_{-1} \\ p_0 \\ p_{+1} \end{bmatrix}. \quad (4.25)$$

This dipolar behavior is visible in Fig. 4.7a, which shows the intensity of the electric field

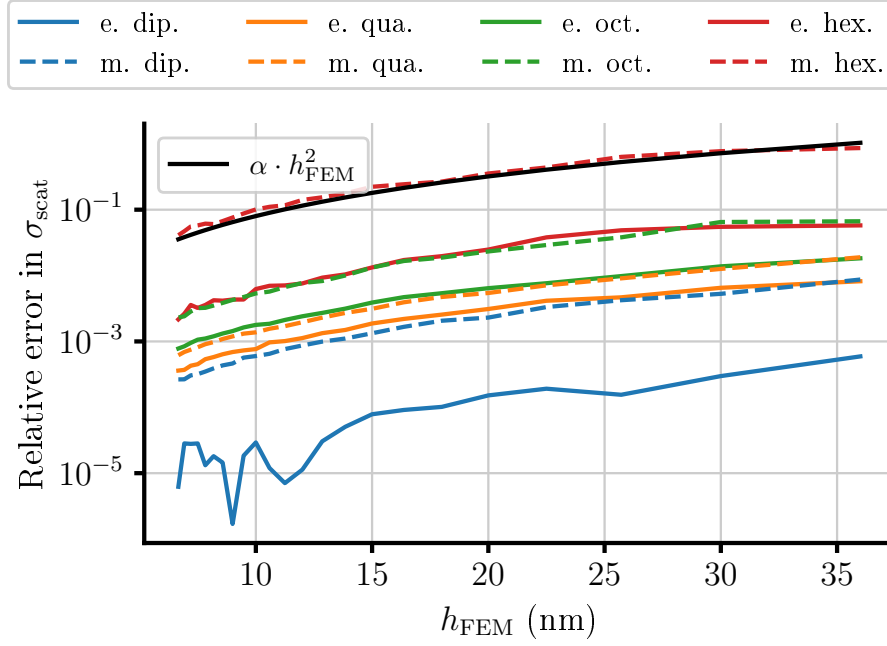


Figure 4.4: Convergence study for the errors in the multipole decomposition of the fields scattered by a silver sphere as a function of the FEM mesh side length in the surrounding medium, h_{FEM} . The sphere is illuminated by a plane wave with a wavelength of $\lambda_0 = 450$ nm. The wave vector of the plane wave is oriented in the $-z$ -direction. Its electric field is linearly polarized in the x -direction. The sphere has a radius of 112.5. The mesh side length of the sphere discretization equals $h_{\text{FEM}}/|\sqrt{\epsilon_{\text{silver}}}|$, being ϵ_{silver} the relative permittivity of the sphere, $\epsilon_{\text{sphere}} = -6.81 + 0.28i$.

on the surface of the nanorod and in the plane x - z -plane at $y = 0$, which contains the major axis of the nanorod. As it can be seen in the figure, the field is strongly localized around the corners of the particle and it resembles the field profile produced by an ideal electric dipole. Such strong field intensities are characteristic of rod-like metallic particles due to plasmonic excitations [232–234]. When one of the two dimensions of the nanorod is much longer than the other two, a low-energy local surface polariton, is sustain [235].

Antenna theory describes how an ideal half-wave dipole antenna, a thin wire made out of a perfect electric conductor, would present a resonance peak in the scattering cross section for an illumination wavelength equals to two times the length of the wire [236]. However, at optical and near infrared frequencies, particles made out of silver can not be assumed to be perfect electric conductors. The incident radiation is not perfectly reflected on the surface of the particle but it penetrates a certain thickness into the particle. The electromagnetic response becomes then governed by collective electron oscillations, called surface plasmons. This different behavior with respect to the predictions from antenna theory leads to a shift of the resonance towards longer wavelengths [237], as it can be seen in the results of Fig. 4.6. However, one could still approximately predict the position of the resonance for a thin wire using a scaling correction of the wavelength predicted by antenna theory [238, 239],

$$\lambda_{\text{eff}} = \lambda_0 \frac{k_0}{\gamma} - 4R. \quad (4.26)$$

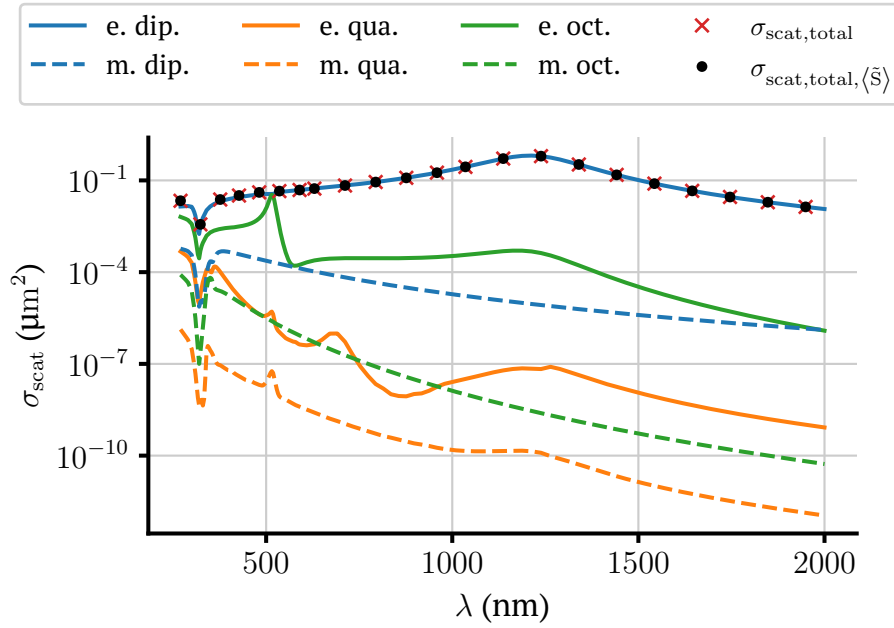


Figure 4.5: Cross section of a nanorod calculated using two different methods: the multipole expansion and the integral of the power flux of the scattered field. The nanorod is a silver ellipsoid with a semi-major axis of 225 nm and semi-minor axis of 37.5 nm. The major axis is oriented along the x -direction. The nanorod is illuminated with a plane wave with the wave vector parallel to the $-z$ -axis and the electric field linearly polarized in the x -direction.

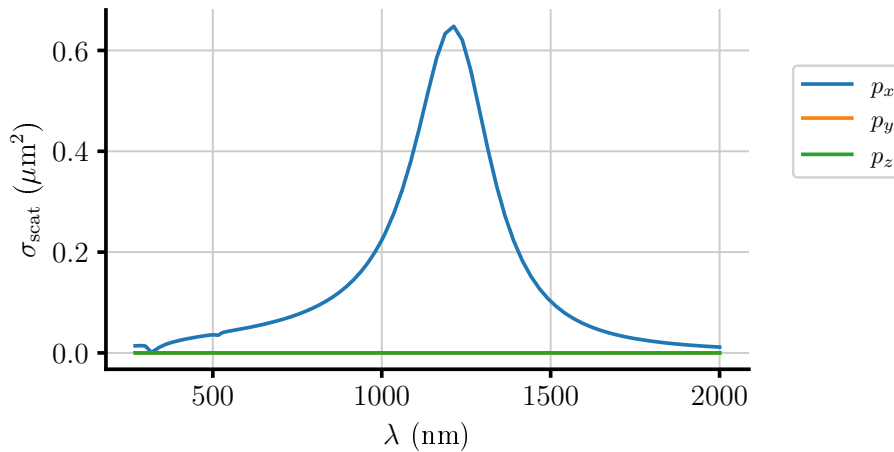


Figure 4.6: Electric dipole contributions to the scattering cross section of the nanorod described in Fig. 4.5 as a function of the wavelength. The contributions are shown in terms of the three Cartesian dipole moments. The peak in the scattering cross section is associated to resonant the excitation of the dipole moment oriented in the x -direction. Symmetry reasons prevent the excitation of any other electrical dipole moment.

In the above equation, λ_{eff} would be the wavelength of the resonance for a half-wavelength antenna. In the case of the nanorod simulated here, that would be $\lambda_{\text{eff}} = 900$ nm, four times the semi-major axes. λ_0 is the wavelength at the resonance peak, k_0 is the wave

4.2. Decomposition of scattered fields into VSWFs using surfaces with general shapes

number in free space, R is the radius of the wire and γ is the propagation constant of the surface charge wave for the TM_0 mode of a cylindrical wire. We compute the value of γ following [240]. Assuming a wire with a constant radius of 37.5 nm, one obtains that an effective wavelength of 900 nm would correspond to an illumination wavelength of 1229 nm. This value of the position of the resonance peak is in very good agreement with the results shown in Fig. 4.6.

Metallic nanorods similar to the one analyzed here have been proposed as an important component of different sensor devices [241–244]. One of the reasons for that is the high sensitivity that they present in the spectral position of the plasmon resonance. A small change in the refractive index of the surrounding medium shifts the resonance of the scattering cross section considerably, allowing to measure minute changes in the refractive index.

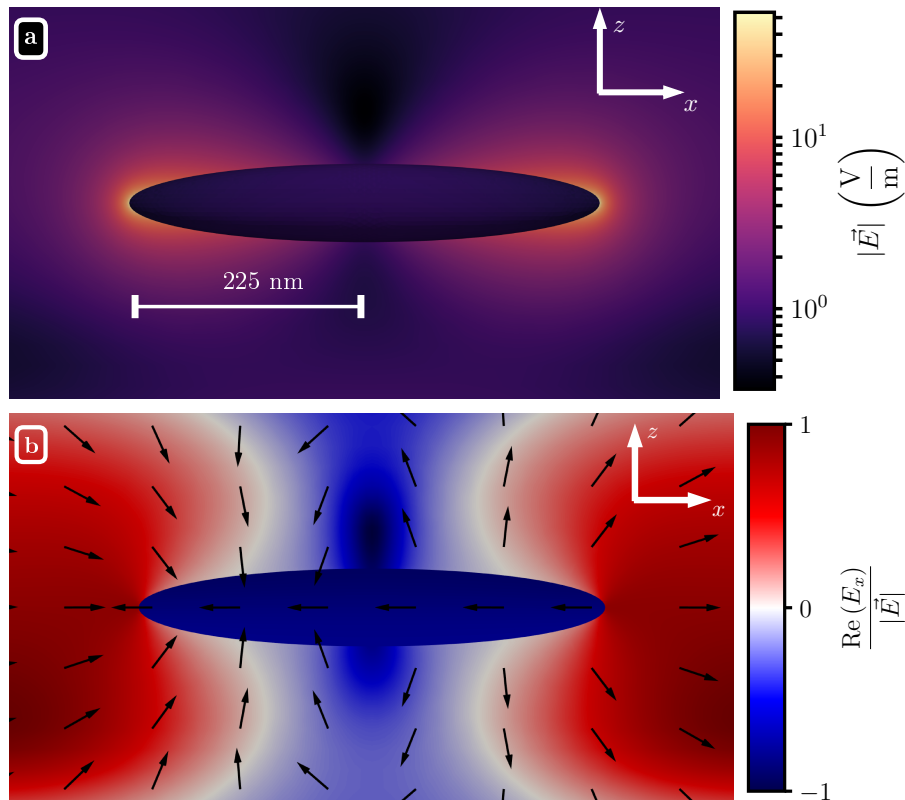


Figure 4.7: **a.** Amplitude of the electric field in close vicinity to the nanorod upon its illumination with a plane wave at a wavelength of 1225 nm. Other properties of the illumination and the nanorod correspond to those described in the caption of Fig. 4.5. The figure shows the amplitude in the x - y -plane at $y = 0$. The amplitude of the field in the surface of the nanorod with $y \leq 0$ is superimposed onto the values of the plane. **b.** Direction of the electric field in the x - z -plane at $y = 0$ along with the real part of the x -component of the electric field.

Decomposition of fields scattered from cylindrically symmetric objects

The decomposition and the FEM implementation proposed in the previous section is a general method that can be used with any structure, entirely independent on its complexity. On the other hand, there are different techniques to obtain the multipole expansion

for simple objects in a more efficient manner. A typical example would be the case of Mie theory for spheres and the extended boundary condition method applicable for homogeneous scatterers that are homotopic to a sphere.

In a similar manner, the decomposition using the FEM can also be simplified if the scattering object has specific symmetries. One particularly interesting case is that of cylindrically symmetric objects. The FEM calculation of three dimensional cylindrically symmetric objects can be simplified and solved using a two dimensional FEM layout. To do that, one needs to apply cylindrically symmetric boundary conditions. Doing this, one obtains the FEM solution of the electric field as a combination of cylindrical Fourier modes ([245] section 4.1.2),

$$\mathbf{E}_{\text{scat}}(\mathbf{r}) = \sum_{m=-\infty}^{\infty} \mathbf{E}_{\text{scat},m}(r, z) e^{im\phi}. \quad (4.27)$$

with r , z , and ϕ being the spatial coordinates in a cylindrical coordinate system. The m -th order in the expansion can be solved for by a two-dimensional instead of a three dimensional wave equation. In practice, the summation in Eqn. (4.27) is truncated and only a finite set of orders, $m = [-n, \dots, n]$ is considered. Therefore, $2n + 1$ different two-dimensional simulations need to be computed. As the VSWFs are also cylindrical Fourier modes, with the mode number given by their multipole order m , the VSWF decomposition of the Fourier modes of the scattered field, $\mathbf{E}_{\text{scat},m}$, vanishes for all the VSWF that do not share the same Fourier order m with the mode of the scattered field. This means that, for a given VSWF with a multipole order m , only the contribution of the scattered mode $\mathbf{E}_{\text{scat},m}$ is needed to perform the expansion. That obviously constitutes a tremendous simplification. Furthermore, Eqns. (4.21) and (4.22) can be reduced to a line instead of a surface integral applied across a one dimensional boundary Γ_1 that surrounds the scatterer in the two dimensional FEM model. The individual amplitude coefficients for cylindrically symmetric objects can then be calculated according to

$$a_{m,n} = -i2\pi k \int_{\Gamma_1} \left\{ (\nabla \times \mathbf{E}_{\text{scat},m}(\mathbf{r})) \times \mathbf{N}_{m,n}^{(1)*} - k\mathbf{M}_{m,n}^{(1)*}(\mathbf{r}) \times \mathbf{E}_{\text{scat},m}(\mathbf{r}) \right\} r \cdot d\mathbf{l}. \quad (4.28)$$

$$b_{m,n} = -i2\pi k \int_{\Gamma_1} \left\{ (\nabla \times \mathbf{E}_{\text{scat},m}(\mathbf{r})) \times \mathbf{M}_{m,n}^{(1)*}(\mathbf{r}) - k\mathbf{N}_{m,n}^{(1)*}(\mathbf{r}) \times \mathbf{E}_{\text{scat},m}(\mathbf{r}) \right\} r \cdot d\mathbf{l}. \quad (4.29)$$

In the above equations, $d\mathbf{l}$ is a differential line element over Γ_1 pointing in a direction normal to Γ_1 .

Therefore, cylindrically symmetric objects need less computational costs for the FEM calculation of the scattered field but also for the posterior evaluation of Eqns. (4.21) and (4.22). The implementation of the multipole decomposition of the field scattered from a cylindrically symmetric object is performed using the cylindrically symmetric setup of the FEM solver [229]. To test the implementation, we compute the decomposition for a core-multi-shell sphere illuminated by a plane wave. As for the case of the homogeneous sphere, analytical expressions exist for the amplitudes of the multipole decomposition of such structures [246]. The convergence test for the error of the decomposition with respect to the mesh side length is shown in Fig. 4.8. The details of the simulation are described in the caption of the figure. As it can be seen, the error follows a similar power law as in the case of the three dimensional test.

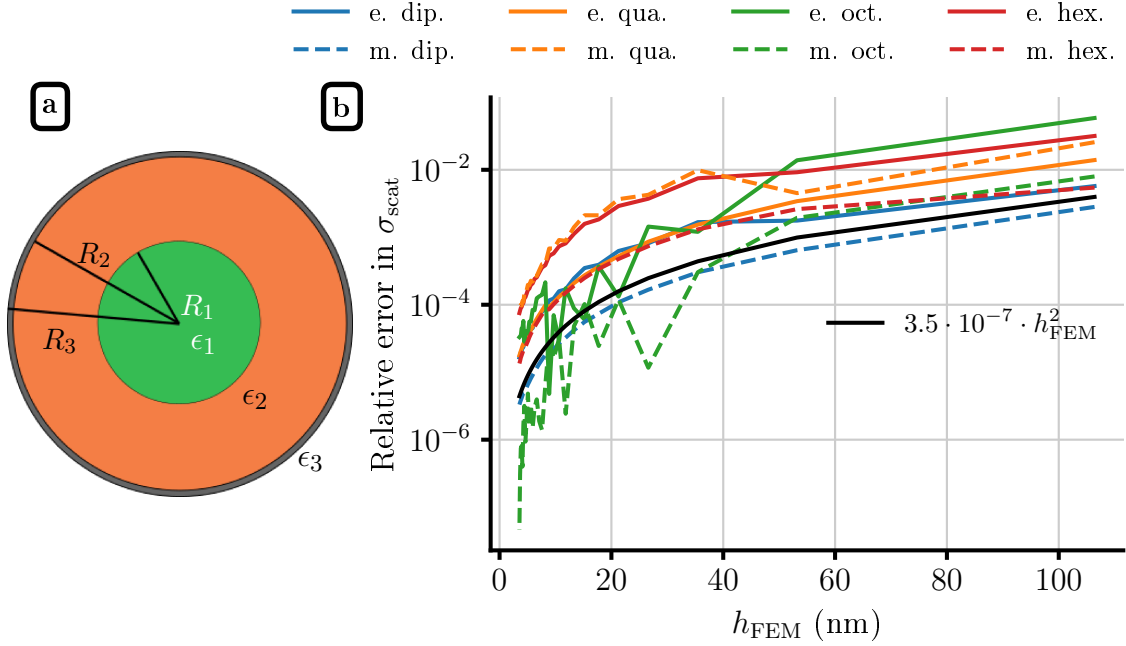


Figure 4.8: Convergence test of the multipole decomposition for a core-multi-shell sphere illuminated by a plane wave. The core-multi-shell sphere is composed of three concentric spheres with radii 100 nm, 200 nm, and 205 nm. Their permittivities are 6.25, 12.25, and $-24.84+4i$ respectively. The wave vector of the plane wave is oriented in the z -direction. The plane wave has a wavelength of 532 nm and its electric field is polarized in the x -direction with an amplitude of 1 V/m. The mesh size of each sphere corresponds to $\lambda \cdot h_{\text{FEM}}$, being λ the corresponding wavelength of the field in each material.

In a second example, the scattering cross section of a core-multi-shell disk composed of three different materials is calculated. The scatterer is illuminated with a circularly polarized plane wave. In this example, the computed multipoles were transformed from the base of electric and magnetic multipoles to the helicity base [222]. As it can be seen, at a wavelength of 1200 nm the disk only scatters light of pure helicity. The details of the geometry of the core-multi-shell disk are given in the caption of Fig. 4.9. Thanks to the reduction in memory and computation effort obtained by the cylindrical setup, the results for 100 different spectral points could be obtained in less than 30 seconds, running 20 simulations in parallel. Note that, because the disk is composed of more than one material, the extended boundary condition method could not be applied to this structure.

We have successfully applied the cylindrical setup of the FEM multipole decomposition in different research fields [A7–A9].

4.3 Calculation of the T-matrix

Description

As already commented in the introduction of the chapter, the T-matrix is a fundamental tool to analyze the interaction of light with isolated scatterers. It provides the field

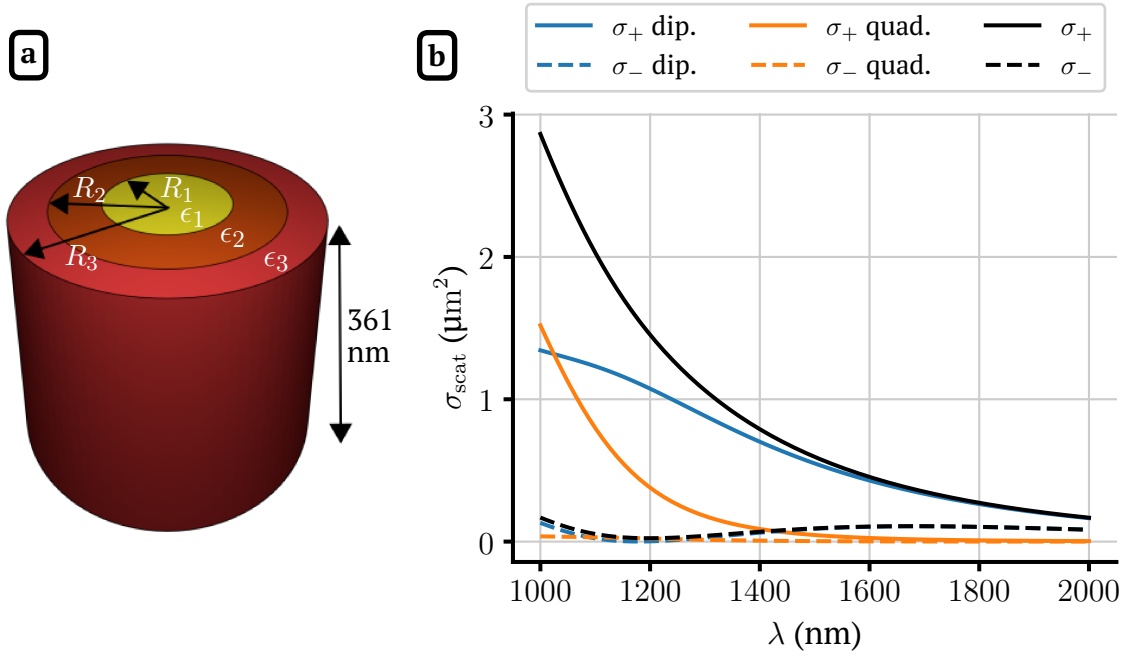


Figure 4.9: Scattering cross section of a core-multi-shell disk decomposed into the fields scattered with both helicities. The disk is illuminated with a right circularly polarized plane wave with an amplitude of 1 V/m. The wave vector of the plane wave is oriented in the $+z$ -direction. The object is composed of three concentric disks with the same height, 361 nm, and radii 157.9 nm, 284.8 nm, and 375 nm. Their corresponding permittivities are 3.61, 11.16, and 4.84, respectively.

radiated by an object for any given illumination field,

$$\mathbf{E}_{\text{scat}} = \underline{T}\mathbf{E}_{\text{inc}}. \quad (4.30)$$

In the most common case used in the T-matrix formalism, both fields, the scattered and the illumination field, \mathbf{E}_{inc} , are expanded into VSWFs. This implies that the vectors in Eqn. (4.30) contain the coefficients of the multipole expansions of the scattered and illumination fields. In principle, the multipole expansion contains an infinite number of multipoles, but in a practical implementation only a finite number of multipoles up to a certain multipole degree n_{max} is considered,

$$\mathbf{E}_{\text{scat}}(\mathbf{r}) = \sum_{n=1}^{n_{\text{max}}} \sum_{m=-n}^n a_{m,n} \mathbf{N}_{m,n}^{(3)}(\mathbf{r}) + b_{m,n} \mathbf{M}_{m,n}^{(3)}(\mathbf{r}), \quad (4.31)$$

$$\mathbf{E}_{\text{inc}}(\mathbf{r}) = \sum_{n=1}^{n_{\text{max}}} \sum_{m=-n}^n c_{m,n} \mathbf{N}_{m,n}^{(1)}(\mathbf{r}) + d_{m,n} \mathbf{M}_{m,n}^{(1)}(\mathbf{r}). \quad (4.32)$$

The cutoff value n_{max} is determined by the value of the admissible error in the expansion. The most general ordering convention of the expansion coefficients in the vectors \mathbf{E}_{scat} and \mathbf{E}_{inc} sets the position of the coefficients following an ascending order based on the values of the multipole order m and multipole degree n with m as the leading index,

$$\mathbf{E}_{\text{scat}} = [a_{-1,1}, a_{0,1}, a_{1,1}, a_{-2,2}, \dots, a_{n_{\text{max}}, n_{\text{max}}}, b_{-1,1}, \dots, b_{n_{\text{max}}, n_{\text{max}}}]^T. \quad (4.33)$$

A method to compute the T-matrix of scatterers with complex geometries using the finite element method was proposed in [222]. The method uses a series of plane wave illuminations to establish a link between the radiated and illumination VSWFs. This work follows a similar procedure to compute the T-matrix. However, instead of illuminating the object with different plane waves, the object is illuminated directly with the regular VSWFs contained in the expansion of \mathbf{E}_{inc} , as it was proposed in [218]. Then, the scattered field is decomposed into the VSWFs using the implementation described in this chapter. This allows to directly obtain one column of \underline{T} for each illumination used.

Example: Design of dual cylinders

There are many different quantities that can be directly obtained from the entries of the T-matrix. Examples are the scattering and extinction cross sections of the particle averaged with respect to all the orientations of an illuminating plane wave (see, e.g., [42] sections 5.2-5.3) or the duality breaking of the particle [213], \mathcal{D} . Such quantities are important when computing experimentally observables quantities in strongly diluted samples of a larger number of identical scatterers.

Concerning the latter property, it remains to be mentioned that a scatterer is dual, i.e. $\mathcal{D} = 0$, when the field that it scatters preserves the helicity in the scattering process independent of the exact details of the illumination field [247, 248]. A direct implication is that, when illuminated with a plane wave of well defined handedness, the scattered field can be decomposed into plane waves of the same handedness. In the previous section we saw how a core-multi-shell disk produces a scattered field of pure helicity when illuminated with a circular polarized plane wave coming from a specific direction. If the disk were dual, it would present the same behavior for any direction of the incident plane wave.

One very interesting property of dual scatterers with a $2\pi/n$ discrete rotational symmetry with $n \geq 3$ is that they do not produce backscattering when they are illuminated with a plane wave when the \mathbf{k} vector is parallel to the symmetry axis of rotation [249]. That means that if one creates a periodic grating with a squared lattice and such a dual scatterer as the periodic unit cell, the grating will have zero back reflections, independently of the periodicity length of the grating. These gratings can be used, for example, to reduce the reflectance of solar cells, as discussed in [250].

To compute the duality breaking of a scatterer, one first needs to convert the T-matrix from the parity basis of electric and magnetic VSWF to the basis of VSWF of pure helicity, \underline{T}^{\pm} . The VSWF of pure helicity have been described in section 2.2. The basis of the T-matrix can be easily changed applying the following transformation [222],

$$\underline{T}^{\pm} = \begin{bmatrix} \underline{T}^{++} & \underline{T}^{+-} \\ \underline{T}^{-+} & \underline{T}^{--} \end{bmatrix} = \frac{1}{2} \begin{bmatrix} \mathbb{I} & \mathbb{I} \\ \mathbb{I} & -\mathbb{I} \end{bmatrix} \underline{T}^{\text{em}} \begin{bmatrix} \mathbb{I} & \mathbb{I} \\ \mathbb{I} & -\mathbb{I} \end{bmatrix} \quad (4.34)$$

being \mathbb{I} the identity matrix and $\underline{T}^{\pm\pm}$ the submatrices that link the scattering VSWFs with helicity given by the first superscript with the illumination VSWFs with helicity given by the second superscript. In the helicity basis, the duality breaking can be obtained as,

$$\mathcal{D} = \frac{\sum_{\forall i,j} |T_{[i,j]}^{+-}|^2 + \sum_{\forall i,j} |T_{[i,j]}^{-+}|^2}{\sum_{\forall i,j} |T_{[i,j]}^{\pm}|^2}. \quad (4.35)$$

\mathcal{D} is bounded between 0 and 1. When \mathcal{D} equals 0, the scatterer is perfectly dual, as no cross-coupling can occur between illumination and scattered fields of opposite helicity. This comes clear looking at Eqn. (4.35). \mathcal{D} is 0 if and only if all the cross-coupling terms $T_{[i,j]}^{+-}$ and $T_{[i,j]}^{-+}$ are 0. On the opposite extreme, a scatterer that would present a duality breaking of 1 would scatter light with opposite helicity to the one of the illumination for any given illumination which is a pure state of the helicity operator.

Regarding the existence of scatterers that present the extreme behaviors of $\mathcal{D} = 0$ or $\mathcal{D} = 1$, it has not been shown that an object with a duality breaking of 1 can exist. Scatterers that can scatter light of pure helicity and opposite to that of the illumination have been shown [251]. However, there this behavior occurs only for specific illuminations. On the other hand, it is possible to obtain scatterers that are dual at certain frequencies [252]. Figure 4.10 shows one of such scatterers. The frequency dependence of the duality breaking for a core-shell disk, sketched in Fig. 4.10a, is shown in Fig. 4.10b. The core-shell disk has been designed to minimize the duality breaking for a wavelength of 1550 nm. The material and geometrical parameters of the disk are shown in the caption of the figure. As one can see, the duality breaking presents a minimum close to 0 at a wavelength of 1550 nm. To be precise, it amounts only to $\mathcal{D} = 0.001$.

To obtain the dual core-shell disk, we combined the cylindrical symmetric setup for the multipole decomposition to compute the T-matrix together with the optimization technique presented in chapter 3.

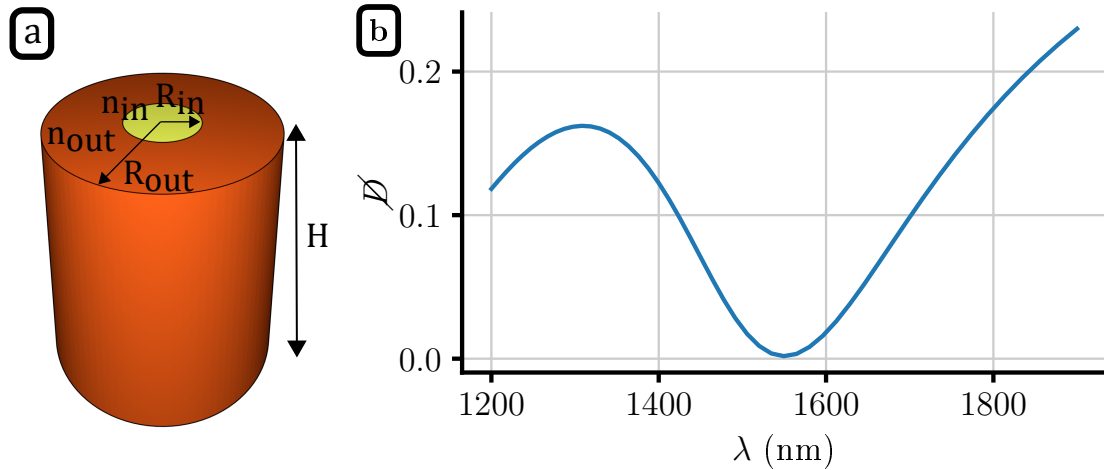


Figure 4.10: **a.** Sketch of the considered core-shell disk. Its geometrical parameters are $R_{in} = 111$ nm, $R_{out} = 237$ nm, and $H = 431$ nm. The core and the shell are made of materials with nondispersive permittivities of $\epsilon_{in} = 10.63$ and $\epsilon_{out} = 5.3$. **b.** Wavelength dependency of the duality breaking, \mathcal{D} , of the optimal core-shell disk around the central wavelength of 1.55 μm .

The implementation to compute the T matrices was also used in other different applications, as to enhance the sensing of chiral molecules using nano disks [A8], or for the calculation of the T-matrices of helices [A10] to analyze the link between proposed measures of geometrical chirality and different electromagnetic quantities as the circular dichroism [253, 254] or the electromagnetic chirality [247].

4.4 Calculation of shape and material derivatives for T-matrices

The T-matrix is used to compute different electromagnetic quantities of single scatterers and it is a point of departure to study the optical response from clusters of scatterers. For this reason, if one aims to design a scatterer for a specific application, the T-matrix of the scatterer would often be involved in the calculation of the objective function. In this context, having access to the derivatives of the T-matrix with respect to the design parameters is of great value in the optimization process.

The procedure to calculate the shape derivatives of the VSWF expansion is not different to the general procedure described in Section 2.3. Once the derivatives of the scattered field with respect to a design parameter x_i are obtained, it is only necessary to propagate them to obtain the derivatives of the expansion coefficients $a_{m,n}$ and $b_{m,n}$. Taking as an example the expression for the decomposition of the electric VSWF, Eqn. (4.21), one gets,

$$\frac{da_{m,n}}{dx_i} = -ik \int_{\Gamma_1} \left\{ \left(\nabla \times \frac{d\mathbf{E}_{\text{scat}}(\mathbf{r})}{dx_i} \right) \times \mathbf{N}_{m,n}^{(1)*}(\mathbf{r}) - k\mathbf{M}_{m,n}^{(1)*}(\mathbf{r}) \times \frac{d\mathbf{E}_{\text{scat}}(\mathbf{r})}{dx_i} \right\} \cdot d\mathbf{S}. \quad (4.36)$$

The derivatives for the magnetic VSWFs follow a similar expression.

Therefore, to obtain the derivatives of the multipole decomposition, one just needs to calculate the multipole decomposition of the derivatives of the scattered field.

The FEM solver JCMSuite [58] has already been able to compute the field derivatives $d\mathbf{E}_{\text{scat}}/dx_i$ and it performs similar calculations to Eqn. (4.36) to compute other surface integral quantities, such as the total power radiated by a scatterer. Because of those reasons, once the multipole expansion was implemented into the solver, it was only necessary to apply a small change to the existing code to calculate the shape and material derivatives of the expansion.

To test the implementation, the material derivative of the T-matrix of a core-multi-shell sphere is computed. The schematic of the sphere is shown in Fig. 4.11a. Figure 4.11b shows the derivatives of one of the T-matrix entries with respect to the permittivity of the intermediate shell, ϵ_2 . The entry corresponds to the scattered coefficient $a_{2,2}$ when it is illuminated with the VSWF $\mathbf{N}_{2,2}^{(1)}(\mathbf{r})$. The results are compared with the analytical values obtained from Mie theory [246].

To compute the scattered field, a three dimensional FEM model was used. The maximum side length of the FEM discretization was $\lambda/10$ and the FEM polynomial order was three. The details of the core-multi-shell sphere are described in the caption of Fig. 4.11. As it can be seen in the figure, the results agree up to the numerical precision of the FEM simulations.

The core-multi-shell sphere is a good test example as there is a well known analytical solution to compare with. However, the FEM based implementation is capable of much more general structures. To test the derivatives with a more interesting case, a second test is done for a silicon helix. The helix is made from a wire with a thickness of 40 nm, a pitch of 80 nm, and it has two turns. Figure 4.12a shows a schematic of the structure. For the test, the helix is illuminated with the VSWF $N_{-1,1}^1(\mathbf{r})$ at a vacuum wavelength of 550 nm. The shape derivative of the T-matrix entry $T_{1,1}$ with respect to the major radius of the helix, R_h , is calculated for different values of R_h . The results are shown in

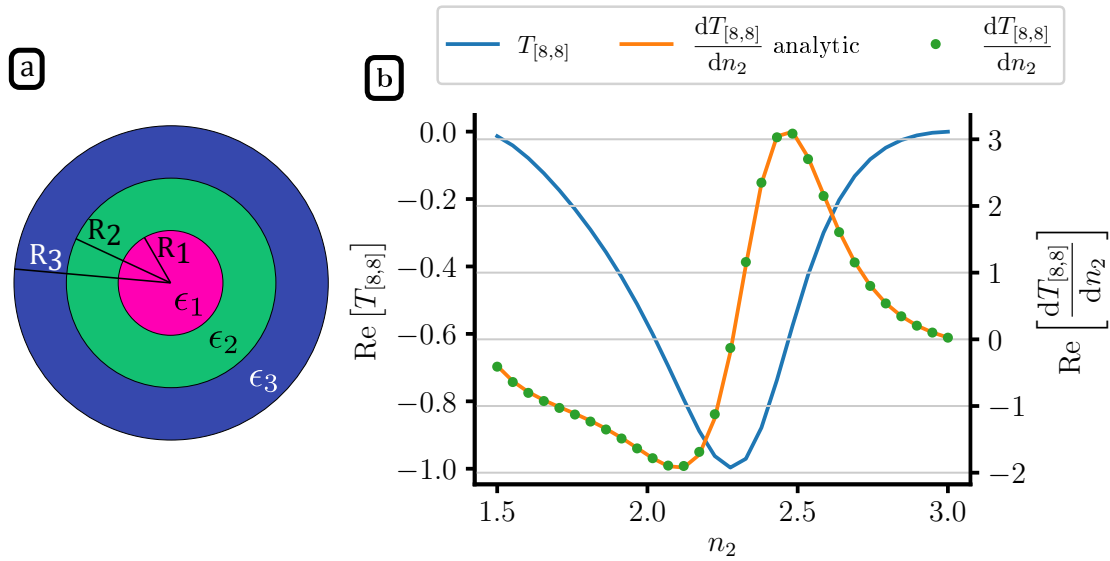


Figure 4.11: **a.** Schematic of the considered core-multi-shell sphere used to test the implementation of the material derivatives of the T-matrix. The core-multi-shell sphere is composed of three concentric spheres with radii 100 nm, 200 nm, and 300 nm respectively. The permittivities ϵ_1 and ϵ_2 are 12.25 and 6.25 respectively. **b.** Material derivative of one of the entries of the T-matrix with respect to the permittivity of the intermediate layer of a core-multi-shell sphere. The entry of the T matrix corresponds to the scattering coefficient $a_{2,2}$ when the sphere is illuminated with the field $N_{2,2}^{(1)}(\mathbf{r})$.

Fig. 4.12. As there are no analytical results for the multipole decomposition of complex structures such as helices available, the derivatives using the direct method were compared with the results obtained from finite difference calculations. As for the case of the core-multi-shell sphere, the results of both methods agree up to a certain precision of the FEM simulation. Note that the results obtained using finite differences do not just require an extra simulation per parameter but they are also less accurate than the ones obtained using the direct method.

4.5 The adjoint method for multi-scattering problems

Description

One of the most relevant applications of the T-matrix is the calculation of the scattered field from clusters composed of many scatterers. Among other applications, the method allows to rigorously solve the response of metalenses or the propagation of light through aperiodic photonic crystals.

Finding the optimal shape or material properties of each of the scatterers to increase the performance of the entire multi particle system, is generally a high dimensional optimization task. In this task, having access to the derivatives of the objective function with respect to the shape or material parameters of the scatterers can drastically improve the convergence of the optimization.

In the previous section, an implementation for computing shape and material derivatives of T-matrices of complex scatterers was described and tested. This numerical method

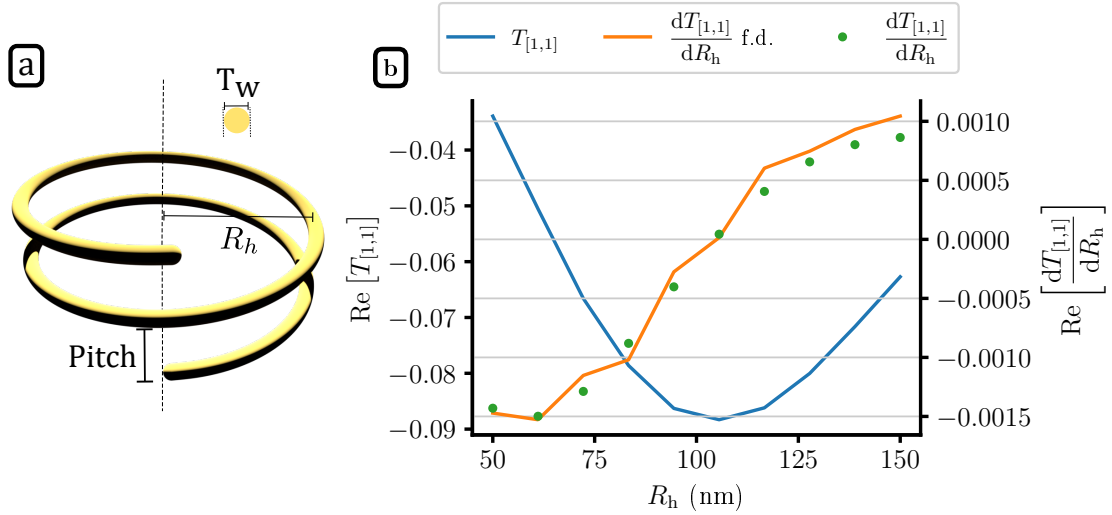


Figure 4.12: **a.** Schematic of the helix used for computing the shape derivatives of the multipole decomposition. The helix is made from a wire with a thickness, T_w , of 40 nm and a pitch of 80 nm. Its refractive index is 3.5. **b.** Derivatives of one of the entries of the T-matrix with respect to the major radius of the helix, R_h . The entry of the T-matrix links the scattering and illumination coefficients $a_{-1,1}$ and $c_{-1,1}$ respectively. The illumination wavelength is 550 nm.

can be used, in combination with a multi-scattering solver, to obtain the derivatives of an objective function that depends on the field scattered by the entire system. The procedure to achieve this consists in combining the multi-scattering formalism with the direct or adjoint methods. Both methods were presented in section 2.3. In multi-scattering problems with clusters composed of a large number of particles, the adjoint method is frequently used due to the large number of design parameters [255].

To describe the implementation of the adjoint method in multi-scattering problems, the multi-scattering formalism must be presented obviously at first.

Let us consider a system composed of a number of N scatterers, specified by their T-matrices \underline{T}_i . The multipole expansion of the field scattered by the scatterer i can be represented by a vector $\mathbf{E}_{\text{scat},i}$. As described in section 4.3, the T-matrix establishes a relation between the field that illuminates the scatterer i , $\mathbf{E}_{\text{inc},i}$, and the corresponding scattered field,

$$\mathbf{E}_{\text{scat},i} = \underline{T}_i \mathbf{E}_{\text{inc},i}. \quad (4.37)$$

In a system with many objects, the field scattered by each object partially illuminates all the other objects. Therefore, the scattered field produced by each object is not only produced by the external illumination as considered up to that point, but also as a response to the fields scattered by the other scatterers. Denoting by $\mathbf{E}_{\text{inc},i,0}$ the external illumination on the scatterer i , one can write the total field illuminating a scatterer as

$$\mathbf{E}_{\text{inc},i} = \mathbf{E}_{\text{inc},i,0} + \sum_{j \neq i} \mathbf{E}_{\text{inc},i,j}, \quad (4.38)$$

where $\mathbf{E}_{\text{inc},i,j}$ denotes the illumination field on the i -th particle due to the field scattered from the j -th particle.

The link between the scattering and the illumination fields of the different scatterers can be calculated using the translation theorems of the VSWF [42, 256, 257]. The translation coefficients allow to construct the transformation matrices between the scattered and the illumination fields, $\underline{M}_{i,j}$,

$$\mathbf{E}_{\text{inc},i,j} = \underline{M}_{i,j} \mathbf{E}_{\text{scat},j}. \quad (4.39)$$

Once matrices $\underline{M}_{i,j}$ are obtained using the translation theorems, the equations describing the whole system can be easily obtained. Denoting by \mathbf{E}_{scat} the vector expanding the scattered fields from all the particles

$$\mathbf{E}_{\text{scat}} = [\mathbf{E}_{\text{scat},1}^T, \mathbf{E}_{\text{scat},2}^T, \dots, \mathbf{E}_{\text{scat},N}^T]^T, \quad (4.40)$$

the system reads as

$$\underline{SM} \mathbf{E}_{\text{scat}} = \mathbf{E}_{\text{scat},\text{inc}}, \quad (4.41)$$

where $\mathbf{E}_{\text{scat},\text{inc}}$ denotes the scattered field due to the external illumination, i.e., without considering the multiple interactions between the different scatterers,

$$\mathbf{E}_{\text{scat},\text{inc}} = \begin{bmatrix} \underline{T}_1 \mathbf{E}_{\text{inc},1,0} \\ \underline{T}_2 \mathbf{E}_{\text{inc},2,0} \\ \underline{T}_3 \mathbf{E}_{\text{inc},3,0} \\ \vdots \\ \underline{T}_N \mathbf{E}_{\text{inc},N,0} \end{bmatrix}, \quad (4.42)$$

and \underline{SM} is the system matrix

$$\underline{SM} = \begin{bmatrix} \mathbb{I} & -\underline{T}_1 \underline{M}_{1,2} & -\underline{T}_1 \underline{M}_{1,3} & \dots & -\underline{T}_1 \underline{M}_{1,N} \\ -\underline{T}_2 \underline{M}_{2,1} & \mathbb{I} & -\underline{T}_2 \underline{M}_{2,3} & \dots & -\underline{T}_2 \underline{M}_{2,N} \\ \vdots & & & & \vdots \\ -\underline{T}_N \underline{M}_{N,1} & -\underline{T}_N \underline{M}_{N,2} & -\underline{T}_N \underline{M}_{N,3} & \dots & \mathbb{I} \end{bmatrix}. \quad (4.43)$$

The solution of the above system gives the total scattered field. Once this system is obtained, the implementation of the adjoint system requires mainly one more fundamental step: the calculation of the partial derivatives of the objective function with respect to the values of the solution \mathbf{E}_{scat} . For this process, it is recommended to use software for automatic differentiation [258, 259], especially for complicated objective functions of \mathbf{E}_{scat} . After this step, one can solve the adjoint system,

$$\underline{SM}^\dagger \lambda = \frac{df_{\text{ob}}}{d\mathbf{E}_{\text{scat}}}. \quad (4.44)$$

Note that here λ is used to denote the adjoint solution and not the wavelength. In the context it is used here, no confusion should appear.

Finally, the calculation of the derivatives of the objective function with respect to some parameter x_i describing the geometry or material of one or more scatterers can be performed. This calculation is equivalent to the one described in Eqn. (2.103) for the FEM,

$$\frac{df_{\text{ob}}}{dx_i} = \lambda^T \left(-\frac{dSM}{dx_i} + \frac{d\mathbf{E}_{\text{scat,inc}}}{dx_i} \right) \quad (4.45)$$

The term $\frac{dSM}{dx_i}$ is obtained using the shape or material derivatives of the individual T-matrices for the single scatterers and applying the chain rule.

Example: metasurface hologram

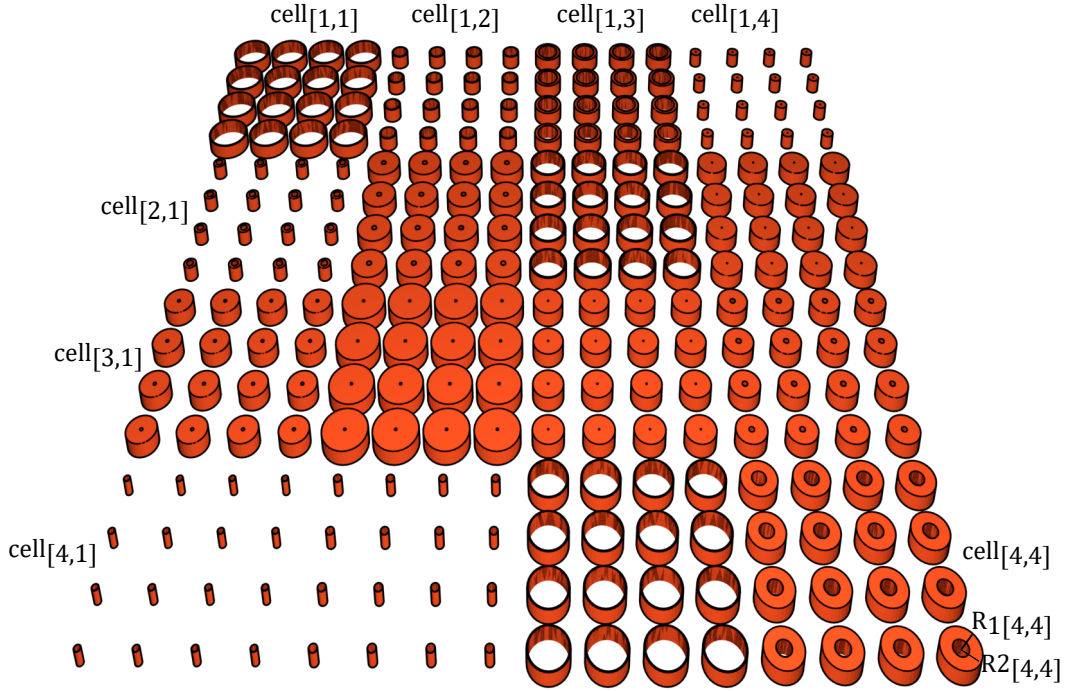


Figure 4.13: Schematic of the hologram used to test the adjoint method. The hologram is composed of a grid of 4 x 4 pixels placed along the plane $z = 0$. Each pixel is composed of a grid of 4 x 4 identical scatterers. The scatterers are disks with a hole in the center. The height of the disks is 300 nm for all the pixels. The disks are made from silicon and they are embedded in a homogeneous medium with a refractive index of 1.44. The refractive index of the disks is 3.6. The inner radii of the disks are $R_1 = [580, 242, 323, 8; 96, 71, 498, 14; 39, 30, 15, 70; 73, 96, 477, 183]$ nm, where the semicolon denotes the beginning of a new row. The outer radii are $R_2 = [601, 265, 426, 174; 175, 502, 533, 443; 397, 601, 412, 411; 80, 99, 497, 467]$ nm.

The adjoint method for the design of multi particle systems was implemented in Matlab. However, the implementation has not yet been integrated together with a package for performing automatic differentiation. To test the implementation, the shape derivatives of the far-field produced by a small metasurface hologram are computed. The metasurface is composed of a 4 x 4 pixel board. Each pixel is composed of a 4 x 4 periodic arrangement of identical scatterers. The scattering elements of each pixel are silicon disks of height 300 nm that have a hole in the center, as shown in Fig. 4.13. The disks of each pixel are described by an inner and an outer radius. The refractive index of the silicon was considered to be 3.6 for an illumination wavelength of 1550 nm. The embedding medium is

considered to have a refractive index of 1.44.

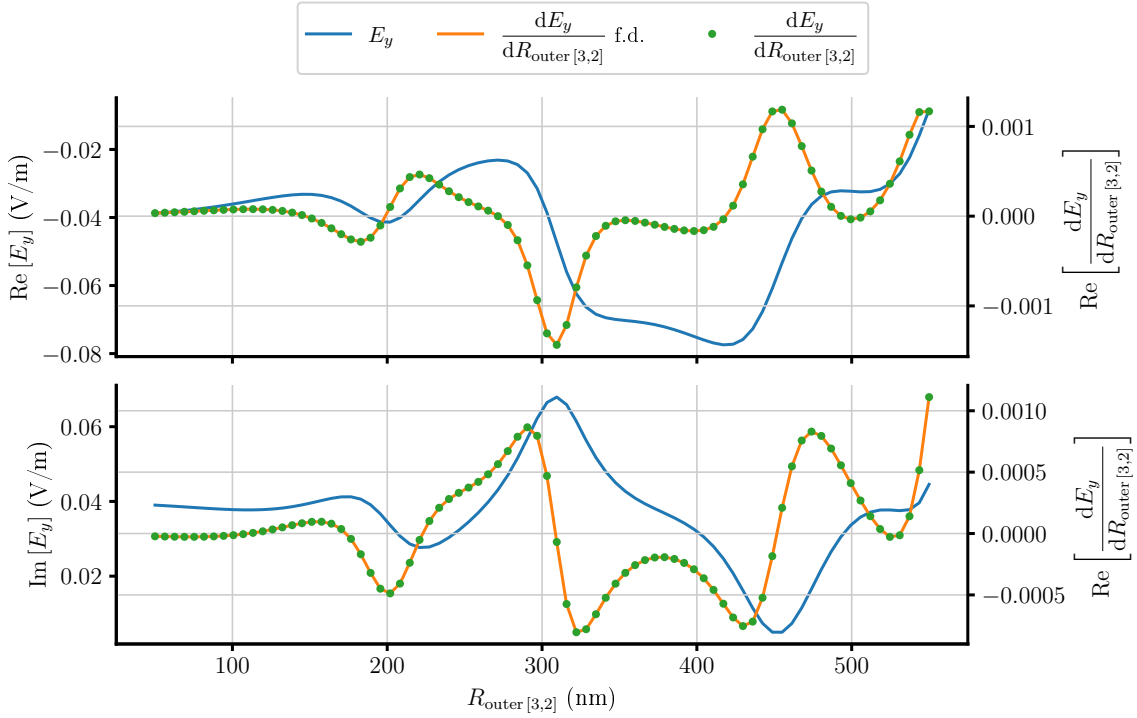


Figure 4.14: Amplitude of the scattered field produced by the hologram described in Fig. 4.13 when it is illuminated by a plane wave. The derivatives of the scattered field are computed with respect to the outer radius of the disks of the pixel [3,2]. The illuminating plane wave has a wave vector oriented along the $-z$ -direction. Its electric field is linearly polarized in the x -direction. The vacuum wavelength of the plane wave is 1550 nm. The amplitude of the scattered field is measured at the point $(0,0,-100\lambda_0)$.

For this test example, the objective function consists of the value of the electric field in a point $\mathbf{x}_{\text{probe}}$ placed 100 wavelengths away from the metasurface, at the point $(0,0,-100\lambda_0)$. The adjoint method was used to compute the derivative of the electric field with respect to the outer radius of the disks of the pixel [3,2]. The results obtained are shown in Fig. 4.14 for different values of the radius. The shape derivatives computed with the adjoint method are compared with results obtained using finite differences. As shown in the figure, the results of both methods are in agreement. The T-matrices of the individual scatterers contain the multipole contributions up to the second, i.e. quadrupolar, order. This results in a system matrix \underline{SM} with a size of 4096 x 4096.

The combination of a multi-scattering solver, the calculation of shape derivatives of individual T-matrices and the adjoint method can be used to design complex multiparticle structures. In the case of metasurface holograms, the method could be used to rigorously calculate the field obtained in the image plane and to design the shape of the scatterers within each pixel. With this method one could design a hologram that creates the desired image, taking into account all the interactions between the scatterers. Of special interest are the interactions between the scatterers of different pixels [260], which when not taken into account, produce undesired effects. However, to solve practical systems, containing a large number of elements, it is necessary to implement an iterative solver for the systems given by Eqns. (4.41) and (4.44) [220]. The reason for that is the quadratic scaling of the system matrix with the number of scatterers, that makes even the storage

of the system matrix in the computer memory impossible.

4.6 Conclusions

This chapter described different numerical implementations of relevance for the analysis and design of isolated scatterers. The main result, the expressions to decompose scattered fields into a VSWF basis using surfaces with general shapes, gave rise to a series of tools that have been implemented into a FEM solver. These tools include a method to obtain the multipole decomposition of complex geometries and the calculation of their T-matrices. Of special interest in the context of the design of photonic devices is the implementation of shape and material derivatives for the T-matrices of complex scatterers. These shape derivatives are not only useful for the design of isolated scatterers, but they can also be combined with multi-scattering solvers and with the use of the adjoint method to help in the design of systems composed of a large number of scatterers. Examples are metasurface holograms, metalenses or aperiodic photonic crystals. This method has been described and its implementation was tested. However, to obtain a more powerful tool, further improvements must be done, as the use of an iterative solver for linear systems and the use of automatic differentiation to calculate complex objective functions.

5 | Application examples

The previous chapters introduced different numerical methods to optimize the design of photonic structures. This chapter is devoted to such design task. We present here the design of two optimal photonic structures: electromagnetic chiral scatterers and waveguide edge couplers. Both structures are of interest from different perspectives. Maximal electromagnetic chiral scatterers present an extraordinary behavior with respect to their interaction with circularly polarized plane waves of different handedness. In this context, we want to study in more detail what can be the frequency range that can support such extreme structures. The second type of structures studied, waveguide edge couplers, are an important component for the interconnection of different photonic elements in photonic integrated circuits. The design of efficient and compact edge couplers is required to the implementation of photonic circuits that will enable the next generation of optical data networks.

The chapter is structured in two main sections, each of them corresponds to the design of each of the two mentioned photonic structures. In each section, we first introduce the structure, explain the main physical concepts related to it, and the relevance of its optimized design. After that, we present the optimization methodology used to design it, and we analyze the performance of the designs obtained.

5.1 Maximal electromagnetic chiral helices

Introduction

One of the applications for the previously established methods is the optimization of electromagnetically chiral objects. Here, the term *chirality* was first introduced in 1892 by Lord Kelvin [261]. He suggested that an object is said to be chiral if it can not be superimposed onto any mirror image of itself by applying any combination of rotations and translations. If the object can be superimposed onto its mirror image, it is said to be achiral.

Chiral objects are present in many different fields of science. Many molecules are chiral, and they often exist as a pair of mirror images, called enantiomers. The enantiomers have exactly the same physical properties except in their interaction with other chiral objects, such as other chiral molecules or, in the context of photonics, when interacting with chiral states of light. In biology, most of the fundamental building blocks of life are chiral, including many carbohydrates and amino-acids [262]. As chiral molecules react differently with other chiral objects, a pair of enantiomers can cause completely different actions on living organisms. For example, the molecule that limes lemons and oranges their odor is a specific enantiomer of limonene while the opposite enantiomer smells like pines [263]. Similarly, the interaction of a chiral molecule, or a chiral object in general, with light depends as well on the handedness of the illumination. This effect has multiple

applications, e.g., as a mechanism for chiral sensing of molecules [242, A7, A8, 253, 264–268], to trigger the production of different enantioselective reactions [269–271], or to implement polarization filters [272].

If one aims to engineer an object that maximizes the difference in its interaction with light of different handedness, one might think that designing a maximally chiral object would be a good design strategy. However, the first problem with this approach is that chirality is a binary property, and it has been shown that no rigorous method to quantify chirality exists [273]. Different measures of chirality have been proposed, see for example [274]. However, all of them lead to some inconsistency. For example, it could be shown that any tetrahedron can be defined as the most chiral one, even though it is only incrementally different from an achiral tetrahedron [275]. Based on the fact that a chiral object interacts differently with light of different handedness, a measure of electromagnetic chirality, χ , that mitigates some of these limitations has been recently proposed [213]. Here, the emphasis should be put on electromagnetic chirality instead of chirality only, as it measures how different the object responses to electromagnetic radiation of different chirality, or more precise helicity. The measure assigns a certain frequency dependent value, χ , to the object based on the interaction of the object with all possible illumination fields of different helicity. This definition of the electromagnetic chirality, which we will denote as em-chirality from now on, is compatible with the geometrical definition of chirality. An achiral object will always present a vanishing χ value for all illumination frequencies. The link between the em-chirality and other electromagnetic quantities, such as circular dichroism [276] and one of the proposed measures for the geometrical chirality has been numerically studied in [A10].

One interesting property of the em-chirality is that it is upper bounded by the total interaction cross section of the particle. This characteristic allows for the definition of a normalized measure of the em-chirality, $\bar{\chi}$. If an object is maximally em-chiral, i.e. if its $\bar{\chi}$ is equal to 1, the object is invisible to any illumination that is a pure state of one of the two eigenstates of the helicity operator ([277] chapter 8). Such extreme objects could be used in very interesting applications. For example, in an angle independent polarization filter, as was proposed in [213], or for sensing schemes of chiral molecules.

The concept of maximally chiral objects with a $\bar{\chi}$ value close to 1 has been studied in the literature. A silver helix with a $\bar{\chi}$ higher than 0.9 has been reported at a wavelength of 200 μm [213]. Also, there are different design rules for obtaining such objects using ideal perfect electric conductors of an extremely thin thickness [278]. However, it is not clear if similar results can be achieved at optical frequencies or in the near infrared.

This section presents the design of optimal silver helices with respect to their $\bar{\chi}$ value. The aim of the work is to find out if it is possible to obtain objects that present high values of $\bar{\chi}$ in different regions of the infrared and optical spectrum. To do that, the work combines different optimization and numerical methods presented within this thesis, such as Bayesian optimization, the method to calculate the T-matrices of complex structures, and the calculation of the shape derivatives of the multipole decomposition.

The reason for using helices as the geometry to be optimized is based on existing results that show that helices present strong differences in their interaction with plane waves of different handedness [272, 278–281, A11]. Also, the optimization of a helix is a simpler task than the optimization of more complex freeform wires, where one needs to impose complicated constraints to avoid self-intersections. Regarding the use of silver as material, we chose it for a few reasons: One reason is that the simulations for the high em-chiral helix at the infrared reported in [213] used silver as material. Also, silver has been reported to be a better material to sustain magnetic resonances at optical fre-

quencies [282]. This effect was also supported by some preliminary simulations that we made at optical frequencies using gold helices, that showed lower em-chiral responses than similar silver helices.

In the following subsections, first the definition of $\bar{\chi}$ is formally introduced. After that, the numerical procedure to perform the optimization is described. Finally, the last subsection presents the optimization results and analyzes the optimal helices. The work and results presented in this section correspond mainly to the results contained in [A12].

Electromagnetic chirality

The definition of the electromagnetic chirality [213] of an object, χ , is based on the measure of the interaction of the scatterer with fields of different helicity. To obtain χ , one needs to first obtain the S-matrix characterizing the scatterer in a basis of VSWFs of pure helicity

$$\begin{bmatrix} \mathbf{G}_{-1,1}^{3,+} \\ \vdots \\ \mathbf{G}_{n_{\max},n_{\max}}^{3,+} \\ \mathbf{G}_{-1,1}^{3,-} \\ \vdots \\ \mathbf{G}_{n_{\max},n_{\max}}^{3,-} \end{bmatrix} = \underline{S}^{\pm} \begin{bmatrix} \mathbf{G}_{-1,1}^{1,+} \\ \vdots \\ \mathbf{G}_{n_{\max},n_{\max}}^{1,+} \\ \mathbf{G}_{-1,1}^{1,-} \\ \vdots \\ \mathbf{G}_{n_{\max},n_{\max}}^{1,-} \end{bmatrix} = \begin{bmatrix} \underline{S}^{++} & \underline{S}^{+-} \\ \underline{S}^{-+} & \underline{S}^{--} \end{bmatrix} \begin{bmatrix} \mathbf{G}_{-1,1}^{1,+} \\ \vdots \\ \mathbf{G}_{n_{\max},n_{\max}}^{1,+} \\ \mathbf{G}_{-1,1}^{1,-} \\ \vdots \\ \mathbf{G}_{n_{\max},n_{\max}}^{1,-} \end{bmatrix}. \quad (5.1)$$

The S-matrix of an object can be obtained from its T-matrix by $\underline{S}^{\pm} = \mathbb{I} + 2\underline{T}^{\pm}$. The T-matrix was introduced in section 4.3 and both the scattering, $\mathbf{G}_{m,n}^{3,\pm}$, and illumination, $\mathbf{G}_{m,n}^{1,\pm}$, vector spherical wave functions of pure helicity were introduced in section 2.2.

Once the S-matrix is obtained, one has to calculate two vectors, \mathbf{v}^+ and \mathbf{v}^- , obtained from the singular values of the block elements of the S-matrix, $\underline{S}^{\pm,\pm}$

$$\mathbf{v}^+ = \begin{bmatrix} \text{svd}(\underline{S}^{+,+}) \\ \text{svd}(\underline{S}^{-,+}) \end{bmatrix} \quad \mathbf{v}^- = \begin{bmatrix} \text{svd}(\underline{S}^{-,-}) \\ \text{svd}(\underline{S}^{+,-}) \end{bmatrix}. \quad (5.2)$$

The summation of the squared entries of the two vectors gives the total interaction cross section of the scatterer [213]

$$\sigma_{\text{int}} = \sum_i v_{[i]}^{+2} + v_{[i]}^{-2}, \quad (5.3)$$

which is linked to the rotationally averaged total scattering cross section of the object ([42] Eqn. 5.140).

The definition of χ is given by the distance between the vectors \mathbf{v}^+ and \mathbf{v}^- ,

$$\chi = \sqrt{\sum_i (v_{[i]}^+ - v_{[i]}^-)^2}. \quad (5.4)$$

The em-chirality χ is bounded between 0 and $\sqrt{\sigma_{\text{int}}}$, therefore one can define the normalized em-chirality $\bar{\chi}$ by dividing χ with $\sqrt{\sigma_{\text{int}}}$,

$$\bar{\chi} = \frac{\chi}{\sqrt{\sigma_{\text{int}}}}. \quad (5.5)$$

In [213] it was shown that an achiral object will always have a χ value of zero. One can see from the definition that if a scatterer has a $\bar{\chi}$ equal to 1, the scatterer will only interact with light of one of the pure states of the helicity operator. It implies that the scatterer will be transparent to light of one of the two helicity eigenstates. Also, for an object to be maximally electromagnetic chiral it has to be dual. Note that the implication is not unidirectional: an achiral object can be dual, as it is the case for the cylinder optimized in section 4.3.

Simulation setup

In this section we will describe the methodology that we use to design em-chiral silver helices. Our intention is to find different optimal helices, each one of them presenting high em-chirality values at a different region of the optical and infrared frequency spectrum.

To find these helices, we use the Bayesian optimization algorithm presented in chapter 3. We provide to the algorithm observations of $\bar{\chi}$ and also of its shape derivatives with respect to the parameters that model the helices. To compute these quantities, we use the finite element method solver JCMSuite [58, 229]. The calculation of the T-matrix using the FEM has been described in section 4.3. Section 4.4 has been describing how to obtain the shape derivatives of the T-matrix.

For the case of the helix, the procedure that we use to obtain the shape derivatives of the actual mesh describing the helix with respect to the parameters of the helix involves a series of steps, as shown in Fig. 5.1. First, the helix is discretized using the internal mesher of JCMSuite. Once the mesh of the helix has been obtained, we need to calculate the derivatives of the vertices of the boundary mesh elements with respect to the parameters that describe the boundary of the helix. Given a helix specified by the radius of the spine, R_h , its thickness, T_w , the pitch, $Pitch$, and the number of turns, N_{turns} , the boundary of the helix can be parametrized with only two parameters θ_h and ϕ_h as

$$\mathbf{x}_{helix}(\theta_h, \phi_h) = \mathbf{x}_{spine}(\theta_h) + \frac{T_w}{2} (\mathbf{v}_1(\theta_h) \cos \phi_h + \mathbf{v}_2(\theta_h) \sin \phi_h), \quad (5.6)$$

where \mathbf{x}_{spine} are the points of the central spine of the helix

$$\mathbf{x}_{spine}(\theta_h) = \left(R_h \cos \theta_h, R_h \sin \theta_h, \frac{Pitch}{2\pi} \theta_h \right) \quad (5.7)$$

and $\mathbf{v}_1(\theta_h)$ and $\mathbf{v}_2(\theta_h)$ are two unitary vectors that are perpendicular to the tangent of the spine of the helix, $\mathbf{v}_3(\theta_h)$. All these vectors are given by

$$\mathbf{v}_1(\theta_h) = -(\cos \theta_h, \sin \theta_h, 0), \quad (5.8)$$

$$\mathbf{v}_2(\theta_h) = \left(-\frac{S_h}{\sqrt{R_h^2 + S_h^2}} \sin \theta_h, -\frac{S_h}{\sqrt{R_h^2 + S_h^2}} \cos \theta_h, -\frac{R_h}{\sqrt{R_h^2 + S_h^2}} \right), \quad (5.9)$$

$$\mathbf{v}_3(\theta_h) = \left(-\frac{R_h}{\sqrt{R_h^2 + S_h^2}} \sin \theta_h, -\frac{R_h}{\sqrt{R_h^2 + S_h^2}} \cos \theta_h, \frac{S_h}{\sqrt{R_h^2 + S_h^2}} \right). \quad (5.10)$$

In the above equation, the slope S_h is equal to $Pitch/2\pi$. The parameter θ_h ranges from 0 to $N_{turns} \cdot 2\pi$ and ϕ_h ranges from 0 to 2π . Note the difference between the parameters of

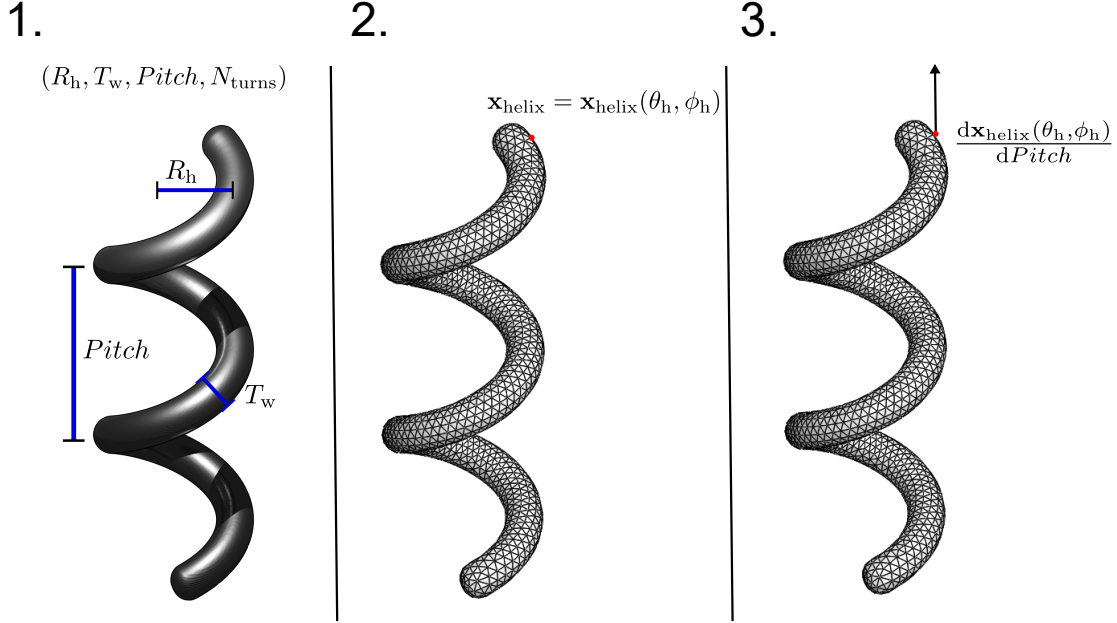


Figure 5.1: Steps needed to compute the shape derivatives of the FEM discretization of a helix. The helix is determined by its design parameters: the radius of the helix spine, R_h , the thickness of the helix wire, T_w , the Pitch of the helix, $Pitch$, and the number of turns of the helix, N_{turns} . Given the parameters, the helix can be discretized using tetrahedra. After obtaining the discretization (1), a Python module is used to determine the parameters θ_h , and ϕ_h , Eqn. (5.6), for each vertex of the helix boundary (2). These parameters are used to evaluate the expressions for the shape derivatives in the vertex (3). The shape derivatives of the vertices are finally passed to JCMSuite.

the helix parametrization, θ_h and ϕ_h that specify the different points of the boundary of the helix and the parameters of the actual optimization, R_h , T_w , $Pitch$ and N_{turns} , used to specify the different helices within the design space.

To model helices with smooth surfaces, we place two hemispheres on the edges of the helix. The parametrization used for the upper hemisphere is

$$\begin{aligned} \mathbf{x}_{helix}(t, \phi_h) = & \mathbf{x}_{spine}(N_{turns} \cdot 2\pi) + \sin t \frac{T_w}{2} \mathbf{v}_3(N_{turns} \cdot 2\pi) \\ & + \cos t \frac{T_w}{2} (\mathbf{v}_1(N_{turns} \cdot 2\pi) \cos \phi_h + \mathbf{v}_2(N_{turns} \cdot 2\pi) \sin \phi_h), \end{aligned} \quad (5.11)$$

where t ranges from 0 to 2π . An analogous expression is used to parametrize the lower hemisphere.

Given a vertex of the FEM discretization of the helix boundary, to calculate the parameter θ_h or t that corresponds to this vertex, we use a local optimizer that searches for the values that minimize the distance between the vertex and the spine of the helix given by Eqn. (5.7). The initial parameter used in this local optimization is an approximation of the final retrieved value based on the z -component of the vertex. Once the value of θ_h or t has been obtained, retrieving the value of ϕ_h is rather simple. One only needs to calculate the angle between the vector $\mathbf{x}_{helix} - \mathbf{x}_{spine}$ and the vector \mathbf{v}_2 .

Once the parameters corresponding to the vertex are retrieved, the final step is to compute the derivatives of the vertex with respect to the design parameters. For that, one only needs to evaluate the expressions for $\frac{dx_{\text{helix}}}{dR_h}$, $\frac{dx_{\text{helix}}}{dT_w}$, $\frac{dx_{\text{helix}}}{dPitch}$, and $\frac{dx_{\text{helix}}}{dN_{\text{turns}}}$. These expressions are analytically derived from Eqns. (5.6)-(5.11).

The described procedure is implemented into a Python module that is then passed to JCMSuite. JCMSuite evaluates the Python module for every vertex of the helix boundary to obtain the shape derivatives of the vertices¹. Then, based on these values, it computes the derivatives of the FEM system matrix as described in section 2.3 to obtain the shape derivatives of the T-matrix, as explained in section 4.4. Figure 4.12 in the previous chapter shows the results for the test of the shape derivatives of the T-matrix of a helix.

To finally obtain the shape derivatives of the em-chirality, χ , one needs to propagate the shape derivatives of the S-matrix along equation (5.4). The part of this operation that requires the most attention is the calculation of the shape derivatives of the singular values, needed to obtain the vectors \mathbf{v}^+ and \mathbf{v}^- , Eqn. (5.2).

Let us denote by \underline{U} , $\underline{\Sigma}$, \underline{V} the matrices that contain the singular value decomposition of, for example, $\underline{S}^{+,+}$,

$$\underline{S}^{+,+} = \underline{U}^\dagger \underline{\Sigma} \underline{V}, \quad (5.12)$$

$$\underline{U}^\dagger \underline{U} = \mathbb{I}, \quad (5.13)$$

$$\underline{V}^\dagger \underline{V} = \mathbb{I}, \quad (5.14)$$

where \dagger denotes the transpose conjugate.

Now, let us assume that we know the shape derivative of $\underline{S}^{+,+}$ with respect to some design parameter x_i . Then, one can obtain the shape derivative of the singular values of $\underline{S}^{+,+}$ as [283]

$$\frac{d\underline{\Sigma}}{dx_i} = \mathbb{I} \circ \left(\text{Re} \left[\underline{U}^\dagger \frac{d\underline{S}^{+,+}}{dx_i} \underline{V} \right] \right), \quad (5.15)$$

where \circ denotes the element-wise multiplication and \mathbb{I} is the identity matrix.

The calculation of the shape derivatives of the singular values is simple once the shape derivatives of the S-matrix have been obtained, if the singular values are not degenerate. However, things become more complicated for the case where one or more singular values are degenerate. The singular value decomposition is discontinuous within the subset of matrices with degenerate singular values [284]. A similar behavior occurs for the eigenvalue decomposition [285]. One simple example of a parametric object for which this can happen is a spheroid, where the value of the major axis is given as a design parameter. If one considers the simpler case of an S-matrix with only the dipole contributions, the submatrices $\underline{S}^{\pm,\pm}$ will have a singular value with a triple degeneracy when the spheroid becomes a sphere. A change in the value of the major axis with respect to this point would lead to submatrices that have a singular value with a double degeneracy, therefore still being degenerate. If instead the infinitesimal change in the parameter leads to a matrix without degenerate singular values, the differentiability of the singular values with respect to the parameter depends on the properties of the parametric matrix [284]. To make the process simpler, we do not consider the derivatives of $\bar{\chi}$ when we detect that

¹The team from JCMwave GmbH created the bridge into JCMSuite for us to be able to pass the shape derivatives of complicated structures to the software using our own Python modules.

any of the singular values are degenerate. As we use Bayesian optimization, the correct functioning of the algorithm does not depend on providing derivative observations or not. The shape derivatives are extra information that the Gaussian processes can use to obtain a better model of the objective function. However, the Gaussian process can incorporate derivative observations for just some of the evaluated points, or even include derivative observations with respect to some parameters and not to the others.

Once the derivatives of the vectors \mathbf{v}^+ and \mathbf{v}^- are obtained, the shape derivatives of χ read as

$$\frac{d\chi}{dx_i} = \frac{\sum_i (v_{[i]}^+ - v_{[i]}^-) \left(\frac{dv_{[i]}^+}{dx_i} - \frac{dv_{[i]}^-}{dx_i} \right)}{\chi}. \quad (5.16)$$

A similar expression can be obtained for the derivatives of the total interaction cross section,

$$\frac{d\sigma_{\text{int}}}{dx_i} = \sum_i 2v_{[i]}^+ \frac{dv_{[i]}^+}{dx_i} + 2v_{[i]}^- \frac{dv_{[i]}^-}{dx_i}. \quad (5.17)$$

Finally, one can obtain the derivatives of $\bar{\chi}$ as

$$\frac{d\bar{\chi}}{dx_i} = \frac{\frac{d\chi}{dx_i} \sqrt{\sigma_{\text{int}}} - \frac{\chi}{2\sqrt{\sigma_{\text{int}}}} \frac{d\sigma_{\text{int}}}{dx_i}}{\sigma_{\text{int}}}, \quad (5.18)$$

As we can see in Eqn. (5.16), the derivative of $\bar{\chi}$ is also not defined when χ equals zero. As for the case in which the discontinuity of the derivatives comes from the singular value decomposition, we simply check if χ is zero and in this case we do not include the derivatives of $\bar{\chi}$ into the optimization process.

Results of the optimization

After having described the simulation and optimization setups, we proceed to optimize the em-chirality of silver helices at a decreasing set of design wavelengths. It is our intention to study how the geometry of an optimal helix changes when operating at lower wavelengths and which upper value for the em-chirality can be obtained when working at optical wavelengths and not in the far-infrared. We would like to see a lower bound for a wavelength where a high em-chirality is obtained. Based on the material properties of silver, it can be expected that this happens somewhere at the wavelengths corresponding to visible light.

The optimizations depart from a design wavelength of $\lambda_0 = 150 \mu\text{m}$ down to a wavelength of $\lambda_0 = 500 \text{ nm}$. The reason for starting at such a long wavelength value is based on existing results for a silver helix [213] that presents a large $\bar{\chi}$ in this frequency region. These results give us an estimation about the bounds to use for the design parameter space.

At the wavelength of $\lambda_0 = 150 \mu\text{m}$ the lower and upper limits of the radius of the helix, R_h , are set to $1 \mu\text{m}$ and $10 \mu\text{m}$ respectively. Both limits are linearly scaled with the wavelength for the optimizations performed at the other different wavelengths. The thickness of the wire can vary between a 5% and a 95% of the value of $2R_h$. A further bound is imposed on the thickness of the wire, it can not be thinner than 20 nm for any of the optimizations.

This extra limit is included to restrict the results to helices that are in the limits of what it is possible to realize experimentally using current fabrication technologies. Moreover, a wire with a thickness of 20 nm is close to the limit for which the electromagnetic response of the object can be described using the macroscopic constitutive relations (see, e.g., [41] section 6.6). The pitch of the helix is bounded between 1.1 and 10 times the thickness of the wire and the optimization limits for the number of turns are 0.1 and 4. The permittivity of silver is interpolated at each wavelength from two different databases [286, 287] depending on the frequency region. One database accounts for the optical and near-infrared regions and the other for wavelengths longer than 1.5 μm .

Regarding the calculation of $\bar{\chi}$, we use finite elements with a polynomial degree of 2. The maximum side length of the helix mesh elements is $\lambda/0.3$ for illumination wavelengths longer than 2 μm and $\lambda/10$ for the optical and near-infrared wavelengths, i.e. shorter than 2 μm . Here, λ refers to the wavelength within the helix. The maximum side length of the elements in the air domain is set to $\lambda_0/15$. Before starting each optimization, a convergence test with respect to the mesh size is done to check the accuracy of the results. When the error with the default mesh size is larger than 1%, the mesh size is further decreased. In many situations it is favorable to use a higher polynomial degree when compared to using smaller mesh elements. However, in this specific application it is important for the accuracy of the results to have an accurate representation of the surface of the helix. Therefore, it is preferable to have smaller mesh elements rather than a higher polynomial degree.

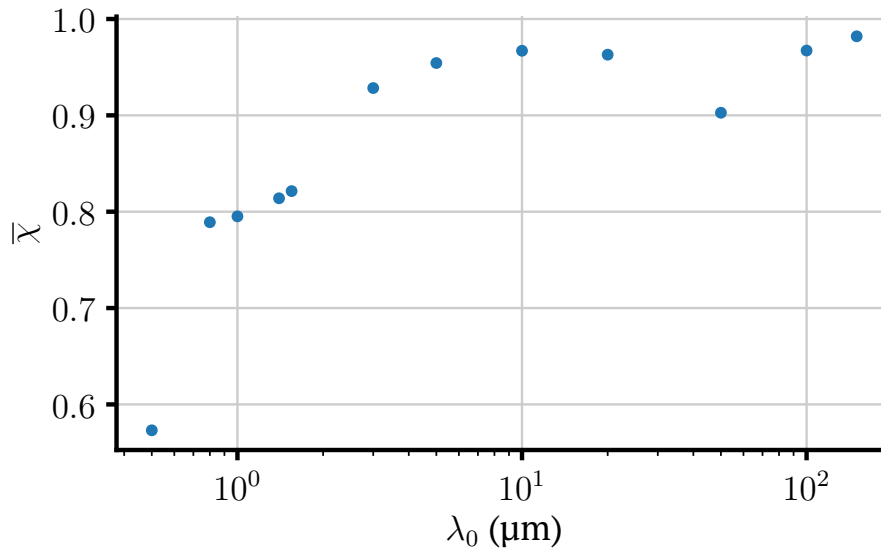


Figure 5.2: Values of the normalized em-chirality, $\bar{\chi}$, of the optimal helices obtained in the optimization runs as a function of the design wavelength. Each point corresponds to the value of a different helix optimized for the corresponding wavelength shown in the x -axis. The design parameters of the optimal helices are shown in Fig. 5.3.

Figure 5.2 shows the optimal values of $\bar{\chi}$ obtained at each optimization wavelength. The corresponding parameters of the optimal helices are shown in Fig. 5.3. As it can be seen in Fig. 5.2, the optimal $\bar{\chi}$ values are all above 0.9 for wavelengths down to 3 μm . However, the optimal $\bar{\chi}$ values already start to decrease with the wavelength from a wavelength of $\lambda_0 = 10 \mu\text{m}$. Below $\lambda_0 = 1 \mu\text{m}$, the decrease is very abrupt and at $\lambda_0 = 500 \text{ nm}$ $\bar{\chi}$ does not reach a value of 0.6.

The two different behaviours for the wavelength regions above and below $\lambda_0 = 3 \mu\text{m}$ be-

comes clear after simultaneously inspecting both Fig. 5.2 and 5.3. Except for the optimal helix found at $\lambda_0 = 150 \mu\text{m}$, all the designs that show a $\bar{\chi}$ above 0.9 have a similar shape. The number of turns keeps more or less constant along this region and it seems to exist a common ratio between the radius of the helix spine R_h and the pitch of the helix. Moreover, the absolute values for both parameters seem to follow a linear scale with the wavelength. These relations seem to indicate that the different optimizations found an optimal design that simply downscales with the wavelength. This behaviour can be expected as at these wavelengths the helices can be well approximated as helices made from a perfect electric conductor. Scaling of the geometrical parameters then indeed scales the operation wavelength. In fact, if one takes the optimal design found at $\lambda_0 = 100 \mu\text{m}$ and scales down the radius and pitch of the helix following the scaling rule for plasmonic materials described in [238], as already done in section 4.2 for the nanorod, one obtains the dashed black line shown in Fig. 5.3. Only for the design wavelengths in the range between $3 \mu\text{m}$ and $10 \mu\text{m}$ this scaling factor with respect to the wavelength slightly differ from unity. The optimal designs clearly follow the scaling design rules for perfect electric conductors under the thin wire approximation. There are still some small differences that can come from the fact that the FEM simulations take the effects produced by the thickness of the wire rigorously into account. Even if the thickness of the wire is much smaller than the illumination wavelength, it can play a significant role in the scattering response of the helix [288].

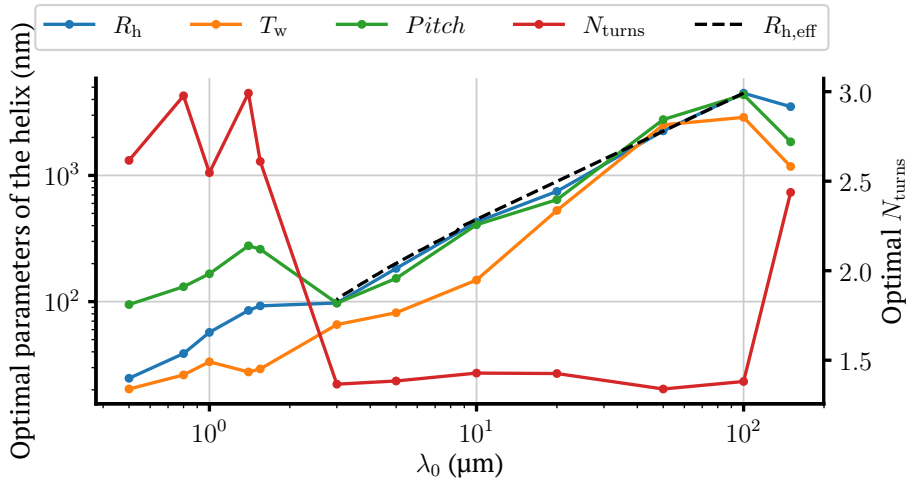


Figure 5.3: Design parameters of the optimal helices obtained in the optimization runs made for different design wavelengths. The design parameters are the radius of the helix spin, R_h , the thickness of the helix wire, T_w , the pitch of the helix, $Pitch$, and the number of turns of the helix, N_{turns} . The schematic of Fig. 5.1 shows the meaning of the different parameters in more detail.

Regarding the results for the shorter wavelengths, one of the reasons explaining the lower $\bar{\chi}$ values at wavelengths below $1.5 \mu\text{m}$ compared to the values obtained at longer wavelengths could be the lower bound of 20 nm imposed for the thickness of the wire. As it can be seen in Fig. 5.3, the thickness of the wire of the helix is lower than 30 nm for all the optimal helices found at wavelengths below $3 \mu\text{m}$. This could indicate that for wavelengths below $3 \mu\text{m}$ the ability to achieve optimal em-chiral values is constrained by the helix thickness. However, the reason behind the drop of the optimal $\bar{\chi}$ values is more likely to be due the plasmonic behaviour of silver at these frequencies. Due to the increase of Ohmic losses and the internal reactance of the silver wire, it becomes more difficult to obtain strong magnetic resonances when one approaches the plasma frequency, as it

was reported in [282, 289, 290]. Obtaining electric and magnetic resonances of a similar strength is crucial to obtain a strong chiral response [247, 291].

To analyze the interactions of a high em-chiral helix with light of different helicities, we consider from now on the helix optimized for a design wavelength of $\lambda_0 = 3 \mu\text{m}$. Figure 5.4 shows the spectral dependent total interaction cross section, σ_{int} , and the normalized em-chirality, $\bar{\chi}$, for wavelengths around the optimization wavelength. The total interaction cross section is obtained as the squared Frobenius norm of the scattering submatrices $\underline{S}^{+,+}$ and $\underline{S}^{-,-}$ respectively as

$$\sigma_{\text{int},+} = \sum_{i,j} |S_{[i,j]}^{+,+}|^2, \quad (5.19)$$

$$\sigma_{\text{int},-} = \sum_{i,j} |S_{[i,j]}^{-,-}|^2. \quad (5.20)$$

As one can see in Fig. 5.4, the maximum in the chirality also corresponds to a resonance peak in the total interaction cross section. It implies that the chirality is not just large at some trivial point where not much light is scattered. Figure 5.5 shows the absorption cross section of the helix when it is illuminated with two circularly polarized plane waves of opposite handedness. The absorption cross sections are shown as a function of the direction of the wave vector of the plane wave used for the illumination. Similar to the results shown in Fig. 5.4 for the total interaction cross section, the absorption is almost two orders of magnitude higher for right circularly polarized plane waves. The strongest difference occurs for plane waves whose wave vectors are parallel to the xy -plane, i.e., perpendicular to the helix axis.

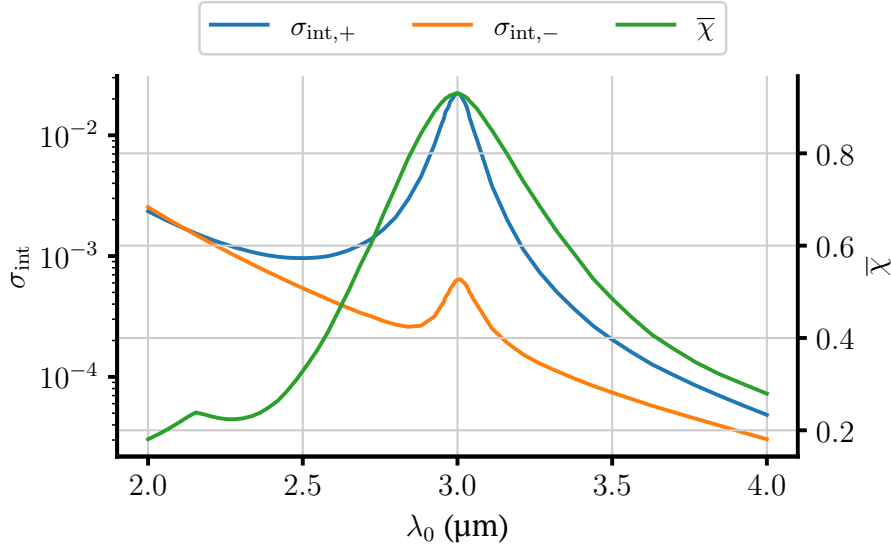


Figure 5.4: Wavelength dependency of the total interaction cross sections, $\sigma_{\text{int},\pm}$, and normalized em-chirality, $\bar{\chi}$, of the optimal helix obtained from the optimization at the design wavelength of $\lambda_0 = 3 \mu\text{m}$. The total interaction cross section is given as a function of the helicity eigenstate of the illumination. The plus and minus signs in the subscript of σ_{int} indicate the eigenvalues ± 1 of the two eigenstates of the helicity operator.

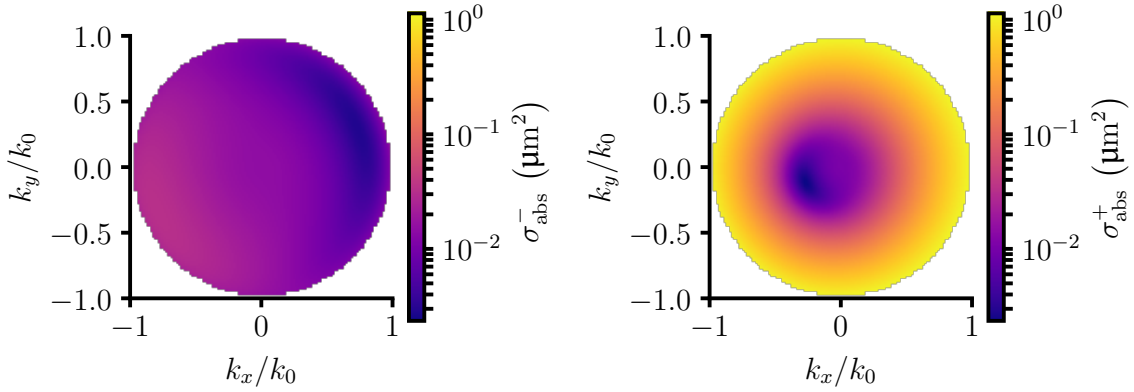


Figure 5.5: Absorption cross section, σ_{abs} , of the optimal helix obtained from the optimization at $\lambda_0 = 3 \mu\text{m}$ depending on the direction of the illuminating plane wave. The helix is illuminated with a circularly polarized plane wave at a wavelength of $\lambda_0 = 3 \mu\text{m}$. The two different plots correspond to the results for the two different circular polarization states, denoted with the plus sign, $\sigma_{\text{abs},+}$, for right circular polarized plane waves and with the minus sign, $\sigma_{\text{abs},-}$, for left circular polarized plane waves. The direction of the wave vector of the plane wave is given as a function of the x and y -components of its unitary vector. $\mathbf{k} = (k_x, k_y, k_z)$ with $|\mathbf{k}|^2 = k_x^2 + k_y^2 + k_z^2 = k_0^2$.

Figure 5.6 shows the intensity of the scattered near-field produced by the helix when illuminated by two circularly polarized plane waves of different handedness and wave vectors parallel to the x -axis. The optimized helix also shows strong differences of around two orders of magnitude in the scattered field intensity. As one can see, for the right circularly polarized plane wave, the scattered field intensity is strongly localized inside the helix. This intense near field is linked to the high absorption of light in the helix.

All these results indicate that the designed helix could serve as the basic constitutive element for an angle independent circular polarization filter. The filter would consist of a slab made from a homogeneous material with a high number of randomly oriented and randomly placed helices embedded into it. To analyze the potential of the design, we will estimate the slab thickness required to absorb 99% of the incoming power flux of a circular polarized beam and compare it to the power absorbed by a beam with opposite handedness. As we optimized the helices assuming that they are embedded into free space, we will assume now for simplicity that the embedded material has a relative permittivity of 1. For this calculation, we will make a series of additional approximations. Mainly, we will neglect scattering and consider that absorption is the only mechanism of interaction of the helices with the incident light. We will also assume that the incoming beam can be approximated by a plane wave. That is, let us assume that the incoming beam has an isotropic power flux with direction $+z$. Lastly, we treat the combination of the slab plus helices as a single homogeneous material, neglecting the discrete nature of the helices. The volume of the optimal helix obtained at $\lambda_0 = 3 \mu\text{m}$ is $0.00106 \mu\text{m}^3$. If we now assume a volume filling fraction of 1%, that implies a density of $\rho_h = 9.65$ helices per cubic μm .

Let us now focus on a volume element of the slab with a square section of side length l equals to $1 \mu\text{m}$ and thickness t , as shown in the sketch of Fig. 5.7. We want to study how the power flux of the incident beam changes along the z -direction within the slab.

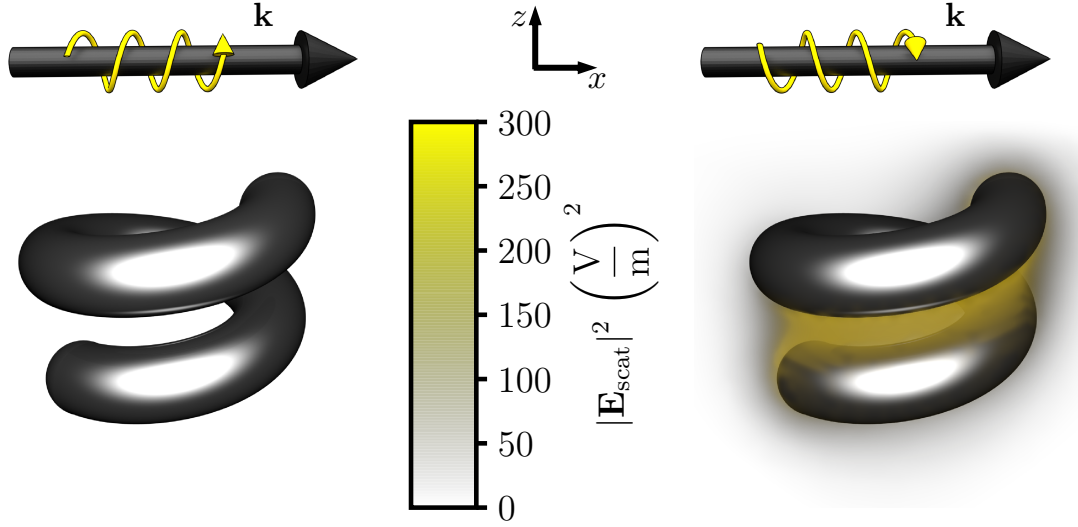


Figure 5.6: Intensity of the field scattered by a helix as a function of the handedness of the illuminating circularly polarized plane wave. The results are shown for the optimal helix obtained from the optimization run at $\lambda_0 = 3\mu\text{m}$. The illumination direction relative to the helix is indicated in the top of the figure.

The absorption cross sections under plane wave illumination of the rotationally averaged optimal helix are for the right and left circularly polarized plane wave $\sigma_{\text{abs},+} = 0.36 \mu\text{m}^2$ and $\sigma_{\text{abs},-} = 0.0075 \mu\text{m}^2$ respectively. We computed these values as the difference between the orientation averaged extinction and scattering cross sections.

The power absorbed by each of the helices equals the product of the illumination power flux times the absorption cross section of the helix

$$P_{\text{abs}}(z) = S_z(z) \sigma_{\text{abs},\pm}. \quad (5.21)$$

In a volume of thickness Δz and area l^2 the power absorbed per unit area equals

$$\frac{P_{\text{abs}}(z + \Delta z) - P_{\text{abs}}(z)}{l^2} = \Delta z \rho_h S_z(z) \sigma_{\text{abs},\pm}, \quad (5.22)$$

where Δz is considered to be thin enough to assume that the power flux remains constant throughout the thickness. Note that the homogenization of the material properties of the slab with the embedded helices is also included through the use of ρ_h .

Therefore, the change in the power flux of the beam per unit of thickness equals,

$$\frac{S_z(z + \Delta z) - S_z(z)}{\Delta z} = -\rho_h S_z(z) \sigma_{\text{abs},\pm}. \quad (5.23)$$

The differential equation for the power flux of the beam along the slab can then be written as

$$\frac{dS_z(z)}{dz} = -S_z(z) \rho_h \sigma_{\text{abs},\pm}. \quad (5.24)$$

Solving the above differential equation one obtains

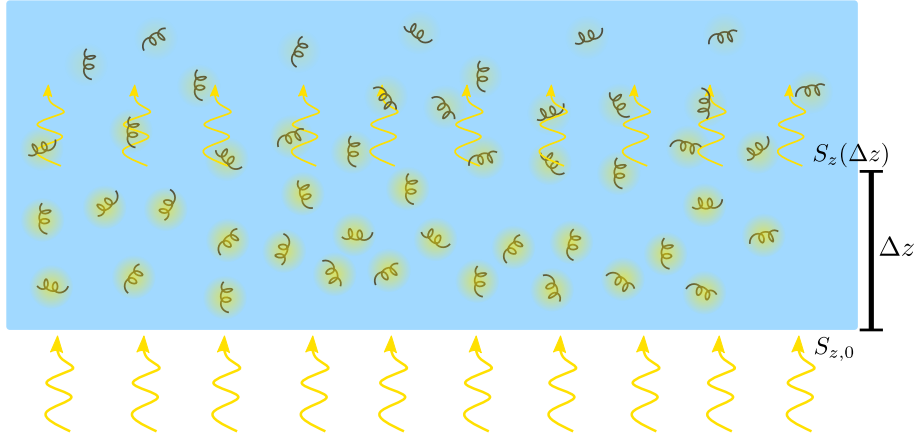


Figure 5.7: Sketch of the proposed angular independent polarization filter. The filter consists of a slab with randomly oriented and randomly placed optimally designed helices. Because the averaged absorption cross section of the helices is different for illumination fields of different helicities, the decay of the field along the slab will be more pronounced for one of the illumination fields.

$$S_z(z) = S_{z,0} e^{-\rho_h \sigma_{\text{abs}, \pm} z}, \quad (5.25)$$

being $S_{z,0}$ the power flux of the incident beam before entering the slab.

Using the values obtained for the absorption cross sections and assuming a filling fraction of 1%, Eqn. (5.25) gives a slab thickness of 1332 nm to absorb 99% of the incident power flux of a right circularly polarized beam. The same slab absorbs only 9% of the incident power flux for the beam with opposite handedness. These results show an extremely compact device that presents a high performance, indicating the potential for photonic applications of structures with high em-chirality values.

Conclusions

In the just presented application, we combined most of the tools developed within the thesis to find helices that offer high em-chirality values at optical and near infrared frequencies. The combination of Bayesian optimization, the tools to compute the T-matrix of isolated scatterers, and the calculation of its shape derivatives allowed us to find optimal helices along a wide range of frequencies going from the deep infrared down to optical frequencies. The results show that it is possible to design scatterers that present large values of $\bar{\chi}$ at frequencies down to 3 μm , but also the difficulties that exist in obtaining similar results at optical frequencies. However, although we could not find silver helices that present extremely large $\bar{\chi}$ values at optical frequencies, it is still not clear if other designs different than a helix could improve the results obtained here.

Once the optimizations were finished, we analyzed the behaviour of the optimal helix obtained for an illumination wavelength of 3 μm . The designed helix shows a strong difference in the interaction with circularly polarized plane waves of different handedness. The interaction is close to two orders of magnitude stronger for one of the handedness, both in scattering and absorption.

To investigate the potential of these highly em-chiral objects, we calculated, based on a series of assumptions, the performance of a possible implementation of an angle in-

dependent circular polarization filter. The results indicate that it is possible to achieve extremely compact devices that at the same time present a high performance. Although a more rigorous analysis is needed to confirm these results and possibly also to reduce the amount of simplifications used, they already give an idea of the potential that such high em-chiral scatterers may have for different applications.

Further developments along the lines of this work can be the optimization of more complex structures, such as wires following a freeform path, to improve the em-chirality values obtained at optical frequencies, or the optimization of designs that are inherently easier to fabricate.

5.2 Waveguide coupler for photonic inter-chip communication

Introduction

Photonic integrated circuits [292–294] emerge as a technological solution to the increasing demand for higher bit rates and lower energy consumption in communication networks [295] and supercomputer clusters [296]. Due to the high data transfer rates that can only be achieved using light as an information carrier, the use of photonic circuits has been also proposed in computing chips [297–302]. First proposals date back to the 1980s [303–305]. A well known problem that this technology could solve is the processor-memory bottleneck [306, 307].

A photonic integrated circuit contains a series of different interconnected optical components, such as lasers [308–310], modulators [311–315], optical switches [316–320], waveguides [321–326] or detectors. These circuits are generally used in the interfaces of the communication ports between the different nodes of an optical communication network.

One of the key technological advances that made it possible to increase the performance of photonic integration circuits is the fabrication of photonic components using the CMOS fabrication process, a technology known as silicon photonics [327–330]. This results in high volume production, high densities, low costs and a better integration with CMOS electronic circuits. The monolithic integration of the different photonic components with CMOS electronic circuits would be a major step in the performance and capabilities of the technology. However, photonic integrated circuits with better performances can currently only be obtained by combining in a single package photonic components fabricated on different material platforms [331, 332]. One of the main challenges to obtain monolithic integration is the fabrication of laser sources on silicon [333–335]. Therefore, frequently light sources are made from III-V semiconductors while all the other passive elements used to steer the light are made from silicon materials. Then, the components from these different material platforms need to be combined.

In a hybrid architecture that combines the beneficial aspects of different material platforms, one promising technique to interconnect the different photonic platforms within the chip package is via three dimensional freeform waveguides, also called photonic wire bonds (PWB) [336–340]. Photonic wire bonds are polymer waveguides with three dimensional freeform geometries. They are fabricated by two-photon polymerization of a negative-tone resist using a technology such as direct laser writing. Photonic wire bonds can be fabricated *in situ* and their geometry can be precisely controlled. This allows for the adaptation of their position to the position of the integrated waveguide facets, avoiding the high-precision alignment problems between optical components.

The basic architecture of this optical communication scheme is depicted in Fig. 5.8. The waveguide facets of two different chips are interconnected using a PWB. At each edge of the PWB, a waveguide edge coupler is placed to efficiently couple the light between the PWB and the waveguide. Additionally, grating couplers may be needed if out-of-plane coupling between the waveguide connected to the PWB and some of the chips is required. All these components play a fundamental role in the overall efficiency of the system and they need to be properly designed to reduce energy losses. The PWB path needs to be optimized to reduce energy losses [341] as well as the shape and dimensions of the edge couplers. It is also desirable that all the components have a footprint as small as possible. In this work, we focus on the optimized design of the edge coupler.

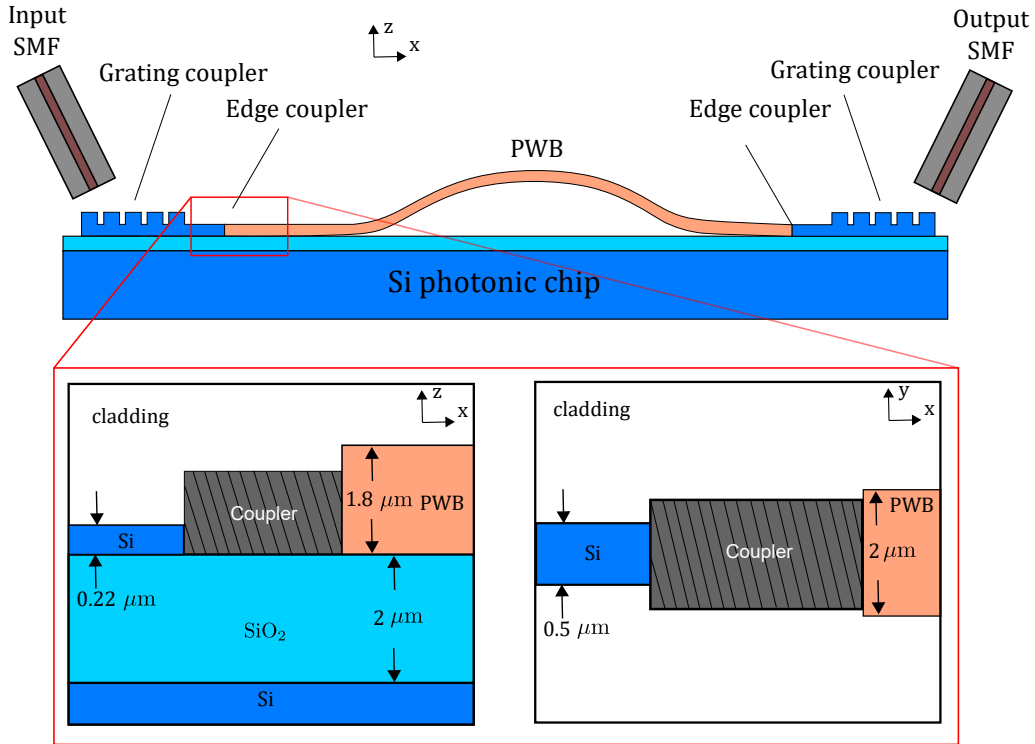


Figure 5.8: Schematic of the architecture for an optical inter-chip communication system.

As shown in Fig. 5.8, in the region of the edge coupler both the silicon waveguide and the PWB are placed on top of a layered substrate, therefore, the bottom part of both waveguides are vertically aligned. The cross sections of both waveguides are shown in Fig. 5.9. The silicon waveguide has a width of $0.5 \mu\text{m}$ and a height of $0.22 \mu\text{m}$. The width and height of the PWB are $2 \mu\text{m}$ and $1.8 \mu\text{m}$ respectively. The substrate is composed of two layers made of silicon (Si) and silica (SiO_2). The silica layer has a thickness of $2 \mu\text{m}$ and we consider the silicon layer to be semi-infinite. The waveguides are immersed in a cladding, characterized by its relative permittivity, $\epsilon_{\text{cladding}}$.

An edge coupler is a passive photonic component used to efficiently connect optical waveguides that have different geometrical cross-sections and that are made from different materials. We aim to design a structure that efficiently couples the fundamental mode of the silicon waveguide into the fundamental mode of the PWB. See section 2.2 for the description of the propagating modes in a waveguide. Figure 5.10 shows the electric field intensity cross section of the fundamental modes of both the silicon waveguide and the PWB. The modes are computed with JCMsuite [58], using two-dimensional layouts consisting of the cross sections of the waveguides. The fundamental mode of the silicon waveguide has an effective refractive index of $n_{\text{eff,PWB}} = 2.458$ and its electric field is predominantly polarized in the y -direction. The fundamental mode of the photonic wire bond is also predominantly polarized in the y -direction and it has an effective refractive index of $n_{\text{eff,PWB}} = 1.473$. If there were not substrate and the cross section of the PWB were a perfect square, then the PWB would have a fundamental mode degenerated into two modes: one y -polarized and another z -polarized. However, the broken symmetry of the structure with respect to the z -direction avoids this degeneracy and produces two modes with different propagation constants. The effective refractive index of the predominantly z -polarized mode has a value 0.0003 lower than the one of the fundamental mode.

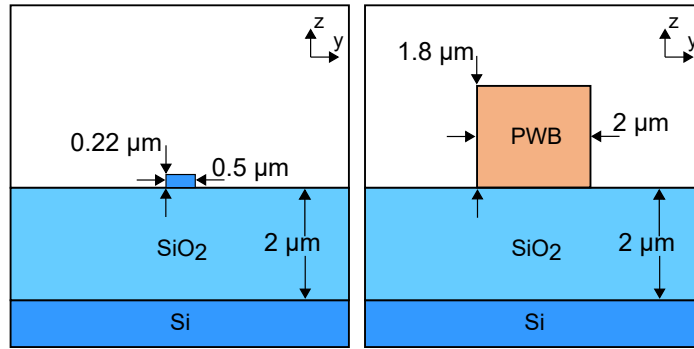


Figure 5.9: Cross sections of the silicon waveguide, left, and the photonic wire bond waveguide, right. Both elements are placed on top of a layered substrate composed of silica (SiO_2) and silicon (Si) and are embedded into a material with a permittivity of $\epsilon_{\text{cladding}}$ at the operating wavelength of $1.55 \mu\text{m}$.

The coupling losses between the two guiding components are due to the mismatch in the field profiles of the fundamental modes. The basic working principle of the edge coupler consists in modifying the field profile along the propagation through the coupler to achieve a better overlap at its edge. Because edge couplers are an important component for the in-plane interconnection between optical fibers and waveguides, their design and performance have been widely studied and multiple reasonable structures have been proposed. The most frequent solution is to use adiabatic linear tapers [342–346]. An adiabatic taper is a waveguide whose lateral dimensions decrease gradually along the direction of propagation of light. Along the taper, the fundamental mode of the waveguide can no longer be confined in the core of the waveguide due to the reduction of the dimensions and the field profile of the mode gradually expands towards the cladding. To reduce losses due to mode conversion into higher modes, the profile of the taper has to change slowly. As a result, adiabatic tapers present high coupling efficiencies but they also require large footprints. In addition to linear tapers, other profiles have been proposed for adiabatic tapers, such as tapers with parabolic [347] or exponential [348] profiles or multi-section tapers [344, 349]. Other types of flat designs, such as meta-material based couplers [350–353], trident tapers [354–357], or combinations of both types [358] have been also designed.

To improve the mode matching in the vertical direction as well, different structures have been proposed. The adiabatic linear taper with a linear vertical profile is a natural extension of the linear taper [359, 360]. Another strategy to improve the vertical overlap, which involves a less complex fabrication process, consists in encapsulating the waveguide inside an additional material layer, generally a polymer, which has a permittivity value close to the one of the waveguide with the lower refractive index [361, 362]. Other design strategies can be found in dedicated review articles [363, 364].

In the following sections, we optimize and analyze the performance of two different design proposals for the silicon waveguide-PWB edge coupler. The first design is a linear planar adiabatic taper covered with an additional layer made of the same polymer as the PWB. A difference with the previously mentioned structures [361, 362], is that in this case the vertical profile of the covering layer also varies along the propagation direction of light. An interesting aspect is to not only see the maximum efficiency achievable with this type of edge coupler but also to see how this efficiency depends on the length of the taper and what is the minimum footprint achievable without considerably penalizing the coupling efficiency. The second design proposed is based on a taper with a flat vertical

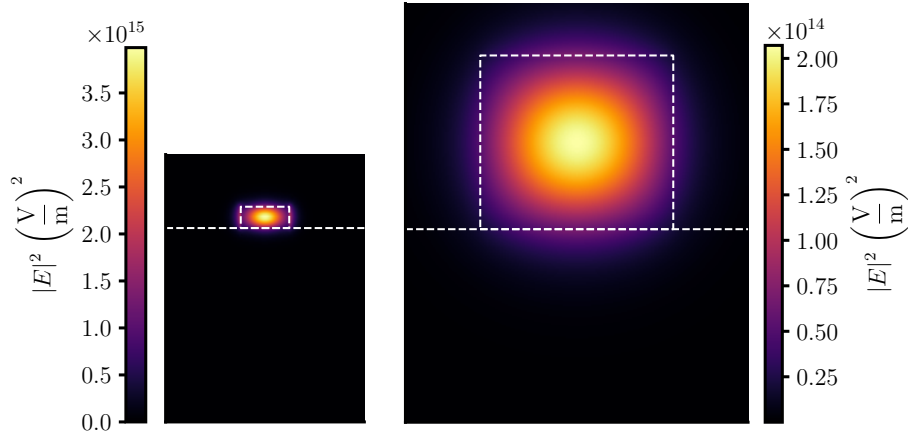


Figure 5.10: Electric field intensity of the fundamental modes of the silicon waveguide, left, and the photonic wire bond, right. The geometrical cross sections of the waveguides are shown in Fig. 5.9. The simulations were done with JCMsuite [58], using a finite element polynomial degree of 3 and a mesh side length of $\lambda/5$. λ is the wavelength of the electromagnetic field in each material. The vacuum wavelength is $\lambda_0 = 1.55 \mu\text{m}$. Both intensity field profiles obtained are normalized to powers of 1 W.

profile and a freeform horizontal profile. We decided to investigate this structure based on the results obtained for a two dimensional simplification of the same coupler [A2]. Finally, we compare the performance of both design proposals and analyze the differences in their working principles.

Parametric waveguide coupler

The schematic of the proposed adiabatic taper is shown in Fig. 5.11. The coupler is parametrized with four parameters: its length, l_{taper} , the height, $h_{\text{PWB,taper}}$, and width, $w_{\text{PWB,taper}}$, of the photonic wire at its edge, and the width of the silicon core of the taper at its edge, $w_{\text{Si,taper}}$.

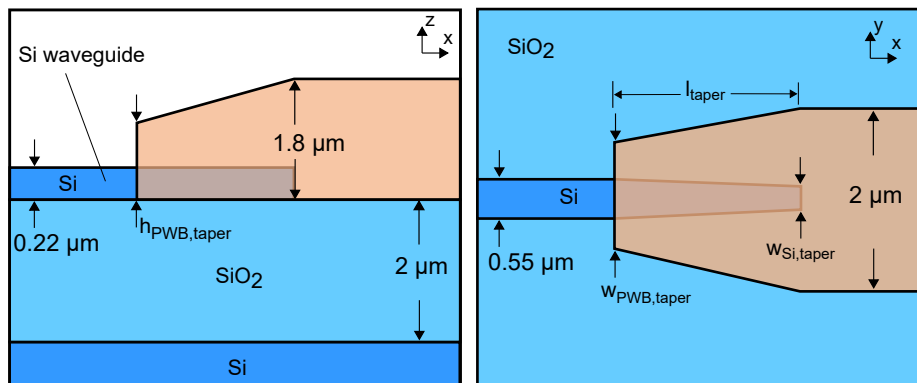


Figure 5.11: Schematic of the parametric waveguide coupler. The coupler is parametrized by its length, l_{taper} , the height, $h_{\text{PWB,taper}}$, and width, $w_{\text{PWB,taper}}$, of the photonic wire bond at its opening facet and by the width of the silicon core of the taper at its edge, $w_{\text{Si,taper}}$.

The coupler is optimized to find the design with the maximum coupling efficiency be-

tween the fundamental modes of both the silicon waveguide and the photonic wire bond. To calculate the coupling efficiency, η_{coupler} , we use a three-dimensional finite element model of the coupler. The coupler is illuminated with the incoming fundamental mode of the silicon waveguide and the total field, $\mathbf{E}(\mathbf{r})$, is computed. After the finite element problem is solved, we obtain the coupling efficiency through the calculation of the mode overlap between the solution $\mathbf{E}(\mathbf{r})$ and the magnetic field profile of the fundamental mode of the photonic wire bond, $\mathbf{H}_{0,\text{PWB}}(\mathbf{r})$,

$$\eta_{\text{coupler}} = \left| \frac{1}{2} \int_S (\mathbf{E}(\mathbf{r}) \times \mathbf{H}_{0,\text{PWB}}(\mathbf{r})) \cdot \hat{\mathbf{x}} dS \right|^2, \quad (5.26)$$

with S being a y - z -plane that cuts the photonic wire bond. This position of S corresponds to the right side in the sketches of Fig. 5.11. The above expression gives us directly the coupling efficiency because the values used for the field intensity of the fundamental mode of the PWB, shown in Fig. 5.10, are normalized to give a power carried by the guided mode of 1 W.

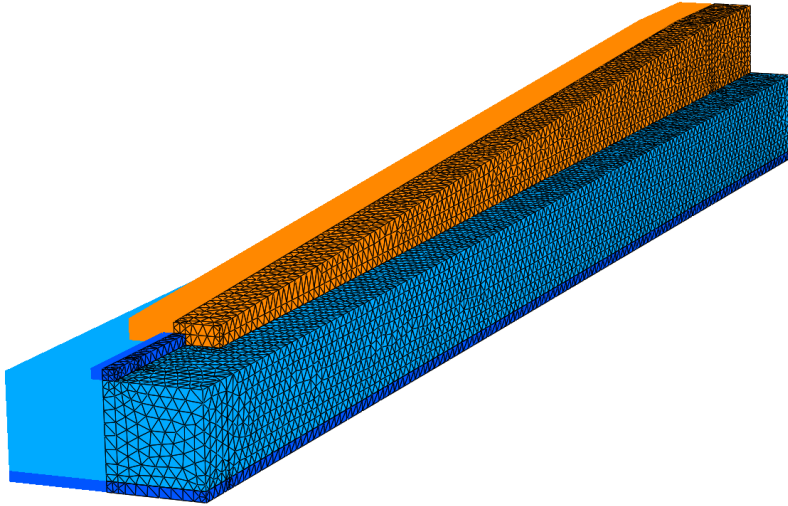


Figure 5.12: FEM discretization of the waveguide coupler. Due to the symmetry of the structure, only half of the device needs to be discretized for the finite element method simulation.

As the coupler is symmetric with respect to the plane $y = 0$, we use a mirror boundary condition to halve the size of the computational domain of the finite element method. Figure 5.12 shows an example of the finite element discretization of the parametric coupler for certain values of the design parameters. We use a finite element mesh side length of $\lambda/1.5$, where λ is the wavelength of the illuminating inside the respective material. The finite element polynomial degree is set to three. The large size used for the mesh elements is because of computational constraints. Our intention is to analyze couplers with lengths up to $60 \mu\text{m}$. That means couplers 100 times longer than the wavelength within the core region of the silicon waveguide and the photonic wire bond. Even using this coarse discretization, the simulation of the longer couplers requires memory capacities exceeding 300 GB. Despite the coarse mesh used, a convergence test showed that the error produced in the coupling efficiency with this mesh is lower than three percent. The adiabatic character of these long tapers, which results in smooth field profiles in the transition between the silicon waveguide and the photonic wire bond, is the main reason for this low error.

To obtain the optimal parameters of the coupler, we use the Bayesian optimization as

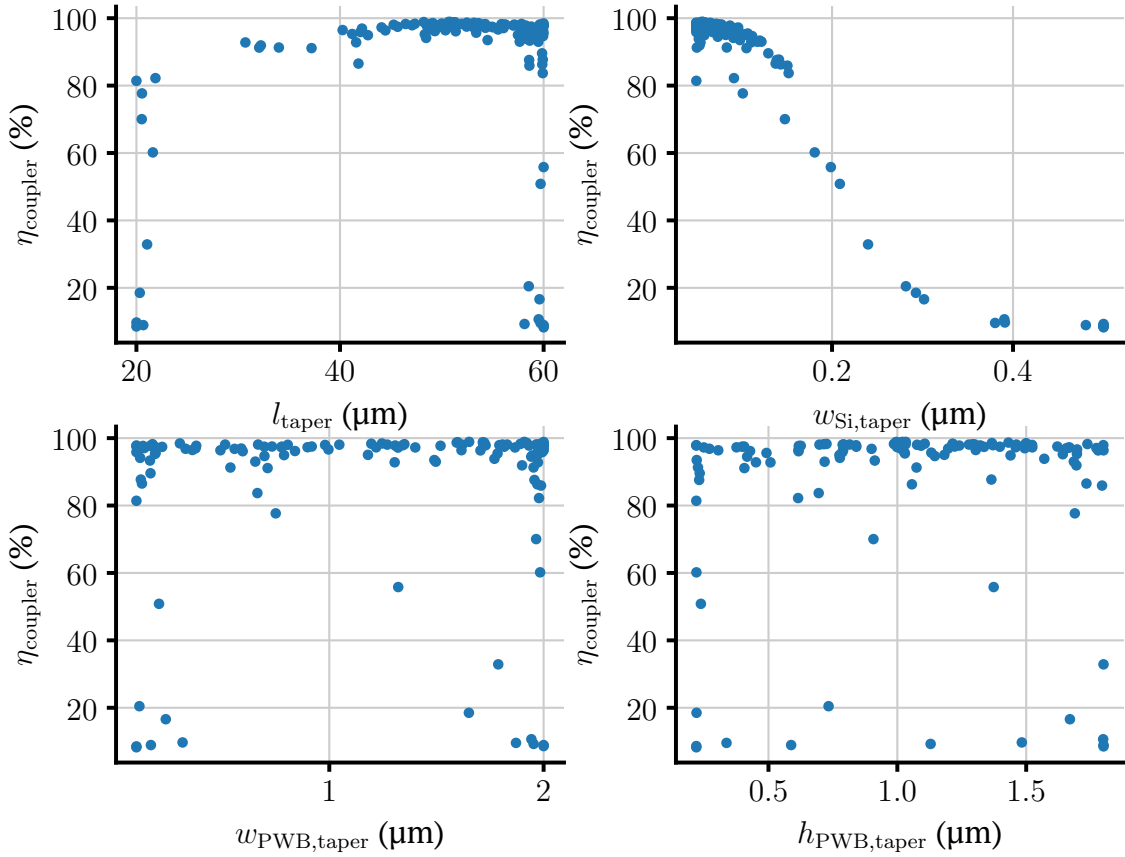


Figure 5.13: Coupling efficiencies of the different designs evaluated during the optimization process of the linear taper edge coupler. Each figure show the projection of the coupling efficiency values over the different parameters of the design space. The parameters are defined in the schematic of Fig. 5.11.

described in chapter 3. In this case, we do not use shape derivatives in the optimization process. The design parameter space is composed of only four parameters and for this problem we expect the objective function to have a smooth behaviour with respect to the design parameters. Under these conditions, and based on the fact that creating an algorithm that provides the shape derivatives to JCMSuite would be a rather time consuming task for this geometry, the benefit of using the shape derivatives is not clear.

We left the optimization to run for a couple of weeks. Let us note that each three dimensional simulation of a candidate design needs a few hours to run on the available computational infrastructure. The values of the coupling efficiency obtained during the optimization process are shown in Fig. 5.13. The figure shows the projection of the evaluation points into each one of the parameters of the design space. The optimization limits used for the design parameters can be seen in the axis of the different plots. The optimal design couples 99% of the input power into the fundamental mode of the photonic wire bond. For values of l_{taper} between 20 and 30 μm , the optimizer did not find designs with efficiencies higher than 90%. A strong correlation between the coupling efficiency and $w_{\text{Si,taper}}$ is also visible. Contrastingly, there is no visible correlation of the coupling efficiency with the parameters $w_{\text{PWB,taper}}$ and $h_{\text{PWB,taper}}$. This lack of correlation can be explained by the fact that at the leftmost side of the taper the field is still strongly confined within the core of the silicon waveguide. Therefore, the field is insensitive to the effect of the dimensions of the photonic wire bond cladding in this region. The optimal

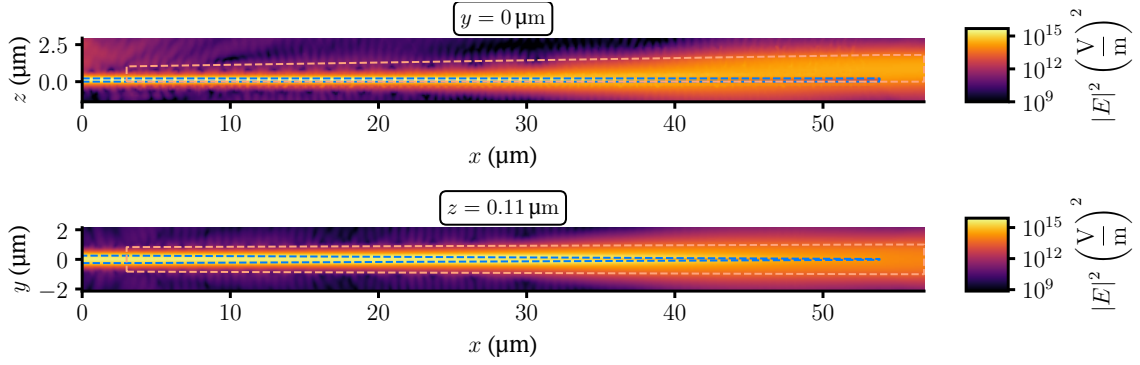


Figure 5.14: Intensity field profile of the optimal linear edge coupler over the planes defined by the equations $y = 0 \mu\text{m}$ and $z = 0.11 \mu\text{m}$. The shape of the optimal coupler is represented in the figures by the dashed lines. The blue dash line represents the boundary profile of the silicon core waveguide. The orange dash line represents the shape of the photonic wire bond boundary. The design parameters of the optimal coupler are: $l_{\text{taper}} = 50.8 \mu\text{m}$, $w_{\text{Si,taper}} = 0.06 \mu\text{m}$, $w_{\text{PWB,taper}} = 1.03 \mu\text{m}$, and $h_{\text{PWB,taper}} = 1.65 \mu\text{m}$.

value obtained for $w_{\text{Si,taper}}$ is also an expected result. The decrease of the width along the taper causes the energy to be less and less confined within the silicon core of the waveguide. As a result, the energy is smoothly radiated into the photonic wire bond without producing reflections, which leads to high coupling efficiencies.

The working principle of the coupler can be analyzed in Figs. 5.14 and 5.15. These figures show the intensity of the field profile of the optimal coupler, i.e. the coupler that offers the highest coupling efficiency among all considered devices. Its design parameters are specified in the caption of both figures. Looking at Fig. 5.14, one can see how in the first $30 \mu\text{m}$ the field is almost entirely confined within the core of the silicon waveguide. As the width is reduced, the energy starts to progressively leak into the photonic wire bond region. The rate of the field profile expansion is also visible in the plots with linear scale color maps of Fig. 5.15. After $20 \mu\text{m}$ of propagation along the taper, the field is still mainly confined within the silicon core region. After $40 \mu\text{m}$, the field intensity within the silicon core is almost zero and the field concentrates near the boundary of the core. After the tip of the taper, the field profile matches the field of the fundamental mode of the photonic wire bond shown in Fig. 5.10.

The wavelength dependence of the coupling efficiency for this optimal design is shown in Fig. 5.16. As one can see, the coupler presents a coupling efficiency higher than 97% in the wavelength window from $1.4 \mu\text{m}$ to $1.7 \mu\text{m}$. One can also appreciate some very small ripple in the curve, most likely due to numerical noise.

To further investigate the effect of the taper length on the coupling efficiency a second optimization run is done. This time the lower and upper optimization bounds for the parameter l_{taper} are $10 \mu\text{m}$ and $20 \mu\text{m}$ respectively. The results are shown in Fig. 5.17. The new results confirm the tendency observed in the results of Fig. 5.13. For tapers shorter than $20 \mu\text{m}$ the maximum efficiency achievable is lower than 85%. Moreover, the coupling efficiency drops below 60% for tapers with a length of $10 \mu\text{m}$. The explanation to this behavior is rather simple. The decrease in length of the coupler leads to a higher reduction of the width per unit length. A less smooth change in the dimensions of the waveguide core causes higher reflections, which results into a lower coupling efficiency.

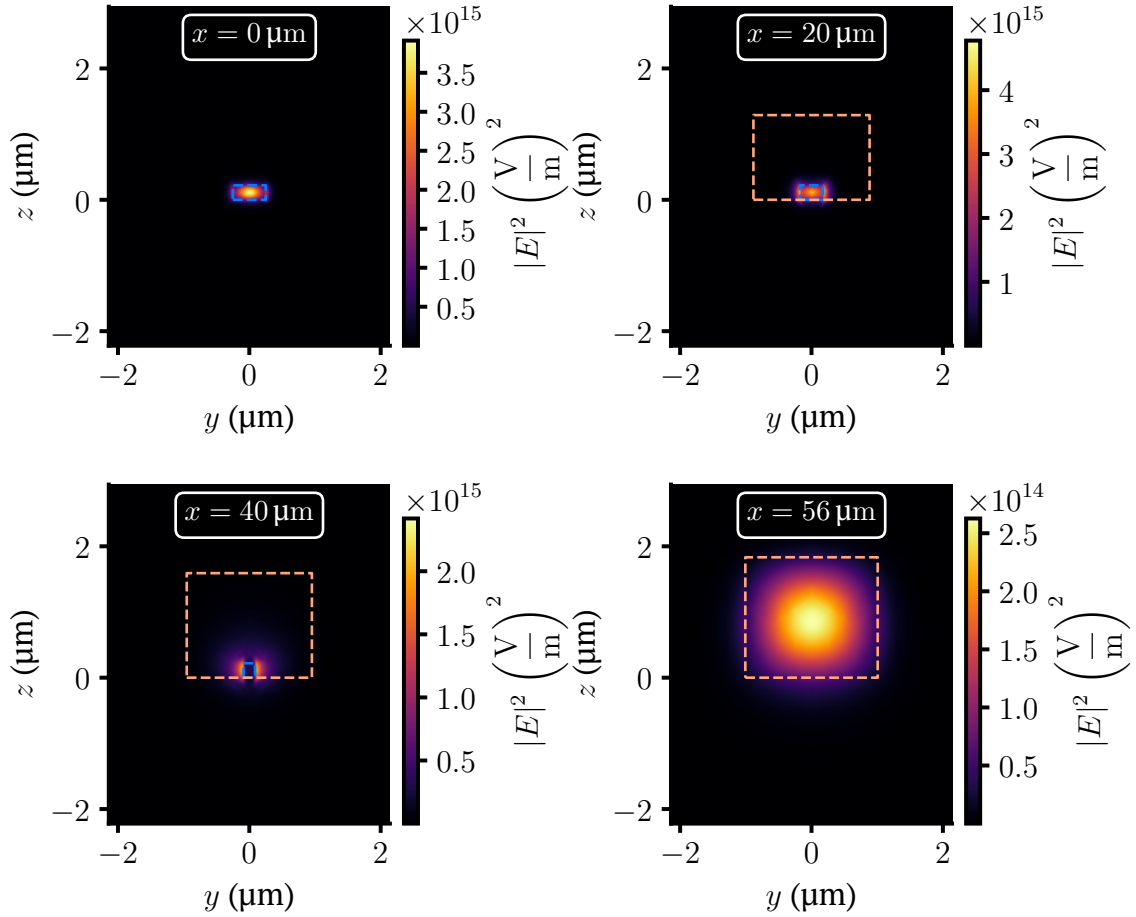


Figure 5.15: Intensity field profile of the optimal linear edge coupler over the planes defined by the equation $x = \text{const}$. The actual values of the x value are indicated in each of the plots. The cross sections of the silicon waveguide and the photonic wire bond are represented in the figures by dashed lines. The blue dashed line represents the boundary of the silicon core waveguide. The orange dashed line represents the boundary of the photonic wire bond. The design parameters of the optimal coupler are: $l_{\text{taper}} = 50.8 \mu\text{m}$, $w_{\text{Si,taper}} = 0.06 \mu\text{m}$, $w_{\text{PWB,taper}} = 1.03 \mu\text{m}$, and $h_{\text{PWB,taper}} = 1.65 \mu\text{m}$.

Overall, the results show that linear adiabatic tapers can achieve excellent coupling efficiencies and for wide wavelength bandwidths. However, these efficiencies are linked to structures with considerably large footprints. There is a strong correlation between the length of the taper and the maximum efficiency achievable. For lengths below $30 \mu\text{m}$, the coupling efficiency decreases rapidly with the reduction of the length. Therefore, if one aims to obtain highly efficient and more compact couplers, further designs must be investigated. To achieve that, the next section proposes the use of freeform edge couplers as possible candidates.

Freeform waveguide coupler

In the previous section 5.2, we optimized and analyzed the designs for a linear taper. The taper achieves coupling efficiencies greater than 99% at the desired central vacuum wavelength of $1.55 \mu\text{m}$. However, the performance of the linear taper drops below 90% for devices shorter than $30 \mu\text{m}$. The results show how the maximum efficiencies of the

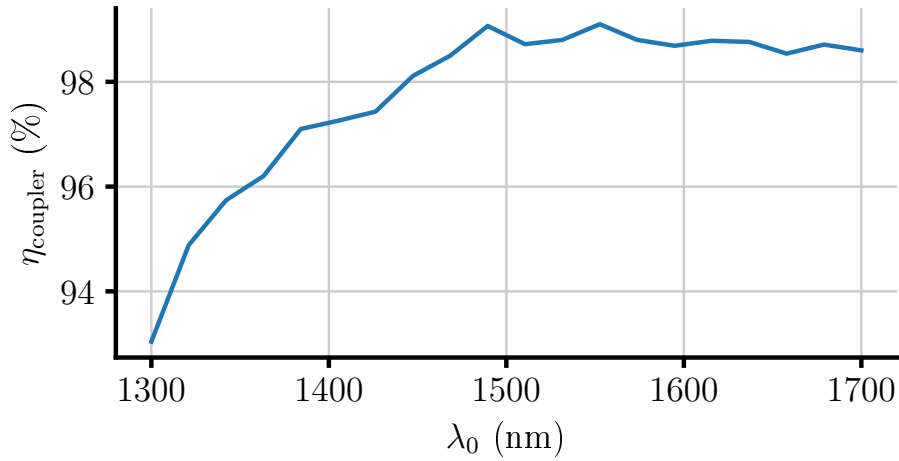


Figure 5.16: Coupling efficiency of the optimal adiabatic taper as a function of the wavelength of the illuminating waveguide mode. The parameters of the optimal coupler are shown in the caption of Fig. 5.14.

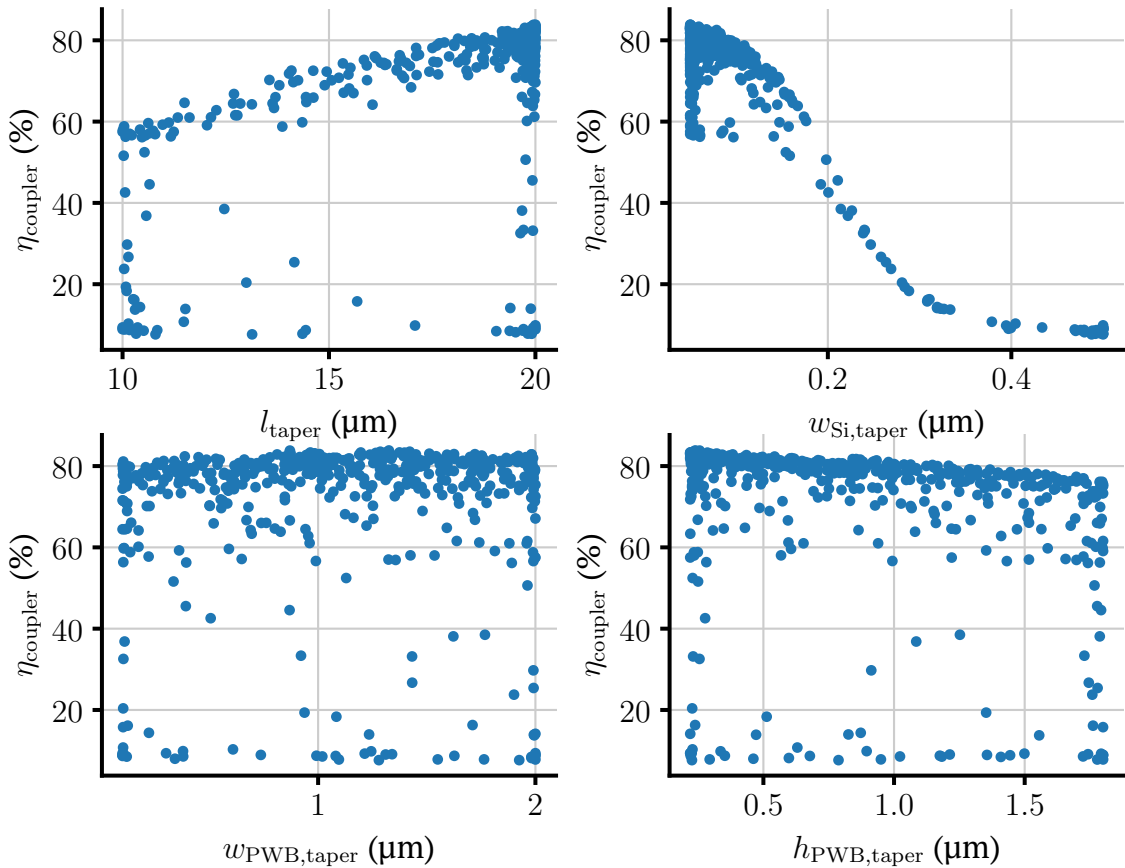


Figure 5.17: Optimization results for the waveguide coupler. Projections of the coupling efficiency over the different parameters of the design space. The parameters are defined in the schematic of Fig. 5.11. Note that the difference with the results shown in Fig. 5.13 is the different search range for the parameter l_{taper} .

optimal linear tapers decrease with the length of the taper. In this section, we study the

performance of a freeform edge coupler. With this design we try to go beyond the coupling efficiencies of the linear taper for compact devices.

The freeform taper can be seen as a natural step forward in the complexity of the shape with respect to the linear taper. As shown in the schematic of Fig. 5.18, its structure also consists of a symmetric device with a silicon core of constant height. The main difference with respect to the linear taper resides on its width profile. The shape of the freeform taper is described using a non-uniform rational basis spline (NURBS) curve [365–367],

$$\mathbf{c}(t) = \frac{\sum_{i=1}^d N_{i,n}(t) w_i \mathbf{p}_i}{\sum_{i=1}^d N_{i,n}(t) w_i}, \quad (5.27)$$

where $\mathbf{c}(t)$ gives the x - y points of the coupler's boundary, $N_{i,n}(t)$ are of order n , w_i are the weights of each b-spline, and \mathbf{p}_i are two dimensional vectors called control points.

For the parametrization of the coupler we set all the weights w_i to 1 and we use b-splines of degree 3, as they ensure the continuity of the boundary and of its tangent. Fixing all the other parameters, the shape of the coupler is only governed by the position of its control points. Furthermore, in the design of the coupler, the control points of the curve are spaced at an equidistance in the x -direction and they are only allowed to move in the y -direction. Based on the results obtained for the linear taper, we also decided to maintain the height of the photonic wire bond constant along the coupler region, as this parameter does not play a crucial role in the coupling efficiency of the device and this simplification results in structures easier to fabricate. Therefore, the only design parameters are the y -coordinates of the control points that describe the shape of the taper.

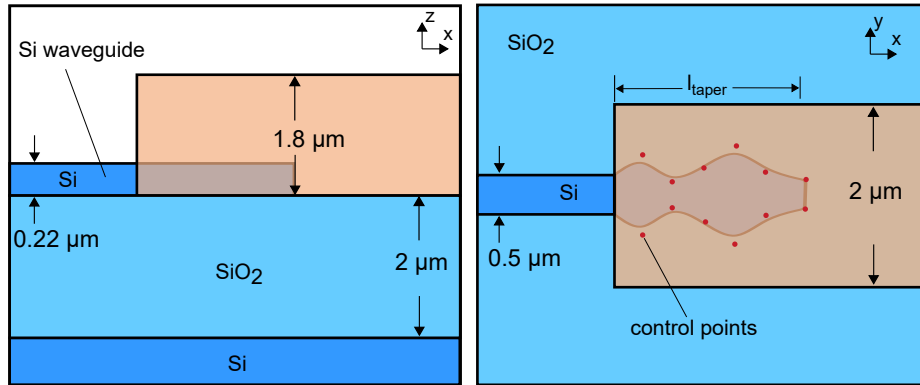


Figure 5.18: Schematic of the freeform waveguide edge coupler. The shape of the coupler is described by a NURBS curve, defined by a series of control points. The control points, shown in the schematic as red dots, are equispaced in the x -direction and they are allowed to move only in the y -direction.

As we did along this thesis for the different optimizations performed, we also use Bayesian optimization to design the freeform taper. To compute the coupling efficiency of the coupler, we follow the same procedure as described in the previous section for the linear taper. We use a three-dimensional finite element model with a mirror symmetry boundary condition. However, as the design space now contains more complex geometries than in the case of the linear taper, some of them producing large reflections and complex interference patterns, the mesh elements size needs to be smaller than the one used for the linear taper. Specifically, we use a mesh size of $\lambda/5$ instead of $\lambda/1.5$.

Because the effective design space is larger when compared to the case of the linear ta-

per, as it contains a much larger number of possible geometries, we first tried to perform the optimization using a two-dimensional simplification of the structure to reduce the calculation times. The results of the optimization using the two-dimensional model are presented in [A2]. There, highly efficient ultra compact designs were achieved. However, we observed that the coupling efficiencies obtained with the two-dimensional model differ considerably from the ones obtained with the three-dimensional model for the same design. The reason for this difference comes from the different height profiles of both the silicon waveguide and the photonic wire bond. The two-dimensional models normally give good approximations when the different structures have similar heights [27, 368–370]. In those cases the vertical distribution of the field profile is similar along the different elements of the device and the mode overlap is mainly determined by the horizontal distribution of the fields. Despite these differences, the results obtained there have been very useful for the three-dimensional model. Among other conclusions, we observed that the use of shape derivatives can significantly reduce the optimization times in this type of structure. Therefore, we decided to provide the shape derivatives of the coupling efficiencies with respect to the coordinates of the control points [371] to the Bayesian optimization. As the height of the coupler remains invariant and the structure can be defined as an extrusion of a two-dimensional profile, the procedure to provide the shape derivatives of the coupler with respect to the design parameters to JCMSuite is simpler than for the case of the helices, described in section 5.1. In this case, the shape derivatives can be directly provided at the same time as one provides the shape of the coupler. Their values are given by

$$\frac{dc(t)}{dp_i} = \frac{N_{i,n}(t)w_i}{\sum_{i=1}^d N_{i,n}(t)w_i}. \quad (5.28)$$

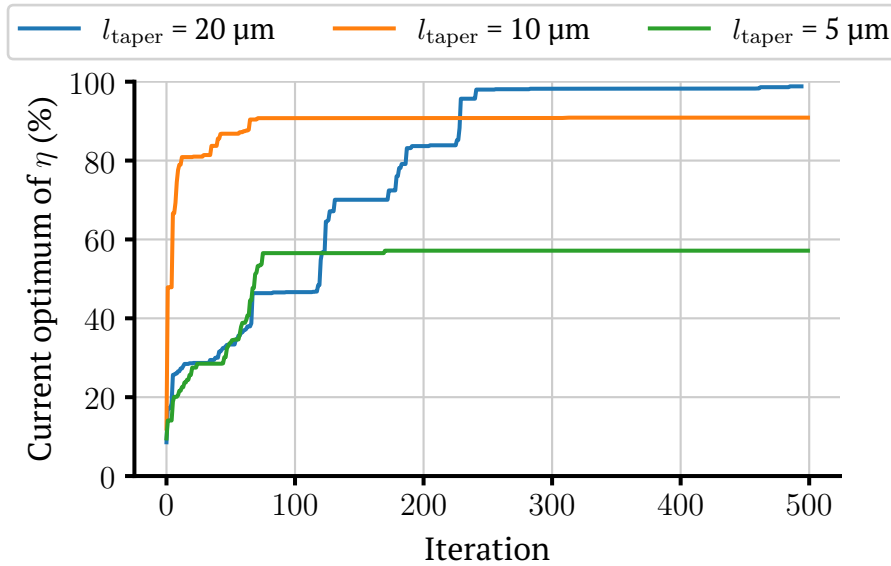


Figure 5.19: Optimization process for the freeform waveguide coupler parametrized with four control points. Cumulative optimum coupling efficiency as a function of the number of iterations ran by the optimizer. The results are shown for couplers with different lengths, l_{taper} . The schematic of the freeform coupler is shown in Fig. 5.18.

The optimization is performed for three different lengths of the coupler, 20 μm , 10 μm ,

and 5 μm using four control points to describe the shape with the NURBS. The cumulative maximums of the coupling efficiency obtained during the optimization process for each of the coupler lengths are shown in Fig. 5.19. As one would expect, the coupling efficiency decreases with the length of the taper. However, the maximum coupling efficiencies obtained with the freeform coupler are significantly higher than the ones obtained with the linear taper. The improvement is especially significant for the case of the taper with a length of 10 μm , the maximum efficiency obtained, $\eta_{\text{coupler}}=91\%$, is 30 absolute percent higher than for the best linear coupler of the same length.

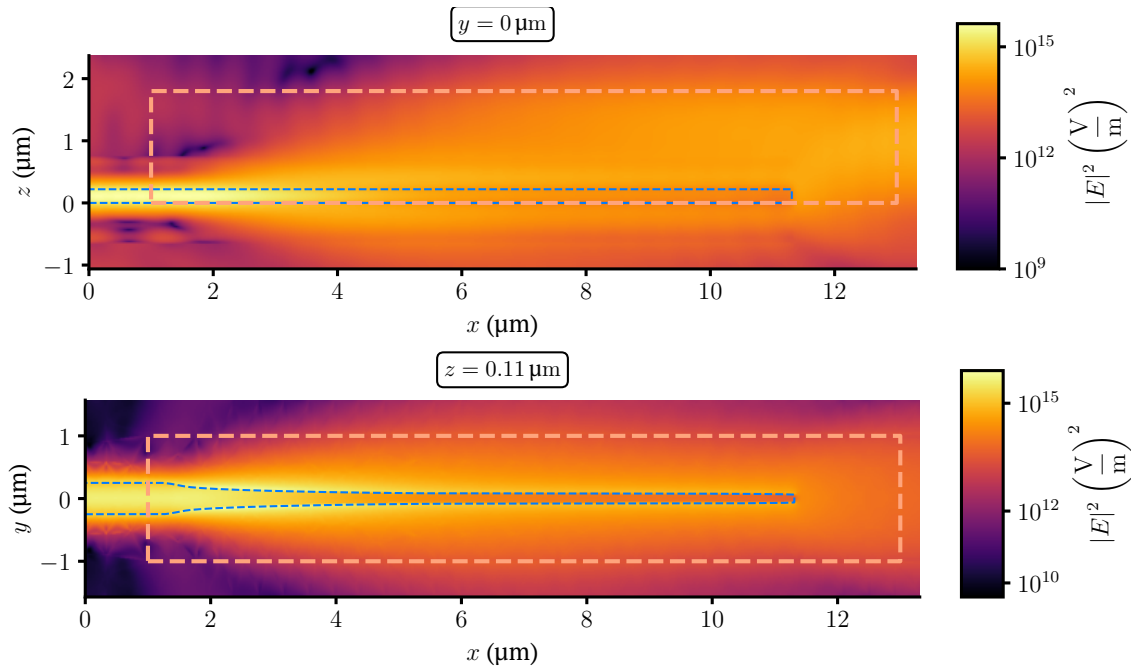


Figure 5.20: Intensity field distribution along the optimal freeform coupler obtained for a coupler length of 10 μm . The coupler achieves a performance of $\eta_{\text{coupler}} = 91\%$.

Figure 5.20 shows the shape and the field distribution of the 10 μm long optimal coupler. As one can see in the figure, the shape of the coupler resembles the one of a parabolic adiabatic taper. The use of four control points to parametrize the boundary restricts the shapes to have a rather smooth profile. This restriction probably favours designs that present more canonical shapes [A2]. The field profile shown in Fig. 5.20 shows also similar features to the 50 μm long adiabatic linear taper shown in Fig. 5.14. The width of the taper is smaller than the width of the input silicon waveguide all along the coupler. This reduction prevents the fundamental mode of the silicon waveguide being confined within the silicon core region and it starts to extend towards the photonic wire bond region. An important difference with the adiabatic linear taper is the rate at which this happens. In the case of the linear taper, we saw how the field stays mainly confined within the silicon core for at least half of the coupler length. In the linear taper the transition between a situation where the field is almost completely confined into the silicon core and a field being mainly expanded into the photonic wire bond happens progressively along the taper. Here, for the freeform coupler, one can observe how after a couple of micrometers the intensity distribution is already extended over the whole photonic wire bond region. Despite this faster transition, the design still presents a high coupling efficiency.

Regarding the dependence of η_{coupler} with respect to the excitation wavelength, the results for the wavelength dependency are shown in Fig. 5.21. The coupler present a peak

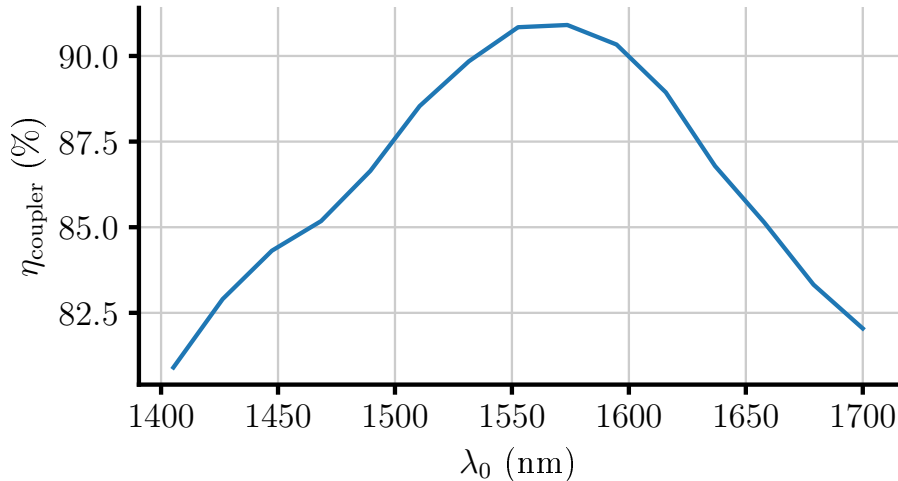


Figure 5.21: Dependency of the coupling efficiency, η_{coupler} , for the optimal freeform edge coupler shown in Fig. 5.20 with respect to the excitation wavelength. The wavelength values are those corresponding to the wavelength in free space. The coupler has been optimized for a wavelength of $1.55 \mu\text{m}$, which corresponds with the position of the peak for the coupling efficiency.

of 91% in the coupling efficiency at the design frequency of $1.55 \mu\text{m}$. As one moves away from the design wavelength, this efficiency declines and it is around 10% lower at wavelengths separated 150 nm from the central wavelength of 1.55. We can see that the decay in the efficiency is faster than for the linear taper. Due to the fact that more compact photonic devices are shorter, they can not present smooth adiabatic transitions of the field profile along the coupler. Instead, they require shape profiles that adapt better to the behavior of the specific design wavelength. In some cases, designs for compact photonic devices even use interference effects between forward and back propagating fields to avoid back reflections [85, 358, 368]. These effects are highly sensitive to the wavelength, which leads to shorter bandwidths for the coupling efficiency.

Conclusions

In this section we analyzed the performance of linear tapers as edge couplers for inter-chip photonic communication architectures. Despite the considerable size of the tapers, we managed to perform fully three dimensional rigorous simulations of the device. We achieved this by exploiting the y mirror symmetry of the taper. As a result of the optimization of the coupler, we obtained devices with coupling efficiencies higher than 99% at the design wavelength. Moreover, the efficiency of the optimal linear taper keeps fairly constant along a wide range of wavelengths.

We also analyzed the dependency of the optimal coupling efficiency with respect to the length of the coupler. In an ideal situation, one would like to achieve ultra-compact devices that offer large efficiencies and for a wide wavelength bandwidth. However, we observed how the efficiency of the proposed linear taper considerably drops down when the tapers shorter than $30 \mu\text{m}$ are considered. For a taper with a length of $10 \mu\text{m}$, the maximum efficiency obtained was lower than 60%.

With the aim of finding more compact devices that offer coupling efficiencies in the order of 90%, we proposed to optimize freeform edge couplers with a flat vertical profile. For the optimization, we combined the use of the Bayesian optimization method presented

in this thesis, with the use of shape derivative information, and a NURBS representation of the shape profile of the coupler. One of the results obtained was the design of an edge coupler, 10 μm in length, that presents a coupling efficiency of 91% at the design wavelength. This result represents an improvement of 30% in the coupling efficiency with respect to the best linear taper of the same length. As we saw, the penalty that one has to pay for this compact and efficient edge coupler is a narrower bandwidth.

Regarding possible future work along these lines, one could analyze the impact of using a larger number of control points to represent the shape of the freeform coupler. This increase would lead to the possibility of more complicated shapes, which could lead to more efficient designs. Another option which might be interesting to consider is the use of a quasi periodic grating with a y profile parameterized with a NURBS curve. This model would combine the advantages of having a freeform shape design with the benefits with respect to the vertical coupling provided by the grating edge coupler.

6 | Conclusions

This work proposes a series of techniques for the design of photonic nanostructures and presents methods to achieve their optimal designs. Photonic inverse design became a field of research by itself a few decades ago. Despite all the progress done along this time in, e.g., numerical methods, parametrizations of the geometry, or optimization algorithms, all these sub-fields of research are still relevant nowadays and progress achieved along these lines still has a major impact in the development of the field. This thesis covers some of these topics: optimization algorithms, numerical methods for the design of structures, and the use of these methods to optimize photonic structures modeled with, e.g., freeform shape parametrizations.

One of the main difficulties in the design of photonic structures is that the electromagnetic simulation of the structure often requires long computational times. We speak here about tens of minutes or even hours. This fact limits the number of simulations that can be done in a reasonable amount of time, which makes it quite a challenge to find designs with good performances. In the first chapter after the theoretical background, that is in chapter 2, we investigate the use of Bayesian optimization with Gaussian processes and the use of derivative information for the design of these computationally expensive structures. As we discuss in the chapter, this optimization technique shows good convergence rates with respect to the number of simulations. However, one problem of Gaussian processes is that they suffer from scalability problems, which limits their efficient use to only computationally more expensive problems. However, the good convergence rates that the method presents would be interesting also for the optimization of structures able to be simulated within a few minutes or even tens of seconds. In this work, we propose and demonstrate two different methods to mitigate the scalability problems: the use of a matrix update scheme for the decomposition of the covariance matrix and the use of a continuously updated local Gaussian process model.

While this chapter has been focusing on the computational aspects independent of the specific scientific problem, we discuss the aspects important to the scientific domain of their application in a following chapter. That is chapter 3. As we are interested in light-matter-interactions, we present a set of tools to design isolated structures. The tools are based on a dedicated method to expand the scattered field from the structure into a basis of VSWFs. This method does not depend on the shape of the surface across which the integrals for the decomposition are calculated. The method was implemented into the finite element solver JCMSuite, which also allows to compute shape and material derivatives of the expansion. However, the expansion can be easily integrated in most of the numerical methods available to solve Maxwell's equations and is quite general in its formulation. We also show a specific implementation for the fast calculation of the decomposition for cylindrically symmetric objects and an implementation for the calculation of the T-matrix of isolated scatterers. Based on these results, we propose a methodology for the adjoint optimization of the design of metasurfaces composed of individual

scatterers. The scatterers can have complicated shapes and each of these shapes can be different than the others.

Finally, we apply the methods described in chapters 2 and 3 to the design of two different photonic structures: optimal electromagnetically chiral helices and waveguide edge couplers.

Maximal electromagnetically chiral objects are interesting structures because of the extreme difference in their response to illuminations with light of different well defined helicity, such as, e.g., circularly polarized plane waves of different handedness. Helices with high values of electromagnetic chirality had already been shown for illumination wavelengths around 200 μm . In this work, we found helices with high em-chirality for wavelengths down to 3 μm and with values above 0.8 for wavelengths down to 800 nm. We also show how the electromagnetic chirality of the helices systematically decreases as one enters the range of optical and near infrared frequencies. We also analyze the properties of one of the optimal helices, showing remarkable differences in its scattering and absorption cross sections for illuminations with circularly polarized plane waves of different handedness. To finalize the study of the optimal electromagnetically chiral helices, we also analyze the performance of angle independent circularly polarized light filters that consists of such extremal scatterers. The results, even if not fully conclusive due to multiple simplifications in the estimation, indicate the potential of such structures for different applications.

The waveguide edge coupler studied in this work is part of an interchip communication architecture for photonic integrated circuits. Its functionality within the architecture is the reduction of energy losses in the interconnection between silicon optical waveguides and photonic wire bonds. The main figure of merit of edge couplers is the power coupling efficiency, although it is also important to obtain designs with small spatial footprints. In this thesis, we optimize linear adiabatic tapers and we also propose and optimize edge couplers with a freeform parametrization. We show designs of linear tapers with efficiencies above 95% for spectral bandwidths longer than 500 nm for a central operational wavelength of 1550 nm. We also obtain compact freeform couplers with efficiencies above 90% for structures with lengths down to 10 μm . The design at 10 μm represents an efficiency 30 absolute percent higher than the optimal linear tapers of the same length.

With regard to future developments along the lines of research presented in this thesis, one could investigate the use of hybrid techniques for optimizations that allow to exploit the statistical tractability provided by Gaussian processes with other methods for pattern recognition such as, e.g., dimensionality reduction procedures. For the topic of design of isolated structures, one interesting continuation of the work would be the implementation of an iterative solver for the calculation of the scattered field in multi particle systems, presented in section 4.5. This code could also serve, among other things, to do a rigorous analysis of the angle independent circularly polarized filter presented in chapter 5. Another improvement for the design of multi particle systems would be the fully automation of the adjoint procedure including a package for the automatic differentiation of the objective functions.

Regarding the design of chiral objects, a natural extension of the work would be the optimization of freeform chiral wires and the use of topology optimization for the design of different types of chiral objects. Here, it would be interesting to also use constraints that lead to designs easier to implement with current manufacturing technologies. The design of freeform wires could be done using the same procedure as we used in this thesis for the design of the helices.

For the last topic presented in the thesis, the design of edge couplers, the most natural way to continue with the work would be to extend the design optimization of the same proposed freeform structure using a larger number of control points and the experimental demonstration of the different optimal designs obtained.

Overall, the developments presented in this thesis provided us with a number of useful tools to optimize different interesting photonic structures and, at the same time, offer interesting topics for future research.

Bibliography

- [A1] P.-I. Schneider, X. Garcia-Santiago, V. Soltwisch, M. Hammerschmidt, S. Burger, and C. Rockstuhl, “Benchmarking five global optimization approaches for nano-optical shape optimization and parameter reconstruction,” *ACS Photonics*, vol. 6, no. 11, pp. 2726–2733, 2019.
- [A2] X. Garcia-Santiago, S. Burger, C. Rockstuhl, and P.-I. Schneider, “Bayesian optimization with improved scalability and derivative information for efficient design of nanophotonic structures,” *Journal of Lightwave Technology*, 2020.
- [A3] X. Garcia-Santiago, P.-I. Schneider, C. Rockstuhl, and S. Burger, “Shape design of a reflecting surface using Bayesian optimization,” *Journal of Physics: Conference Series*, vol. 963, p. 012 003, 2018.
- [A4] P.-I. Schneider, X. Garcia-Santiago, C. Rockstuhl, and S. Burger, “Global optimization of complex optical structures using Bayesian optimization based on Gaussian processes,” in *Digital Optical Technologies 2017*, vol. 10335, 2017, pp. 141–149.
- [A5] D. Werdehausen, X. Garcia-Santiago, S. Burger, I. Staude, T. Pertsch, C. Rockstuhl, and M. Decker, “Modelling optical materials at the single scatterer level - the transition from homogeneous to heterogeneous materials,” *Advanced Optical Materials*, vol. n/a, 2020.
- [A6] X. Garcia-Santiago, M. Hammerschmidt, S. Burger, C. Rockstuhl, I. Fernandez-Corbaton, and L. Zschiedrich, “Decomposition of scattered electromagnetic fields into vector spherical wave functions on surfaces with general shapes,” *Physical Review B*, vol. 99, no. 4, p. 045 406, 2019.
- [A7] F. Graf, J. Feis, X. Garcia-Santiago, M. Wegener, C. Rockstuhl, and I. Fernandez-Corbaton, “Achiral, helicity preserving, and resonant structures for enhanced sensing of chiral molecules,” *ACS Photonics*, vol. 6, no. 2, pp. 482–491, 2019.
- [A8] J. Feis, D. Beutel, J. Köpfler, X. Garcia-Santiago, C. Rockstuhl, M. Wegener, and I. Fernandez-Corbaton, “Helicity-preserving optical cavity modes for enhanced sensing of chiral molecules,” *Physical Review Letters*, vol. 124, no. 3, p. 033 201, 2020.
- [A9] A. Rahimzadegan, D. Arslan, D. Dams, A. Groner, X. Garcia-Santiago, R. Alaei, I. Fernandez-Corbaton, T. Pertsch, I. Staude, and C. Rockstuhl, “Beyond dipolar Huygens’ metasurfaces for full-phase coverage and unity transmittance,” *Nanophotonics*, 2019.
- [A10] P. Gutsche, X. Garcia-Santiago, P.-I. Schneider, K. M. McPeak, M. Nieto-Vesperinas, and S. Burger, “Role of geometric shape in chiral optics,” *Symmetry*, vol. 12, no. 1, p. 158, 2020.
- [A11] X. Garcia-Santiago, S. Burger, C. Rockstuhl, and I. Fernandez-Corbaton, “Measuring the electromagnetic chirality of 2D arrays under normal illumination,” *Optics Letters*, vol. 42, no. 20, pp. 4075–4078, 2017.
- [A12] X. Garcia-Santiago, M. Hammerschmidt, S. Burger, J. Sachs, P. Fisher, M. Knöller, T. Arens, F. Hettlich, R. Griesmaier, I. Fernandez-Corbaton, and C. Rockstuhl,

- “Towards maximal electromagnetically chiral scatterers at optical frequencies,” *In preparation*, vol. 0, no. 0, pp. 1–15, 2020.
- [1] T. Hiramoto, “Five nanometre CMOS technology,” *Nature Electronics*, vol. 2, no. 12, pp. 557–558, 2019.
 - [2] M. Waldow, H. Schneider, F. Tu, B. Szafranek, K. Gries, D. Rhinow, S. Vollmar, A. Krugmann, R. Schoenberger, and W. Pauls, “High-end EUV photomask repairs for 5nm technology and beyond,” in *Photomask Technology 2020*, International Society for Optics and Photonics, vol. 11518, 2020, p. 1 151 808.
 - [3] D. De Simone and G. Vandenberghe, “Printability study of EUV double patterning for CMOS metal layers,” in *Extreme Ultraviolet (EUV) Lithography X*, International Society for Optics and Photonics, vol. 10957, 2019, 109570Q.
 - [4] H. H. Radamson, X. He, Q. Zhang, J. Liu, H. Cui, J. Xiang, Z. Kong, W. Xiong, J. Li, and J. Gao, “Miniaturization of CMOS,” *Micromachines*, vol. 10, no. 5, p. 293, 2019.
 - [5] G. Kramer, M. De Andrade, R. Roy, and P. Chowdhury, “Evolution of optical access networks: Architectures and capacity upgrades,” *Proceedings of the IEEE*, vol. 100, no. 5, pp. 1188–1196, 2012.
 - [6] M. Ma, *Current research progress of optical networks*. Springer, 2009.
 - [7] E. Commission, *Energy roadmap 2050*. Publications Office of the European Union, 2012.
 - [8] J. Rogelj, M. Den Elzen, N. Höhne, T. Fransen, H. Fekete, H. Winkler, R. Schaeffer, F. Sha, K. Riahi, and M. Meinshausen, “Paris agreement climate proposals need a boost to keep warming well below 2 °C,” *Nature*, vol. 534, no. 7609, pp. 631–639, 2016.
 - [9] J. A. Altabas, O. Gallardo, G. S. Valdecasa, M. Squartecchia, D. Izquierdo, S. Sarmiento, M. Barrio, J. A. Lazaro, I. Garces, and J. B. Jensen, “Roadmap for next generation optical networks based on quasi-coherent receivers,” in *2020 22nd International Conference on Transparent Optical Networks (ICTON)*, IEEE, 2020, pp. 1–4.
 - [10] Y. Ji, J. Zhang, Y. Xiao, and Z. Liu, “5g flexible optical transport networks with large-capacity, low-latency and high-efficiency,” *China Communications*, vol. 16, no. 5, pp. 19–32, 2019.
 - [11] G. Wilson, M. M. Al-Jassim, W. Metzger, S. W. Glunz, P. Verlinden, X. Gang, L. Mansfield, B. J. Stanbery, K. Zhu, and Y. e. a. Yan, “The 2020 photovoltaic technologies roadmap,” *Journal of Physics D: Applied Physics*, 2020.
 - [12] A. Rajagopal, K. Yao, and A. K. Y. Jen, “Toward perovskite solar cell commercialization: A perspective and research roadmap based on interfacial engineering,” *Advanced Materials*, vol. 30, no. 32, p. 1 800 455, 2018.
 - [13] A. Louwen, W. Van Sark, R. Schropp, and A. Faaij, “A cost roadmap for silicon heterojunction solar cells,” *Solar Energy Materials and Solar Cells*, vol. 147, pp. 295–314, 2016.
 - [14] A. Zekry, *A road map for transformation from conventional to photovoltaic energy generation and its challenges*, 2020.
 - [15] S. E. Sofia, H. Wang, A. Bruno, J. L. Cruz-Campa, T. Buonassisi, and I. M. Peters, “Roadmap for cost-effective, commercially-viable perovskite silicon tandems for the current and future PV market,” *Sustainable Energy & Fuels*, vol. 4, no. 2, pp. 852–862, 2020.
 - [16] T. S. Humble and E. P. DeBenedictis, “Quantum realism,” *Computer*, vol. 52, no. 6, pp. 13–17, 2019.
 - [17] M. Y. Vardi, “Quantum hype and quantum skepticism,” *Communications of the ACM*, vol. 62, no. 5, pp. 7–7, 2019.

- [18] National Academies of Sciences, Engineering, and Medicine, *Quantum computing: progress and prospects*, E. Grumblin and M. Horowitz, Eds. National Academies Press, 2019.
- [19] G. A. Quantum and collaborators, “Hartree-Fock on a superconducting qubit quantum computer,” *Science*, vol. 369, no. 6507, pp. 1084–1089, 2020.
- [20] Y. Alexeev, D. Bacon, K. R. Brown, R. Calderbank, L. D. Carr, F. T. Chong, B. DeMarco, D. Englund, E. Farhi, B. Fefferman, *et al.*, “Quantum computer systems for scientific discovery,” *arXiv preprint arXiv:1912.07577*, 2019.
- [21] E. I. Amoiralis and I. K. Nikolos, “Freeform deformation versus B-spline representation in inverse airfoil design,” *Journal of Computing and Information Science in Engineering*, vol. 8, no. 2, 2008.
- [22] S. Harries, C. Abt, and M. Brenner, “Upfront CAD—parametric modeling techniques for shape optimization,” in *Advances in Evolutionary and Deterministic Methods for Design, Optimization and Control in Engineering and Sciences*, Springer, 2019, pp. 191–211.
- [23] O. Sigmund and S. Torquato, “Design of materials with extreme thermal expansion using a three-phase topology optimization method,” *Journal of the Mechanics and Physics of Solids*, vol. 45, no. 6, pp. 1037–1067, 1997.
- [24] M. Y. Wang, X. Wang, and D. Guo, “A level set method for structural topology optimization,” *Computer Methods in Applied Mechanics and Engineering*, vol. 192, no. 1-2, pp. 227–246, 2003.
- [25] J. S. Jensen and O. Sigmund, “Systematic design of photonic crystal structures using topology optimization: Low-loss waveguide bends,” *Applied Physics Letters*, vol. 84, no. 12, pp. 2022–2024, 2004.
- [26] P. I. Borel, A. Harpøth, L. H. Frandsen, M. Kristensen, P. Shi, J. S. Jensen, and O. Sigmund, “Topology optimization and fabrication of photonic crystal structures,” *Optics Express*, vol. 12, no. 9, pp. 1996–2001, 2004.
- [27] Y. Augenstein and C. Rockstuhl, “Inverse design of nanophotonic devices with structural integrity,” *ACS Photonics*, vol. 7, no. 8, pp. 2190–2196, 2020.
- [28] K. S. Friis and O. Sigmund, “Robust topology design of periodic grating surfaces,” *Journal of the Optical Society of America B*, vol. 29, no. 10, pp. 2935–2943, 2012.
- [29] F. Wang, B. S. Lazarov, and O. Sigmund, “On projection methods, convergence and robust formulations in topology optimization,” *Structural and Multidisciplinary Optimization*, vol. 43, no. 6, pp. 767–784, 2011.
- [30] F. Wang, J. S. Jensen, and O. Sigmund, “Robust topology optimization of photonic crystal waveguides with tailored dispersion properties,” *Journal of the Optical Society of America B*, vol. 28, no. 3, pp. 387–397, 2011.
- [31] H. Men, K. Y. K. Lee, R. M. Freund, J. Peraire, and S. G. Johnson, “Robust topology optimization of three-dimensional photonic-crystal band-gap structures,” *Optics Express*, vol. 22, no. 19, pp. 22 632–22 648, 2014.
- [32] D. Piccinotti, K. F. MacDonald, S. Gregory, I. Youngs, and N. I. Zheludev, “Artificial intelligence for photonics and photonic materials,” *Reports on Progress in Physics*, 2020.
- [33] M. H. Tahersima, K. Kojima, T. Koike-Akino, D. Jha, B. Wang, C. Lin, and K. Parsons, “Deep neural network inverse design of integrated photonic power splitters,” *Scientific Reports*, vol. 9, no. 1, pp. 1–9, 2019.
- [34] D. Liu, Y. Tan, E. Khoram, and Z. Yu, “Training deep neural networks for the inverse design of nanophotonic structures,” *ACS Photonics*, vol. 5, no. 4, pp. 1365–1369, 2018.

- [35] T. W. Hughes, M. Minkov, Y. Shi, and S. Fan, "Training of photonic neural networks through in situ backpropagation and gradient measurement," *Optica*, vol. 5, no. 7, pp. 864–871, 2018.
- [36] K. Yao, R. Unni, and Y. Zheng, "Intelligent nanophotonics: Merging photonics and artificial intelligence at the nanoscale," *Nanophotonics*, vol. 8, no. 3, pp. 339–366, 2019.
- [37] J. Jiang, D. Sell, S. Hoyer, J. Hickey, J. Yang, and J. A. Fan, "Free-form diffractive metagrating design based on generative adversarial networks," *ACS Nano*, vol. 13, no. 8, pp. 8872–8878, 2019.
- [38] J. Jiang and J. A. Fan, "Global optimization of dielectric metasurfaces using a physics-driven neural network," *Nano Letters*, vol. 19, no. 8, pp. 5366–5372, 2019.
- [39] J. C. Maxwell, *A dynamical theory of the electromagnetic field*. Wipf and Stock Publishers, 1996.
- [40] A. Kirsch and F. Hettlich, *Mathematical Theory of Time-harmonic Maxwell's Equations*. Springer, 2016.
- [41] J. D. Jackson, *Classical Electrodynamics*. Wiley, 1999.
- [42] M. I. Mishchenko, L. D. Travis, and A. A. Lacis, *Scattering, absorption, and emission of light by small particles*. Cambridge University Press, 2002.
- [43] C. Jingyang, X. Penggen, and L. Shu, "Vector wave function expansion for solving electromagnetic scattering by buried objects," *Journal of Electronics (China)*, vol. 8, no. 3, pp. 239–246, 1991.
- [44] Y.-L. Xu, "Electromagnetic scattering by an aggregate of spheres," *Applied Optics*, vol. 34, no. 21, pp. 4573–4588, 1995.
- [45] I. Fernandez Corbaton, "Helicity and duality symmetry in light matter interactions: Theory and applications," PhD thesis, Macquarie University, Faculty of Science, Engineering, Department of Physics, and Astronomy, 2014.
- [46] I. Bialynicki-Birula, "Photon wave function," in *Progress in Optics*, vol. 36, Elsevier, 1996, pp. 245–294.
- [47] M. Ibanescu, Y. Fink, S. Fan, E. L. Thomas, and J. D. Joannopoulos, "An all-dielectric coaxial waveguide," *Science*, vol. 289, no. 5478, pp. 415–419, 2000.
- [48] A. W. Snyder and J. Love, *Optical waveguide theory*. Springer Science & Business Media, 2012.
- [49] A. Taflove, A. Oskooi, and S. G. Johnson, *Advances in FDTD computational electrodynamics: photonics and nanotechnology*. Artech house, 2013.
- [50] M. Boroditsky, R. Coccioli, and E. Yablonovitch, "Analysis of photonic crystals for light-emitting diodes using the finite-difference time domain technique," in *Physics and Simulation of Optoelectronic Devices VI*, International Society for Optics and Photonics, vol. 3283, 1998, pp. 184–190.
- [51] B. R. Archambeault, O. M. Ramahi, and C. Brench, *EMI/EMC computational modeling handbook*. Springer Science & Business Media, 2012, vol. 630.
- [52] C.-p. Yu and H.-c. Chang, "Compact finite-difference frequency-domain method for the analysis of two-dimensional photonic crystals," *Optics Express*, vol. 12, no. 7, pp. 1397–1408, 2004.
- [53] Y. Shi, W. Shin, and S. Fan, "Multi-frequency finite-difference frequency-domain algorithm for active nanophotonic device simulations," *Optica*, vol. 3, no. 11, pp. 1256–1259, 2016.
- [54] J. T. Costa, M. G. Silveirinha, and S. I. Maslovski, "Finite-difference frequency-domain method for the extraction of effective parameters of metamaterials," *Physical Review B*, vol. 80, no. 23, p. 235 124, 2009.
- [55] P. Monk, "Analysis of a finite element method for Maxwell's equations," *SIAM Journal on Numerical Analysis*, vol. 29, no. 3, pp. 714–729, 1992.

- [56] P. Monk, *Finite element methods for Maxwell's equations*. Oxford University Press, 2003.
- [57] S. Burger, L. Zschiedrich, J. Pomplun, and F. Schmidt, "JCMSuite: An adaptive FEM solver for precise simulations in nano-optics," in *Integrated Photonics and Nanophotonics Research and Applications*, Optical Society of America, 2008, ITuE4.
- [58] J. Pomplun, S. Burger, L. Zschiedrich, and F. Schmidt, "Adaptive finite element method for simulation of optical nano structures," *Physica Status Solidi (B)*, vol. 244, no. 10, pp. 3419–3434, 2007.
- [59] S. Brenner and R. Scott, *The mathematical theory of finite element methods*. Springer Science & Business Media, 2007, vol. 15.
- [60] P. Yeh, *Optical waves in layered media*. Wiley New York, 1988, vol. 95.
- [61] H. Benisty, R. Stanley, and M. Mayer, "Method of source terms for dipole emission modification in modes of arbitrary planar structures," *Journal of the Optical Society of America A*, vol. 15, no. 5, pp. 1192–1201, 1998.
- [62] G. Mie, "Contributions to the optics of turbid media, particularly of colloidal metal solutions," *Contributions to the optics of turbid media, particularly of colloidal metal solutions Transl. into ENGLISH from Ann. Phys.(Leipzig)*, v. 25, no. 3, 1908 p 377-445, 1976.
- [63] T. Wriedt, *Mie theory: a review*. Springer, 2012, pp. 53–71.
- [64] I. Stroud, *Boundary representation modelling techniques*. Springer Science & Business Media, 2006.
- [65] SAS, Open CASCADE, *Open CASCADE Technology*, version 7.4, Oct. 2020. [Online]. Available: <http://www.opencascade.org>.
- [66] F. Machado, N. Malpica, and S. Borromeo, "Parametric CAD modeling for open source scientific hardware: Comparing OpenSCAD and FreeCAD Python scripts," *Plos one*, vol. 14, no. 12, e0225795, 2019.
- [67] The FreeCAD Team, *FreeCad*, version 0.18.4, Jul. 2020. [Online]. Available: <https://www.freecadweb.org>.
- [68] G. E. Farin and G. Farin, *Curves and surfaces for CAGD: a practical guide*. Morgan Kaufmann, 2002.
- [69] H. Si, "TetGen, a Delaunay-based quality tetrahedral mesh generator," *ACM Transactions on Mathematical Software (TOMS)*, vol. 41, no. 2, 11, 2015.
- [70] T. ANSYS, *5.0 user's guide*, 2008.
- [71] V. N. Parthasarathy, C. M. Graichen, and A. F. Hathaway, "A comparison of tetrahedron quality measures," *Finite Elements in Analysis and Design*, vol. 15, no. 3, pp. 255–261, 1994.
- [72] P. M. Knupp, "Algebraic mesh quality metrics," *SIAM Journal on Scientific Computing*, vol. 23, no. 1, pp. 193–218, 2001.
- [73] E. Popov, *Gratings: theory and numeric applications*. Institut Fresnel, 2012.
- [74] L. W. Zschiedrich, "Transparent boundary conditions for Maxwell's equations: Numerical concepts beyond the PML method," PhD thesis, 2009.
- [75] L. Zschiedrich, R. Klose, A. Schädle, and F. Schmidt, "A new finite element realization of the perfectly matched layer method for Helmholtz scattering problems on polygonal domains in two dimensions," *Journal of Computational and Applied Mathematics*, vol. 188, no. 1, pp. 12–32, 2006.
- [76] A. Schädle, L. Zschiedrich, S. Burger, R. Klose, and F. Schmidt, "Domain decomposition method for Maxwell's equations: Scattering off periodic structures," *Journal of Computational Physics*, vol. 226, no. 1, pp. 477–493, 2007.
- [77] F. Rapetti, "High order edge elements on simplicial meshes," *ESAIM: Mathematical Modelling and Numerical Analysis-Modélisation Mathématique et Analyse Numérique*, vol. 41, no. 6, pp. 1001–1020, 2007.

- [78] D. Felbacq, *Advanced Numerical and Theoretical Methods for Photonic Crystals and Metamaterials*, ser. 2053-2571. Morgan & Claypool Publishers, 2016, 1-1 to 1–15.
- [79] E. Sonnendrücker and A. Ratnani, “Advanced finite element methods,” *Lecture notes at the Max-Planck-Institut für Plasmaphysik und Zentrum Mathematik, TU München*, 2016.
- [80] J. R. Magnus and H. Neudecker, *Matrix differential calculus with applications in statistics and econometrics*. John Wiley & Sons, 2019.
- [81] S. Burger, L. Zschiedrich, J. Pomplun, F. Schmidt, and B. Bodermann, “Fast simulation method for parameter reconstruction in optical metrology,” in *Metrology, Inspection, and Process Control for Microlithography XXVII*, International Society for Optics and Photonics, vol. 8681, 2013, p. 868 119.
- [82] M. Kollmann, “Sensitivity analysis: The direct and adjoint method,” Master’s thesis, Johannes Kepler Universität Linz, 2010.
- [83] T. W. Hughes, I. A. D. Williamson, M. Minkov, and S. Fan, “Forward-mode differentiation of Maxwell’s equations,” *ACS Photonics*, vol. 6, no. 11, pp. 3010–3016, 2019.
- [84] L. N. Trefethen and D. Bau, *Numerical linear algebra*. 1997, vol. 50.
- [85] C. M. Lalau-Keraly, S. Bhargava, O. D. Miller, and E. Yablonovitch, “Adjoint shape optimization applied to electromagnetic design,” *Optics Express*, vol. 21, no. 18, pp. 21 693–21 701, 2013.
- [86] P. Hansen, “Adjoint sensitivity analysis for nanophotonic structures,” PhD thesis, Stanford University, 2014.
- [87] J. S. Jensen and O. Sigmund, “Topology optimization for nano-photonics,” *Laser & Photonics Reviews*, vol. 5, no. 2, pp. 308–321, 2011.
- [88] Y. Elesin, B. S. Lazarov, J. S. Jensen, and O. Sigmund, “Design of robust and efficient photonic switches using topology optimization,” *Photonics and Nanostructures-Fundamentals and Applications*, vol. 10, no. 1, pp. 153–165, 2012.
- [89] R. Bellman, *Dynamic Programming*. Dover Publications, 2003.
- [90] G. Hughes, “On the mean accuracy of statistical pattern recognizers,” *IEEE Transactions on Information Theory*, vol. 14, no. 1, pp. 55–63, 1968.
- [91] T. Oommen, D. Misra, N. K. C. Twarakavi, A. Prakash, B. Sahoo, and S. Bandopadhyay, “An objective analysis of support vector machine based classification for remote sensing,” *Mathematical Geosciences*, vol. 40, no. 4, pp. 409–424, 2008.
- [92] J. Kennedy and R. Eberhart, “Particle swarm optimization,” in *Proceedings of ICNN’95-International Conference on Neural Networks*, IEEE, vol. 4, 1995, pp. 1942–1948.
- [93] R. Eberhart and J. Kennedy, “Particle swarm optimization,” in *Proceedings of the IEEE International Conference on Neural Networks*, Citeseer, vol. 4, 1995, pp. 1942–1948.
- [94] Y. Shi and R. C. Eberhart, “Empirical study of particle swarm optimization,” in *Proceedings of the 1999 Congress on Evolutionary Computation-CEC99 (Cat. No. 99TH8406)*, IEEE, vol. 3, 1999, pp. 1945–1950.
- [95] Y. Wang, M. Miao, J. Lv, L. Zhu, K. Yin, H. Liu, and Y. Ma, “An effective structure prediction method for layered materials based on 2d particle swarm optimization algorithm,” *The Journal of Chemical Physics*, vol. 137, no. 22, p. 224 108, 2012.
- [96] B. S. Darki and N. Granpayeh, “Improving the performance of a photonic crystal ring-resonator-based channel drop filter using particle swarm optimization method,” *Optics Communications*, vol. 283, no. 20, pp. 4099–4103, 2010.
- [97] K. Price, R. M. Storn, and J. A. Lampinen, *Differential evolution: a practical approach to global optimization*. Springer Science & Business Media, 2006.

- [98] R. Storn and K. Price, "Differential evolution—a simple and efficient heuristic for global optimization over continuous spaces," *Journal of Global Optimization*, vol. 11, no. 4, pp. 341–359, 1997.
- [99] D. S. Weile and E. Michielssen, "Genetic algorithm optimization applied to electromagnetics: A review," *IEEE Transactions on Antennas and Propagation*, vol. 45, no. 3, pp. 343–353, 1997.
- [100] M. F. Schubert, F. W. Mont, S. C., D. J. Poxson, J. K. Kim, and E. F. Schubert, "Design of multilayer antireflection coatings made from co-sputtered and low-refractive-index materials by genetic algorithm," *Optics Express*, vol. 16, no. 8, pp. 5290–5298, 2008.
- [101] A. K. Qin, V. L. Huang, and P. N. Suganthan, "Differential evolution algorithm with strategy adaptation for global numerical optimization," *IEEE Transactions on Evolutionary Computation*, vol. 13, no. 2, pp. 398–417, 2008.
- [102] T. Feichtner, O. Selig, M. Kiunke, and B. Hecht, "Evolutionary optimization of optical antennas," *Physical Review Letters*, vol. 109, no. 12, p. 127 701, 2012.
- [103] S. Kirkpatrick, C. D. Gelatt, and M. P. Vecchi, "Optimization by simulated annealing," *Science*, vol. 220, no. 4598, pp. 671–680, 1983.
- [104] E. H. L. Aarts and P. J. M. van Laarhoven, "Simulated annealing: A pedestrian review of the theory and some applications," in *Pattern Recognition Theory and Applications*, P. A. Devijver and J. Kittler, Eds., Springer Berlin Heidelberg, 1987, pp. 179–192.
- [105] H. Szu and R. Hartley, "Fast simulated annealing," *Physics Letters A*, vol. 122, no. 3-4, pp. 157–162, 1987.
- [106] L. Ingber, "Simulated annealing: Practice versus theory," *Mathematical and Computer Modelling*, vol. 18, no. 11, pp. 29–57, 1993.
- [107] H. Parviainen, *PyDe: Global optimization using differential evolution in Python*, <https://github.com/hpparvi/PyDE>, version 1.5, Feb. 2016.
- [108] P. e. a. Virtanen, "SciPy 1.0: Fundamental Algorithms for Scientific Computing in Python," *Nature Methods*, vol. 17, pp. 261–272, 2020. doi: <https://doi.org/10.1038/s41592-019-0686-2>.
- [109] M. G. et al, *GNU Scientific Library Reference Manual (3rd Ed.)* 2008, isbn: 0954612078. [Online]. Available: <http://www.gnu.org/software/gsl/>.
- [110] S. M. e. a. Castillo-Hair, *PSO: Particle swarm optimization with constraint support*, <https://github.com/tisimst/pyswarm>, version 1.5, Sep. 2015.
- [111] S. Yang and X. Yao, "Population-based incremental learning with associative memory for dynamic environments," *IEEE Transactions on Evolutionary Computation*, vol. 12, no. 5, pp. 542–561, 2008.
- [112] M. Sebag and A. Ducoulombier, "Extending population-based incremental learning to continuous search spaces," in *International Conference on Parallel Problem Solving from Nature*, Springer, 1998, pp. 418–427.
- [113] M. Pelikan and H. Mühlenbein, "Marginal distributions in evolutionary algorithms," in *Proceedings of the International Conference on Genetic Algorithms Mendel*, Cite-seer, vol. 98, 1998, pp. 90–95.
- [114] M. Pelikan and H. Mühlenbein, "The bivariate marginal distribution algorithm," in *Advances in Soft Computing*, 1999, pp. 521–535.
- [115] L. Lozada-Chang and R. Santana, "Univariate marginal distribution algorithm dynamics for a class of parametric functions with unitation constraints," *Information Sciences*, vol. 181, no. 11, pp. 2340–2355, 2011.
- [116] H. Muhlenbein and T. Mahnig, "Convergence theory and applications of the factorized distribution algorithm," *Journal of Computing and Information Technology*, vol. 7, no. 1, pp. 19–32, 1999.

- [117] R. Santana, “A markov network based factorized distribution algorithm for optimization,” in *European Conference on Machine Learning*, Springer, 2003, pp. 337–348.
- [118] D. R. Jones, “A taxonomy of global optimization methods based on response surfaces,” *Journal of Global Optimization*, vol. 21, no. 4, pp. 345–383, 2001.
- [119] S. Carr, R. Garnett, and C. Lo, “BASC: Applying Bayesian optimization to the search for global minima on potential energy surfaces,” in *International Conference on Machine Learning*, 2016, pp. 898–907.
- [120] J. Kirschner, M. Mutný, N. Hiller, R. Ischebeck, and A. Krause, “Adaptive and safe Bayesian optimization in high dimensions via one-dimensional subspaces,” K. Chaudhuri and R. Salakhutdinov, Eds., ser. *Proceedings of Machine Learning Research*, vol. 97, *Proceeding of Machine Learning Research*, 2019, pp. 3429–3438.
- [121] B. Shahriari, K. Swersky, Z. Wang, R. P. Adams, and N. De Freitas, “Taking the human out of the loop: A review of Bayesian optimization,” *Proceedings of the IEEE*, vol. 104, no. 1, pp. 148–175, 2015.
- [122] R. Jin, W. Chen, and T. W. Simpson, “Comparative studies of metamodelling techniques under multiple modelling criteria,” *Structural and Multidisciplinary Optimization*, vol. 23, no. 1, pp. 1–13, 2001.
- [123] P. Ye and G. Pan, “Global optimization method using adaptive and parallel ensemble of surrogates for engineering design optimization,” *Optimization*, vol. 66, no. 7, pp. 1135–1155, 2017.
- [124] K. Holmström, “An adaptive radial basis algorithm (ARBF) for expensive black-box global optimization,” *Journal of Global Optimization*, vol. 41, no. 3, pp. 447–464, 2008.
- [125] C. E. Rasmussen and C. K. I. Williams, *Gaussian processes for machine learning*. MIT press Cambridge, MA, 2006.
- [126] M. Kuss, “Gaussian process models for robust regression, classification, and reinforcement learning,” PhD thesis, Technische Universität Darmstadt, Darmstadt, Germany, 2006.
- [127] J. Bernardo, J. Berger, A. Dawid, A. Smith, *et al.*, “Regression and classification using Gaussian process priors,” *Bayesian Statistics*, vol. 6, p. 475, 1998.
- [128] J. Q. Shi and T. Choi, *Gaussian process regression analysis for functional data*. CRC Press, 2011.
- [129] F. A. Viana, R. T. Haftka, and L. T. Watson, “Efficient global optimization algorithm assisted by multiple surrogate techniques,” *Journal of Global Optimization*, vol. 56, no. 2, pp. 669–689, 2013.
- [130] J. Močkus, “On Bayesian methods for seeking the extremum,” in *Optimization techniques IFIP technical conference*, 1975, pp. 400–404.
- [131] J. Močkus, *Bayesian approach to global optimization: theory and applications*. 2012, vol. 37.
- [132] J. Močkus, “On a Bayesian method for seeking an extremum,” *Automatika I Vychislitel'naja Tekhnika*, no. 3, 1972.
- [133] M. Pelikan, D. E. Goldberg, and E. Cantú-Paz, “BOA: The Bayesian optimization algorithm,” in *Proceedings of the Genetic and Evolutionary Computation Conference GECCO-99*, vol. 1, 1999, pp. 525–532.
- [134] T. Bayes and N. Price, “Lii. An essay towards solving a problem in the doctrine of chances. By the late rev. Mr. Bayes, F. R. S. communicated by Mr. Price, in a letter to John Canton, A. M. F. R. S.,” *Philosophical Transactions of the Royal Society*, vol. 53, pp. 370–418, 1763.

- [135] J. Snoek, O. Rippel, K. Swersky, R. Kiros, N. Satish, N. Sundaram, M. Patwary, M. Prabhath, and R. Adams, “Scalable Bayesian optimization using deep neural networks,” in *International Conference on Machine Learning*, 2015, pp. 2171–2180.
- [136] F. Hutter, H. H. Hoos, and K. Leyton-Brown, “Sequential model-based optimization for general algorithm configuration,” in *International Conference on Learning and Intelligent Optimization*, Springer, 2011, pp. 507–523.
- [137] J. Bergstra and Y. Bengio, “Random search for hyper-parameter optimization,” *Journal of Machine Learning Research*, vol. 13, no. 1, pp. 281–305, 2012.
- [138] R. Martinez-Cantin, “Bayesopt: A Bayesian optimization library for nonlinear optimization, experimental design and bandits,” *Journal of Machine Learning Research*, vol. 15, no. 1, pp. 3735–3739, 2014.
- [139] P. I. Frazier, “Bayesian optimization,” in *Recent Advances in Optimization and Modeling of Contemporary Problems*, INFORMS, 2018, pp. 255–278.
- [140] C. Oh, E. Gavves, and M. Welling, “BOCK: Bayesian optimization with cylindrical kernels,” *arXiv preprint arXiv:1806.01619*, 2018.
- [141] P. I. Frazier and J. Wang, “Bayesian optimization for materials design,” in *Information Science for Materials Discovery and Design*, 2016, pp. 45–75.
- [142] A. Marco, P. Hennig, J. Bohg, S. Schaal, and S. Trimpe, “Automatic LQR tuning based on Gaussian process global optimization,” in *2016 IEEE International Conference on Robotics and Automation (ICRA)*, IEEE, 2016, pp. 270–277.
- [143] P. Murugan, “Hyperparameters optimization in deep convolutional neural network/Bayesian approach with Gaussian process prior,” *arXiv preprint arXiv:1712.07233*, 2017.
- [144] N. Srinivas, A. Krause, S. M. Kakade, and M. Seeger, “Gaussian process optimization in the bandit setting: No regret and experimental design,” *Proceeding of the International Conference on Machine Learning*, pp. 1105–1122, 2010.
- [145] W. K. Härdle, M. Müller, S. Sperlich, and A. Werwatz, *Nonparametric and semi-parametric models*. Springer Science & Business Media, 2012.
- [146] S. Efromovich, *Nonparametric curve estimation: methods, theory, and applications*. Springer Science & Business Media, 2008.
- [147] L. Györfi, M. Kohler, A. Krzyzak, and H. Walk, *A distribution-free theory of non-parametric regression*. Springer Science & Business Media, 2006.
- [148] R. M. Neal, “Bayesian learning for neural networks,” PhD thesis, University of Toronto, 1995.
- [149] J. Sacks, W. J. Welch, T. J. Mitchell, and H. P. Wynn, “Design and analysis of computer experiments,” *Statistical Science*, vol. 4, no. 4, pp. 409–423, 1989.
- [150] V. Perrone, R. Jenatton, M. Seeger, and C. Archambeau, “Multiple adaptive Bayesian linear regression for scalable Bayesian optimization with warm start,” *arXiv preprint arXiv:1712.02902*, 2017.
- [151] D. Eriksson, M. Pearce, J. Gardner, R. D. Turner, and M. Poloczek, “Scalable global optimization via local Bayesian optimization,” in *Advances in Neural Information Processing Systems*, 2019, pp. 5496–5507.
- [152] G. van Veenendaal, “Tree-GP: A scalable Bayesian global numerical optimization algorithm,” Master’s thesis, 2015.
- [153] P. Abrahamsen, *A review of Gaussian random fields and correlation functions*, 1997.
- [154] M. L. Stein, *Interpolation of spatial data: some theory for kriging*. Springer Science & Business Media, 2012.
- [155] H. Mohammadi, R. L. Riche, N. Durrande, E. Touboul, and X. Bay, “An analytic comparison of regularization methods for Gaussian processes,” *arXiv preprint arXiv:1602.00853*, 2016.

- [156] L. Foster, A. Waagen, N. Aijaz, M. Hurley, A. Luis, J. Rinsky, C. Satyavolu, M. J. Way, P. Gazis, and A. Srivastava, “Stable and efficient Gaussian process calculations,” *Journal of Machine Learning Research*, vol. 10, no. 31, pp. 857–882, 2009.
- [157] J. R. Koehler and A. B. Owen, “Computer experiments,” *Design and Analysis of Experiments*, vol. 13, pp. 261–308, 1996.
- [158] E. Solak, R. Murray-Smith, W. E. Leithead, D. J. Leith, and C. E. Rasmussen, “Derivative observations in Gaussian process models of dynamic systems,” in *Advances in Neural Information Processing Systems*, 2003, pp. 1057–1064.
- [159] J. Riihimäki and A. Vehtari, “Gaussian processes with monotonicity information,” in *Proceedings of the Thirteenth International Conference on Artificial Intelligence and Statistics*, 2010, pp. 645–652.
- [160] A. Papoulis and S. U. Pillai, *Probability, random variables, and stochastic processes*. Tata McGraw-Hill Education, 2002.
- [161] A. Wu, M. C. Aoi, and J. W. Pillow, “Exploiting gradients and Hessians in Bayesian optimization and Bayesian quadrature,” *arXiv preprint arXiv:1704.00060*, 2017.
- [162] E. Charniak, “Bayesian networks without tears,” *AI Magazine*, vol. 12, no. 4, pp. 50–50, 1991.
- [163] M. A. Osborne, R. Garnett, and S. J. Roberts, “Gaussian processes for global optimization,” in *3rd International Conference on Learning and Intelligent Optimization (LION3)*, 2009, pp. 1–15.
- [164] P. Hennig and C. J. Schuler, “Entropy search for information-efficient global optimization,” *Journal of Machine Learning Research*, vol. 13, no. 1, pp. 1809–1837, 2012.
- [165] H.-M. Gutmann, “A radial basis function method for global optimization,” *Journal of Global Optimization*, vol. 19, no. 3, pp. 201–227, 2001.
- [166] M. Locatelli, “Bayesian algorithms for one-dimensional global optimization,” *Journal of Global Optimization*, vol. 10, no. 1, pp. 57–76, 1997.
- [167] N. De Freitas, A. Smola, and M. Zoghi, “Exponential regret bounds for Gaussian process bandits with deterministic observations,” *Proceeding of the International Conference on Machine Learning*, pp. 1743–1750, 2012.
- [168] E. Kaufmann, O. Cappé, and A. Garivier, “On Bayesian upper confidence bounds for bandit problems,” in *Artificial Intelligence and Statistics*, 2012, pp. 592–600.
- [169] C. Zhu, R. H. Byrd, P. Lu, and J. Nocedal, “Algorithm 778: L-BFGS-B: Fortran subroutines for large-scale bound-constrained optimization,” *ACM Transactions on Mathematical Software (TOMS)*, vol. 23, no. 4, pp. 550–560, 1997.
- [170] F. E. Curtis and X. Que, “A quasi-Newton algorithm for nonconvex, nonsmooth optimization with global convergence guarantees,” *Mathematical Programming Computation*, vol. 7, no. 4, pp. 399–428, 2015.
- [171] J. Nocedal and S. Wright, *Numerical optimization*. Springer Science & Business Media, 2006.
- [172] S. Molesky, Z. Lin, A. Y. Piggott, W. Jin, J. Vucković, and A. W. Rodriguez, “Inverse design in nanophotonics,” *Nature Photonics*, vol. 12, no. 11, p. 659, 2018.
- [173] Y. Augenstein, A. Vetter, B. V. Lahijani, H. P. Herzig, C. Rockstuhl, and M.-S. Kim, “Inverse photonic design of functional elements that focus Bloch surface waves,” *Light: Science & Applications*, vol. 7, no. 1, pp. 1–9, 2018.
- [174] T. Phan, D. Sell, E. W. Wang, S. Doshay, K. Edee, J. Yang, and J. A. Fan, “High-efficiency, large-area, topology-optimized metasurfaces,” *Light: Science & Applications*, vol. 8, no. 1, pp. 1–9, 2019.
- [175] Y. Chen, Y. Chi, J. Fan, and C. Ma, “Gradient descent with random initialization: Fast global convergence for nonconvex phase retrieval,” *Mathematical Programming*, vol. 176, no. 1–2, pp. 5–37, 2019.

-
- [176] J. Wu, M. Poloczek, A. G. Wilson, and P. Frazier, “Bayesian optimization with gradients,” in *Advances in Neural Information Processing Systems*, 2017, pp. 5267–5278.
- [177] J. Snoek, H. Larochelle, and R. P. Adams, “Practical Bayesian optimization of machine learning algorithms,” in *Advances in Neural Information Processing Systems*, 2012, pp. 2951–2959.
- [178] G. H. Golub and C. F. Van Loan, *Matrix Computations. 4th Edition*. The Johns Hopkins University Press, Baltimore, 2013.
- [179] C. L. Lawson, R. J. Hanson, D. R. Kincaid, and F. T. Krogh, “Basic linear algebra subprograms for fortran usage,” *ACM Transactions on Mathematical Software*, vol. 5, no. 3, pp. 308–323, 1979.
- [180] E. Anderson, Z. Bai, J. Dongarra, A. Greenbaum, A. McKenney, J. Du Croz, S. Hammarling, J. Demmel, C. Bischof, and D. Sorensen, “LAPACK: A portable linear algebra library for high-performance computers,” in *Proceedings of the 1990 ACM/IEEE Conference on Supercomputing*, IEEE Computer Society Press, 1990, pp. 2–11.
- [181] P. C. Hansen, “The truncated svd as a method for regularization,” *BIT Numerical Mathematics*, vol. 27, no. 4, pp. 534–553, 1987.
- [182] M. N. Gibbs, “Bayesian Gaussian processes for regression and classification,” PhD thesis, Citeseer, 1998.
- [183] R. A. Brown, “Building a balanced k-d tree in $o(kn \log n)$ time,” *arXiv preprint arXiv:1410.5420*, 2014.
- [184] J. L. Bentley, “K-d trees for semidynamic point sets,” in *Proceedings of the 6th Annual Symposium on Computational Geometry*, 1990, pp. 187–197.
- [185] Y. Chen, L. Zhou, Y. Tang, J. P. Singh, N. Bouguila, C. Wang, H. Wang, and J. Du, “Fast neighbor search by using revised k-d tree,” *Information Sciences*, vol. 472, pp. 145–162, 2019.
- [186] A. Beygelzimer, S. Kakade, and J. Langford, “Cover trees for nearest neighbor,” in *Proceedings of the 23rd International Conference on Machine Learning*, 2006, pp. 97–104.
- [187] M. Izbicki and C. Shelton, “Faster cover trees,” in *International Conference on Machine Learning*, 2015, pp. 1162–1170.
- [188] K. L. Cheung and A. W.-C. Fu, “Enhanced nearest neighbour search on the r-tree,” *ACM SIGMOD Record*, vol. 27, no. 3, pp. 16–21, 1998.
- [189] A. Guttman, “R-trees: A dynamic index structure for spatial searching,” in *Proceedings of the 1984 ACM SIGMOD International Conference on Management of Data*, 1984, pp. 47–57.
- [190] Y. Manolopoulos, A. Nanopoulos, A. N. Papadopoulos, and Y. Theodoridis, *R-trees: Theory and Applications*. Springer Science & Business Media, 2010.
- [191] J. Zhao, C. Long, S. Xiong, C. Liu, and Z. Yuan, “A new k nearest neighbours algorithm using cell grids for 3d scattered point cloud,” *Elektronika ir Elektrotechnika*, vol. 20, no. 1, pp. 81–87, 2014.
- [192] L. A. Piegl and W. Tiller, “Algorithm for finding all k nearest neighbors,” *Computer-Aided Design*, vol. 34, no. 2, pp. 167–172, 2002.
- [193] P. Goyal, J. S. Challa, D. Kumar, A. Bhat, S. Balasubramaniam, and N. Goyal, “Grid-R-tree: A data structure for efficient neighborhood and nearest neighbor queries in data mining,” *International Journal of Data Science and Analytics*, vol. 10, no. 1, pp. 25–47, 2020.
- [194] L. A. Rastrigin, “Systems of extremal control,” *Nauka*, 1974.
- [195] F. Hoffmeister and T. Bäck, “Genetic algorithms and evolution strategies: Similarities and differences,” in *International Conference on Parallel Problem Solving from Nature*, 1990, pp. 455–469.

- [196] T. Coenen, F. B. Arango, A. F. Koenderink, and A. Polman, “Directional emission from a single plasmonic scatterer,” *Nature Communications*, vol. 5, p. 3250, 2014.
- [197] E. Rusak, I. Staude, M. Decker, J. Sautter, A. E. Miroshnichenko, D. A. Powell, D. N. Neshev, and Y. S. Kivshar, “Hybrid nanoantennas for directional emission enhancement,” *Applied Physics Letters*, vol. 105, p. 221 109, 2014.
- [198] B. Stout, A. Devilez, B. Rolly, and N. Bonod, “Multipole methods for nanoantennas design: Applications to Yagi-Uda configurations,” *Journal of the Optical Society of America B*, vol. 28, no. 5, pp. 1213–1223, 2011.
- [199] D. S. Filonov, A. E. Krasnok, A. P. S., P. V. Kapitanova, E. A. Nenasheva, Y. S. Kivshar, and P. A. Belov, “Experimental verification of the concept of all-dielectric nanoantennas,” *Applied Physics Letters*, vol. 100, no. 20, p. 201 113, 2012.
- [200] A. Pors, M. Willatzen, O. Albrechtsen, and S. I. Bozhevolnyi, “From plasmonic nanoantennas to split-ring resonators: Tuning scattering strength,” *Journal of the Optical Society of America B*, vol. 27, no. 8, pp. 1680–1687, 2010.
- [201] D. Vercruysse, X. Zheng, Y. Sonnefraud, N. Verellen, G. D. Martino, L. Lagae, G. V. AE, V. Moshchalkov, S. Maier, and P. V. Dorpe, “Directional fluorescence emission by individual v-antennas explained by mode expansion,” *ACS Nano*, vol. 8, no. 8, pp. 8232–8241, 2014.
- [202] H. Shen, R. Y. Chou, Y. Y. Hui, Y. He, Y. Cheng, H. Changand, L. Tong, Q. Gong, and G. Lu, “Directional fluorescence emission from a compact plasmonic-diamond hybrid nanostructure,” *Laser & Photonics Reviews*, vol. 10, p. 647, 2016.
- [203] C. W. Heaps and G. C. Schatz, “Modeling super-resolution SERS using a T-matrix method to elucidate molecule-nanoparticle coupling and the origins of localization errors,” *Journal of Chemical Physics*, vol. 146, p. 224 201, 2017.
- [204] W. Liu and Y. S. Kivshar, “Multipolar interference effects in nanophotonics,” *Philosophical Transactions of the Royal Society A*, vol. 375, p. 20 160 317, 2017.
- [205] P. Grahn, A. Shevchenko, and M. Kaivola, “Electromagnetic multipole theory for optical nanomaterials,” *New Journal of Physics*, vol. 14, no. 9, p. 093 033, 2012.
- [206] D. A. Powell, “Interference between the modes of an all-dielectric meta-atom,” *Physical Review Applied*, vol. 7, p. 034 006, 2017.
- [207] J. Petschulat, J. Yang, C. Menzel, C. Rockstuhl, A. Chipouline, P. Lalanne, A. Tünnermann, F. Lederer, and T. Pertsch, “Understanding the electric and magnetic response of isolated metaatoms by means of a multipolar field decomposition,” *Optics Express*, vol. 18, no. 14, pp. 14 454–14 466, 2010.
- [208] M. Khorasaninejad and F. Capasso, “Metalenses: Versatile multifunctional photonic components,” *Science*, vol. 358, no. 6367, eaam8100, 2017.
- [209] N. Yu and F. Capasso, “Optical metasurfaces and prospect of their applications including fiber optics,” *Journal of Lightwave Technology*, vol. 33, no. 12, pp. 2344–2358, 2015.
- [210] A. Arbabi, E. Arbabi, S. M. Kamali, Y. Horie, S. Han, and A. Faraon, “Miniature optical planar camera based on a wide-angle metasurface doublet corrected for monochromatic aberrations,” *Nature Communications*, vol. 7, no. 13682, pp. 1–9, 2016.
- [211] M. F. Schumann, S. Wiesendanger, J. C. Goldschmidt, B. Bläsi, K. Bittkau, U. W. Paetzold, A. Sprafke, R. B. Wehrspohn, C. Rockstuhl, and M. Wegener, “Cloaked contact grids on solar cells by coordinate transformations: Designs and prototypes,” *Optica*, vol. 2, no. 10, pp. 850–853, 2015.
- [212] P. Manley, S. Burger, F. Schmidt, and M. Schmid, “Design principles for plasmonic nanoparticle devices,” in *Progress in Nonlinear Nano-optics*, Springer, 2015, pp. 223–247.

- [213] I. Fernandez-Corbaton, M. Fruhnert, and C. Rockstuhl, "Objects of maximum electromagnetic chirality," *Physical Review X*, vol. 6, no. 3, p. 031 013, 2016.
- [214] B. Auguié, W. R. C. Somerville, S. Roache, and E. C. L. Ru, "Numerical investigation of the Rayleigh hypothesis for electromagnetic scattering by a particle," *Journal of Optics*, vol. 18, no. 7, p. 075 007, 2016.
- [215] R. H. T. .Bates, "Analytic constraints on electromagnetic field computations," *IEEE Transactions on Microwave Theory and Techniques*, vol. 23, no. 8, pp. 605–623, 1975.
- [216] P. van den Berg and J. Fokkema, "The Rayleigh hypothesis in the theory of diffraction by a cylindrical obstacle," *IEEE Transactions on Antennas and Propagation*, vol. 27, no. 5, pp. 577–583, 1979.
- [217] P. C. Waterman, "Matrix formulation of electromagnetic scattering," *Proceedings of the IEEE*, vol. 53, no. 8, pp. 805–812, 1965.
- [218] G. Demésy, J.-C. Auger, and B. Stout, "Scattering matrix of arbitrarily shaped objects: Combining finite elements and vector partial waves," *Journal of the Optical Society of America A*, vol. 35, no. 8, pp. 1401–1409, 2018.
- [219] T. Wriedt and Y. Eremin, "The generalized multipole technique for light scattering," *Springer Series on Atomic, Optical, and Plasma Physics*, 2018.
- [220] A. Egel, L. Pattelli, G. Mazzamuto, D. S. Wiersma, and U. Lemmer, "CELES: CUDA-accelerated simulation of electromagnetic scattering by large ensembles of spheres," *Journal of Quantitative Spectroscopy and Radiative Transfer*, vol. 199, pp. 103–110, 2017.
- [221] P. Waterman and C. V. McCarthy, "Numerical solution of electromagnetic scattering problems," MITRE CORP BEDFORD MA, Tech. Rep., 1968.
- [222] M. Fruhnert, I. Fernandez-Corbaton, V. Yannopapas, and C. Rockstuhl, "Computing the T-matrix of a scattering object with multiple plane wave illuminations," *Beilstein Journal of Nanotechnology*, vol. 8, pp. 614–626, 2017.
- [223] I. Fernandez-Corbaton, S. Nanz, R. Alaaee, and C. Rockstuhl, "Exact dipolar moments of a localized electric current distribution," *Optics Express*, vol. 23, no. 26, pp. 33 044–33 064, 2015.
- [224] R. Alaaee, C. Rockstuhl, and I. Fernandez-Corbaton, "An electromagnetic multipole expansion beyond the long-wavelength approximation," *Optics Communications*, vol. 407, pp. 17–21, 2018.
- [225] B. Blankrot and C. Heitzinger, "Efficient computational design and optimization of dielectric metamaterial structures," *IEEE Journal on Multiscale and Multiphysics Computational Techniques*, vol. 4, pp. 234–244, 2019.
- [226] E. Cartan, *Les systemes differentiels exterieure et leur applications geometriques*. Hermann, 1971, isbn: 9782705656843.
- [227] D. Colton and R. Kress, *Inverse acoustic and electromagnetic scattering theory*. Springer Science & Business Media, 2012.
- [228] Q. Hu and J. Zou, "A nonoverlapping domain decomposition method for Maxwell's equations in three dimensions," *SIAM Journal of Numerical Analysis*, vol. 41, pp. 1682–1708, 2003.
- [229] JCMwave GmbH, *JCMsuite*, version 3.18.24, Sep. 2020. [Online]. Available: <https://www.jcmwave.com>.
- [230] H. U. Yang, J. D'Archangel, M. L. Sundheimer, E. Tucker, G. D. Boreman, and M. B. Raschke, "Optical dielectric function of silver," *Physical Review B*, vol. 91, no. 23, p. 235 137, 2015.
- [231] L. Demkowicz, *Computing with hp-adaptive finite elements: Volume 1 one and two dimensional elliptic and Maxwell problems*. Chapman and Hall/CRC, 2006.

- [232] A. Pucci, F. Neubrech, J. Aizpurua, T. Cornelius, and M. L. de La Chapelle, “Electromagnetic nanowire resonances for field-enhanced spectroscopy,” in *One-Dimensional Nanostructures*, Springer, 2008, pp. 175–215.
- [233] H. Chen, L. Shao, Q. Li, and J. Wang, “Gold nanorods and their plasmonic properties,” *Chemical Society Reviews*, vol. 42, no. 7, pp. 2679–2724, 2013.
- [234] O. Nicoletti, M. Wubs, N. A. Mortensen, W. Sigle, P. A. Van Aken, and P. A. Midgley, “Surface plasmon modes of a single silver nanorod: An electron energy loss study,” *Optics Express*, vol. 19, no. 16, pp. 15 371–15 379, 2011.
- [235] S. Link, M. B. Mohamed, and M. A. El-Sayed, “Simulation of the optical absorption spectra of gold nanorods as a function of their aspect ratio and the effect of the medium dielectric constant,” *The Journal of Physical Chemistry B*, vol. 103, no. 16, pp. 3073–3077, 1999.
- [236] T. A. Milligan, *Modern antenna design*. John Wiley & Sons, 2005.
- [237] F. Neubrech, T. Kolb, R. Lovrincic, G. Fahsold, A. Pucci, J. Aizpurua, T. W. Cornelius, M. E. Toimil-Molares, R. Neumann, and S. Karim, “Resonances of individual metal nanowires in the infrared,” *Applied Physics Letters*, vol. 89, no. 25, p. 253 104, 2006.
- [238] L. Novotny, “Effective wavelength scaling for optical antennas,” *Physical Review Letters*, vol. 98, no. 26, p. 266 802, 2007.
- [239] D. B. Rutledge, S. E. Schwarz, and A. T. Adams, “Infrared and submillimetre antennas,” *Infrared Physics*, vol. 18, no. 5–6, pp. 713–729, 1978.
- [240] Z. Wang, X. Cao, A. Ma, Y. Li, and Q. Zhou, “Analytical solution of metal nanowires at visible and near-infrared wavelength,” *Progress In Electromagnetics Research*, vol. 63, pp. 47–58, 2018.
- [241] A. Jakab, C. Rosman, Y. Khalavka, J. Becker, A. Trüger, U. Hohenester, and C. Sönnichsen, “Highly sensitive plasmonic silver nanorods,” *ACS Nano*, vol. 5, no. 9, pp. 6880–6885, 2011.
- [242] D. Vestler, I. Shishkin, E. A. Gurvitz, M. E. Nasir, A. Ben-Moshe, A. P. Slobozhanyuk, A. V. Krasavin, T. Levi-Belenkova, A. S. Shalin, and P. Ginzburg, “Circular dichroism enhancement in plasmonic nanorod metamaterials,” *Optics Express*, vol. 26, no. 14, pp. 17 841–17 848, 2018.
- [243] X. Liu, D. Li, X. Sun, Z. Li, H. Song, H. Jiang, and Y. Chen, “Tunable dipole surface plasmon resonances of silver nanoparticles by cladding dielectric layers,” *Scientific Reports*, vol. 5, p. 12 555, 2015.
- [244] P. Berini, “Surface plasmon photodetectors and their applications,” *Laser & Photonics Reviews*, vol. 8, no. 2, pp. 197–220, 2014.
- [245] E. Blank, “The discontinuous Galerkin method for Maxwell’s equations,” PhD thesis, Karlsruhe institute of technology, 2013.
- [246] C. Mätzler, “MATLAB functions for mie scattering and absorption, version 2,” *IAP Research Report*, vol. 8, no. 1, p. 9, 2002.
- [247] I. Fernandez-Corbaton, X. Zambrana-Puyalto, N. Tischler, X. Vidal, M. L. Juan, and G. Molina-Terriza, “Electromagnetic duality symmetry and helicity conservation for the macroscopic Maxwell’s equations,” *Physical Review Letters*, vol. 111, no. 6, p. 060 401, 2013.
- [248] X. Zambrana-Puyalto, I. Fernandez-Corbaton, M. Juan, X. Vidal, and G. Molina-Terriza, “Duality symmetry and kerker conditions,” *Optics Letters*, vol. 38, no. 11, pp. 1857–1859, 2013.
- [249] I. Fernandez-Corbaton, “Forward and backward helicity scattering coefficients for systems with discrete rotational symmetry,” *Optics Express*, vol. 21, no. 24, pp. 29 885–29 893, 2013.

- [250] E. Slivina, A. Abass, D. Bätzner, B. Strahm, C. Rockstuhl, and I. Fernandez-Corbaton, “Insights into backscattering suppression in solar cells from the helicity-preservation point of view,” *Physical Review Applied*, vol. 12, no. 5, p. 054 003, 2019.
- [251] X. Zambrana-Puyalto, X. Vidal, M. L. Juan, and G. Molina-Terriza, “Dual and anti-dual modes in dielectric spheres,” *Optics Express*, vol. 21, no. 15, pp. 17 520–17 530, 2013.
- [252] A. Rahimzadegan, C. Rockstuhl, and I. Fernandez-Corbaton, “Core-shell particles as building blocks for systems with high duality symmetry,” *Physical Review Applied*, vol. 9, p. 054 051, 5 2018.
- [253] M. Schäferling, D. Dregely, M. Hentschel, and H. Giessen, “Tailoring enhanced optical chirality: Design principles for chiral plasmonic nanostructures,” *Physical Review X*, vol. 2, no. 3, p. 031 010, 2012.
- [254] P. Gutsche and M. Nieto-Vesperinas, “Optical chirality of time-harmonic wave-fields for classification of scatterers,” *Scientific Reports*, vol. 8, no. 9416, pp. 1–13, 2018.
- [255] A. Zhan, T. K. Fryett, S. Colburn, and A. Majumdar, “Inverse design of optical elements based on arrays of dielectric spheres,” *Applied Optics*, vol. 57, no. 6, pp. 1437–1446, 2018.
- [256] O. R. Cruzan, “Translational addition theorems for spherical vector wave functions,” *Quarterly of Applied Mathematics*, vol. 20, pp. 33–40, 1962.
- [257] S. Stein, “Addition theorems for spherical wave functions,” *Quarterly of Applied Mathematics*, vol. 19, pp. 15–24, 1961.
- [258] M. Bartholomew-Biggs, S. Brown, B. Christianson, and L. Dixon, “Automatic differentiation of algorithms,” *Journal of Computational and Applied Mathematics*, vol. 124, no. 1-2, pp. 171–190, 2000.
- [259] J. Bradbury, R. Frostig, P. Hawkins, M. J. Johnson, C. Leary, D. Maclaurin, and S. Wanderman-Milne, *JAX: Composable transformations of Python+NumPy programs*, version 0.1.55, 2018. [Online]. Available: <http://github.com/google/jax>.
- [260] A. Rahimzadegan, D. Arslan, R. S. Suryadharma, S. Fasold, M. Falkner, T. Pertsch, I. Staude, and C. Rockstuhl, “Disorder-induced phase transitions in the transmission of dielectric metasurfaces,” *Physical Review Letters*, vol. 122, no. 1, p. 015 702, 2019.
- [261] W. T. B. Kelvin, *The molecular tactics of a crystal*. Clarendon Press, 1894.
- [262] Y.-P. Xue, C.-H. Cao, and Y.-G. Zheng, “Enzymatic asymmetric synthesis of chiral amino acids,” *Chemical Society Reviews*, vol. 47, no. 4, pp. 1516–1561, 2018.
- [263] M. J. Cope, “SAC 92. Understanding chirality: How molecules that are mirror images of each other can act differently in the body,” in *Analytical Proceedings*, Royal Society of Chemistry, vol. 30, 1993, pp. 498–500.
- [264] E. Mohammadi, K. L. Tsakmakidis, A. N. Askarpour, P. Dehkhoda, A. Tavakoli, and H. Altug, “Nanophotonic platforms for enhanced chiral sensing,” *ACS Photonics*, vol. 5, no. 7, pp. 2669–2675, 2018.
- [265] M. Hentschel, M. Schäferling, X. Duan, H. Giessen, and N. Liu, “Chiral plasmonics,” *Science Advances*, vol. 3, no. 5, e1602735, 2017.
- [266] M. Schäferling, X. Yin, N. Engheta, and H. Giessen, “Helical plasmonic nanostructures as prototypical chiral near-field sources,” *ACS Photonics*, vol. 1, no. 6, pp. 530–537, 2014.
- [267] H.-H. Jeong, A. G. Mark, M. Alarcón-Correa, I. Kim, P. Oswald, T.-C. Lee, and P. Fischer, “Dispersion and shape engineered plasmonic nanosensors,” *Nature Communications*, vol. 7, no. 11331, pp. 1–7, 2016.

- [268] S. M. Kelly, T. J. Jess, and N. C. Price, "How to study proteins by circular dichroism," *Biochimica et Biophysica Acta (BBA)-Proteins and Proteomics*, vol. 1751, no. 2, pp. 119–139, 2005.
- [269] R. D. Richardson, M. G. J. Baud, C. E. Weston, H. S. Rzepa, M. K. Kuimova, and M. J. Fuchter, "Dual wavelength asymmetric photochemical synthesis with circularly polarized light," *Chemical Science*, vol. 6, no. 7, pp. 3853–3862, 2015.
- [270] G. Yang, Y. Y. Xu, Z. D. Zhang, L. H. Wang, X. H. He, Q. J. Zhang, C. Y. Hong, and G. Zou, "Circularly polarized light triggered enantioselective thiolene polymerization reaction," *Chemical Communications*, vol. 53, no. 10, pp. 1735–1738, 2017.
- [271] C. He, G. Yang, Y. Kuai, S. Shan, L. Yang, J. Hu, D. Zhang, Q. Zhang, and G. Zou, "Dissymmetry enhancement in enantioselective synthesis of helical polydiacetylene by application of superchiral light," *Nature Communications*, vol. 9, no. 5117, pp. 1–8, 2018.
- [272] A. S. Chadha, D. Zhao, and W. Zhou, "An all-dielectric broadband high-transmission efficiency circular polarizer," in *Photonic and Phononic Properties of Engineered Nanostructures IV*, International Society for Optics and Photonics, vol. 8994, 2014, p. 89941M.
- [273] P. W. Fowler, "Quantification of chirality: Attempting the impossible," *Symmetry: Culture and Science*, vol. 16, no. 4, pp. 321–334, 2005.
- [274] A. B. Buda and K. Mislow, "A hausdorff chirality measure," *Journal of the American Chemical Society*, vol. 114, no. 15, pp. 6006–6012, 1992.
- [275] A. B. Buda, T. A. der Heyde, and K. Mislow, "On quantifying chirality," *Angewandte Chemie International Edition in English*, vol. 31, no. 8, pp. 989–1007, 1992.
- [276] R. W. Woody, "Circular dichroism," in *Methods in Enzymology*, vol. 246, Elsevier, 1995, pp. 34–71.
- [277] W.-K. Tung, *Group theory in physics: an introduction to symmetry principles, group representations, and special functions in classical and quantum physics*. World Scientific Publishing Company, 1985.
- [278] H. A. Wheeler, "A helical antenna for circular polarization," *Proceedings of the IRE*, vol. 35, no. 12, pp. 1484–1488, 1947.
- [279] J. K. Gansel, M. Wegener, S. Burger, and S. Linden, "Gold helix photonic metamaterials: A numerical parameter study," *Optics Express*, vol. 18, no. 2, pp. 1059–1069, 2010.
- [280] A. S. Chadha, D. Zhao, and W. Zhou, "Comparative study of metallic and dielectric helix photonic metamaterial," *Optical Materials Express*, vol. 4, no. 12, pp. 2460–2467, 2014.
- [281] P. Gutsche, R. Mäusle, and S. Burger, "Circular polarization phenomena in chiral nano-optical devices," in *Light, Energy and the Environment*, Optical Society of America, 2016, JW4A.4.
- [282] A. Ishikawa, T. Tanaka, and S. Kawata, "Negative magnetic permeability in the visible light region," *Physical Review Letters*, vol. 95, no. 23, p. 237 401, 2005.
- [283] Z.-Q. Wan and S.-X. Zhang, "Automatic differentiation for complex valued SVD," *arXiv preprint arXiv:1909.02659*, 2019.
- [284] K. A. O'Neil, "Critical points of the singular value decomposition," *SIAM Journal on Matrix Analysis and Applications*, vol. 27, no. 2, pp. 459–473, 2005.
- [285] N. van der Aa, H. Ter Morsche, and R. Mattheij, "Computation of eigenvalue and eigenvector derivatives for a general complex-valued eigensystem," *The Electronic Journal of Linear Algebra*, vol. 16, 2007.
- [286] K. M. McPeak, S. V. Jayanti, S. J. Kress, S. Meyer, S. Iotti, A. Rossinelli, and D. J. Norris, "Plasmonic films can easily be better: Rules and recipes," *ACS Photonics*, vol. 2, no. 3, pp. 326–333, 2015.

- [287] H.-J. Hagemann, W. Gudat, and C. Kunz, "Optical constants from the far infrared to the x-ray region: Mg, Al, Cu, Ag, Au, Bi, C, and Al₂O₃," *Journal of the Optical Society of America*, vol. 65, no. 6, pp. 742–744, 1975.
- [288] D. S. Jones, "A thin wire approximation," *SIAM Journal on Applied Mathematics*, vol. 50, no. 2, pp. 547–558, 1990.
- [289] M. W. Klein, C. Enkrich, M. Wegener, C. M. Soukoulis, and S. Linden, "Single-slit split-ring resonators at optical frequencies: Limits of size scaling," *Optics Letters*, vol. 31, no. 9, pp. 1259–1261, 2006.
- [290] J. Zhou, T. Koschny, M. Kafesaki, E. N. Economou, J. B. Pendry, and C. M. Soukoulis, "Saturation of the magnetic response of split-ring resonators at optical frequencies," *Physical Review Letters*, vol. 95, no. 22, p. 223 902, 2005.
- [291] I. Fernandez-Corbaton, D. Beutel, C. Rockstuhl, A. Pausch, and W. Klopper, "Computation of electromagnetic properties of molecular ensembles," *ChemPhysChem*, 2020.
- [292] R. Nagarajan, C. H. Joyner, R. P. Schneider, J. S. Bostak, T. Butrie, A. G. Dentai, V. G. Dominic, P. W. Evans, M. Kato, M. Kauffman, *et al.*, "Large-scale photonic integrated circuits," *IEEE Journal of Selected Topics in Quantum Electronics*, vol. 11, no. 1, pp. 50–65, 2005.
- [293] T. L. Koch and U. Koren, "Semiconductor photonic integrated circuits," *IEEE Journal of Quantum Electronics*, vol. 27, no. 3, pp. 641–653, 1991.
- [294] J. S. Orcutt, A. Khilo, M. A. Popović, C. W. Holzwarth, B. Moss, H. Li, M. S. Dahlem, T. D. Bonifield, F. X. Kärtner, E. P. Ippen, *et al.*, "Demonstration of an electronic photonic integrated circuit in a commercial scaled bulk CMOS process," in *Conference on Lasers and Electro-Optics*, Optical Society of America, 2008, CTuBB3.
- [295] J. Chovan and F. Uherek, "Photonic integrated circuits for communication systems," *Radioengineering*, vol. 27, no. 2, pp. 357–363, 2018.
- [296] M. A. Taubenblatt, "Optical interconnects for high-performance computing," *Journal of Lightwave Technology*, vol. 30, no. 4, pp. 448–457, 2011.
- [297] A. Hadke, "Design and evaluation of an optical CPU-DRAM interconnect," PhD thesis, University of California, Davis, 2009.
- [298] A. Hadke, T. Benavides, R. Amirtharajah, M. Farrens, and V. Akella, "Design and evaluation of an optical CPU-DRAM interconnect," in *2008 IEEE International Conference on Computer Design*, IEEE, 2008, pp. 492–497.
- [299] T. Alexoudi, N. Terzenidis, S. Pitris, M. Moralis-Pegios, P. Maniotis, C. Vagionas, C. Mitsolidou, G. Mourgias-Alexandris, G. T. Kanellos, A. Miliou, *et al.*, "Optics in computing: From photonic network-on-chip to chip-to-chip interconnects and disintegrated architectures," *Journal of Lightwave Technology*, vol. 37, no. 2, pp. 363–379, 2019.
- [300] P. Maniotis, "Computing architectures exploiting optical interconnect and optical memory technologies," PhD thesis, School of Informatics, Aristotle University of Thessaloniki, 2017.
- [301] T. Alexoudi, G. T. Kanellos, and N. Pleros, "Optical RAM and integrated optical memories: A survey," *Light: Science & Applications*, vol. 9, no. 91, pp. 1–16, 2020.
- [302] N. Savage, "Linking with light [high-speed optical interconnects]," *IEEE Spectrum*, vol. 39, no. 8, pp. 32–36, 2002.
- [303] P. R. Haugen, S. Rychnovsky, A. Husain, and L. D. Hutcheson, "Optical interconnects for high speed computing," *Optical Engineering*, vol. 25, no. 10, p. 251 076, 1986.
- [304] B. O. Kahle, E. C. Parish, T. A. Lane, and J. A. Quam, "Optical interconnects for interprocessor communications in the Connection Machine," in *Proceedings 1989*

- IEEE International Conference on Computer Design: VLSI in Computers and Processors*, IEEE Computer Society, 1989, pp. 58–59.
- [305] L. D. Hutcheson, “Optical computing: Evolution or revolution?” *Information System Management*, vol. 5, no. 2, pp. 83–89, 1988.
- [306] S. Borkar and A. A. Chien, “The future of microprocessors,” *Communications of the ACM*, vol. 54, no. 5, pp. 67–77, 2011.
- [307] D. Efnusheva, A. Cholakoska, and A. Tentov, “A survey of different approaches for overcoming the processor-memory bottleneck,” *International Journal of Computer Science and Information Technology*, vol. 9, no. 2, pp. 151–163, 2017.
- [308] S. Keyvaninia, G. Roelkens, D. Van Thourhout, C. Jany, M. Lamponi, A. Le Liepvre, F. Lelarge, D. Make, G.-H. Duan, D. Bordel, *et al.*, “Demonstration of a heterogeneously integrated III-V/SOI single wavelength tunable laser,” *Optics Express*, vol. 21, no. 3, pp. 3784–3792, 2013.
- [309] J. Van Campenhout, L. Liu, P. R. Romeo, D. Van Thourhout, C. Seassal, P. Regreny, L. Di Cioccio, J.-M. Fedeli, and R. Baets, “A compact SOI-integrated multiwavelength laser source based on cascaded InP microdisks,” *IEEE Photonics Technology Letters*, vol. 20, no. 16, pp. 1345–1347, 2008.
- [310] A. Abbasi, J. Verbist, J. Van Kerrebrouck, F. Lelarge, G.-H. Duan, X. Yin, J. Bauwelinck, G. Roelkens, and G. Morthier, “28 Gb/s direct modulation heterogeneously integrated C-band InP/SOI DFB laser,” *Optics Express*, vol. 23, no. 20, pp. 26 479–26 485, 2015.
- [311] A. Huang, C. Gunn, G.-L. Li, Y. Liang, S. Mirsaidi, A. Narashimha, and T. Pinguet, “A 10 Gb/s photonic modulator and WDM MUX/DEMUX integrated with electronics in 0.13 μm SOI CMOS,” in *2006 IEEE International Solid State Circuits Conference-Digest of Technical Papers*, IEEE, 2006, pp. 922–929.
- [312] G. T. Reed, G. Mashanovich, F. Y. Gardes, and D. J. Thomson, “Silicon optical modulators,” *Nature Photonics*, vol. 4, no. 8, pp. 518–526, 2010.
- [313] D. Morini, G. Rasigade, and L. Vivien, *High data-rate SOI optical modulator including a modified structure for reducing the capacitive effect between doped areas and a substrate*, US Patent 8,693,811, 2014.
- [314] R. Soref and B. Bennett, “Electrooptical effects in silicon,” *IEEE Journal of Quantum Electronics*, vol. 23, no. 1, pp. 123–129, 1987.
- [315] N. C. Helman, J. E. Roth, D. P. Bour, H. Altug, and D. A. B. Miller, “Misalignment-tolerant surface-normal low-voltage modulator for optical interconnects,” *IEEE Journal of Selected Topics in Quantum Electronics*, vol. 11, no. 2, pp. 338–342, 2005.
- [316] Z. Cheng, J. Dong, and X. Zhang, “Ultracompact optical switch using a single semisymmetric Fano nanobeam cavity,” *Optics Letters*, vol. 45, no. 8, pp. 2363–2366, 2020.
- [317] M. A. Meerasha, T. S. Meetei, G. Madhupriya, I. R. Rajan, M. Varadharajaperumal, and K. Pandiyan, “The design and analysis of a CMOS-compatible silicon photonic ON–OFF switch based on a mode-coupling mechanism,” *Journal of Computational Electronics*, pp. 1–9, 2020.
- [318] M. Cai, S. Wang, Z. Liu, Y. Wang, T. Han, and H. Liu, “Graphene electro-optical switch modulator by adjusting propagation length based on hybrid plasmonic waveguide in infrared band,” *Sensors*, vol. 20, no. 10, p. 2864, 2020.
- [319] M. Babaei, A. Zarifkar, and M. Miri, “Compact and broadband 2 x 2 optical switch based on hybrid plasmonic waveguides and curved directional couplers,” *Applied Optics*, vol. 59, no. 4, pp. 975–984, 2020.
- [320] Ö. Boyraz, P. Koonath, V. Raghunathan, and B. Jalali, “All optical switching and continuum generation in silicon waveguides,” *Optics Express*, vol. 12, no. 17, pp. 4094–4102, 2004.

- [321] G. Li, J. Yao, H. Thacker, A. Mekis, X. Zheng, I. Shubin, Y. Luo, J.-H. Lee, K. Raj, J. E. Cunningham, *et al.*, “Ultralow-loss, high-density SOI optical waveguide routing for macrochip interconnects,” *Optics Express*, vol. 20, no. 11, pp. 12 035–12 039, 2012.
- [322] G. Z. Mashanovich, M. M. Milošević, M. Nedeljkovic, N. Owens, B. Xiong, E. J. Teo, and Y. Hu, “Low loss silicon waveguides for the mid-infrared,” *Optics Express*, vol. 19, no. 8, pp. 7112–7119, 2011.
- [323] J. Cardenas, C. B. Poitras, J. T. Robinson, K. Preston, L. Chen, and M. Lipson, “Low loss etchless silicon photonic waveguides,” *Optics Express*, vol. 17, no. 6, pp. 4752–4757, 2009.
- [324] Y. Ma, Y. Zhang, S. Yang, A. Novack, R. Ding, A. E.-J. Lim, G.-Q. Lo, T. Baehr-Jones, and M. Hochberg, “Ultralow loss single layer submicron silicon waveguide crossing for SOI optical interconnect,” *Optics Express*, vol. 21, no. 24, pp. 29 374–29 382, 2013.
- [325] A. Layadi, A. Vonsovici, R. Orobtcouk, D. Pascal, and A. Koster, “Low-loss optical waveguide on standard SOI/SIMOX substrate,” *Optics Communications*, vol. 146, no. 1-6, pp. 31–33, 1998.
- [326] P. Dong, W. Qian, S. Liao, H. Liang, C.-C. Kung, N.-N. Feng, R. Shafiqi, J. Fong, D. Feng, A. V. Krishnamoorthy, *et al.*, “Low loss shallow-ridge silicon waveguides,” *Optics Express*, vol. 18, no. 14, pp. 14 474–14 479, 2010.
- [327] B. Jalali and S. Fathpour, “Silicon photonics,” *Journal of Lightwave Technology*, vol. 24, no. 12, pp. 4600–4615, 2006.
- [328] D. Thomson, A. Zilkie, J. E. Bowers, T. Komljenovic, G. T. Reed, L. Vivien, D. Marris-Morini, E. Cassan, L. Virot, J.-M. Fédéli, *et al.*, “Roadmap on silicon photonics,” *Journal of Optics*, vol. 18, no. 7, p. 073 003, 2016.
- [329] Y. Ding, H. Ou, J. Xu, and C. Peucheret, “Silicon photonic integrated circuit mode multiplexer,” *IEEE Photonics Technology Letters*, vol. 25, no. 7, pp. 648–651, 2013.
- [330] M. Hochberg, N. C. Harris, R. Ding, Y. Zhang, A. Novack, Z. Xuan, and T. Baehr-Jones, “Silicon photonics: The next fabless semiconductor industry,” *IEEE Solid-State Circuits Magazine*, vol. 5, no. 1, pp. 48–58, 2013.
- [331] T. Komljenovic, D. Huang, P. Pintus, M. A. Tran, M. L. Davenport, and J. E. Bowers, “Photonic integrated circuits using heterogeneous integration on silicon,” *Proceedings of the IEEE*, vol. 106, no. 12, pp. 2246–2257, 2018.
- [332] M. J. R. Heck, J. F. Bauters, M. L. Davenport, J. K. Doylend, S. Jain, G. Kurczveil, S. Srinivasan, Y. Tang, and J. E. Bowers, “Hybrid silicon photonic integrated circuit technology,” *IEEE Journal of Selected Topics in Quantum Electronics*, vol. 19, no. 4, p. 6 100 117, 2012.
- [333] D. Liang and J. E. Bowers, “Recent progress in lasers on silicon,” *Nature Photonics*, vol. 4, no. 8, pp. 511–517, 2010.
- [334] S. Keyvaninia, S. Verstuyft, L. Van Landschoot, F. Lelarge, G.-H. Duan, S. Mes-saoudene, J. M. Fedeli, T. De Vries, B. Smalbrugge, E. J. Geluk, *et al.*, “Heterogeneously integrated III-V/silicon distributed feedback lasers,” *Optics Letters*, vol. 38, no. 24, pp. 5434–5437, 2013.
- [335] A. Y. Liu, R. W. Herrick, O. Ueda, P. M. Petroff, A. C. Gossard, and J. E. Bowers, “Reliability of InAs/GaAs quantum dot lasers epitaxially grown on silicon,” *IEEE Journal of Selected Topics in Quantum Electronics*, vol. 21, no. 6, pp. 690–697, 2015.
- [336] N. Lindenmann, G. Balthasar, D. Hillerkuss, R. Schmogrow, M. Jordan, J. Leuthold, W. Freude, and C. Koos, “Photonic wire bonding: A novel concept for chip-scale interconnects,” *Optics Express*, vol. 20, no. 16, pp. 17 667–17 677, 2012.
- [337] N. Lindenmann, S. Dottermusch, M. L. Goedecke, T. Hoose, M. R. Billah, T. P. Onanuga, A. Hofmann, W. Freude, and C. Koos, “Connecting silicon photonic cir-

- cuits to multicore fibers by photonic wire bonding,” *Journal of lightwave Technology*, vol. 33, no. 4, pp. 755–760, 2015.
- [338] M. R. Billah, M. Blaicher, T. Hoose, P.-I. Dietrich, P. Marin-Palomo, N. Lindenmann, A. Nestic, A. Hofmann, U. Troppenz, M. Moehrle, *et al.*, “Hybrid integration of silicon photonics circuits and InP lasers by photonic wire bonding,” *Optica*, vol. 5, no. 7, pp. 876–883, 2018.
- [339] N. Lindenmann, G. Balthasar, R. Palmer, S. Schuele, J. Leuthold, W. Freude, and C. Koos, “Photonic wire bonding for single-mode chip-to-chip interconnects,” in *8th IEEE International Conference on Group IV Photonics*, IEEE, 2011, pp. 380–382.
- [340] A. Nestic, M. Blaicher, T. Hoose, A. Hofmann, M. Lauermann, Y. Kutuvantavida, M. Nöllenburg, S. Randel, W. Freude, and C. Koos, “Photonic-integrated circuits with non-planar topologies realized by 3D-printed waveguide overpasses,” *Optics Express*, vol. 27, no. 12, pp. 17 402–17 425, 2019.
- [341] F. Negrodo, M. Blaicher, A. Nestic, P. Kraft, J. Ott, W. Dörfler, C. Koos, and C. Rockstuhl, “Fast and reliable method to estimate losses of single-mode waveguides with an arbitrary 2D trajectory,” *Journal of the Optical Society of America A*, vol. 35, no. 6, pp. 1063–1073, 2018.
- [342] T. A. Ramadan and R. M. Osgood, “Adiabatic couplers: Design rules and optimization,” *Journal of Lightwave Technology*, vol. 16, no. 2, p. 277, 1998.
- [343] Y. Liu, W. Sun, H. Xie, N. Zhang, K. Xu, Y. Yao, S. Xiao, and Q. Song, “Adiabatic and ultracompact waveguide tapers based on digital metamaterials,” *IEEE Journal of Selected Topics in Quantum Electronics*, vol. 25, no. 3, pp. 1–6, 2018.
- [344] Y. Fu, T. Ye, W. Tang, and T. Chu, “Efficient adiabatic silicon-on-insulator waveguide taper,” *Photonics Research*, vol. 2, no. 3, A41–A44, 2014.
- [345] V. R. Almeida, R. R. Panepucci, and M. Lipson, “Nanotaper for compact mode conversion,” *Optics Letters*, vol. 28, no. 15, pp. 1302–1304, 2003.
- [346] J. Cardenas, C. B. Poitras, K. Luke, L.-W. Luo, P. A. Morton, and M. Lipson, “High coupling efficiency etched facet tapers in silicon waveguides,” *IEEE Photonics Technology Letters*, vol. 26, no. 23, pp. 2380–2382, 2014.
- [347] S. J. Hettrick, J. Wang, C. Li, J. S. Wilkinson, and D. P. Shepherd, “An experimental comparison of linear and parabolic tapered waveguide lasers and a demonstration of broad-stripe diode pumping,” *Journal of Lightwave Technology*, vol. 22, no. 3, p. 845, 2004.
- [348] G. Ren, S. Chen, Y. Cheng, and Y. Zhai, “Study on inverse taper based mode transformer for low loss coupling between silicon wire waveguide and lensed fiber,” *Optics Communications*, vol. 284, no. 19, pp. 4782–4788, 2011.
- [349] P. Suchoski and R. V. Ramaswamy, “Design of single-mode step-tapered waveguide sections,” *IEEE Journal of Quantum Electronics*, vol. 23, no. 2, pp. 205–211, 1987.
- [350] P. Cheben, D. X. Xu, S. Janz, and A. Densmore, “Subwavelength waveguide grating for mode conversion and light coupling in integrated optics,” *Optics Express*, vol. 14, no. 11, pp. 4695–4702, 2006.
- [351] P. Cheben, P. J. Bock, J. H. Schmid, J. Lapointe, S. Janz, D.-X. Xu, A. Densmore, A. Delâge, B. Lamontagne, and T. J. Hall, “Refractive index engineering with subwavelength gratings for efficient microphotonic couplers and planar waveguide multiplexers,” *Optics Letters*, vol. 35, no. 15, pp. 2526–2528, 2010.
- [352] V. Donzella, A. Sherwali, J. Flueckiger, S. T. Fard, S. M. Grist, and L. Chrostowski, “Sub-wavelength grating components for integrated optics applications on SOI chips,” *Optics Express*, vol. 22, no. 17, pp. 21 037–21 050, 2014.
- [353] P. Cheben, J. H. Schmid, S. Wang, D.-X. Xu, M. Vachon, S. Janz, J. Lapointe, Y. Painchaud, and M.-J. Picard, “Broadband polarization independent nanophotonic

- coupler for silicon waveguides with ultra-high efficiency,” *Optics Express*, vol. 23, no. 17, pp. 22 553–22 563, 2015.
- [354] N. Hatori, T. Shimizu, M. Okano, M. Ishizaka, T. Yamamoto, Y. Urino, M. Mori, T. Nakamura, and Y. Arakawa, “A hybrid integrated light source on a silicon platform using a trident spot-size converter,” *Journal of Lightwave Technology*, vol. 32, no. 7, pp. 1329–1336, 2014.
- [355] N. Hatori, Y. Urino, T. Shimizu, M. Okano, T. Yamamoto, M. Mori, T. Nakamura, and Y. Arakawa, “Quantum dot laser for a light source of an athermal silicon optical interposer,” in *Photonics*, Multidisciplinary Digital Publishing Institute, vol. 2, 2015, pp. 355–364.
- [356] K. Itou, Y. Kuno, Y. Hayashi, J. Suzuki, and N. Hojo, “Crystalline/amorphous si integrated optical couplers for 2D/3D,” *IEEE Journal of Selected Topics in Quantum Electronics*, vol. 22, 2016.
- [357] X. Mu, S. Wu, L. Cheng, X. Tu, and H. Y. Fu, “A compact adiabatic silicon photonic edge coupler based on silicon nitride/silicon trident structure,” in *2019 18th International Conference on Optical Communications and Networks (ICOON)*, IEEE, 2019, pp. 1–3.
- [358] M. Teng, A. Honardoost, Y. Alahmadi, S. S. Polkoo, K. Kojima, H. Wen, C. K. Renshaw, P. LiKamWa, G. Li, S. Fathpour, *et al.*, “Miniaturized silicon photonics devices for integrated optical signal processors,” *Journal of Lightwave Technology*, vol. 38, no. 1, pp. 6–17, 2020.
- [359] L. Vivien, S. Laval, E. Cassan, X. Le Roux, and D. Pascal, “2-D taper for low-loss coupling between polarization-insensitive microwaveguides and single-mode optical fibers,” *Journal of Lightwave Technology*, vol. 21, no. 10, p. 2429, 2003.
- [360] A. Sure, T. Dillon, J. Murakowski, C. Lin, D. Pustai, and D. W. Prather, “Fabrication and characterization of three-dimensional silicon tapers,” *Optics Express*, vol. 11, no. 26, pp. 3555–3561, 2003.
- [361] S. J. McNab, N. Moll, and Y. A. Vlasov, “Ultra-low loss photonic integrated circuit with membrane-type photonic crystal waveguides,” *Optics Express*, vol. 11, no. 22, pp. 2927–2939, 2003.
- [362] B. B. Bakir, A. V. De Gyves, R. Orobtcouk, P. Lyan, C. Porzier, A. Roman, and J.-M. Fedeli, “Low-loss (< 1 db) and polarization-insensitive edge fiber couplers fabricated on 200-mm silicon-on-insulator wafers,” *IEEE Photonics Technology Letters*, vol. 22, no. 11, pp. 739–741, 2010.
- [363] R. Marchetti, C. Lacava, L. Carroll, K. Gradkowski, and P. Minzioni, “Coupling strategies for silicon photonics integrated chips,” *Photonics Research*, vol. 7, no. 2, pp. 201–239, 2019.
- [364] X. Mu, S. Wu, L. Cheng, and H. Y. Fu, “Edge couplers in silicon photonic integrated circuits: A review,” *Applied Sciences*, vol. 10, no. 4, p. 1538, 2020.
- [365] L. Piegl, “On NURBS: A survey,” *IEEE Computer Graphics and Applications*, vol. 11, no. 1, pp. 55–71, 1991.
- [366] D. F. Rogers, *An introduction to NURBS: with historical perspective*. Elsevier, 2000.
- [367] L. Piegl and W. Tiller, *The NURBS book*. Springer Science & Business Media, 2012.
- [368] C. Sideris, E. Garza, and O. P. Bruno, “Ultrafast simulation and optimization of nanophotonic devices with integral equation methods,” *ACS Photonics*, vol. 6, no. 12, pp. 3233–3240, 2019.
- [369] L. H. Frandsen and O. Sigmund, “Inverse design engineering of all-silicon polarization beam splitters,” in *Photonic and Phononic Properties of Engineered Nanostructures VI*, International Society for Optics and Photonics, vol. 9756, 2016, 97560Y.

- [370] B. Shen, P. Wang, R. Polson, and R. Menon, “An integrated-nanophotonics polarization beamsplitter with $2.4 \times 2.4 \mu\text{m}^2$ footprint,” *Nature Photonics*, vol. 9, no. 6, pp. 378–382, 2015.
- [371] X. Qian, “Full analytical sensitivities in NURBS based isogeometric shape optimization,” *Computer Methods in Applied Mechanics and Engineering*, vol. 199, no. 29-32, pp. 2059–2071, 2010.

Appendices

A | Definition of the vector spherical wave functions

This appendix shows the definition of the vector spherical wave functions (VSWFs) $\mathbf{N}_{m,n}^J(\mathbf{r})$ and $\mathbf{M}_{m,n}^J(\mathbf{r})$, presented in section 2.2. This definition is obtained from [42], appendix C. Using spherical coordinates to represent a vector \mathbf{E}

$$\mathbf{E} = E_r \hat{\mathbf{r}} + E_\theta \hat{\boldsymbol{\theta}} + E_\phi \hat{\boldsymbol{\phi}} = (E_r, E_\theta, E_\phi), \quad (\text{A.1})$$

the VSWFs can be written as,

$$\mathbf{M}_{m,n}^J(\mathbf{r}) = E_{mn} (0, i\pi_{mn}(\theta), -\tau_{mn}(\theta)) Z_n^J(kr) e^{im\phi}, \quad (\text{A.2})$$

$$\mathbf{N}_{m,n}^J(\mathbf{r}) = E_{mn} (N_{m,nr}^J, N_{m,n\theta}^J, N_{m,n\phi}^J) e^{im\phi}, \quad (\text{A.3})$$

with the spherical vector components being

$$N_{m,nr}^J(\mathbf{r}) = n(n+1) P_n^m(\cos\theta) \frac{Z_n^J(kr)}{kr}, \quad (\text{A.4})$$

$$N_{m,n\theta}^J(\mathbf{r}) = \tau_{mn}(\theta) \frac{-nZ_n^J(kr) + krZ_{n-1}^J(kr)}{kr}, \quad (\text{A.5})$$

$$N_{m,n\phi}^J(\mathbf{r}) = i\pi_{mn}(\theta) \frac{-nZ_n^J(kr) + krZ_{n-1}^J(kr)}{kr}. \quad (\text{A.6})$$

The functions π_{mn} and τ_{mn} are defined as,

$$\pi_{mn}(\theta) = \frac{m}{\sin\theta} P_n^m(\cos\theta), \quad (\text{A.7})$$

$$\tau_{mn}(\theta) = \frac{n}{\tan\theta} P_n^m(\cos\theta) - \frac{(n+m)}{\sin\theta} P_{n-1}^m(\cos\theta), \quad (\text{A.8})$$

and $P_n^m(x)$ are the associated legendre polynomials,

$$P_n^m(x) = (-1)^m \frac{(1-x^2)^{m/2}}{2^l l!} \frac{d^{l+m}}{dx^{l+m}} (x^2-1)^l, \quad (\text{A.9})$$

The superscript J denotes solutions with different radial dependence. The radial dependence is given in terms of the different Bessel functions

$$Z_n^{(1)}(x) = j_n(x) = \sqrt{\frac{\pi}{2x}} J_{n+0.5}(x), \quad (\text{A.10})$$

$$Z_n^{(2)}(x) = y_n(x) = \sqrt{\frac{\pi}{2x}} Y_{n+0.5}(x), \quad (\text{A.11})$$

$$Z_n^{(3)}(x) = j_n(x) + iy_n(x), \quad (\text{A.12})$$

$$Z_n^{(4)}(x) = j_n(x) - iy_n(x). \quad (\text{A.13})$$

Finally, the values E_{mn} are normalization constants given by

$$E_{mn} = \sqrt{\frac{(2n+1)(n-m)!}{4\pi(n+1)(n+m)!}}. \quad (\text{A.14})$$

B | Multipole decomposition of a plane wave

The expansion of a plane wave, $\mathbf{E}(\mathbf{r}) = \mathbf{A}e^{i\mathbf{k}\cdot\mathbf{r}}$, into regular VSWFs is given by,

$$\mathbf{E}(\mathbf{r}) = \sum_{n=1}^{\infty} \sum_{m=-n}^n c_{\text{pw},m,n} \mathbf{N}_{m,n}^1(\mathbf{r}) + d_{\text{pw},m,n} \mathbf{M}_{m,n}^1(\mathbf{r}), \quad (\text{B.1})$$

with the complex coefficients $a_{\text{pw},m,n}$ and $b_{\text{pw},m,n}$

$$c_{\text{pw},m,n} = (-1)^m 4\pi \sqrt{\frac{2n+1}{4\pi n(n+1)}} \mathbf{A} \cdot \left(-i\pi_{m,n}^*(\theta)\hat{\theta} - \tau_{m,n}^*(\theta)\hat{\phi} \right) e^{-im\phi}, \quad (\text{B.2})$$

$$d_{\text{pw},m,n} = (-1)^m 4\pi \sqrt{\frac{2n+1}{4\pi n(n+1)}} \mathbf{A} \cdot \left(\tau_{m,n}^*(\theta)\hat{\theta} - i\pi_{m,n}^*(\theta)\hat{\pi} \right) e^{-im\phi}, \quad (\text{B.3})$$

where $\pi_{m,n}(\theta)$ and $\tau_{m,n}^*(\theta)$ are defined in Eqns. (A.7)-(A.8) and the angles θ and ϕ define the direction, $\hat{\mathbf{k}}$, of the wave vector,

$$\hat{\mathbf{k}}(\theta, \phi) = \hat{\mathbf{r}}(\theta, \phi) = (\sin(\theta) \cos(\phi), \sin(\theta) \sin(\phi), \cos(\theta)). \quad (\text{B.4})$$

The above vector is given in the Cartesian base.

If one defines the transversal electric, $\hat{\mathbf{v}}_{\text{TE}}(\theta, \phi)$, and transversal magnetic, $\hat{\mathbf{v}}_{\text{TM}}(\theta, \phi)$, unitary polarization vectors of a plane wave as

$$\hat{\mathbf{v}}_{\text{TE}}(\theta, \phi) = \hat{\phi}(\theta, \phi), \quad \hat{\mathbf{v}}_{\text{TM}}(\theta, \phi) = \hat{\theta}(\theta, \phi), \quad (\text{B.5})$$

one obtains that the multipole expansion of the plane wave

$$\mathbf{E}(\mathbf{r}) = (A_{\text{TE}}\hat{\mathbf{v}}_{\text{TE}}(\theta, \phi) + A_{\text{TM}}\hat{\mathbf{v}}_{\text{TM}}(\theta, \phi)) e^{i\mathbf{k}(\theta, \phi)\cdot\mathbf{r}} \quad (\text{B.6})$$

is given by

$$c_{\text{pw},m,n} = 4\pi(-1)^m \sqrt{\frac{2n+1}{4\pi n(n+1)}} \left(-iA_{\text{TE}} \pi_{m,n}^*(\theta) + A_{\text{TM}} \tau_{m,n}^*(\theta) \right) e^{-im\phi}, \quad (\text{B.7})$$

$$d_{\text{pw},m,n} = 4\pi(-1)^m \sqrt{\frac{2n+1}{4\pi n(n+1)}} \left(A_{\text{TE}} \tau_{m,n}^*(\theta) - iA_{\text{TM}} \pi_{m,n}^*(\theta) \right) e^{-im\phi}. \quad (\text{B.8})$$

Acknowledgements

If I did things right during these last four years, every person mentioned in this page should already know before reading it how thankful I am to him/her. In this sense, this section should be unnecessary. Considering that I left the writing of this text for the last day before the deadline, as you may have already imagined, I would actually be quite happy with this implicit type of acknowledging.

Where I grew up we usually have this vision that obvious things are meant either to not be said or to only be said using irony. However, sometimes is not that bad to say nice things even if obvious. Anyway, as there are so many people that I wanted to mention here, I have to confess that I got scared of how much I should write, so I just decided that I'll skip mentioning most of you and I will just mention here the people that contributed more directly to the work. However, I still feel necessary to write the following

```
if not yourself.name in self.section.acknowledgements.text:
    if yourself.boolean_thoughts["I miss my name here"]:
        self.section.acknowledgements.text.append(f"Be sure, {yourself.name}, that
I value all the help and nice moments that we spend together along these four years")
```

This is probably the block of code written in the context of this thesis that I'm more certain about.

Thanks Carsten for your supervision. I really value your effort and your guidance towards the completion of this thesis. I've learnt a lot during these years, but if there is one thing I am satisfied with, it is the group of people I was lucky enough to work with. Thanks for the part of responsibility that falls to you in the building of such a nice group.

If being part of this group was not lucky enough, I was part of another one in Berlin: The Computational Nano Optics group of the Zuse-Institut Berlin. Thanks Sven for your supervision during the time that I spent there and of course to all of you guys for the nice and fun moments we spent together. When one can exchange the terms workmate and friend almost indistinguishably, it should be clear how lucky one is to have fallen into these two groups I've been part of.

To make this short, thanks Martin for the countless times you helped me regarding the FEM simulations and thanks Philipp for introducing and guiding me through the topic of Bayesian optimization, also for the many work we did together. Gràcies Ivan per les discussions sobre scattering electromagnètic, però sobretot per les llargues i disteses xerrades, no sempre, gairebé mai, de física.

As visible, I did not ask anyone for help with the English corrections in this section. This is the only part of the document where one could let himself to do so. To justify it, I could say that this page is a little bit more personal, so it should include also my English mistakes as they come out. If this defence of ignorance does not convince you, don't worry, the actual reason why I did not ask for help is a different one: An extrapolation of

Acknowledgements

the errors I made on this page may give you an idea of how much I should thank Phil and Philipp for their help with the English corrections.

To finalize, thanks to The Bike Team of our group at TFP to help me keeping the mind fresh during the writing process in the middle of the corona lockdown, of course always keeping the 1.5 meters of distance.

Selbstständigkeitserklärung

Eidesstattliche Versicherung gemäß § 13 Absatz 2 Ziffer 3 der Promotionsordnung des Karlsruher Instituts für Technologie (KIT) für die KIT-Fakultät für Physik:

1. Bei der eingereichten Dissertation zu dem Thema
Numerical methods for shape optimization of photonic nanostructures
handelt es sich um meine eigenständig erbrachte Leistung.
2. Ich habe nur die angegebenen Quellen und Hilfsmittel benutzt und mich keiner unzulässigen Hilfe Dritter bedient. Insbesondere habe ich wörtlich oder sinngemäß aus anderen Werken übernommene Inhalte als solche kenntlich gemacht.
3. Die Arbeit oder Teile davon habe ich wie folgt/ bislang nicht¹ an einer Hochschule des In- oder Auslands als Bestandteil einer Prüfungs- oder Qualifikationsleistung vorgelegt.

Titel der Arbeit: Numerical methods for shape optimization of photonic nanostructures
Hochschule und Jahr: KIT-Fakultät für Physik

Art der Prüfungs- oder Qualifikationsleistung: Dissertation

4. Die Richtigkeit der vorstehenden Erklärungen bestätige ich.
5. Die Bedeutung der eidesstattlichen Versicherung und die strafrechtlichen Folgen einer unrichtigen oder unvollständigen eidesstattlichen Versicherung sind mir bekannt.

Ich versichere an Eides statt, dass ich nach bestem Wissen die reine Wahrheit erkläre und nichts verschwiegen habe.

Ort und Datum

Unterschrift

¹Nicht Zutreffendes streichen. Bei Bejahung sind anzugeben: der Titel der andernorts vorgelegten Arbeit, die Hochschule, das Jahr der Vorlage und die Art der Prüfungs- oder Qualifikationsleistung.